COMPUTATION OF BIFURCATIONS FOR THE NAVIER-STOKES EQUATIONS

A thesis submitted to the University of Manchester
for the degree of Doctor of Philosophy
in the Faculty of Engineering and Physical Sciences

2010

Hanadi Hassan Zahed
School of Mathematics

Contents

Word count 60254

List of Tables

List of Figures

The University of Manchester

Hanadi Hassan Zahed
Doctor of Philosophy
Computation of Bifurcations for the Navier-Stokes Equations
August 12, 2010

We investigate a two-dimensional boundary layer flow in a channel with a suction slot on the upper wall by solving the steady Navier-Stokes equations to compute steady state solutions and we investigate their stability using global stability analysis together with linear temporal simulation and a continuation method. Our primary aim in this work is to investigate bifurcations occurring in separated flows at large Reynolds numbers (R). Another motivation is to investigate the stability of a separated flow. The 2D steady Navier-Stokes equations in stream-function (ψ)-vorticity (ω) are solved numerically using a hybrid finite difference and spectral method combined with pseudo arc length continuation techniques to track turning points and bifurcations.

We are able to calculate two branches of solutions and the turning point bifurcation in this particular problem. Global stability results indicate that the first solution on the lower branch, where the separation bubble is short, is stable, while the second solution on the upper branch, where the separation bubble is large, is unstable. The presence of the turning point is confirmed by the changing signs in the eigenvalue spectrum, as it moves from the lower, stable solution branch to the upper, unstable solution branch. The numerical simulation confirms the stability of the lower branch solutions and confirms that the upper branch is unstable; it is also in good agreement with global stability behaviour.

Declaration

No portion of the work referred to in this thesis has been submitted in support of an application for another degree or qualification of this or any other university or other institute of learning.

Copyright Statement

i. The author of this thesis (including any appendices and/or schedules to this thesis) owns any copyright in it (the "Copyright") and s/he has given The University of Manchester the right to use such Copyright for any administrative, promotional, educational and/or teaching purposes.

ii. Copies of this thesis, either in full or in extracts, may be made **only** in accordance with the regulations of the John Rylands University Library of Manchester. Details of these regulations may be obtained from the Librarian. This page must form part of any such copies made.

iii. The ownership of any patents, designs, trade marks and any and all other intellectual property rights except for the Copyright (the "Intellectual Property Rights") and any reproductions of copyright works, for example graphs and tables ("Reproductions"), which may be described in this thesis, may not be owned by the author and may be owned by third parties. Such Intellectual Property Rights and Reproductions cannot and must not be made available for use without the prior written permission of the owner(s) of the relevant Intellectual Property Rights and/or Reproductions.

iv. Further information on the conditions under which disclosure, publication and exploitation of this thesis, the Copyright and any Intellectual Property Rights and/or Reproductions described in it may take place is available

from the Head of the School of Mathematics.

Dedication

To my dear parents, my beloved husband Abdulhadi, and my precious children Mohammed, Hanan and Ahmed.

Acknowledgements

First and foremost, I give thanks to God for the grace and mercy he has shown me. I depend on Him and I could not have accomplished this work without Him.

Words cannot express my deep gratitude to my supervisor, Professor Jitesh Gajjar, for his friendly support, help, and encouragement throughout my research for this thesis. His generosity with his time, his advice and patience were invaluable to me, as was the gracious permission to use his code. It was a great privilege to work with him.

Before all, I want to thank my parents who give me their prayers and unconditional love, my patient and helpful husband Abdulhadi, who made it possible for me to work on this thesis and still keep our family going. I could not have done this without him. And finally, my children, who patiently accepted my absences and who are the blessings in my life.

I like to thank my examiner Prof Stefan Braun and Dr Richard Hewitt for their advice. I would also like to express my heartfelt gratitude to my friends Bharathi Boppana, for her help and much appreciated advice, Aisha Tarmann, for her linguistic assistance, and to all my friends here in the Mathematics Department of Manchester University, as well as all my family and friends in my home country. Finally, my gratitude goes to my friends and colleagues at Taiba University, especially Dr. Hassan Agwo for his academic advice. I am also grateful to my University, Taibah University, for the privilege to study here in the UK.

Chapter 1

Introduction

1.1 Introduction

In the study of fluid dynamics one of the most difficult and fundamental problems is the study of flow separation from a solid body and the resulting global changes in the flow field occurring after this separation.

In this thesis, we investigate the stability and compute solutions and bifurcations of the two-dimensional Navier-Stokes and related equations for boundary layer flow in a channel with suction on the upper wall. We use different methods to obtain a description of the flow structure, especially the formation of laminar separation bubbles in the case of large Reynolds number (Re). To compute steady state solutions and investigate stability and bifurcations, we solve the Navier-Stokes equations using global stability analysis combined with linear temporal simulation and a continuation method.

We also aim to develop the mathematical tools for studying the steady state problem and track bifurcations in separated flows. It is necessary in our research to gain a firm understanding of the steady flow solutions before we work with unsteady state solutions. It is important to identify the parameters which lead

to loss of stability and then use continuation methods to follow bifurcations and investigate the different states and their properties. The main objective will be obtaining the solutions for large Reynolds numbers.

As discussed by Gajjar & Azzam (2004), the correct description of the flow features for large Reynolds numbers is an important aspect of the steady incompressible fluid flow past a circular cylinder problem and others. One of the reasons for computing the steady flow is the need of an accurate solution of the steady flow before a departure from the steady state can be described. Another reason is that steady flow description is the basis of the asymptotic theory for the above mentioned and other related problems. Finally, the techniques developed in the work of Gajjar and Azzam will be applied to the problems included in this work.

Bifurcation theory studies the changes in the qualitative character of the solutions, especially equilibrium solutions of nonlinear systems with variable parameters. A nonlinear system may consist of a system of algebraic, ordinary differential, or partial differential equations. Here we are interested in bifurcation problems governed by the Navier-Stokes equations.

In our efforts to find numerical solutions to the problems described by partial differential equations in this thesis, we employ the finite difference method in x-direction combined with Chebychev collocation in y-direction to discretize the domain. Newton linearization with correction terms is used to linearize the equations and finally, we solve the resulting linear system of equations with a direct solver.

Before starting work with the main problem of our research, we began with the study of two test problems which were used to develop and test the techniques that we came to utilize in our work.

In the following sections we will introduce the basics of our methods which we

have used in this thesis, the spectral method, finite difference method, Chebychev collocation, continuation methods, and Navier-Stokes equations.

Chapter two is devoted to a description of a portion of the boundary layer theory and separation, as well as a review of the relevant literature.

In chapter three, we will discuss in detail the two test problems with all their possible solutions. The performance of the methods will be outlined based on the obtained results.

In chapter four, we present our work with the main problem, the two-dimensional boundary layer flow in a channel with suction on the upper wall. We describe in detail our computations with their results for the basic flow, global stability analysis and bifurcation analysis, as well as linear temporal simulation.

Chapter five studies the different boundary conditions in the two-dimensional boundary layer flow in a channel with suction on the upper wall.

The results of global stability analysis and linear temporal simulation for one of these boundary conditions are described in chapter six.

Finally, the conclusions of our work in this thesis are presented in chapter seven.

1.2 Spectral Methods, Finite Difference Methods, and Chebychev Collocation

Several methods for obtaining the solution of incompressible and steady Navier-Stokes equations, have been used in earlier works, for example, finite difference, finite element, and spectral methods.

1.2.1 Spectral Methods

The point of spectral methods is to describe the function as an expansion in terms of some basis functions, generally orthogonal polynomials, or Fourier approximation trigonometric functions. The most important elements of these are the trial functions (approximating functions) and the test functions (weight functions). For a truncated series expansion of the solution the trial functions are used as the basis functions, whereas we use the test functions to make sure that the differential equation is satisfied by the truncated series expansion as closely as possible. We can arrive at this by minimizing the residual, which is the error in the differential equation resulting from the use of truncated expansion, in place of the exact solution, in relations to a suitable norm. The residual must satisfy a suitable orthogonality condition in relations to each of the test functions.

Spectral methods give us many advantages over finite difference and related methods and they offer a whole different way for getting solutions of ordinary differential equations, or partial differential equations. One of these advantages is the concept of spectral accuracy. Using spectral methods with an increased number of points, the accuracy of the approximation (for smooth functions) increases exponentially. On the other hand, finite difference method truncation error is reduced by a factor of 4 only when the number of points of a second order method is doubled. For a more detailed explanation, see Canuto *et al.* (1987)

1.2.2 Finite Differences

There are many practical problems in applied sciences and engineering which can be illustrated by using mathematical models constructed with partial differential equations. There are also several numerical techniques to solve these problems,

for example, the method of finite differences which depends on formulae to approximate the derivatives.

Assume that a function ϕ and its derivatives are single-valued functions and continuous. Using a Taylor's series expansion, we have

$$\phi(x+h) = \phi(x) + h\phi'(x) + \frac{h^2}{2!}\phi''(x) + \frac{h^3}{3!}\phi'''(x) + \dots \tag{1.1}$$

$$\phi(x-h) = \phi(x) - h\phi'(x) + \frac{h^2}{2!}\phi''(x) - \frac{h^3}{3!}\phi'''(x) + \dots \tag{1.2}$$

for small h.

Subtracting equations (1.1) and (1.2), we obtain

$$\left(\frac{\partial\phi}{\partial x}\right) = \frac{\phi(x+h) - \phi(x-h)}{2h} + O\left(h^2\right). \tag{1.3}$$

Also, adding equations (1.1) and (1.2), we obtain

$$\left(\frac{\partial^2\phi}{\partial x^2}\right) = \frac{\phi(x+h) - 2\phi(x) + \phi(x-h)}{h^2} + O\left(h^2\right). \tag{1.4}$$

Now, considering the function $\phi = \phi(x, y)$ and dividing the domain of solution in the $x - y$ plane into equal rectangles (or equal squares, depending on the problem) as shown in figure (1.1), where $\Delta x = h$ & $\Delta y = k$, the node (x_i, y_j) can be determined by:

$x_i = x_0 + i\ \Delta x \qquad , \qquad y_j = y_0 + j\Delta y.$

At the points (x_i, y_j) we try to approximate a derivative of a function $\phi(x, y)$. We use $\omega_{i,j}$ as denoting the approximate value of $\phi(x, y)$ at the point (x_i, y_j).

The first and second derivatives in x may be approximated by,

$$\left(\frac{\partial\phi}{\partial x}\right)_{i,j} = \frac{\omega_{i+1,j} - \omega_{i-1,j}}{2h} + O\left(h^2\right), \tag{1.5}$$

$$\left(\frac{\partial^2\phi}{\partial x^2}\right)_{i,j} = \frac{\omega_{i+1,j} - 2\omega_{i,j} + \omega_{i-1,j}}{h^2} + O\left(h^2\right). \tag{1.6}$$

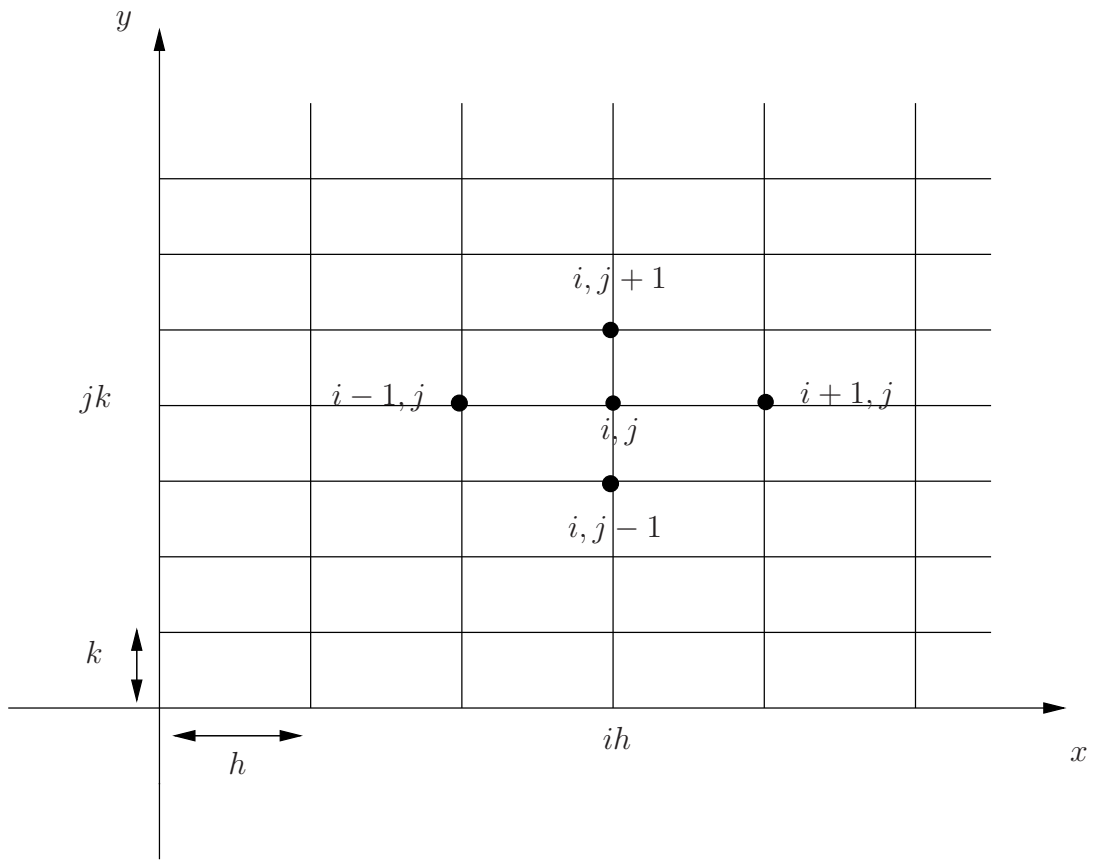

Figure 1.1: Finite difference approximations.

These approximations are centered at the points (x_i, y_j), and are called central-difference-approximations, (we use the Taylor series in the variable x for each point in the interior of the grid to generate the centered-difference formula). The truncation errors $O(h^2)$ which have arisen from replacing the first and second derivatives $\left(\frac{\partial \phi}{\partial x}\right)_{i,j}$ and $\left(\frac{\partial^2 \phi}{\partial x^2}\right)_{i,j}$ with the approximation, can be easily obtaind by using Tayler series expansion for $\omega(i+1, j)$ and $\omega(i-1, j)$ for small h.

When we use the method of finite differences to solve a boundary value problem every derivative appearing in the equation, as well as in the boundary condition, is replaced by an appropriate difference approximation. From the finite difference techniques central differences are preferably used for reasons of greater accuracy. See Conte & de Boor (1981) and Burden & Faires (2001).

1.2.3 Chebychev Collocation

Collocation is the name for one of a number of different spectral methods which are distinguished by the choices of test functions. Collocation methods are employed with respect to the physical space values of the unknown function and they use the values of the function at specific physical points as the basic representation and thus require the differential equation to be satisfied exactly at the collocation points. Expansion functions are only used to evaluate derivatives. Generally the physical grid points are identical with the collocation points for the differential eaquation as well as those for the boundary conditions. See Canuto *et al.* (1987).

Here we will discuss one of the spectral methods, which is called Chebychev collocation. In Chebychev collocation, we use Chebychev polynomials to represent a function in terms of expansions. The Chebychev polynomials are orthogonal on $[-1, 1]$ with respect to the test function or weight function w, where

$$w = \frac{1}{\sqrt{1-x^2}}. \tag{1.7}$$

In Chebychev collocation, a function is described in terms of expansions using Chebychev polynomials which are defined by

$$T_n(x) = \cos\left(n\cos^{-1}(x)\right), \qquad \text{for each} \qquad n \geq 0 \qquad \text{and} \qquad x \in [-1, 1]. \tag{1.8}$$

Thus

$$T_0(x) = \cos 0 = 1 \qquad \text{and} \qquad T_1(x) = \cos\left(\cos^{-1}(x)\right) = x. \tag{1.9}$$

For $n \geq 1$, by substituting $\theta = \cos^{-1}(x)$ into equation (1.8) we get this equation,

$$T_n(\theta(x)) \equiv T_n(\theta) = \cos(n\theta), \qquad \text{where} \qquad \theta \in [0, \pi]. \tag{1.10}$$

We get a recurrence relation by noting that,

$$T_{n+1}(\theta) = \cos(n\theta)\cos\theta - \sin(n\theta)\sin\theta, \tag{1.11}$$

and

$$T_{n-1}(\theta) = \cos(n\theta)\cos\theta + \sin(n\theta)\sin\theta. \tag{1.12}$$

By adding these equations we get,

$$T_{n+1}(\theta) = 2\cos(n\theta)\cos\theta - T_{n-1}(\theta). \tag{1.13}$$

Returning to the variable x, equation (1.13), has the form

$$T_{n+1}(x) = 2xT_n(x) - T_{n-1}(x), \tag{1.14}$$

from which we can find $T_2(x), T_3(x), \ldots$ etc. The recurrence relation defined by (1.14) shows that $T_n(x)$ is a polynomial of degree n with leading coefficient 2^{n-1}.

Further, it is clear from (1.8) that,

$$|T_n(x)| \leq 1, \qquad \text{for all } -1 \leq x \leq 1. \tag{1.15}$$

Chebychev polynomials are used to minimize the approximation error and can be also used to reduce the degree of an approximating polynomial with very little loss of accuracy, because they have a minimum maximum absolute value that is spread evenly on an interval, see Burden & Faires (2001).

In a collocation method we may represent a smooth function with respect to its values at a set of discrete points. By analytic derivatives of the interpolating polynomial, we approximate derivatives of the function. The following Gauss-Lobatto points (1.16), are commonly used.

$$y_j = \cos\left(\frac{j\pi}{N}\right) \qquad j = 0, 1, \ldots, N. \tag{1.16}$$

At these points, we suppose that the given function is approximated and we describe by u_j the approximate values of the function $u(y_j)$.

A given differential equation requires us to approximate the derivatives at the node points. Following Canuto *et al.* (1987) and Trefethen (2000), we can write $\left(\frac{du}{dy}\right)_{i,p} = \sum_{j=0}^{N} D_{p,j} u_{i,j}$, where $D_{p,j}$ are the elements of the Chebychev collocation differentiation matrix $\mathbf{D}$. The elements of the matrix $\mathbf{D}$ are given by

$$D_{p,j} = \begin{cases} \frac{c_p(-1)^{p+j}}{c_j(y_p - y_j)} & p \neq j, \\ -\frac{y_j}{2\left(1-y_j^2\right)} & 1 \leq p = j \leq N-1, \\ \frac{2N^2+1}{6} & p = j = 0, \\ -\frac{2N^2+1}{6} & p = j = N, \end{cases} \tag{1.17}$$

where

$$c_p = \begin{cases} 2 & p = 0, N, \\ 1, & \text{otherwise} \end{cases} \tag{1.18}$$

Thus the first and second derivatives in matrix form can be written as

$$\begin{pmatrix} \frac{d\omega_0}{dy} \\ \frac{d\omega_1}{dy} \\ \vdots \\ \frac{d\omega_N}{dy} \end{pmatrix} = \mathbf{D} \begin{pmatrix} \omega_0 \\ \omega_1 \\ \vdots \\ \omega_N \end{pmatrix}, \qquad \textit{and} \qquad \begin{pmatrix} \frac{d^2\omega_0}{dy^2} \\ \frac{d^2\omega_1}{dy^2} \\ \vdots \\ \frac{d^2\omega_N}{dy^2} \end{pmatrix} = \mathbf{D}^2 \begin{pmatrix} \omega_0 \\ \omega_1 \\ \vdots \\ \omega_N \end{pmatrix}. \tag{1.19}$$

where $\mathbf{D}$ is the first derivative and $\mathbf{D^2}$ is the second derivative which are calculated by multiplying the first order matrix by itself.

The details of the methods used in this section are described in Canuto *et al.* (1987), Fornberg (1996), Trefethen (2000) and Burden & Faires (2001).

1.3 Continuation Methods

In this section, we discuss continuation methods as described in Seydel (1994), in more detail, to help us and the reader understand the analysis of our work in the next chapters.

Here, the continuation method is explained based on the following system of nonlinear algebraic equations,

$$\mathbf{f}(\mathbf{y}, \lambda) = 0, \tag{1.20}$$

which defines implicity curves of solutions and here $\mathbf{y}$ denotes an n-dimensional vector. In this work, $\mathbf{f}$ must be smooth enough that all necessary derivatives exist. Also, here we want to calculate the bifurcation diagram for the fixed points of an equation (1.20). The easiest way to follow the branches numerically is to follow the next recursive procedure.

First, we approximate an initial solution $\left(\mathbf{y}^{(1)}, \lambda_{(1)}\right)$ and then use the continuation method (predictor-corrector) to get further solutions $\left(\mathbf{y}^{(2)}, \lambda_{(2)}\right)$, $\left(\mathbf{y}^{(3)}, \lambda_{(3)}\right)$, ..., on the branch until one reaches a goal point.

From the above discussion, we note that each step is split with predictor-corrector methods into two steps as follows

$$\left(\mathbf{y}^{(j)}, \lambda_{(j)}\right) \overset{predictor}{\longrightarrow} \left(\bar{\mathbf{y}}^{(j)}, \bar{\lambda}_{(j)}\right) \overset{corrector}{\longrightarrow} \left(\mathbf{y}^{(j+1)}, \lambda_{(j+1)}\right),$$

where $j = 1, 2, 3, \ldots$

In the first step, we use an explicit method for the predictor, while in the second one, we use an implicit method, for the corrector, see Figure (1.2).

The predictor $\left(\bar{\mathbf{y}}^{(j)}, \bar{\lambda}_{(j)}\right)$ is not generally a solution of the equation $\mathbf{f}(\mathbf{y}, \lambda) = 0$. It just produces an initial guess for corrector iterations that leads us to a solution of the equation $\mathbf{f}(\mathbf{y}, \lambda) = 0$. The corrector iteration is shown by dots in Figure (1.2). Step length or step size is the name for the distance between two solutions $\left(\mathbf{y}^{(j)}, \lambda_{(j)}\right)$ and $\left(\mathbf{y}^{(j+1)}, \lambda_{(j+1)}\right)$ which follow each other. In particular when $\mathbf{y}^{(j+1)}$ is not yet known we use the step size freely because this distance is not easy to measure. Besides equation $\mathbf{f}(\mathbf{y}, \lambda) = 0$, we need a connection that gives us the location of a solution on the branch.

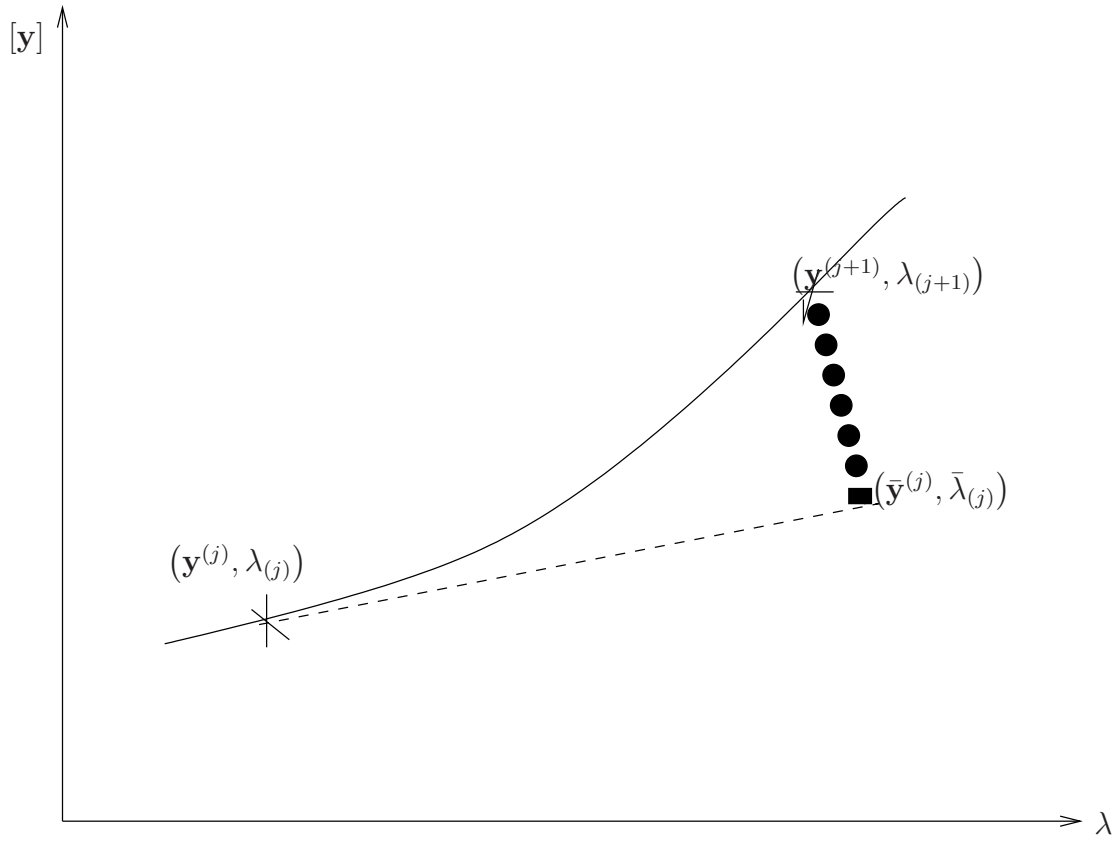

Figure 1.2: Predictor-corrector principle.

Continuation methods vary as predictor, parameterization strategy, corrector, and step length control change. Actually, the first three items can be chosen independently of each other, but the last one which is the step-length control must be related to the predictor, the corrector, and the underlying parameterization, as mentioned in Seydel (1994).

1.3.1 Predictors

Here we discuss and use ODE methods, as discussed in Seydel (1994), which are ordinary differential equations methods based on $\mathbf{f}(\mathbf{y}, \lambda)$ and its derivatives.

If we determine $\left(\mathbf{y}^{(1)}, \lambda_{(1)}\right)$ it follows that the initial iterator for $\mathbf{y}$ is $\bar{\mathbf{y}}^{(1)} = \mathbf{y}^{(1)}$ and $\bar{\lambda}_{(1)} = \lambda_{(1)}$, as shown in Figure (1.3).

We iterate by using Newton's method after having obtained the initial iterator by moving horizontally from $\left(\mathbf{y}^{(1)}, \lambda_{(1)}\right)$.

In Figure (1.4), we show that by following the tangent line to the branch at $\left(\mathbf{y}^{(1)}, \lambda_{(1)}\right)$ we get a better initial iterator.

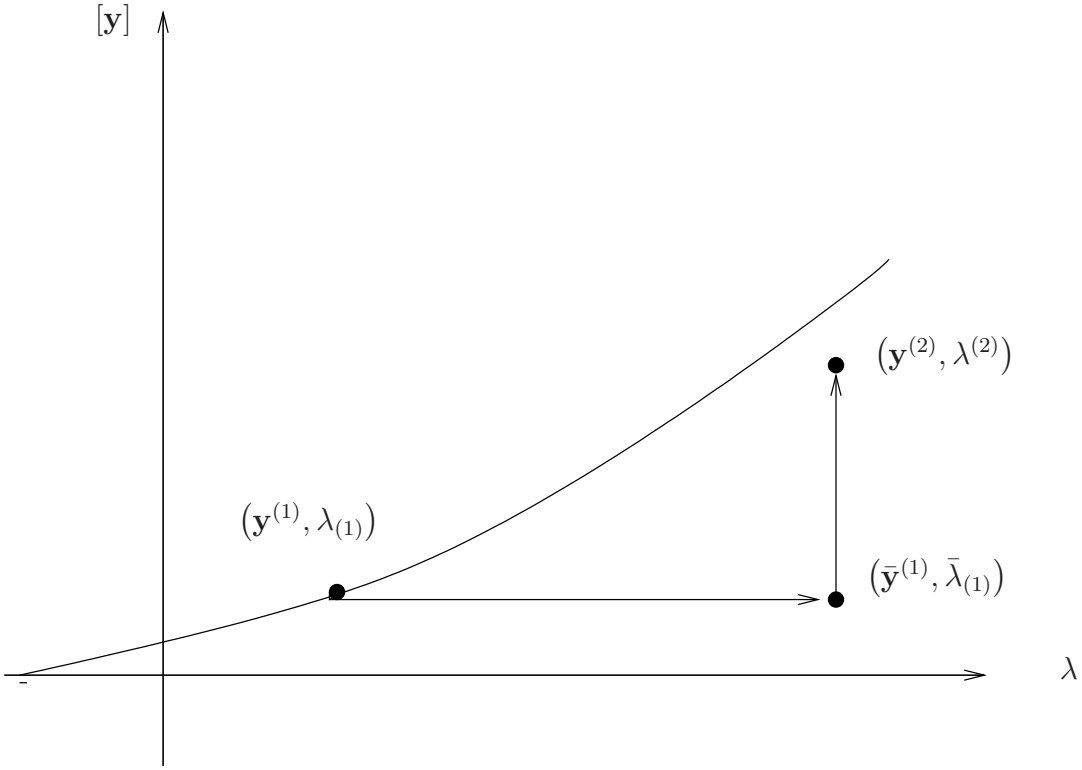

Figure 1.3: The initial iterate and the next iterate using continuation method.

We consider a small change $d\mathbf{f}$ of the equation $\mathbf{f}(\mathbf{y}, \lambda) = 0$ to obtain the slope of the tangent line and so arrive at,

$$0 = d\mathbf{f} = \mathbf{f}_{\mathbf{y}} d\mathbf{y} + \mathbf{f}_{\lambda} d\lambda. \tag{1.21}$$

From the above equation we get the slope of the branch $\frac{d\mathbf{y}}{d\lambda}$ as,

$$\frac{d\mathbf{y}}{d\lambda} = -{\mathbf{f}_{\mathbf{y}}}^{-1} \mathbf{f}_{\lambda}, \tag{1.22}$$

under the condition that ${\mathbf{f}_{\mathbf{y}}}^{-1}$ exist or $det\left(\mathbf{f}_{\mathbf{y}}\left(\mathbf{y}^{(1)}, \lambda_{(1)}\right)\right) \neq 0$.

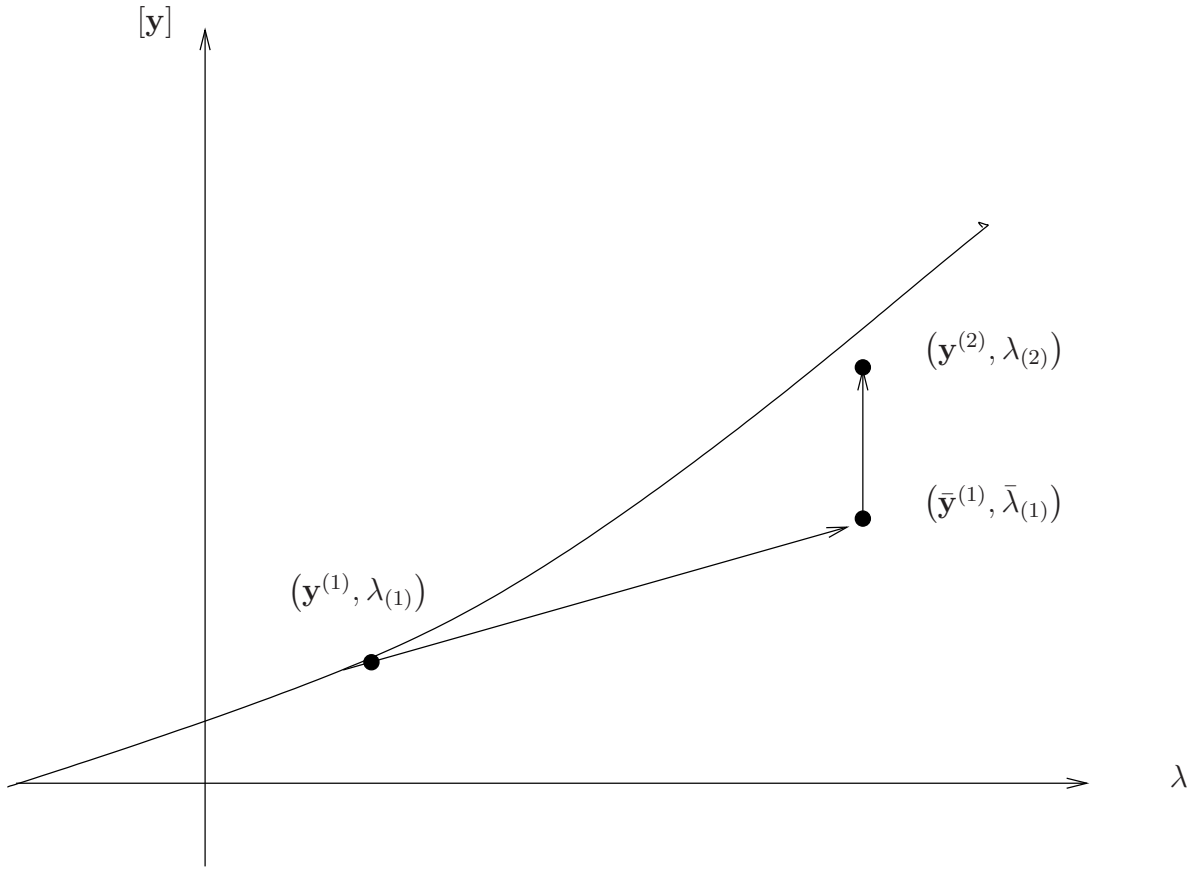

Figure 1.4: The initial iterate and the next iterate using continuation method.

To get the branch on which $\left(\mathbf{y}^{(1)}, \lambda_{(1)}\right)$ lies, we must integrate this system starting from the initial value $\left(\mathbf{y}^{(1)}, \lambda_{(1)}\right)$. If we have the singularity, when $\mathbf{f_y} = 0$, this procedure fails and these points are turning points (bifurcation points).

To overcome this singularity we change the parameter to the arclength s. In this case we have $\mathbf{y} = \mathbf{y}(s), \lambda = \lambda(s)$ and $\mathbf{f} = \mathbf{f}\left(\mathbf{y}(s), \lambda(s)\right)$.

Therefore, we get

$$0 = \mathbf{f_y}\frac{d\mathbf{y}}{ds} + f_\lambda \frac{d\lambda}{ds}, \tag{1.23}$$

where the following relation is satisfied by the arclength s,

$$\left(\frac{dy_1}{ds}\right)^2 + \cdots + \left(\frac{dy_n}{ds}\right)^2 + \left(\frac{d\lambda}{ds}\right)^2 = 1. \tag{1.24}$$

An implicit system of $n+1$ differential equations for the $n+1$ unknowns

$$\left(\frac{dy_1}{ds}\right), \ldots, \left(\frac{dy_n}{ds}\right), \left(\frac{d\lambda}{ds}\right), \tag{1.25}$$

is expressed by equations (1.23) and (1.24).

At the point $\left(\mathbf{y}^{(1)}, \lambda_{(1)}\right)$ we get an equation for the slope of the branch by differentiating the equations $\mathbf{f}\left(\mathbf{y}\left(s\right); \lambda\left(s\right)\right) = 0$ with respect to s, as

$$\mathbf{J}\frac{d\mathbf{y}}{ds} + f_\lambda \frac{d\lambda}{ds} = 0, \tag{1.26}$$

where $\mathbf{J} = \mathbf{f}_\mathbf{y}$ is the Jacobian matrix of first-order partial derivatives of $\mathbf{f}$ with respect to $\mathbf{y}$. The definition of s in vector notation is

$$\left(\frac{d\mathbf{y}}{ds}\right)^T \left(\frac{d\mathbf{y}}{ds}\right) + \left(\frac{d\lambda}{ds}\right)^2 = 1. \tag{1.27}$$

In the initial iterate for Newton's method, we calculate the derivatives $\mathbf{J}$ and $\frac{d\lambda}{ds}$ and then get,

$$\bar{\mathbf{y}}^{(1)} = \mathbf{y}^{(1)} + \frac{d\mathbf{y}}{ds}\Delta s, \tag{1.28}$$

$$\bar{\lambda}_{(1)} = \lambda_{(1)} + \frac{d\lambda}{ds}\Delta s. \tag{1.29}$$

To obtain $\frac{d\mathbf{y}}{ds}$ and $\frac{d\lambda}{ds}$, we rewrite equation (1.26) as,

$$\mathbf{J}\frac{d\mathbf{y}}{ds} = -\mathbf{f}_\lambda \ \frac{d\lambda}{ds}. \tag{1.30}$$

To determine $\frac{d\mathbf{y}}{ds}$ in terms of $\frac{d\lambda}{ds}$ we can solve the equation (1.30), if $\mathbf{J}$ is non-singular. The critical point which satisfies $\mathbf{f}_\mathbf{y}\left(\mathbf{y}^{(1)}, \lambda_{(1)}\right) = 0$, is called a turning point (limit point) when $\mathbf{f}_\lambda\left(\mathbf{y}^{(1)}, \lambda_{(1)}\right) \neq 0$ and a bifurcation point when $\mathbf{f}_\lambda\left(\mathbf{y}^{(1)}, \lambda_{(1)}\right) = 0$.

Then, to determine $\frac{d\mathbf{y}}{ds}$ and $\frac{d\lambda}{ds}$, assuming $\mathbf{z} = \frac{d\mathbf{y}}{ds}/\frac{d\lambda}{ds}$, equation (1.30) can be written as,

$$\mathbf{J}\mathbf{z} = -\mathbf{f}_\lambda, \tag{1.31}$$

if $\mathbf{z}$ is a unique solution of (1.31), then $\frac{d\mathbf{y}}{ds} = \mathbf{z}\frac{d\lambda}{ds}$. After substituting $\frac{d\mathbf{y}}{ds}$ into equation (1.27) we can easily get,

$$\frac{d\lambda}{ds} = \pm\frac{1}{\sqrt{\mathbf{z}^T\mathbf{z}+1}}, \tag{1.32}$$

$$\frac{d\mathbf{y}}{ds} = \pm\frac{\mathbf{z}}{\sqrt{\mathbf{z}^T\mathbf{z}+1}}. \tag{1.33}$$

The correct choice of sign at the initial point of a branch ensures that we can continue the branch. First, let the vector between the last two points be $(\Delta\mathbf{y}, \Delta\lambda)$ and after that choose the sign so that

$$\begin{pmatrix}\Delta\mathbf{y}\\ \Delta\lambda\end{pmatrix}^T \begin{pmatrix}d\mathbf{y}/ds\\ d\lambda/ds\end{pmatrix} > 0. \tag{1.34}$$

This ensures we are continuing (along the arc) in the same direction as in our previous step.

We can update $\mathbf{y}^{(1)}, \lambda_{(1)}$ to get $\bar{\mathbf{y}}^{(1)}, \bar{\lambda}_{(1)}$ as,

$$\bar{\mathbf{y}}^{(1)} = \mathbf{y}^{(1)} + \frac{d\mathbf{y}}{ds}\Delta s, \tag{1.35}$$

$$\bar{\lambda}_{(1)} = \lambda_{(1)} + \frac{d\lambda}{ds}\Delta s. \tag{1.36}$$

1.3.2 Corrector

Corrector methods are typically used to solve the equation $\mathbf{f}(\mathbf{y}, \lambda) = 0$. (See Seydel (1994)).

To begin with, we characterize correctors that result from a predictor, as shown in figure (1.5). The parameterizing equation determines the final limit $\left(\mathbf{y}^{(2)}, \lambda_{(2)}\right)$ of the corrector iteration. Here we use arclength parameterization (step length Δs).

Then, for the $(n+1)$ - dimensional vector $\mathbf{Y} = (\mathbf{y}, \lambda)$, we consider one step

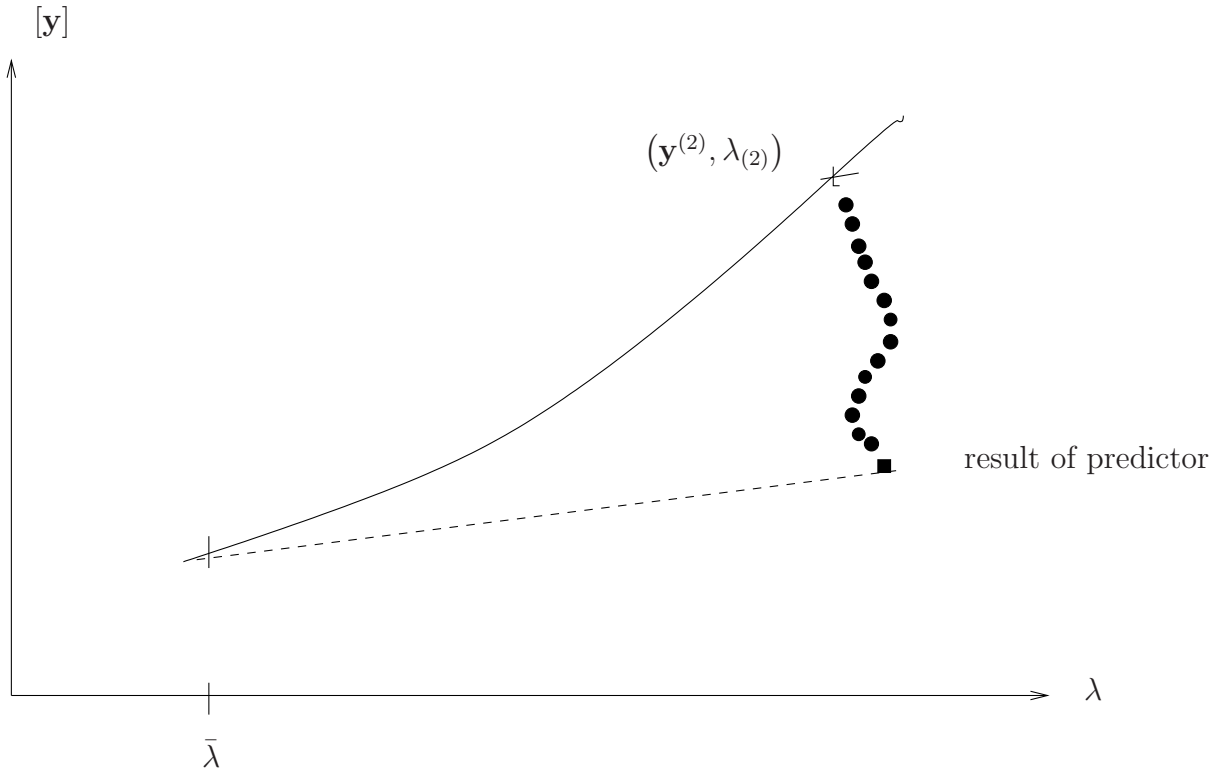

Figure 1.5: Iteration of a corrector.

of the Newton iteration.

$$\mathbf{f}_{\mathbf{y}}\Delta\mathbf{y} + \mathbf{f}_{\lambda}\Delta\lambda = -\mathbf{f}\left(\mathbf{y}^{(\nu)}, \lambda_{(\nu)}\right), \tag{1.37}$$

$$\mathbf{y}^{(\nu+1)} = \mathbf{y}^{(\nu)} + \Delta\mathbf{y} \quad ; \quad \lambda_{(\nu+1)} = \lambda_{(\nu)} + \Delta\lambda. \tag{1.38}$$

The n equations in $n+1$ unknown $\Delta\mathbf{y}, \Delta\lambda$ make up the system of linear equations.

In order to complete the system we can attach one more equation which parameterizes the course of the corrector iteration.

A sequence of corrector iterations $\mathbf{Y}^{(\nu)}$ defined by equation (1.37)

$$\left(\mathbf{y}^{(\nu)}, \lambda_{(\nu)}\right), \qquad \nu = 1, 2, \ldots, \tag{1.39}$$

and beginning with the predictor,

$$\left(\bar{\mathbf{y}}^{(1)}, \bar{\lambda}_{(1)}\right) := \left(\mathbf{y}^{(1)}, \lambda_{(1)}\right), \tag{1.40}$$

converge to a solution $\left(\mathbf{y}^{(2)}, \lambda_{(2)}\right)$ shown by dots in Figure (1.2), and there hits the branch that is the intersection of the curve defined by $\mathbf{f}(\mathbf{y}, \lambda) = 0$.

Since $\mathbf{f}\left(\mathbf{y}^{(\nu)}, \lambda_{(\nu)}\right) \neq 0$ in general we can obtain Newton's method from the equation $\mathbf{f}\left(\mathbf{y}^{(\nu)} + \Delta\mathbf{y}; \lambda_{(\nu)} + \Delta\lambda\right) = 0$ where,

$$\mathbf{f}\left(\mathbf{y}^{(\nu)} + \Delta\mathbf{y}; \lambda_{(\nu)} + \Delta\lambda\right) = \mathbf{f}\left(\mathbf{y}^{(\nu)}, \lambda_{(\nu)}\right) + \mathbf{J}\left(\mathbf{y}^{(\nu)}, \lambda_{(\nu)}\right) \Delta\mathbf{y}^{(\nu)} + \frac{\partial \mathbf{f}}{\partial \lambda}\left(\mathbf{y}^{(\nu)}, \lambda_{(\nu)}\right) \Delta\lambda^{(\nu)}, \tag{1.41}$$

so

$$\mathbf{f}\left(\mathbf{y}^{(\nu)}, \lambda_{(\nu)}\right) + \mathbf{J}\left(\mathbf{y}^{(\nu)}, \lambda_{(\nu)}\right) \Delta\mathbf{y}^{(\nu)} + \frac{\partial \mathbf{f}}{\partial \lambda}\left(\mathbf{y}^{(\nu)}, \lambda_{(\nu)}\right) \Delta\lambda^{(\nu)} = 0, \tag{1.42}$$

or

$$\mathbf{J}\left(\mathbf{y}^{(\nu)}, \lambda_{(\nu)}\right) \Delta\mathbf{y}^{(\nu)} + \frac{\partial \mathbf{f}}{\partial \lambda}\left(\mathbf{y}^{(\nu)}, \lambda_{(\nu)}\right) \Delta\lambda^{(\nu)} = -\mathbf{f}\left(\mathbf{y}^{(\nu)}, \lambda_{(\nu)}\right). \tag{1.43}$$

We need to add one more equation to the resulting system to obtain a unique solution.

In order to obtain a unique solution, we assume that the iterates move perpendicular to the direction of the previous point on the branch, this yields that

$$\left(\mathbf{y}^{(\nu)} - \bar{\mathbf{y}}_k\right)^T \Delta\mathbf{y}^{(\nu)} + \left(\lambda^{(\nu)} - \bar{\lambda}_k\right)^T \Delta\lambda^{(\nu)} = 0, \tag{1.44}$$

equations (1.43) and (1.44) can be written in matrix form as,

$$\begin{pmatrix} \mathbf{J}\left(\mathbf{y}^{(\nu)}, \lambda_{(\nu)}\right) & \frac{\partial \mathbf{f}}{\partial \lambda}\left(\mathbf{y}^{(\nu)}, \lambda_{(\nu)}\right) \\ \left(\mathbf{y}^{(\nu)} - \bar{\mathbf{y}}_k\right)^T & \left(\lambda^{(\nu)} - \bar{\lambda}_k\right)^T \end{pmatrix} \begin{pmatrix} \Delta\mathbf{y}^{(\nu)} \\ \Delta\lambda^{(\nu)} \end{pmatrix} = \begin{pmatrix} -\mathbf{f}\left(\mathbf{y}^{(\nu)}, \lambda_{(\nu)}\right) \\ 0 \end{pmatrix}. \tag{1.45}$$

where

$$\mathbf{y}^{(\nu+1)} = \mathbf{y}^{(\nu)} + \Delta\mathbf{y}^{(\nu)}, \tag{1.46}$$

$$\lambda_{(\nu+1)} = \lambda_{(\nu)} + \Delta\lambda^{(\nu)}, \tag{1.47}$$

and we continue until we are successful in obtaining convergence, by iterating the procedure. The calculation of the Jacobian in each step gives appropriate approximations for the next step.

Solutions are sought by this algorithm preferably at pre-determined intervals of arclength Δs, rather than of the parameter $\Delta\lambda$.

During each Newton iteration, using a presumed value of λ , we compute $\mathbf{J}, \mathbf{f}$ and $\Delta\mathbf{y}$. At each iteration, both λ and the solution $\mathbf{y}$ must be updated for the solution of the augmented system.

In Salinger *et al.* (2002) (LOCA), the bordering algorithm uses the sparse nature of $\mathbf{J}$ to solve instead,

$$\mathbf{Ja} = -\mathbf{f}, \tag{1.48}$$

$$\mathbf{Jb} = -\frac{\partial \mathbf{f}}{\partial \lambda}, \tag{1.49}$$

where $\mathbf{a}$ and $\mathbf{b}$ are temporary vectors. We find the new updates by

$$\Delta\lambda = -\left(n + \left(\mathbf{y}^{(\nu)} - \bar{\mathbf{y}}_k\right)^T \cdot \mathbf{a}\right) / \left(\frac{\partial \lambda}{\partial s} + \left(\mathbf{y}^{(\nu)} - \bar{\mathbf{y}}_k\right)^T \cdot \mathbf{b}\right), \tag{1.50}$$

$$\Delta\mathbf{y} = \mathbf{a} + \Delta\lambda\mathbf{b}. \tag{1.51}$$

This way is better computationally than to build the $(N+1)\times(N+1)$ (1.45) system (provided $\mathbf{J}$ is not close to being singular) and solve it once, since the resulting matrix would be more dense than the original Jacobian.

1.3.3 Parameterization

Seydel (1994) describes a branch as a connected curve consisting of points in $(\mathbf{y}, \lambda)$ space which are solutions of $\mathbf{f}(\mathbf{y}, \lambda) = 0$. This curve has to be parameterized. When we introduce parameterization we can calculate terms like the previous solution because parameterization is a mathematical way to determine each solution on the branch. It is a kind of measure along the branch. Even though the control variable λ seems to be the first choice of parameter because it has the advantage of having physical significance, we can encounter difficulties at turning points.

We use a general parameterization for the branch, assuming that there is a variable s, so that the branch can be written as $(\mathbf{y}(s); \lambda(s))$, thus we do not have to decide which parameterization we will use. Our preferred parameterization is always arclength, which is the obvious choice for s, even though several parameterizations are possible.

1.3.4 Arclength

As described by Seydel (1994) and cited in the previous section, to parameterize a branch, arclength s can be used. It is defined by the relation

$$\left(\frac{d\lambda}{ds}\right)^2 + \left(\frac{d\mathbf{y}}{ds}\right)^2 = 1. \tag{1.52}$$

In this case we do not face a problem at turning points, because this choice means pulling the imaginary particle in the direction tangent to the branch. Multiplying the arclength equation (1.24) by ds^2, we get a corresponding equation $\mathbf{f}(\mathbf{y}, \lambda, s) = 0$, for which resulting parameterizing equation has the form

$$0 = \sum_{i=1}^{n} \left(y_i - y_i(s_j)\right)^2 + \left(\lambda - \lambda(s_j)\right)^2 - \left(s - s_j\right)^2. \tag{1.53}$$

At discretized arclength distance $\Delta s = s - s_j$, we fix the solution $(\mathbf{y}(s), \lambda(s))$ by joining equation (1.53) with equation $\mathbf{f}(\mathbf{y}, \lambda) = 0$, if the solution calculated earlier during continuation is $(\mathbf{y}^j, \lambda_j) = (\mathbf{y}(s_j), \lambda(s_j))$.

1.4 Navier-Stokes Equations

The Navier-Stokes equations are the basic equations in fluid dynamics. As described by Canuto *et al.* (1987), the incompressible Navier-Stokes equations basically comprise four different formulations, i.e., streamfunction-vorticity, primitive

variable (velocity and pressure), streamfunction and velocity-vorticity formulations.

On a domain Ω, the non dimensional incompressible Navier-Stokes equations are written as,

$$\mathbf{u}_t + \mathbf{u} \cdot \nabla \mathbf{u} = -\nabla p + \frac{1}{Re} \nabla^2 \mathbf{u}, \tag{1.54}$$

$$\nabla \cdot \mathbf{u} = 0, \tag{1.55}$$

where $\mathbf{u}$ is the velocity vector, p is the pressure and Re is the Reynolds number.

Equation (1.54) is called the momentum equation, and equation (1.55) is called the continuity constraint equation. For the pressure no initial or boundary conditions are necessary.

Vorticity ($\boldsymbol{\omega}$) is one of the characteristics of a flow and is defined by

$$\boldsymbol{\omega} = \nabla \times \mathbf{u}. \tag{1.56}$$

It is the term for the local rotation rate of the fluid. Taking the curl of equation (1.54) we obtain a dynamical equation for the vorticity in the form,

$$\boldsymbol{\omega}_t + \mathbf{u} \cdot \nabla \boldsymbol{\omega} = \boldsymbol{\omega} \cdot \nabla \mathbf{u} + \frac{1}{Re} \nabla^2 \boldsymbol{\omega}. \tag{1.57}$$

In two-dimensional flow, the streamfunction ψ can be combined with the vorticity ω to yield a concise description for this flow. The streamfunction relation to the velocity is expressed by

$$u = \psi_y, \tag{1.58}$$

$$v = -\psi_x, \tag{1.59}$$

and to the vorticity by

$$\nabla^2 \psi = -\omega, \tag{1.60}$$

where $\boldsymbol{\omega} = (0, 0, \omega)$ and $\mathbf{u} = (u, v, 0)$.

Equation (1.54) reduces to

$$\omega_t + \psi_y \omega_x - \psi_x \omega_y = \frac{1}{Re} \nabla^2 \omega. \tag{1.61}$$

The streamlines with ψ = constant give the instantaneous direction of the flow. The corresponding boundary conditions depend on the problem.

1.5 Some Historical Facts About the Continuation Method

In the last half of the last century, two new techniques have been introduced to obtain the numerical solution of nonlinear system of equations. The first technique is known as predictor-corrector continuation method, while the second one is known as a piecewise linear (PL) method.

Many scientists and engineers used the first technique to improve the convergence properties, especially when adequate starting values are not available. Lemke-Howson used the second technique, see (Lemke & Howson (1964)) in solving nonlinear complementarity problems to calculate fixed points of set-valued maps. In this work we are dealing with the first technique (predictor-corrector continuation method).

Modern mathematics has found that continuation methods are valuable tools. Basic ideas of continuation were developed in the 1960s and published in early papers by Haselgrove (1961) and Klopfenstein (1961). The analysis of these methods has been developed in 1970s and later by Keller (1977) and others, even though some basic ideas had appeared earlier than that, see Cliffe *et al.* (2000). From the 1960s and later, many authors used continuation methods to research problems in applications, such as flow research, chemical reactions, solidification, and combustion, see Seydel (1994). Many scientists and researchers are still

adding more developments to the predictor-corrector continuation method.

There are many developments for the continuation method which became essential for many steplength algorithms. Time has shown that simple continuation principles are applied successfully to most problems and many authors used them successfully in many applications. The developments many of the methods are described in numerous books such as Allgower & Georg (1990), Seydel (1994), and Govaerts (2000).

Many developments for the numerical analysis of the continuation methods have been reported in the late 1970s by numerous authors. As a direct result of these developments, several codes for the method became available, beginning with PITCON (see Rheinboldt (1986)) and AUTO (see Doedel & Kernevez (1986)). In recent times AUTO added some developments to the code, including the discretization of the boundary value problems, steady state, and time dependence. The PITCON code deals with parameter-dependent nonlinear problems, see Cliffe *et al.* (2000).

In the last years there have been extensive applications of the numerical bifurcation methods to different problems in fluid dynamics. Comprehensive treatment of numerical bifurcation techniques have also been introduced.

Discretization errors of bifurcation problems have been analyzed. Multiparameter problems and the construction of numerical approaches based on the use of singularity theory became the focus of attention after reliable algorithms for numerical path following and simple bifurcation phenomena were devised.

One of the main aims of numerical continuation methods is the accurate determination of certain points on a smooth curve. For example, turning points may be of concern in the case of the equation representing a branch of solutions for a nonlinear eigenvalue problem which involves the eigenvalue parameter λ. Such a turning point can signify a change in the stability of the solutions in

engineering and physics applications. There is an enormous amount of literature for calculating turning points, see for example Seydel (1994).

At present, continuation is used widely, even though not one particular continuation method can be recommended exclusively. A vast number of possible continuation methods can be obtained from combining the different elements (predictor, parameterization, corrector, step-control) in a variety of ways. Each one of these ways has its own merit. An encouraging fact for engineers and scientists is that simple continuation principles work sufficiently well, even on complicated problems.

Chapter 2

Boundary Layer Theory and Boundary Layer Separation

The investigation of flow separation from a solid body and the resulting global changes in the flow field is one of the most difficult and basic problems in fluid dynamics.

As mentioned in Sychev *et al.* (1998), attempts at a solution were first made by Helmholtz and Kirchhoff as early as (1868) and (1869) respectively, by describing separated flow past a blunt body, but they could not provide an adequate explanation of the reason for separation. In the beginning of the 20th century Prandtl (1905) was the first to have an explanation for the physical phenomenon of flow separation at high Reynolds numbers as being associated with the separation of boundary layers. His work became the basis for all further study of the asymptotic behavior of fluid motion. Prandtl's boundary layer theory laid the foundation for the explanation of the physical nature of flow separation phenomena. The boundary layer theory has been instrumental in the study of many different aspects of fluid flow at high Reynolds numbers.

Prandtl's theory states that we must subdivide a high Reynolds number flow

past a rigid body into two regions, an outer region and an inner region. While we may regard the outer region and main part of the flow as inviscid, however, near the wall, there is always an thin inner region, which has a thickness of $O\left(Re^{-\frac{1}{2}}\right)$, where the flow is mainly viscous, no matter how large the Reynolds numbers are. This narrow inner region was called the boundary layer by Prandtl and flow separation occurs because of the special characteristics of this layer.

One of the characteristics of this region is that it is affected by the no slip condition, which means that the streamwise velocity of the fluid particles must be zero at the wall, if the wall is rigid and stationary.

Prandtl's boundary layer theory uses a hierarchical approach to the calculation of the outer inviscid flow, first ignoring the presence of the boundary layer and then analyzing it by using the pressure gradient which is related to the external slip velocity, and which we have derived from the outer flow field.

Pressure gradients along the wall determine flow separation in the boundary layer. If the pressure decreases in the direction of the flow the boundary layer remains attached to the wall, but the boundary layer separates from the body surface when the pressure starts to rise.

This separation occurs because the kinetic energy of the fluid particles is less near the wall than inside of the boundary layer and therefore the velocity decreases, meaning that even a small increase in pressure in the outer flow can cause the particles to reverse their direction and form the recirculating region characteristic of separated flow.

To understand the conditions for flow separation we must first investigate how an adverse pressure gradient affects the structure of flow near the point where the zero streamline detaches from the solid wall. In a steady flow the separation point is the point where the skin friction first reaches zero, as shown in Figure (2.1). This means that the analysis of boundary layer separation from a smooth surface

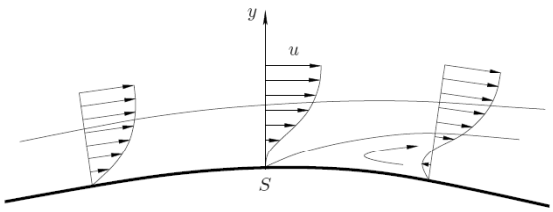

Figure 2.1: Boundary layer separation.

is relevant to the study of the solution of the boundary layer equations close to the point of zero friction. The solutions of the boundary layer equations, which are a parabolic, non-linear, viscous subset of the fully elliptical governing Navier-Stokes equations governing the boundary layer, give a corresponding normal velocity of $O\left(Re^{-\frac{1}{2}}\right)$ at the edge of the boundary layer.

Many studies have been undertaken about this subject and in general they assumed that pressure distribution along the body surface is regular at the separation point, meaning that the positive pressure gradient is distributed along a finite section of the surface and itself is finite, see Sychev *et al.* (1998) and Anderson (2005).

The study of the phenomenon of separation with increasing values of the Reynolds number is one of the most interesting aspects of fluid dynamics. High Reynolds number flows relate to rather fast flows of fluids with small viscosity, such as air and water. The Reynolds number Re is defined by $Re = \frac{LU}{\nu}$ and is a dimensionless ratio of inertial to viscous forces, where U is velocity, L is length and ν stands for kinematic viscosity.

To describe a viscous fluid flow we generally use the Navier Stokes equations with corresponding boundary and initial conditions. Basically, in flows which have arbitrary Reynolds numbers the Navier-Stokes equations can be solved numerically, but with higher Reynolds numbers, resolving flow features in thin regions such as boundary layer is a common difficulty. Important to the accuracy

of a finite difference solution is the size of the grid in relation to the scale of the solution. As the solution is being numerically approximated to get to a good solution, grid spacing must be of a small enough size to be able to resolve the flow field (Briley (1971)).

In the study of boundary layer separation with high Reynolds numbers which has many applications in different fields, another interesting aspect is the study of laminar separation in a two dimensional incompressible boundary layer flow. As mentioned by Alam & Sandham (2000), laminar separation bubble is the name for the phenomenon which occurs when an adverse pressure gradient causes a laminar boundary layer separation from a surface with a resulting turbulent flow which may reattach to the surface downstream.

Below we will give an overview of some of the literature which deals with the problem of laminar boundary layer separation.

2.1 Literature Review

One of the earliest publications concerning laminar separation bubbles was by Jones (1938) and it led the way for a number of experimental investigations into the basic structure and features of laminar separation bubbles.

Figure (2.2) shows the typical structure of a two-dimensional laminar boundary layer separation bubble in a model by Horton (1968) that is still in use today.

Horton shows in this figure that, first, the recirculation region contains slow-moving fluid near the separation point, but that at the center of the recirculation vortex near the reattachment point the recirculation velocities are stronger. Secondly, at the separation point he observes the streamline gradually rising away from the wall as it separates, but reattaching quickly to the wall after the boundary layer has transitioned to turbulence. The high-velocity region close to the

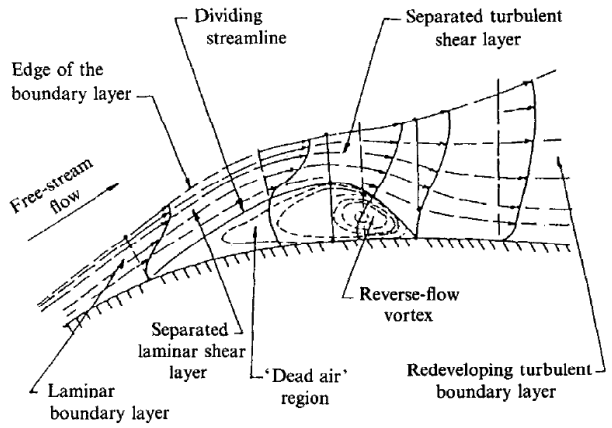

Figure 2.2: The classical structure of a laminar separation bubble. (Horton (1968)).

reattachment point is marked by a strong pressure gradient, whereas near the separation point within the separated region, the wall pressure remains constant.The 'dead air' region is the area immediately downstream of the separation point, where the flow close to the wall is practically stationary. The unstable separated shear layer transitions to turbulence and reattaches behind the reverse-flow vortex.

In aerodynamics, in their work on laminar boundary layer separation from the leading edge of a thin aerofoil, Owen & Klanfer (1955) define the term 'bubble' as the area between the point of separation and the point of reattachment of the flow. They classify bubbles into two different types according to their length, or to be more exact: their size compared to the thickness of the laminar boundary layer at the separation point. This order of magnitude of the bubble depends mainly on the Reynolds number, which depends on the displacement thickness δ_s^* at the point of separation.

This means that a bubble of separated flow will be longer or shorter depending on whether the Reynolds number is less or greater than a certain critical value, which in turn corresponds to the stability or instability of the flow. In their work

they determined that long bubbles had lengths of the order of $10^4\delta_s^*$ whereas the length of short bubbles was of the order of $10^2\delta_s^*$.

Marquillie & Ehrenstein (2002) have presented a numerical method which is capable of computing the two dimensional separating boundary layer flow over a bump and gives us a clear description of the numerical solution procedure, which uses a mapping that transforms the present geometry into a Cartesian coordinate system. This is then solved by using the Chebychev collocation and finite differences discretization. The fractional time step procedure which is used to enforce the divergence free condition is then compared to the influence matrix technique. While they reproduce numerically self-induced vortex shedding, they also investigate the separation structure for increasing Reynolds numbers.

More recently, a numerical investigation to compute the stability of separating boundary layer flow over a backward facing two-dimensional bump has been presented by Marquillie & Ehrenstein (2003). The latter work is concerned with local versus global stability of separation bubbles in relation to the onset of nonlinear oscillations of the global flow field. It is less concerned with locating the critical Reynolds numbers numerically than with clarifying the mechanisms of instability. Topological changes near or at the point of reattachment seem to be the major causes of change from convective to absolute instability at low frequencies. Below the critical Reynolds number the steady state flow becomes convectively unstable, whereas above the critical Reynolds number the numerically computed flow field undergoes self sustained, two dimensional, low frequency oscillations upstream from the separation bubble, which leads to vortex shedding downstream.

In many practical problems it is important to know the conditions under which boundary layer separation occurs. The conditions which lead to separation, the structural characteristics of the separation bubble, as well as temporal development of separation after the introduction of an adverse pressure gradient,

can all lead to problems such as dynamic flow stall.

Earlier research into unsteady boundary layer flows at high Reynolds numbers has presented model problems where the adverse pressure gradient is determined by the surface geometry, for example, the impulsively-started circular cylinder (see Nakamura & Watanabe (1985) for a review), the flat plate (see Marxen & Henningson (2007) for a review), or the flow past the leading edge of an airfoil (for review see Degani *et al.* (1996)).

Another model problem, the geometry of the flow through a channel with a suction in the upper wall, allows for adjustment of the magnitude of the adverse pressure gradient with the proportionate changes on the boundary layer of the lower wall, simply through modifications of the suction strength. In the following review we discuss the results of researchers who used this geometry in their work.

Among the first researchers to work with two-dimensional incompressible Navier Stokes equations in simulating laminar separation bubbles were Pauley *et al.* (1990). In their paper they describe a numerical study of the separation of a two dimensional laminar boundary layer under the influence of an abruptly imposed, external, adverse pressure gradient, using time-accurate numerical solutions of the Navier-Stokes equations, in order to gain more understanding of the physics of this flow. To solve the incompressible Navier-Stokes equations for a fluid with constant viscosity they used a fractional timestep method which was second-order accurate in space and time. Computations made for different suction strengths at each of three different Reynolds numbers showed that when the adverse pressure gradient was weak, a closed, steady separation bubble developed and the separated region was very thin, while the separated region became longer and small oscillations in skin friction developed when increased suction and therefore a stronger pressure gradient was applied. However, up to the critical value of suction strength $S = 0.12$, when vortex shedding begins, the separation

bubble remained steady. They also established that periodic vortex shedding from the separation was created by a strong adverse pressure gradient and there were similarities to experimental results for laminar separation bubbles in the general features of the time-averaged results. In comparing their work with the steady separation experiments of Gaster (1966), they found that the phenomenon which he called 'bursting' actually is the same as time-averaged, periodic shedding. They also arrived at the conclusion that the shedding Strouhal number, which is based on the boundary layer momentum thickness at separation and the local boundary layer edge velocity, was constant and independent of the pressure gradient as well as of the Reynolds number.

Hsiao & Pauley (1994) compared three methods, the triple deck method of marginal separation, the full Navier Stokes computation and the interactive boundary layer (IBL) method for solving the steady two-dimensional marginal separation of an incompressible boundary layer flow, primarily in order to determine the suitability of the triple-deck method of marginal separation in practical application. They applied these three methods independently to solve the same flow field at different Reynolds numbers. They reported that the full Navier-Stokes computation at high Reynolds numbers did not produce stable solutions of laminar flow, whereas the other two methods performed well. The secondary objective of their work was to determine the boundary condition describing the external flow. To determine the solution of skin friction near the separation point they used the incompressible unsteady Navier-Stokes equations and solved them by using a fractional step method. In the Navier Stokes computation separation occurred at high suction strength, while near the reattachment point the instantaneous skin friction curve formed oscillations and the boundary became unstable. Hsiao, following the earlier work of Pauley *et al.* (1990), classified the separation bubble as steady when the oscillations of the skin friction curve didn't pass

through zero skin friction condition (where the critical value of suction strength S, defined as the part of the through flow removed through the suction port, in Pauley is $S = 0.12$), while the oscillations of the skin friction curve passed through the zero line at the critical value of suction strength $S = 0.09$ for the Navier-Stokes computation. They presented two different comparisons, the first one between the IBL method and the triple deck method of marginal separation, and the second one between the Navier-Stokes computation and the IBL method at low Reynolds numbers. From these two comparisons the critical value of Γ (deviation from marginal separation condition) involved in the basic equation of marginal separation relates directly to the critical value of suction strength S, above which the separation bubble becomes unsteady.

Alam & Sandham (2000) have numerically computed laminar separation bubbles with turbulent reattachment. The numerical method used in their study is the pseudo-spectral method. They have carried out simulations with short laminar bubbles in two and three dimensions. They used simulation data to get velocity profiles to compute stability characteristics of mean flow profiles in the separated flow region and they have shown that reverse flow of the order of $15 - 20\%$ is required for local profiles to become absolutely unstable. They mention the distinction first made by Gaster (1966), between absolute instability, meaning disturbances growing in time, and convective instability, i.e., disturbances growing in space, and its importance for the study of laminar separation bubbles. They propose that the explanation for the profuse vortex shedding mentioned by Pauley *et al.* (1990), could be an effect which the presence of an area of local instability has on the bubble as a whole. They also considered the possibility that this phenomenon, the global response of the bubble as a whole to an area of instability, may be related to what is referred to as 'bursting', i.e., when a short bubble bursts to form either a long bubble, or does not reattach at all.

In their comparison between two-dimensional and fully three-dimensional simulations they proposed that three-dimensional simulations are characterized by the breakdown of Λ-vortices, which leads to a full transition to turbulence, while the two-dimensional simulations do not seem to sufficiently explain the features of the short separation bubbles.

One of the recent studies which employ this geometry is Cassel *et al.* (2007) where a flow similar to that investigated by Pauley *et al.* (1990) and Alam & Sandham (2000) is studied. Computing the full unsteady, two-dimensional Navier-Stokes equations, they obtained results which determined general features of flow as well as flow behaviors within certain limits. In their solutions they found that within specific limits of the Reynolds number Re and suction rate α there are different regimes which comprise steady separation where (when $Re = 5000$ and $\alpha = 0.08$), a steady recirculation region along the lower wall developed after some time, whereas in their example of unsteady separation (when $Re = 10000$ and $\alpha = 0.30$) they showed accompanying vortex shedding under the suction slot on the lower wall. They found it to their advantage to use the unsteady boundary layer equations as a reduced model, compared to the full Navier-Stokes equations. They investigated sub-optimal control of the unsteady separation by using the unsteady boundary layer equations along with the quasi-steady control equation as the state equations. In order to determine their ability to suppress the unsteady separation process they investigated different combinations of domain and boundary-based performance measures and penalty functions. This sub-optimal control approach yielded considerable insight into the suitability of different methods for controlling unsteady flow separation. The results obtained by Cassel suggest a more efficient use of different combinations of performance measures and penalty functions in the search for a domain or boundary-based control mechanism that will provide the optimal control over unsteady boundary

layer separation.

The geometry employed in Pauley *et al.* (1990), Hsiao & Pauley (1994), Alam & Sandham (2000) and Cassel *et al.* (2007) is the same as the one employed in the present work.

Chapter 3

Two Test Problems

3.1 Introduction

In this chapter, we describe two test problems. The first problem is a nonlinear equation which models the temperature distribution in a reacting material. The main objectives in this problem are to find the solutions of a nonlinear two dimensional partial differential equation with one unknown, and to find the turning points by using continuation methods. The second test problem involves the two-dimensional Navier-Stokes equations. We developed the appropriate numerical technique to solve this problem.

The reason for studying these two test problems separately is that this allowed us to check the numerical method to implement in our main problem and to obtain the principles for constructing good local, global and derivative-approximating algorithms that became the basis of our algorithms for the main problem, even though the algorithms for multivariable problems are more complex than the ones in these test problems.

The most important methods and techniques used to find the solution of the nonlinear equations we are working with here, have been discussed in the previous

chapter.

In this chapter, in sections 3.2.1 to 3.2.3, we discuss the formulation of the first test problem and the numerical techniques used, as well as the boundary conditions. In section 3.2.4 we consider the continuation method for calculating the bifurcation diagram to follow the turning point. The turning point tracking algorithm in section 3.2.5 is used to find the turning point, and finally the results obtained are discussed in section 3.2.6. The second test problem is discussed in section 3.3 and we come to the final conclusions for both problems in section 3.4.

3.2 The First Test Problem

We present a 2D test problem for one nonlinear equation which models the temperature distribution in a reacting material, using a numerical technique based on finite differences in one direction, combined with spectral Chebychev collocation in the other direction.

Our goal here is to give a description of the techniques for solving the nonlinear equations and calculating the turning points. Our problem has many applications, for example in the theory of thermal ignition, see Bazley & Wake (1978).

3.2.1 Problem Formulation

When we have a reacting material with an exothermic reaction, where reactant consumption is neglected, the equations governing the steady-state thermal regime are investigated and can be written as described by Bazley & Wake (1978) and Seydel (1994) as

$$\frac{\partial \theta}{\partial t} = \nabla^2 \theta + \lambda e^{\frac{\theta}{1+\varepsilon\theta}}. \tag{3.1}$$

Here the variable $\theta = (T - T_a)\, E/\,(RT_a^2)$ is a normalized temperature, with

T : the local, absolute temperature,

Ta: the surface temperature,

R: gas constant,

E: Arrhenius activation energy,

$\varepsilon = RT_a/E$, nondimensional parameter,

λ : nondimensional parameter, and

$\nabla^2\theta$: Laplacian (with respect to dimensionless space variables).

A temperature model within a material with exothermic reaction is given by equation (3.1). We limit ourselves to the steady state situation in a unit square with $0 \le x \le 1$, $0 \le y \le 1$ and then,

$$\nabla^2\theta = -\lambda e^{\frac{\theta}{1+\varepsilon\theta}} \qquad \text{inside the square,} \tag{3.2}$$

$$\theta = 0 \qquad \text{on the boundary.} \tag{3.3}$$

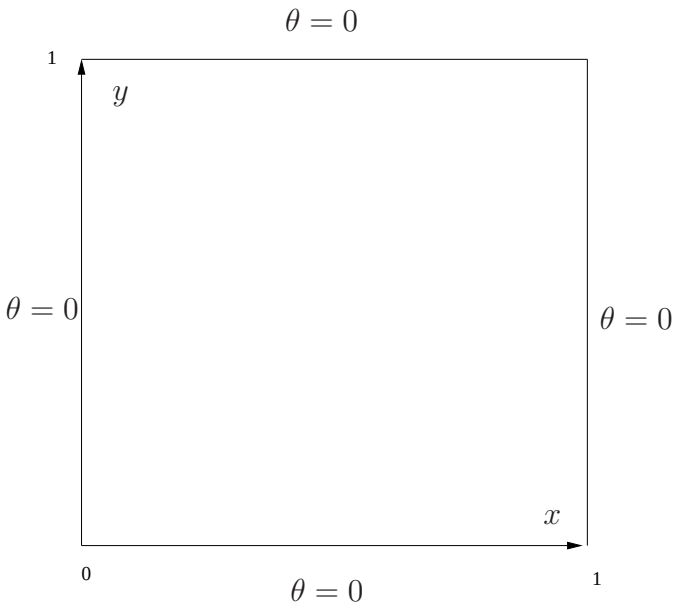

Figure 3.1: The boundary conditions of a temperature model within a material with exothermic reaction.

The equations with the boundary conditions have to be solved to obtain the

variable θ (a normalized temperature), (see Figure 3.1).

3.2.2 Numerical Method

Equation (3.2) is discretized using central differences in the x-direction and Chebychev collocation in the y-direction. When we use finite difference combined with spectral method, we can directly solve the sparse block tridiagonal matrix which has arisen from the discretization. We start by transforming the domains. After that, we discretize them, and then we use Newton linearization to solve the resulting nonlinear equations.

Suppose that we are trying to approximate a derivative of a function $\theta(x, y)$ at the points x_i, y_j. Denote the approximate value of $\theta(x, y)$ at the point x_i, y_j by $\theta_{i,j}$.

The x-domain is simply discretized into a uniform grid defined over $[x_{min}, x_{max}]$ given by,

$$x = x_k = x_{min} + (k-1)\Delta x, \qquad k = 1, 2, \ldots, m$$

and

$$\Delta x = \frac{x_{max} - x_{min}}{m-1},$$

where $x_{max} = 1$ and $x_{min} = 0$, then

$$\Delta x = \frac{1}{m-1}.$$

Thus, the first and second derivatives in x-direction are discretized using central differencing in the interior of the domain:

$$\left(\frac{\partial \theta}{\partial x}\right)_{kj} = \frac{\theta_{k+1,j} - \theta_{k-1,j}}{(2\Delta x)}, \tag{3.4}$$

$$\left(\frac{\partial^2\theta}{\partial x^2}\right)_{kj} = \frac{\theta_{k+1,j} - 2\theta_{k,j} + \theta_{k-1,j}}{(\Delta x)^2}. \tag{3.5}$$

To apply the Chebychev collocation, the y domain $0 \leq y \leq 1$ is first mapped linearly into $-1 \leq z \leq 1$. Here z_j is the set of Chebychev points given by

$$z_j = -\cos\left(\frac{j\pi}{N}\right), \qquad j = 0, 1, \ldots, N \tag{3.6}$$

and they are linearly related to y_j by the expression $y_j = \frac{z_j+1}{2}$.

Then the first derivative in y is given by:

$$\left(\frac{\partial\theta}{\partial y}\right)_{kj} = \left(\frac{2}{y_{\max}}\right)\sum_{p=0}^{N}(D1)_{j,p}\,\theta_{k,p}, \tag{3.7}$$

For second derivative terms we can use these similar expressions.

$$\left(\frac{\partial^2\theta}{\partial y^2}\right)_{kj} = \left(\frac{2}{y_{\max}}\right)^2\sum_{p=0}^{N}(D2)_{j,p}\,\theta_{k,p}, \tag{3.8}$$

where $D1_{j,p}$ and $D2_{j,p}$ are the elements of the Chebychev collocation differentiation matrix $\mathbf{D}$, see equation (1.19), where ($y_{\max} = 1$).

The Discrete Form

The discrete form of the equation (3.2) is given by

$$\frac{\theta_{k+1j} - 2\theta_{kj} + \theta_{k-1j}}{\Delta x^2} + \left(\frac{\partial^2\theta}{\partial y^2}\right)_{kj} = -\lambda e^{\frac{\theta_{kj}}{1+\varepsilon\theta_{kj}}}, \tag{3.9}$$

$$\text{where,} \qquad 2 \leq k \leq m-1,$$

$$1 \leq j \leq N-1.$$

Also, the boundary conditions are given by

$$\begin{aligned} \theta_{kj} &= 0 \quad \text{for} \quad k = 1, m \quad \text{and} \quad 0 \leq j \leq N, \\ \theta_{kj} &= 0 \quad \text{for} \quad j = 0, N \quad \text{and} \quad 1 \leq k \leq m. \end{aligned} \tag{3.10}$$

Linearizing the Equation

The discretization gives a set of non-linear equations. By using a Newton linearization technique these equations are solved by

$$\begin{aligned} \theta_{kj} &= T_{kj} + q_{kj}, \\ \text{where} \qquad |q_{kj}| &\ll 1, \end{aligned} \tag{3.11}$$

where (q) is a correction term and T is some initial guess.

By substituting of (3.11) into (3.9) and (3.10) we obtain

$$\begin{aligned} &\frac{q_{k+1j} - 2q_{kj} + q_{k-1j} + T_{k+1j} - 2T_{kj} + T_{k-1j}}{\Delta x^2} + \left(\frac{\partial^2 T}{\partial y^2}\right)_{kj} + \left(\frac{\partial^2 q}{\partial y^2}\right)_{kj} \\ &= -\lambda e^{\left(T_{kj}+q_{kj}\right)\left(1+\varepsilon\left(T_{kj}+q_{kj}\right)\right)^{-1}}. \end{aligned} \tag{3.12}$$

Now

$$\begin{aligned} \left(T_{kj} + q_{kj}\right)\left(1 + \varepsilon T_{kj} + \varepsilon q_{kj}\right)^{-1} &= \left(T_{kj} + q_{kj}\right)\left[\left(1 + \varepsilon T_{kj}\right)\left(1 + \frac{\varepsilon q_{kj}}{1 + \varepsilon T_{kj}}\right)\right]^{-1}, \\ &= \left(T_{kj} + q_{kj}\right)\left(1 + \varepsilon T_{kj}\right)^{-1}\left(1 + \frac{\varepsilon q_{kj}}{1 + \varepsilon T_{kj}}\right)^{-1}, \\ &\simeq \left(T_{kj} + q_{kj}\right)\left(1 + \varepsilon T_{kj}\right)^{-1}\left(1 - \frac{\varepsilon q_{kj}}{1 + \varepsilon T_{kj}} + ...\right), \\ &\simeq \left(1 + \varepsilon T_{kj}\right)^{-1}\left(\left(T_{kj} + q_{kj}\right) - \frac{\left(T_{kj} + q_{kj}\right)\varepsilon q_{kj}}{1 + \varepsilon T_{kj}}\right), \\ &\simeq \left(\frac{1}{1 + \varepsilon T_{kj}}\right)\left(\left(T_{kj} + q_{kj}\right) - \frac{\varepsilon T_{kj} q_{kj}}{1 + \varepsilon T_{kj}}\right), \\ &\simeq \left(\frac{1}{1 + \varepsilon T_{kj}}\right)\left(T_{kj} + q_{kj}\left(1 - \frac{\varepsilon T_{kj}}{1 + \varepsilon T_{kj}}\right)\right), \\ &\simeq \left(\frac{1}{1 + \varepsilon T_{kj}}\right)\left(T_{kj} + q_{kj}\left(\frac{1 + \varepsilon T_{kj} - \varepsilon T_{kj}}{1 + \varepsilon T_{kj}}\right)\right), \\ &\simeq \left(\frac{1}{1 + \varepsilon T_{kj}}\right)\left(T_{kj} + q_{kj}\left(\frac{1}{1 + \varepsilon T_{kj}}\right)\right), \\ &\simeq \left(\frac{1}{1 + \varepsilon T_{kj}}\right)\left(T_{kj} + \frac{q_{kj}}{1 + \varepsilon T_{kj}}\right). \end{aligned} \tag{3.13}$$

Hence

$$(T_{kj}+q_{kj})\left(1+\varepsilon T_{kj}+\varepsilon q_{kj}\right)^{-1} \simeq \frac{T_{kj}}{1+\varepsilon T_{kj}}+\frac{q_{kj}}{\left(1+\varepsilon T_{kj}\right)^2}. \tag{3.14}$$

By substituting equation (3.14) into equation (3.12), we obtain

$$\frac{T_{k+1j}-2T_{kj}+T_{k-1j}}{\Delta x^2}+\frac{q_{k+1j}-2q_{kj}+q_{k-1j}}{\Delta x^2}+\left(\frac{\partial^2 T}{\partial y^2}\right)_{kj}+\left(\frac{\partial^2 q}{\partial y^2}\right)_{kj}$$
$$=-\lambda e^{\frac{T_{kj}}{1+\varepsilon T_{kj}}+\frac{q_{kj}}{\left(1+\varepsilon T_{kj}\right)^2}},$$

or (3.15)

$$\frac{q_{k+1j}-2q_{kj}+q_{k-1j}}{\Delta x^2}+\left(\frac{\partial^2 q}{\partial y^2}\right)_{kj}+\frac{\lambda e^{\frac{T_{kj}}{1+\varepsilon T_{kj}}}}{\left(1+\varepsilon T_{kj}\right)^2}q_{kj}=R_{kj}, \tag{3.16}$$

where

$$R_{kj}=-\left(\frac{T_{k+1j}-2T_{kj}+T_{k-1j}}{\Delta x^2}\right)-\left(\frac{\partial^2 T}{\partial y^2}\right)_{kj}-\lambda e^{\frac{T_{kj}}{1+\varepsilon T_{kj}}}. \tag{3.17}$$

The boundary conditions are dealt with via,

$$T_{kj}+q_{kj}=0,$$

giving

$$\begin{aligned} q_{kj} &= -T_{kj} \quad \text{for} \quad j=0,N \quad \text{and} \quad 1\le k\le m, \\ q_{kj} &= -T_{kj} \quad \text{for} \quad k=1,m \quad \text{and} \quad 0\le j\le N. \end{aligned}$$

Thus

$$\frac{1}{\Delta x^2}\left[q_{k+1j}-2q_{kj}+q_{k-1j}\right]+\left(D^2 q\right)_{kj}+\lambda F_{kj}q_{kj}=R_{kj}, \tag{3.18}$$
$$\text{for}\ , \qquad 2 \le k\le m-1,$$

where

$$\begin{aligned} F_{kj} &= \frac{e^{\frac{T_{kj}}{1+\varepsilon T_{kj}}}}{\left(1+\varepsilon T_{kj}\right)^2}, \\ R_{kj} &= -\frac{1}{\Delta x^2}\left[T_{k+1j}-2T_{kj}+T_{k-1j}\right]-\left(D^2 T\right)_{kj}-\lambda e^{\frac{T_{kj}}{1+\varepsilon T_{kj}}}. \end{aligned}$$

Therefore, the matrix form of equation (3.18) can be written as

$$\frac{1}{\Delta x^2}\mathbf{I}Q_{k-1} + \left[-\frac{2}{\Delta x^2}\mathbf{I} + D^2 + \lambda F\right] Q_k + \frac{1}{\Delta x^2}\mathbf{I}Q_{k+1} = R_k, \quad (3.19)$$

where $\mathbf{I}$ is an identity matrix and $\mathbf{0}$ is a zero matrix, each of size $(N+1) \times (N+1)$.

It is seen that (3.19) leads to a linear system of the form

$$\mathbf{A}_k\mathbf{Q}_{k-1} + \mathbf{B}_k\mathbf{Q}_k + \mathbf{C}_k\mathbf{Q}_{k+1} = \mathbf{R}_k. \quad (3.20)$$

where $\mathbf{A}_k$, $\mathbf{B}_k$ and $\mathbf{C}_k$ are $(N+1)\times(N+1)$ matrices, and $\mathbf{Q}_k$ is a vector at each node $x = x_k$

$$\mathbf{Q}_k = \begin{bmatrix} Q_1 \\ Q_2 \\ \vdots \\ Q_m \end{bmatrix}, \quad (3.21)$$

and

$$\mathbf{Q}_k = (q_{k0}, q_{k1}, q_{k2}, \ldots, q_{kN})^T. \quad (3.22)$$

Here q_{kj} denotes the value of the temperature at $x = x_k$ and $y = y(z_j)$. When we use central differences in the x-direction the result is that a block tridiagonal matrix and the matrices $\mathbf{A}_k, \mathbf{B}_k, \mathbf{C}_k$ are dense matrices of size $(N+1)\times(N+1)$. The result of the linear system (3.20) when written in matrix form is:

$$\mathbf{MQ} = \mathbf{R}, \quad (3.23)$$

where

$$\begin{aligned} \mathbf{Q} &= (Q_1, Q_2, Q_3, \ldots, Q_m)^T, \\ \mathbf{R} &= (R_1, R_2, R_3, \ldots, R_m)^T, \end{aligned}$$

and

$$\mathbf{M} = \begin{bmatrix} \mathbf{B}_1 & & & & & & & \\ \mathbf{A}_2 & \mathbf{B}_2 & \mathbf{C}_2 & & & & & \\ & \mathbf{A}_3 & \mathbf{B}_3 & \mathbf{C}_3 & & & & \\ & & \mathbf{A}_4 & \mathbf{B}_4 & \mathbf{C}_4 & & & \\ & & & \ddots & \ddots & \ddots & & \\ & & & & & \mathbf{A}_{m-1} & \mathbf{B}_{m-1} & \mathbf{C}_{m-1} \\ & & & & & & & \mathbf{B}_m \end{bmatrix}. \tag{3.24}$$

Taking advantage of the sparsity pattern of the block tridiagonal matrix $\mathbf{M}$, we solved the linear system (3.23) for all the vectors $\mathbf{Q}_k$, $1 \leq k \leq m$, by using a direct solver.

3.2.3 The Boundary Conditions

When we use Newton linearization, the boundary condition becomes

$$\begin{aligned} q_{kj} &= -T_{kj} \quad \text{for} \quad k = 1, m \quad 0 \leq j \leq N, \\ q_{kj} &= -T_{kj} \quad \text{for} \quad j = 0, N \quad 1 \leq k \leq m. \end{aligned} \tag{3.25}$$

The x boundary condition is implemented through the establishment of the matrix equations of the form (3.20) for the case $k = 1$, which is taken in isolation, as are the cases $k = 2$ and $k = m$. First though, the y boundary conditions are included in the problem and the final forms of the matrices in (3.20) are given for $2 \leq k \leq m - 1$.

Now the matrices for $2 \leq k \leq m - 1$ are given by

$$\mathbf{A}_k = \frac{1}{\Delta x^2}\mathbf{I}, \tag{3.26}$$

$$\mathbf{B}_k = \frac{-2}{\Delta x^2}\begin{pmatrix} 1 & 0 & . & . & 0 \\ 0 & 1 & & & . \\ . & & 1 & & . \\ . & & & 1 & 0 \\ 0 & . & . & 0 & 1 \end{pmatrix} + \lambda \begin{pmatrix} F_{k0} & 0 & . & . & 0 \\ 0 & F_{k1} & & & . \\ . & & . & & . \\ . & & & . & 0 \\ 0 & . & . & 0 & F_{kN} \end{pmatrix} + \mathbf{D}^2, \tag{3.27}$$

$$\text{where} \qquad \mathbf{D}^2\mathbf{Q}_k = \begin{pmatrix} (D^2q)_{k0} \\ (D^2q)_{k1} \\ \vdots \\ (D^2q)_{kN} \end{pmatrix}, \tag{3.28}$$

$$\left(D^2q\right)_{kj} = 4\left[\left(D_N^2\right)_{k0} q_{0j} + \left(D_N^2\right)_{k1} q_{1j} + \cdots + \left(D_N^2\right)_{kN} q_{Nj}\right], \tag{3.29}$$

$$\mathbf{C}_k = \frac{1}{\Delta x^2}\mathbf{I}, \tag{3.30}$$

$$\mathbf{R}_k = \begin{pmatrix} R_{k0} \\ R_{k1} \\ \vdots \\ R_{kN-1} \\ R_{kN} \end{pmatrix} = \begin{pmatrix} -T_{k0} \\ R_{k1} \\ \vdots \\ R_{kN-1} \\ -T_{kN} \end{pmatrix},$$

$$\text{where} \qquad (\mathbf{R})_{kj} = -\frac{1}{\Delta x^2}\left[\mathbf{T}_{k+1} - 2\mathbf{T}_k + \mathbf{T}_{k-1}\right] - \left(\mathbf{D}^2\mathbf{T}\right)_k - \lambda\mathbf{H}_k,$$

$$\text{where} \qquad \mathbf{H}_k = e^{\frac{T_{kj}}{1+\varepsilon T_{kj}}}.$$

Now the matrices for $k = 1$ are given by

$$\mathbf{A}_1\mathbf{Q}_0 + \mathbf{B}_1\mathbf{Q}_1 + \mathbf{C}_1\mathbf{Q}_2 = \mathbf{R}_1,$$

$$\mathbf{Q}_0 = (q_{00}, q_{01}, \ldots, q_{0N})^T = (0, 0, \ldots, 0)^T.$$

Then,

$$\mathbf{A}_1 = \mathbf{0}.$$

Since

$$\mathbf{Q}_1 = (q_{10}, q_{11}, \ldots, q_{1N})^T,$$

$$\mathbf{B}_1 = \mathbf{I},$$

$$\begin{aligned} \mathbf{Q}_2 &= (q_{20}, q_{21}, \ldots, q_{2N})^T = (0, 0, \ldots, 0)^T, \\ \mathbf{C}_1 &= \mathbf{0}. \end{aligned}$$

Then

$$\mathbf{R}_1 = \begin{pmatrix} -T_{10} \\ -T_{11} \\ \vdots \\ -T_{1N} \end{pmatrix}.$$

Now the matrices for $k = m$ are given by

$$\mathbf{A}_m \mathbf{Q}_{m-1} + \mathbf{B}_m \mathbf{Q}_m + \mathbf{C}_m \mathbf{Q}_{m+1} = \mathbf{R}_m, \tag{3.31}$$

$$\begin{aligned} \mathbf{A}_m &= \mathbf{0}, \\ \mathbf{B}_m &= \mathbf{I}, \\ \mathbf{C}_m &= \mathbf{0}, \end{aligned}$$

$$\begin{aligned} \mathbf{R}_m &= \begin{pmatrix} R_{m0} \\ R_{m1} \\ \vdots \\ R_{mN} \end{pmatrix}, \\ \mathbf{Q}_m &= (q_{m0}, q_{m1}, \ldots, q_{mN})^T, \\ &= (-T_{m0}, -T_{m1}, \ldots, -T_{mN})^T, \end{aligned}$$

$$\text{and consequently} \qquad \mathbf{R}_m = \begin{pmatrix} R_{m0} \\ R_{m1} \\ \vdots \\ R_{mN} \end{pmatrix} = \begin{pmatrix} -T_{m0} \\ -T_{m1} \\ \vdots \\ -T_{mN} \end{pmatrix}.$$

3.2.4 Continuation

To calculate the bifurcation diagram to follow the turning point, we use the continuation method.

In equation (3.2) of the problem formulation, we need to find $\theta(x, y; \lambda; \epsilon)$.

From the solutions which we have obtained for the test problem in section 3.2.1 to 3.2.3 we discretize equation (3.2) to get

$$\begin{aligned} \frac{\theta_{k+1j} - 2\theta_{kj} + \theta_{k-1j}}{(\Delta x)^2} + \left(\frac{\partial^2 \theta}{\partial y^2}\right)_{kj} + \lambda e^{\frac{\theta_{kj}}{1+\varepsilon\theta_{kj}}} &= 0, \qquad (3.32) \\ 2 \leq k &\leq m-1, \\ 1 \leq j &\leq N-1, \end{aligned}$$

with the boundary condition

$$\begin{aligned} \theta_{kj} &= 0 \qquad k = 1, m \qquad 0 \leq j \leq N, \\ \theta_{kj} &= 0 \qquad j = 0, N \qquad 1 \leq k \leq m. \qquad (3.33) \end{aligned}$$

Suppose we have a solution $\boldsymbol{\theta} = \bar{\boldsymbol{\theta}}$ and $\lambda = \bar{\lambda}$ for a given ε which is a solution to (3.32).

Then we want to obtain a predictor for $\left(\boldsymbol{\theta}^{(0)}, \lambda^{(0)}\right)$, by using the same method which has been discussed in section (1.3.1). The initial iterate for Newton's method can be obtained by

$$\boldsymbol{\theta}^{(0)} = \bar{\boldsymbol{\theta}} + \left(\frac{d\boldsymbol{\theta}}{ds}\right)\Delta s, \qquad (3.34)$$

$$\lambda^{(0)} = \bar{\lambda} + \left(\frac{d\lambda}{ds}\right)\Delta s. \qquad (3.35)$$

and we can also find $\frac{d\boldsymbol{\theta}}{ds}$ and $\frac{d\lambda}{ds}$ from

$$\frac{d\lambda}{ds} = \pm\frac{1}{\sqrt{\mathbf{z}^T\mathbf{z}+1}}, \tag{3.36}$$

$$\frac{d\boldsymbol{\theta}}{ds} = \pm\frac{\mathbf{z}}{\sqrt{\mathbf{z}^T\mathbf{z}+1}}. \tag{3.37}$$

Now to find $\mathbf{z}$ let us linearize perturbation $(U_{kj}, \Delta\lambda)$ of the solution $\left(\bar{\boldsymbol{\theta}}; \bar{\lambda}\right)$

$$\theta_{kj} = \bar{\theta}_{kj} + U_{kj} \qquad \text{where } |U_{kj}| \ll 1, \tag{3.38}$$

$$\lambda_{kj} = \bar{\lambda}_{kj} + \Delta\lambda \qquad \text{where } |\Delta\lambda| \ll 1, \tag{3.39}$$

then substituting into (3.32) and neglecting the second-order terms. This leads to

$$\frac{U_{k+1j} - 2U_{kj} + U_{k-1j}}{(\Delta x)^2} + \left(\frac{\partial^2 U}{\partial y^2}\right)_{kj} + \bar{\lambda}\left(\frac{U_{kj}}{\left(1+\varepsilon\bar{\theta}_{kj}\right)^2}\right) e^{\frac{\bar{\theta}_{kj}}{1+\varepsilon\bar{\theta}_{kj}}} +$$

$$\Delta\lambda e^{\frac{\bar{\theta}_{kj}}{1+\varepsilon\,\bar{\theta}_{kj}}} = -\frac{\bar{\theta}_{k+1j} - 2\,\bar{\theta}_{kj} + \bar{\theta}_{k-1j}}{(\Delta x)^2} - \left(\frac{\partial^2\,\bar{\theta}}{\partial y^2}\right)_{kj} - \bar{\lambda}e^{\frac{\bar{\theta}_{kj}}{1+\varepsilon\,\bar{\theta}_{kj}}}, \tag{3.40}$$

$$2 \le k \le m-1,$$

$$1 \le j \le N-1,$$

with the boundary condition,

$$U_{kj} = -\bar{\theta}_{kj} \qquad k = 1, m \qquad 0 \le j \le N, \tag{3.41}$$

$$U_{kj} = -\bar{\theta}_{kj} \qquad j = 0, N \qquad 1 \le k \le m. \tag{3.42}$$

Then we rewrite equation (3.40) as

$$\left(\mathbf{J} \qquad \frac{\partial\mathbf{f}}{\partial\lambda}\right)(U \qquad \Delta\lambda)^T = -\mathbf{f}\left(\bar{\theta}, \bar{\lambda}\right), \tag{3.43}$$

where

$$\left(\frac{\partial \mathbf{f}}{\partial \lambda}\right)_{kj} = e^{\frac{\bar{\theta}_{kj}}{1+\varepsilon\,\bar{\theta}_{kj}}}, \tag{3.44}$$

and

$$\mathbf{J} = \begin{bmatrix} \mathbf{B}_1 & & & & & & & \\ \mathbf{A}_2 & \mathbf{B}_2 & \mathbf{C}_2 & & & & & \\ & \mathbf{A}_3 & \mathbf{B}_3 & \mathbf{C}_3 & & & & \\ & & \mathbf{A}_4 & \mathbf{B}_4 & \mathbf{C}_4 & & & \\ & & & \ddots & \ddots & \ddots & & \\ & & & & & \mathbf{A}_{m-1} & \mathbf{B}_{m-1} & \mathbf{C}_{m-1} \\ & & & & & & & \mathbf{B}_m \end{bmatrix}. \tag{3.45}$$

To find the unique solution $\mathbf{z}$ in equation

$$\mathbf{J}\mathbf{z} = -\frac{\partial \mathbf{f}}{\partial \lambda}, \tag{3.46}$$

we construct the Jacobian matrix $\mathbf{J}$ and vector $\left(\frac{\partial \mathbf{f}}{\partial \lambda}\right)$. Then after we find the unique solution $\mathbf{z}$, we obtain $\frac{d\lambda}{ds}$ and $\frac{d\boldsymbol{\theta}}{ds}$ from equations (3.36) and (3.37). Then the branch is continued by determining the appropriate choice of sign.

After we obtain $\frac{d\lambda}{ds}$ and $\frac{d\boldsymbol{\theta}}{ds}$, we update the initial iterate for Newton's method as

$$\boldsymbol{\theta}^{(0)} = \bar{\boldsymbol{\theta}} + \left(\frac{d\boldsymbol{\theta}}{ds}\right)\Delta s, \tag{3.47}$$

$$\lambda^{(0)} = \bar{\lambda} + \left(\frac{d\lambda}{ds}\right)\Delta s, \tag{3.48}$$

where Δs is chosen.

Since the predictor step is given, the $\boldsymbol{\theta}^{(0)}$and $\lambda^{(0)}$ can be used by the same corrector method, which has been discussed in section (1.3.2) where we have obtained the solution for $\mathbf{a}$ and $\mathbf{b}$, being temporary vectors. By using $\mathbf{a}$ and $\mathbf{b}$ we obtain the new updates for $\Delta\lambda$ and $\Delta\boldsymbol{\theta}$.

3.2.5 The Turning Point Tracking Algorithm

Newton's method is used by the turning point tracking algorithm to converge to a turning point, and to track it as a function of a second parameter, simple zero order continuation is used. A single eigenvalue $\lambda = 0$ with associated real-valued null vector $\mathbf{y}$ is found at a turning point bifurcation. The turning point is characterized by the following formulation where the solution is on the steady state solution branch, which is determined by the first vector equation (3.49), which is one of the n scalar equations. The second vector equation (3.50) determines that there is a real-valued eigenvector $\mathbf{y}$, which corresponds to a zero eigenvalue, and the last scalar equation (3.51) specifies the length of the null vector at length 1, as seen in Salinger *et al.* (2002) (LOCA) and Seydel (1994)

$$\mathbf{f} = \mathbf{0}, \tag{3.49}$$

$$\mathbf{J}\mathbf{y} = \mathbf{0}, \tag{3.50}$$

$$\phi \cdot \mathbf{y} = 1. \tag{3.51}$$

Here ϕ is a constant vector and is chosen to be the same initial guess for $\mathbf{y}$. The values of $\boldsymbol{\theta}$, $\mathbf{y}$, and λ are specified by this set of $2n + 1$ equations.

The following is the form of a full Newton method for this system which can be solved by using bordering algorithms, see Salinger *et al.* (2002) (LOCA)

$$\begin{bmatrix} \mathbf{J} & \mathbf{0} & \frac{\partial \mathbf{f}}{\partial \lambda} \\ \frac{\partial \mathbf{J}\mathbf{y}}{\partial \boldsymbol{\theta}} & \mathbf{J} & \frac{\partial \mathbf{J}\mathbf{y}}{\partial \lambda} \\ \mathbf{0} & \phi & 0 \end{bmatrix} \begin{bmatrix} \Delta\boldsymbol{\theta} \\ \Delta\mathbf{y} \\ \Delta\lambda \end{bmatrix} = - \begin{bmatrix} \mathbf{f} \\ \mathbf{J}\mathbf{y} \\ \phi \cdot \mathbf{y} - 1 \end{bmatrix}. \tag{3.52}$$

The following four linear solves of the matrix $\mathbf{J}$ and some simple algebra can appropriately formulate the linear equations in the Newton iteration for the turning point algorithm (3.52):

$$\mathbf{Ja} = -\mathbf{f}, \tag{3.53}$$

$$\mathbf{Jb} = -\frac{\partial \mathbf{f}}{\partial \lambda}, \tag{3.54}$$

$$\mathbf{Jc} = -\frac{\partial \mathbf{Jy}}{\partial \boldsymbol{\theta}}\mathbf{a}, \tag{3.55}$$

$$\mathbf{Jd} = -\frac{\partial \mathbf{Jy}}{\partial \boldsymbol{\theta}}\mathbf{b} - \frac{\partial \mathbf{Jy}}{\partial \lambda}. \tag{3.56}$$

The variables $\mathbf{a}, \mathbf{b}, \mathbf{c}$ and $\mathbf{d}$ are temporary vectors of length n. Just as this matrix is solved, in Newton iteration each of the four linear solves of $\mathbf{J}$ are performed by the application code in the same way. By reusing a factorization for a direct solver and the preconditioner for a preconditioned iterative solver, work can be saved in the second, third and fourth solves. Usually $\boldsymbol{\theta}$ and λ come from a steady solution near the turning point as located by an arclength continuation run, and the algorithm requires initial guesses for them.

From the last section we obtained $\mathbf{a}$ and $\mathbf{b}$, when we used continuation method, so now we want to obtain $\frac{\partial \mathbf{Jy}}{\partial \boldsymbol{\theta}}\mathbf{a}$, note that $\mathbf{J}(\boldsymbol{\theta}, \lambda)$ acting on vector $\mathbf{U}$ is defined by

$$[\mathbf{J}(\boldsymbol{\theta}, \lambda)\mathbf{U}]_{kj} \to \frac{U_{k+1j} - 2U_{kj} + U_{k-1j}}{(\Delta x)^2} + \left(D_y^2 U\right)_{kj} + \lambda \mathbf{f}(\boldsymbol{\theta}_{kj}) U_{kj}, \tag{3.57}$$

where

$$\mathbf{f}(\boldsymbol{\theta}) = \frac{e^{\frac{\theta}{1+\varepsilon\theta}}}{(1+\varepsilon\theta)^2}. \tag{3.58}$$

Now by taking the derivative $\mathbf{a}$ of the (3.57), the vector $\frac{\partial \mathbf{Jy}}{\partial \boldsymbol{\theta}}\mathbf{a}$ is defined by

$$\frac{\partial \mathbf{Jy}}{\partial \boldsymbol{\theta}}\mathbf{a} = \lim_{\sigma \to 0} \frac{\mathbf{J}(\boldsymbol{\theta} + \sigma\mathbf{a}, \lambda)\mathbf{y} - \mathbf{J}(\boldsymbol{\theta}, \lambda)\mathbf{y}}{\sigma}. \tag{3.59}$$

Hence we can see that

$$\left[\frac{\partial \mathbf{JU}}{\partial \boldsymbol{\theta}}\mathbf{a}\right]_{kj} \to \lambda \mathbf{f}'(\boldsymbol{\theta}_{kj}) \mathbf{U}_{kj} \mathbf{a}_{kj}, \tag{3.60}$$

or

$$\left[\frac{\partial \mathbf{Jy}}{\partial \boldsymbol{\theta}}\mathbf{a}\right]_{kj} = \lambda \mathbf{f}'\left(\boldsymbol{\theta}_{kj}\right)\mathbf{y}_{kj}\mathbf{a}_{kj}, \tag{3.61}$$

where

$$\mathbf{f}'\left(\boldsymbol{\theta}\right) = \frac{e^{\frac{\theta}{1+\varepsilon\theta}} \quad \left[1-2\varepsilon\left(1+\varepsilon\theta\right)\right]}{\left(1+\varepsilon\theta\right)^4}. \tag{3.62}$$

Hence by substituting (3.62) for (3.61) we obtain

$$\left(\frac{\partial \mathbf{Jy}}{\partial \boldsymbol{\theta}}\mathbf{a}\right)_{kj} = \lambda \frac{e^{\frac{\theta}{1+\varepsilon\theta}} \quad \left[1-2\varepsilon\left(1+\varepsilon\theta\right)\right]}{\left(1+\varepsilon\theta\right)^4}\mathbf{y}_{kj}\mathbf{a}_{kj}, \tag{3.63}$$

also, in the same way, we obtain $\frac{\partial \mathbf{Jy}}{\partial \boldsymbol{\theta}}\mathbf{b}$

$$\left(\frac{\partial \mathbf{Jy}}{\partial \boldsymbol{\theta}}\mathbf{b}\right)_{kj} = \lambda \frac{e^{\frac{\theta}{1+\varepsilon\theta}} \quad \left[1-2\varepsilon\left(1+\varepsilon\theta\right)\right]}{\left(1+\varepsilon\theta\right)^4}\mathbf{y}_{kj}\mathbf{b}_{kj}. \tag{3.64}$$

Since

$$\mathbf{y} = \phi = \frac{\mathbf{b}}{||\mathbf{b}||} \tag{3.65}$$

where $||\mathbf{b}|| = \sqrt{\mathbf{b}^T\mathbf{b}}$, the equation (3.51) is initially satisfied from this scaling. Also, we have calculated $\frac{\partial \mathbf{Jy}}{\partial \lambda}$ from equation (3.57),

$$\frac{\partial \mathbf{Jy}}{\partial \lambda} = \mathbf{f}\left(\boldsymbol{\theta}\right)\mathbf{y},$$

then from equation (3.58) we obtained

$$\frac{\partial \mathbf{Jy}}{\partial \lambda} = \frac{e^{\frac{\theta}{1+\varepsilon\theta}}}{\left(1+\varepsilon\theta\right)^2}\mathbf{y}.$$

Here we can obtain $\mathbf{c}$ and $\mathbf{d}$ by substituting the values into equations (3.55) and (3.56).

Finally, after we have all values for the variables $\mathbf{a}, \mathbf{b}, \mathbf{c}$ and $\mathbf{d}$, we can calculate the correction terms such that

$$\Delta\lambda = \frac{1-\phi\cdot\mathbf{c}}{\phi\cdot\mathbf{d}}, \tag{3.66}$$

$$\Delta\boldsymbol{\theta} = \mathbf{a} + \Delta\lambda\mathbf{b}, \tag{3.67}$$

$$\Delta \mathbf{y} = \mathbf{c} + \Delta\lambda \mathbf{d} - \mathbf{y}. \tag{3.68}$$

By these results, we can obtain the values of $\boldsymbol{\theta}$, $\mathbf{y}$, and λ such that

$$\begin{aligned} \boldsymbol{\theta} &= \bar{\boldsymbol{\theta}} + \Delta\boldsymbol{\theta}, \\ \lambda &= \bar{\lambda} + \Delta\lambda, \\ \mathbf{y} &= \bar{\mathbf{y}} + \Delta\mathbf{y}. \end{aligned}$$

To converge to the next turning point at the next value of a second parameter we use a small change of simple zero order continuation, after convergence to a turning point. The constant vector is set to $\phi = \mathbf{y}$ and the initial guesses for λ and $\mathbf{y}$ are the converged values at the previous turning point.

3.2.6 Results and Solutions

In this section, a number of results for the $2D$ test problem for one nonlinear equation will be discussed. These results are obtained using the Chebychev collocation in y-direction and second order finite differences in x-direction. We take $N+1$ to be the number of the Chebychev collocation points in the y-direction and m is the number of points in x-direction.

The problem in $2D$ is given by

$$\begin{aligned} \nabla^2\theta &= -\lambda e^{\frac{\theta}{1+\varepsilon\theta}} \qquad \text{inside the square} \\ \theta &= 0 \qquad\qquad\qquad\quad \text{on the boundary.} \end{aligned}$$

To find out the turning points, the above equation is solved in Seydel (1994) using the standard five-point star for discretizing the Laplacian on a uniform square mesh with N^2 interior grid points,

$$\left(\frac{i}{N+1}, \frac{j}{N+1}\right), \qquad i, j = 1, 2, \ldots, N. \tag{3.69}$$

N	m	λ_c	θ_c
10	101	6.80804	1.39289
10	121	6.80803	1.38684
10	141	6.80807	1.38965
10	161	6.80802	1.39822

Table 3.1: Comparison of λ_c and θ_c obtained from different grid sizes for $\varepsilon = 0$, for $m = 101, 121, 141, 161$ and $N = 10$.

Bazley & Wake (1978) also solved the above equation by using the variational method and the modified model which is exactly solvable for the two simple geometries of the infinite slab and the infinite circular cylinder.

In the present study, using the numerical method described in the previous sections, numerical solutions were obtained for different grid sizes and different values of ε.

Numerical results were obtained using the continuation method for different values of ε, producing branching diagrams and turning points.

For $\varepsilon = 0$ with $N = 10$ and $m = 101$ we observe a good convergence to the steady solution, which means the Chebychev and second order finite differences code converge very well with fewer than 4 Newton iterations.

Figure (3.2) shows the relation between parameter λ and temperature $max\,|\theta|$, for $\varepsilon = 0$ with $N = 10$ and $m = 101$. It is observed that as the parameter λ increases, the temperature $max\,|\theta|$ increases also.

By applying continuation method in 2D test problem equations, the plots of the parameter λ and the temperature $max\,|\theta|$ for different values of m and N, and fixed value of $\varepsilon = 0$, are shown in figures (3.3), (3.4) and tables (3.1) and (3.2). These plots clearly illustrate branching diagrams and also show grid independence in different figures. From these figures and tables we can observe a good convergence to the steady solution which proves our method to be appropriate.

To find out the turning point we are calculating solutions for various values

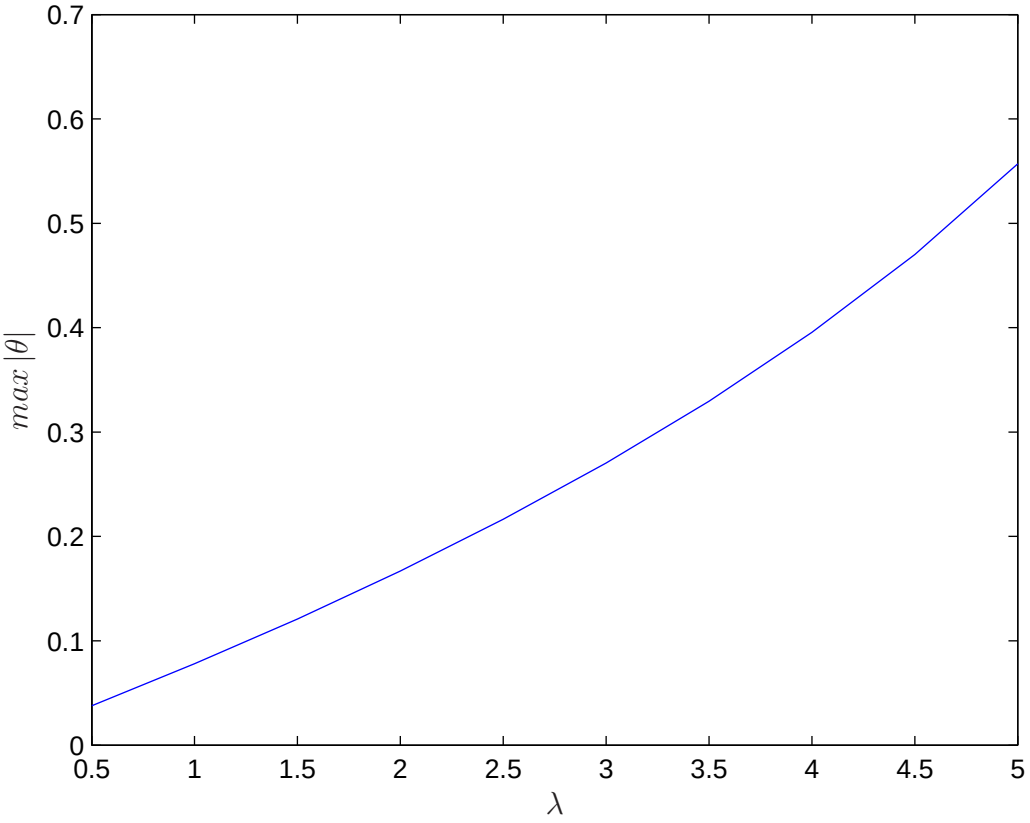

Figure 3.2: The relation between parameter λ and temperature ($max\,|\theta|$) where $\varepsilon = 0$, $m = 101$ and $N = 10$.

N	m	λ_c	θ_c
30	101	6.80802	1.38799
40	101	6.80803	1.38924
45	101	6.80803	1.39269
50	101	6.80804	1.38933

Table 3.2: Comparison of λ_c and θ_c obtained from different grid sizes for $\varepsilon = 0$, for $N = 30, 40, 45, 50$ and $m = 101$.

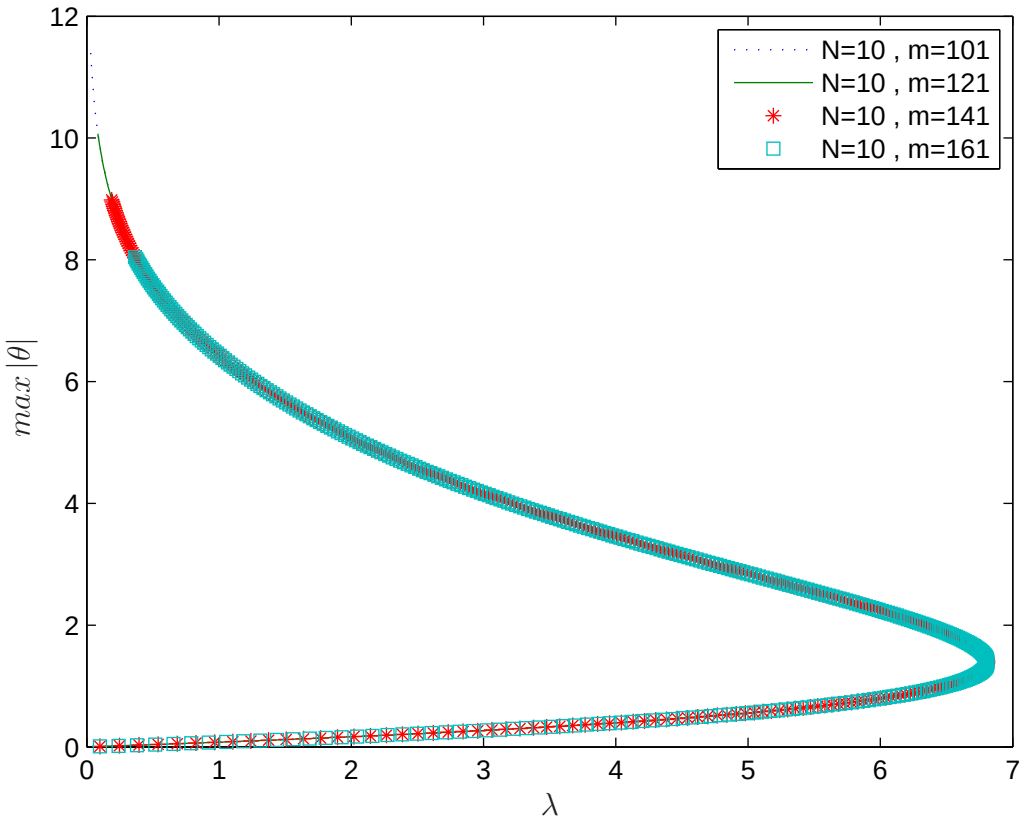

Figure 3.3: λ and $max\,|\theta|$ obtained from different grid sizes $m = 101, 121, 141, 161$ and $N = 10$, for $\varepsilon = 0$.

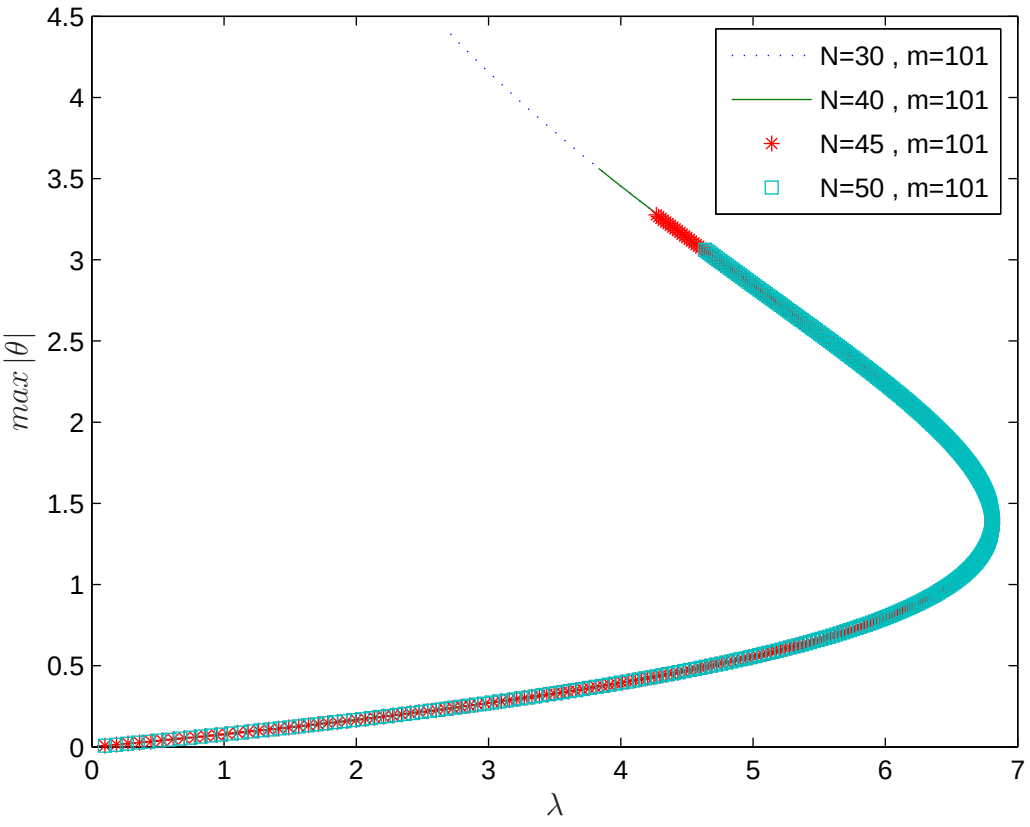

Figure 3.4: λ and $max\,|\theta|$ obtained from different grid sizes for $\varepsilon = 0$, for $N = 30, 40, 45, 50$ and $m = 101$.

ε	λ_{c1}	λ_{c2}
0.00000	6.80805	
0.02000	6.96178	
0.04000	7.12616	
0.06000	7.30269	
0.08000	7.49320	
0.10000	7.70002	
0.12000	7.92618	
0.14000	8.17570	
0.16000	8.45418	
0.18000	8.76991	
0.20000	9.13619	7.10164
0.20500	9.23814	7.54772
0.21000	9.34526	7.98139
0.21500	9.45828	8.39986
0.22000	9.57818	8.80032
0.22500	9.70625	9.17979
0.23000	9.84447	9.53490
0.24000	9.99608	9.86111
0.25000	Non	

Table 3.3: The critical values of λ_c versus ε, when $N = 10$ and $m = 101$.

of λ and ε, when $N = 10$ and $m = 101$, which can be observed in table (3.3), and figure (3.5). Also in figures (3.6) and (3.7), we can see that every variation in the value of ε gives us a different branching diagram and turning point.

When we use these figures to compare our solutions with the solutions available in the literature, we observe that our results agree with those published in Bazley & Wake (1978), as well as Seydel (1994), namely, for $\varepsilon = 0$ there is only one turning point, for $\varepsilon > 0$ there are two turning points and finally, there is no turning point when $\varepsilon > \varepsilon_0$ (note: the value of ε_0 here, as well as in the literature, is $\varepsilon_0 \leq 0.25$). Thus we can infer from the above table and figures that the numerical method adopted to determine the turning points seems to be in good agreement with the literature.

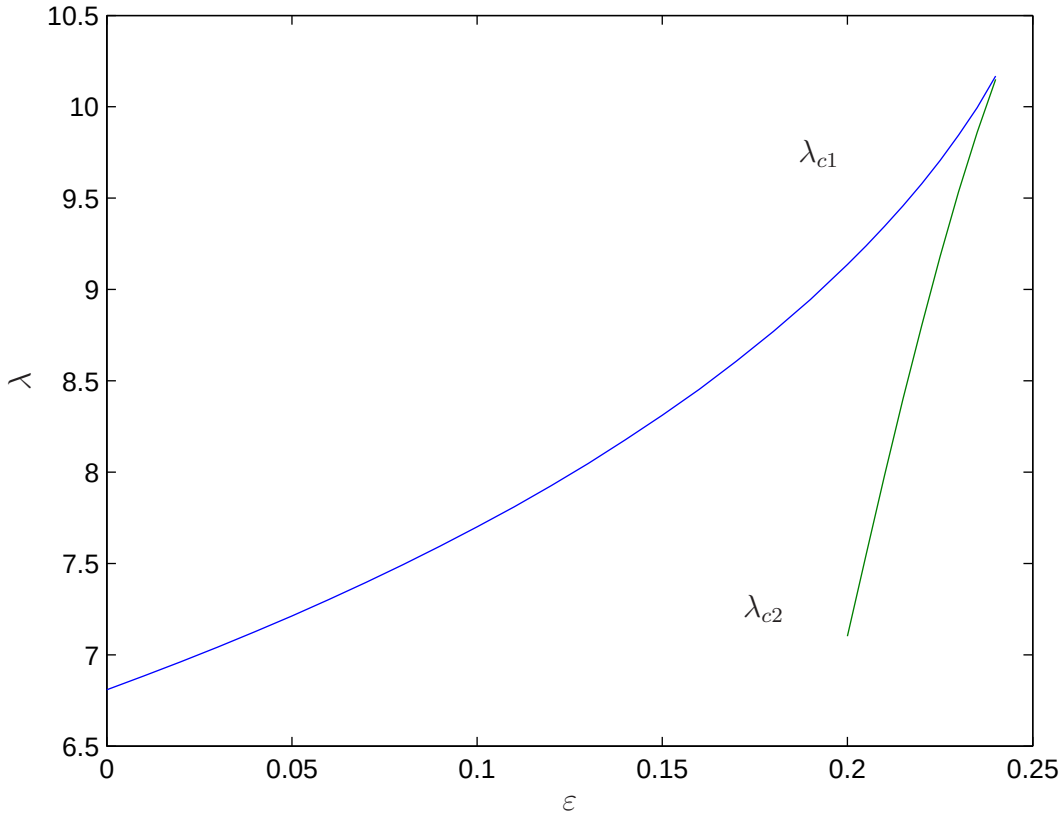

Figure 3.5: The critical values of λ_{c1} and λ_{c2} versus ε when $N = 10$ and $m = 101$.

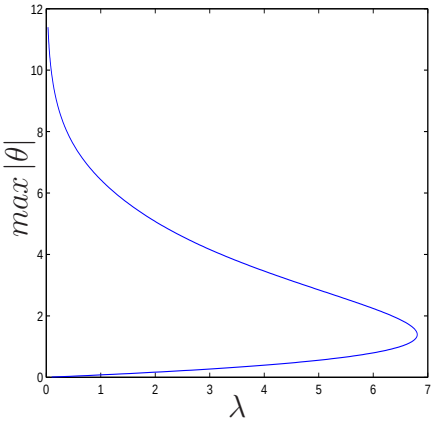

(a) $\varepsilon = 0$

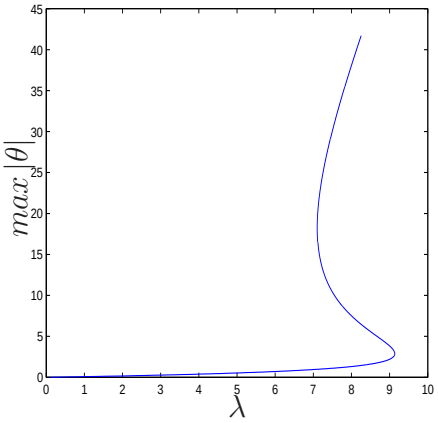

(b) $\varepsilon_0 = .25 > \varepsilon = .20 > 0$

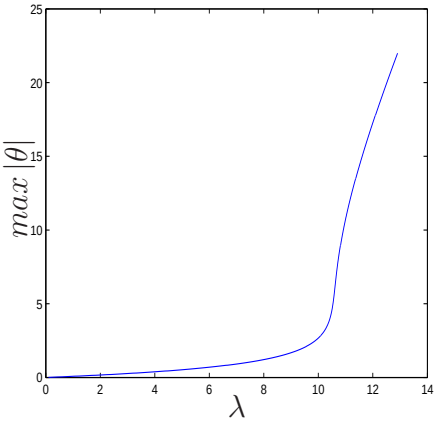

(c) $\varepsilon = .25 = \varepsilon_0$

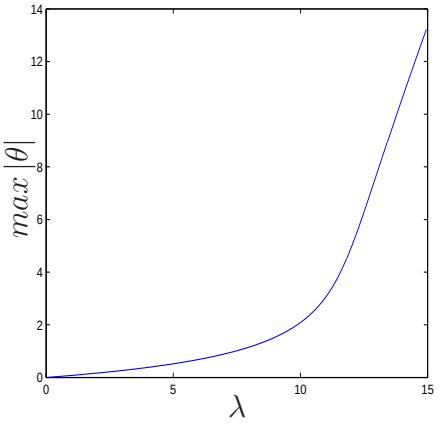

(d) $\varepsilon = .29 > \varepsilon_0 = .25$

Figure 3.6: Comparison of turning points obtained from different values of ε when $N = 10$ and $m = 101$.

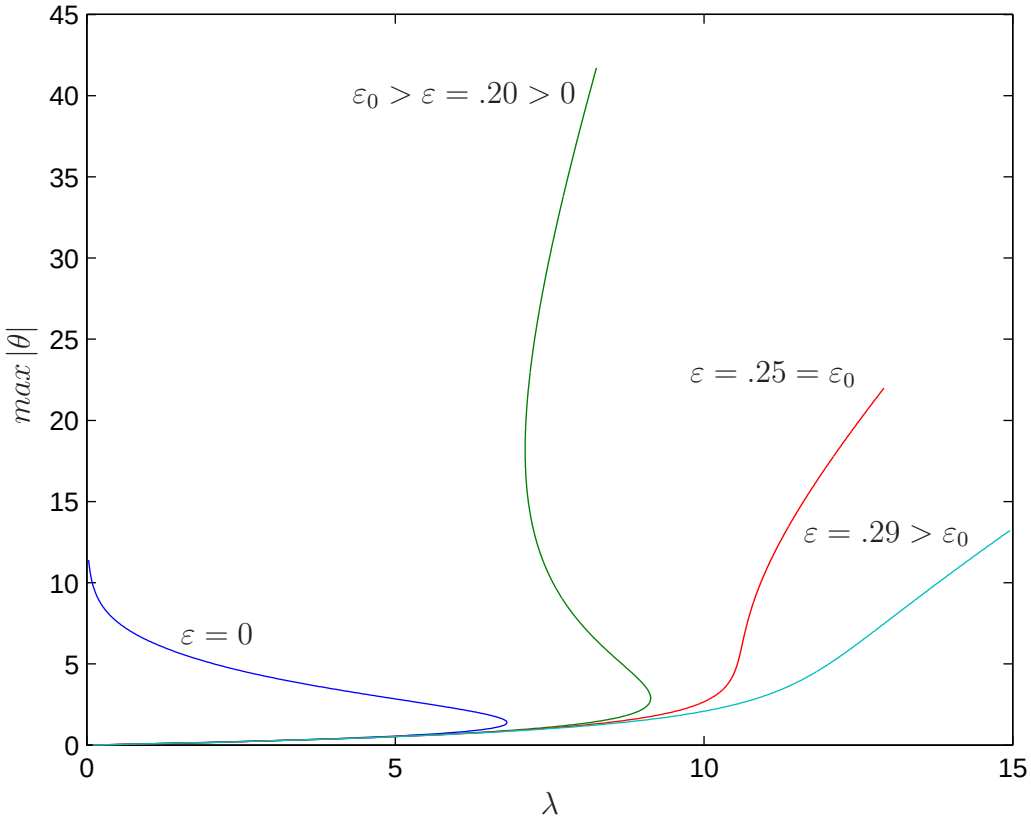

Figure 3.7: Comparison of turning points obtained from different values of ε when $N = 10$ and $m = 101$.

3.3 The Second Test Problem

In this section we consider the Navier-Stokes equations using numerical techniques similar to those described earlier in the first test problem. With the Navier-Stokes equations we find the main difficulty to be in the nonlinearity. We can use a Newton linearization and work in terms of correction terms, as we have seen in the previous sections. Together with the discretization the linearization leads to a linear system.

Here, we combine the use of Newton linearization with a direct solver for the ensuing block tridiagonal system of equations to solve the vorticity streamfunction form of the equations. All the numerical techniques employed here in the solution of this particular problem have been used earlier in our work with the previous problem.

3.3.1 Problem Formulation

The idea and formulation of the incompressible Navier-Stokes equations have been discussed in chapter 1. The form of the steady-state Navier-Stokes equations in streamfunction-vorticity formulation which we use for our test problem is

$$\psi_y \omega_x - \psi_x \omega_y = \frac{1}{Re}\left(\omega_{xx} + \omega_{yy}\right) + F_1\left(x, y\right), \tag{3.70}$$

$$\omega = \left(\psi_{xx} + \psi_{yy}\right), \tag{3.71}$$

where

$$F_1\left(x, y\right) = \left(\left(y-1\right) Re^{\frac{1}{2}} + 1\right) e^{-Re^{\frac{1}{2}} y} Re \sin\left(x\right) \cos\left(x\right) - \frac{1}{Re} \sin\left(x\right)$$
$$\left(\left(Re-1\right)^2 e^{-Re^{\frac{1}{2}} y} + y - 1\right),$$

for $x, y \in D$, $D = [0, \pi] \times [0, 1]$. The term F is added to ensure that the solution below satisfies the equation exactly.

The corresponding boundary conditions for the flow are given by (see Figure 3.8)

$$\begin{array}{llllll}
\psi = 0 & \& \quad \omega = 0 & \text{for} & x = 0, & 0 \le y \le 1, \\
\psi = 0 & \& \quad \omega = 0 & \text{for} & x = \pi\ , & 0 \le y \le 1, \\
\psi = 0 & \& \quad \omega = Re \sin x & \text{for} & y = 0, & 0 \le x \le \pi, \\
\psi = e^{-Re^{\frac{1}{2}}} \sin(x) & \& \quad \omega = (Re-1)\, e^{-Re^{\frac{1}{2}}} \sin(x) & \text{for} & y = 1, & 0 \le x \le \pi.
\end{array}$$

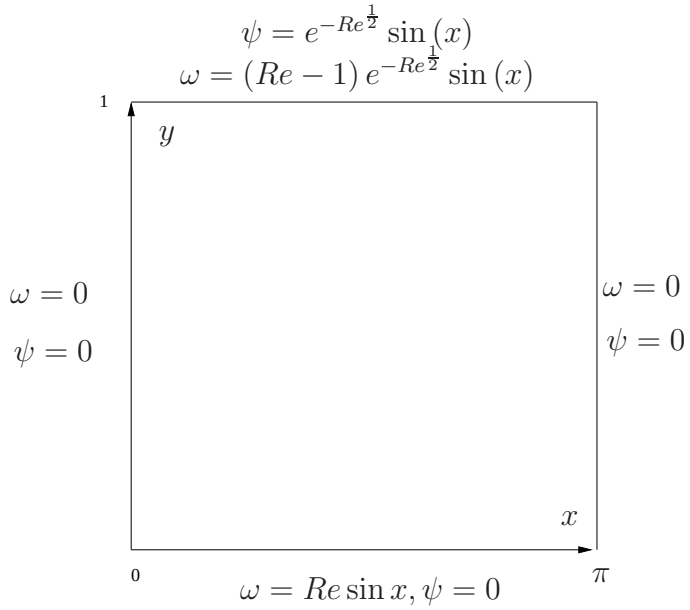

Figure 3.8: The boundary conditions of the test problem of Navier-Stokes equations.

The exact solution to (3.70) and (3.71) is

$$\psi = \left(y + e^{-Re^{\frac{1}{2}}y} - 1\right) \sin x, \tag{3.72}$$

$$\omega = \left(e^{-Re^{\frac{1}{2}}y}(Re-1) - (y-1)\right) \sin x. \tag{3.73}$$

The equations with the boundary condition have to be solved to obtain ψ and ω. The equations are solved first by transforming the domain, then discretized by using the finite difference method on a uniform grid in the x-direction combined with Chebychev collocation in the y-direction domain. As in the previous problem, when we use finite difference combined with spectral method, we can directly

solve the sparse block tridiagonal matrix which has arisen from the discretization.

3.3.2 Results and Solutions

The computational details for the numerical solution procedures which we have developed in working with this test problem are given in Appendix A.

As the result of our work here we obtain an extremely sparse and large linear system from linearization together with discretization, where the number of unknowns is $2(N+1)m$, and values used are $m = 50$ for finite difference points and $N = 20$ for Chebychev points, with Reynolds number $Re = 10$. We can also conclude that there is good convergence to the steady solution. The code converges well with Chebychev collocation in y-direction and second order finite differences in x-direction, with fewer than 5 Newton iterations. We used Matlab and Fortran to solve the equations.

3.4 Conclusion

The numerical techniques which we have used in our work with both test problems have proven to be useful for implementation in the main problem of this thesis. In the first test problem we observed that our result is in good agreement with the literature. Working with the second test problem, the Navier-Stokes equations, we arrived at a good convergence with the steady state solutions. Therefore, we will implement these numerical techniques in our main work with the 2D boundary layer flow in a channel, discussed in the next chapter.

Chapter 4

Two-Dimensional Boundary Layer Flow in a Channel with Suction on the Upper Wall

4.1 Introduction

In this chapter we investigate bifurcations occurring in separated flows at large Reynolds numbers Re. Our aim is the investigation of the stability of a separated flow using global stability analysis together with linear temporal simulation and the continuation algorithm by solving the steady Navier-Stokes equations. The framework of our problem is a two-dimensional boundary layer flow in a channel with suction on the upper wall. The area of interest for this present study is the lower wall of the channel, where the changes in response to the changing magnitudes of suction with the resulting adverse pressure gradients can be observed.

The flow in a channel is only one of many practical applications which have shown the importance of studying the separated boundary layer flow with large

Reynolds numbers in order to understand and better control stability. Working with Navier-Stokes equations and using numerical techniques, the importance lies in resolving the very thin boundary layers present with this kind of flow.

There are several previous studies of channel flow with suction. Pauley *et al.* (1990) made a numerical investigation, as well as Hsiao & Pauley (1994) and Alam & Sandham (2000), who investigated the same problem with different initial and boundary conditions.

In the following sections we will first present the problem formulation and then describe our use of the numerical techniques. These techniques have been employed successfully because the discretization of the non linear equations with a Newton linearization results in a linear system with a block tridiagonal structure, which is then easily solved with a direct solver. Furthermore, in section 4.7 we will give a detailed discussion of our results and solutions for the basic flow. We then describe our work with global stability analysis and the relevant results in section 4.8. Linear temporal simulation with its results is discussed in section 4.9, and we come to conclusions in section 4.10.

4.2 Problem Formulation

Our problem concerns the flow of an incompressible fluid flowing through a channel with a very simple geometry, which consists of a test wall at the lower wall and a suction port on the upper wall (control wall). By adjusting the suction strength we create an adverse pressure gradient which leads to marginal separation conditions in the laminar boundary layer on the test wall.

The governing, non-dimensional, steady-state, 2-D, incompressible Navier-Stokes equations are solved in terms of streamfunction (ψ) and vorticity (ω) formulation describing the total flow and written as,

$$\psi_y\omega_x - \psi_x\omega_y = \frac{1}{Re}\left(\omega_{xx} + \omega_{yy}\right), \tag{4.1}$$

$$\omega = \left(\psi_{xx} + \psi_{yy}\right). \tag{4.2}$$

The Reynolds number here is given by $Re = \frac{UL}{\nu}$, while L is the characteristic entrance length, and the inlet velocity is U, with ν being the kinematic viscosity of the fluid.

The flow domain is $0 \leq x \leq x_{max}$ and $0 \leq y \leq y_{max}$.

The corresponding boundary conditions for the flow (see Figure 4.1) are given by

$$\begin{array}{llllll}
\psi = 0, & \psi_y = 0 & \text{for} & y = 0, & 0 \leq x \leq x_{max}, \\
\psi_y = 1 - \beta\hat{\psi}_s, & \omega = 0 & \text{for} & y = y_{max}, & 0 \leq x \leq x_{max}, \\
\psi = y, & \omega = 0 & \text{for} & x = 0, & 0 \leq y \leq y_{max}, \\
\psi_{xx} = 0, & \omega - \psi_{yy} = 0 & \text{for} & x = x_{max}, & 0 \leq y \leq y_{max},
\end{array}$$

where

β is the suction ratio (control size),

y_{max} is channel height,

$\hat{\psi}_s$ is a function defined by

$$\hat{\psi}_s = -\left[-\left(s_0\left(\frac{b_s}{2y_{max}}\right)\right) + \frac{s_0}{\pi}\left[\ln\left|\frac{\sinh\left[\frac{\pi(x-1-b_s)}{2y_{max}}\right]}{\sinh\left[\frac{\pi(x-1)}{2y_{max}}\right]}\right|\right]\right],$$

b_s is the set equal to 0.062,

and $s_0 = \frac{y_{max}}{b_s}$.

The function $\hat{\psi}_s$ is the same as that used by Hsiao & Pauley (1994) and Braun (2006) and corresponds to taking a distribution of source singularites between

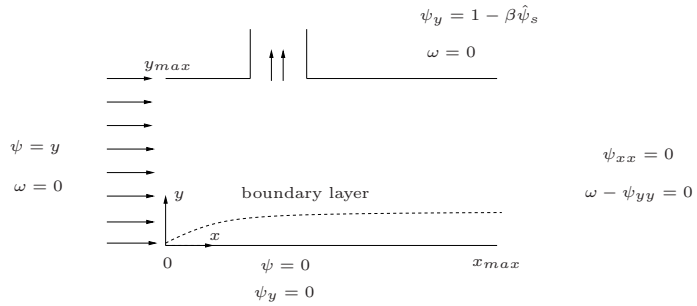

Figure 4.1: Sketch of channel with suction with boundary conditions.

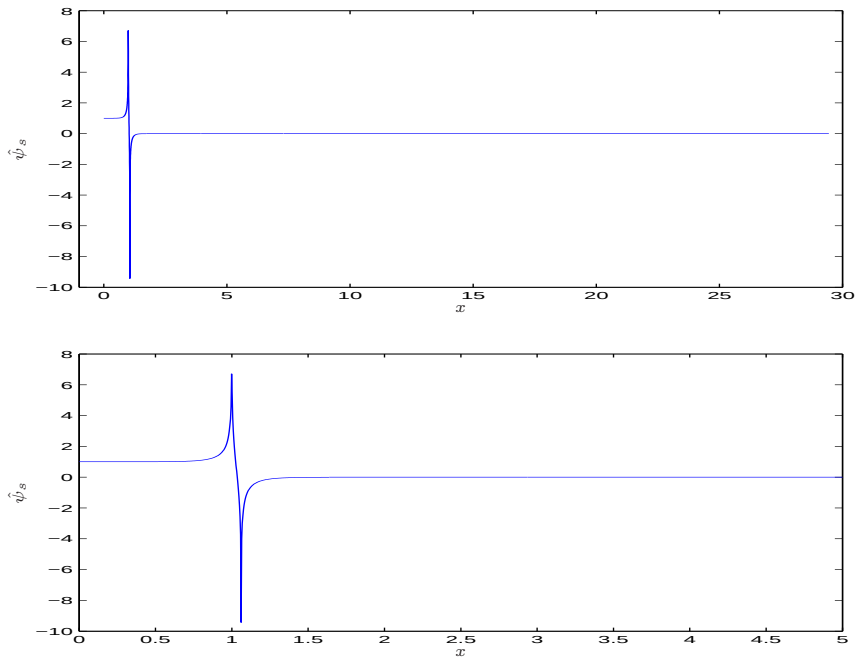

(a) Snapshot of the figure above

Figure 4.2: plots for the function $\hat{\psi}_s$ where $y_{max} = 0.3$, $Re = 50000$, $\beta = 0.0997$, $N = 100$ and $m = 1501$.

$x = 1$ and $x = 1 + b_s$ for the outer inviscid flow. There is a singularity in $\hat{\psi}_s$ at $x = 1$ but in our numerical work, we approximated $\hat{\psi}_s(1)$ by $\hat{\psi}_s(1.0001)$. The plot of the distribution of the function $\hat{\psi}_s$ for $y_{max} = 0.3$, $Re = 50000$, $\beta = 0.0997$, $N = 100$ and $m = 1501$ is shown in figure (4.2).

The equations with the boundary condition have to be solved to obtain ψ and ω. In the calculations reported below $y_{max} = 0.3$ was usually taken, but other

values were also considered.

4.3 Numerical Solution Procedure

All the numerical techniques employed in the solution of this particular problem have been used earlier in our work with the previous problem discussed in chapter 3, but appear here with an added element of complexity.

These equations (4.1) and (4.2) are solved first by transforming, then discretizing the domain, by using the finite difference method for the first and second derivative on a non-uniform grid in the x-direction, combined with the Chebychev collocation in the y-direction domain, which is suitable for our problem here because it clusters points at the boundaries and this is important in the resolution of boundary layers. As in chapter three, when we use finite difference combined with spectral method and discretization, we find the main difficulty to be in the non-linearity. Here we use Newton linearization and correction terms to linearize the equations. We can directly solve the sparse block tridiagonal matrix which has arisen from the discretization by combining the use of Newton linearization with a direct solver to solve the vorticity streamfunction form of the equation.

4.3.1 Discretization in y-Direction

For the y-direction we work with function values using the Chebychev collocation. In Chebychev space the mapping $(0, y_{max}) \longrightarrow (-1, 1)$ is used such that the collocation points are given by

$$z = z_j = -\cos\left(\frac{j\pi}{N}\right) \qquad j = 0, 1, \ldots, N, \tag{4.3}$$

and

$$y = y\left(z_j\right) = y_j = \frac{y_{max}}{2}\left(1 + z_j\right), \qquad j = 0, 1, \ldots, N. \tag{4.4}$$

We also define $\psi_{k,j} = \psi\left(x = x_k, y = y_j\right)$ and $\omega_{k,j} = \omega\left(x = x_k, y = y_j\right)$.

Then, the first derivative in y is given by

$$\left(\frac{\partial \Gamma}{\partial y}\right)_{k,j} = \frac{2}{y_{max}} \sum_{i=0}^{N} \left(D1\right)_{j,i} \Gamma_{k,i}, \tag{4.5}$$

and the second derivative in y is given by

$$\left(\frac{\partial^2 \Gamma}{\partial y^2}\right)_{k,j} = \left(\frac{2}{y_{max}}\right)^2 \sum_{i=0}^{N} \left(D2\right)_{j,i} \Gamma_{k,i}, \tag{4.6}$$

where Γ can be either streamfunction (ψ) or vorticity (ω), while the respective elements of the Chebychev collocation differentiation matrix of $\mathbf{D}$ and $\mathbf{D^2}$ are $D1_{j,i}$ and $D2_{j,i}$ (see equation (1.17)).

Near the boundary we need greater numerical accuracy. Chebychev Collocation clusters points at boundaries and therefore gives us greater resolution. In our work here we use a non-uniform grid in y-direction and we solve our problem by using this following mapping,

$$y = f\left(z\right),$$

$$f\left(z\right) = y_j \left(\left(1 - a_g\right) \left(\frac{y_j}{b}\right)^2 + a_g \right), \tag{4.7}$$

where $b = y_{max}$, and in our work here $a_g = 1$.

4.3.2 Discretization in x-Direction

By using functions $x = f\left(\xi\right)$ where

$$\frac{d}{dx} = \frac{d\xi}{dx}\frac{d}{d\xi}, \qquad \text{and} \qquad \frac{d^2}{dx^2} = \frac{d^2\xi}{dx^2}\frac{d}{d\xi} + \left(\frac{d\xi}{dx}\right)^2 \frac{d^2}{d\xi^2},$$

The x-domain is simply discretized into a uniform grid defined over $[\xi_{\min}, \xi_{\max}]$ given by,

$$\xi = \xi_k = \xi_{\min} + (k-1)\triangle\xi \qquad k = 1, 2, \ldots, m \tag{4.8}$$

and

$$\triangle\xi = \frac{\xi_{\max} - \xi_{\min}}{m-1}, \tag{4.9}$$

where $\xi_{\max} = 0.93$, and $\xi_{\min} = \left(\frac{2}{\pi}\right)\tan^{-1}\left(\frac{-b1}{a1}\right)$,

while $b1 = 1$ and $a1 = \pi$.

To allow for a non-uniform grid in the x-direction we use a transform in the x-direction similar to one employed by Logue (2008), given by,

$$x_k = f(\xi_k) = b1 + (a1)\tan\left(\frac{\pi}{2}\xi_k\right),$$

where x_k and ξ_k are the physical variable and the computational variable respectively, while $b1 = 1$ is the location of the gathering of the grid points and $a1 = \pi$ is the parameter for their distribution at $b1$.

Thus the first and second derivatives in the x-direction are discretized using central differencing in the interior of the domain by

$$\left(\frac{\partial\Gamma}{\partial\xi}\right)_{kj} = \frac{\Gamma_{k+1,j} - \Gamma_{k-1,j}}{(2\Delta\xi)}, \tag{4.10}$$

and

$$\left(\frac{\partial^2\Gamma}{\partial\xi^2}\right)_{kj} = \frac{\Gamma_{k+1,j} - 2\Gamma_{k,j} + \Gamma_{k-1,j}}{(\Delta\xi)^2}, \tag{4.11}$$

where Γ also can be either streamfunction (ψ) or vorticity (ω).

4.3.3 The Discrete Form

By using functions $y = f(z)$ and $x = f(\xi)$ where

$$\frac{d}{dy} = \frac{dz}{dy}\frac{d}{dz} \qquad \text{and} \qquad \frac{d}{dx} = \frac{d\xi}{dx}\frac{d}{d\xi},$$

we also have

$$\frac{d^2}{dy^2} = \frac{d^2z}{dy^2}\frac{d}{dz} + \left(\frac{dz}{dy}\right)^2\frac{d^2}{dz^2} \qquad \text{and} \qquad \frac{d^2}{dx^2} = \frac{d^2\xi}{dx^2}\frac{d}{d\xi} + \left(\frac{d\xi}{dx}\right)^2\frac{d^2}{d\xi^2},$$

for the equations (4.1) and (4.2) we obtain,

$$\left[\frac{dz}{dy}\frac{d\psi}{dz}\right]\left[\frac{d\xi}{dx}\frac{d\omega}{d\xi}\right]-\left[\frac{d\xi}{dx}\frac{d\psi}{d\xi}\right]\left[\frac{dz}{dy}\frac{d\omega}{dz}\right]=\frac{1}{Re}\left[\frac{d^2\xi}{dx^2}\frac{d\omega}{d\xi}+\left(\frac{d\xi}{dx}\right)^2\frac{d^2\omega}{d\xi^2}\right.$$
$$\left.+\frac{d^2z}{dy^2}\frac{d\omega}{dz}+\left(\frac{dz}{dy}\right)^2\frac{d^2\omega}{dz^2}\right], \tag{4.12}$$

and

$$\omega=\frac{d^2\xi}{dx^2}\frac{d\psi}{d\xi}+\left(\frac{d\xi}{dx}\right)^2\frac{d^2\psi}{d\xi^2}+\frac{d^2z}{dy^2}\frac{d\psi}{dz}+\left(\frac{dz}{dy}\right)^2\frac{d^2\psi}{dz^2}. \tag{4.13}$$

Then, by using first and second order discretization in x and y for the above equations, we get the following discrete equation:

$$\left(\frac{dz}{dy}\right)(D_z\psi)_{kj}\left(\frac{d\xi}{dx}\right)\frac{\omega_{k+1j}-\omega_{k-1j}}{2\Delta\xi}-\left(\frac{dz}{dy}\right)(D_z\omega)_{kj}\left(\frac{d\xi}{dx}\right)\frac{\psi_{k+1j}-\psi_{k-1j}}{2\Delta\xi}$$
$$=\frac{1}{Re}\left(\frac{d^2\xi}{dx^2}\right)\frac{\omega_{k+1j}-\omega_{k-1j}}{2\Delta\xi}+\frac{1}{Re}\left(\frac{d\xi}{dx}\right)^2\frac{\omega_{k+1j}-2\omega_{kj}+\omega_{k-1j}}{(\Delta\xi)^2}$$
$$+\frac{1}{Re}\left(\frac{d^2z}{dy^2}\right)(D_z\omega)_{kj}+\frac{1}{Re}\left(\frac{dz}{dy}\right)^2\left(D_z^2\omega\right)_{kj}, \tag{4.14}$$

and

$$\omega_{kj}=\left(\frac{d^2\xi}{dx^2}\right)\frac{\psi_{k+1j}-\psi_{k-1j}}{2\Delta\xi}+\left(\frac{d\xi}{dx}\right)^2\frac{\psi_{k+1j}-2\psi_{kj}+\psi_{k-1j}}{(\Delta\xi)^2}$$
$$+\left(\frac{d^2z}{dy^2}\right)(D_z\psi)_{kj}+\left(\frac{dz}{dy}\right)^2\left(D_z^2\psi\right)_{kj},$$
$$1\le k\le m \qquad and \qquad 0\le j\le N. \tag{4.15}$$

The corresponding boundary conditions are given by

$\psi_{k0}=0,$	$(\psi_y)_{k0}=0$	for	$y=0,$	$1\le k\le m,$
$(\psi_y)_{kN}=1-\beta\hat{\psi}_s,$	$\omega_{kN}=0$	for	$y=y_{max},$	$1\le k\le m,$
$\psi_{1j}=y_j,$	$\omega_{1j}=0$	for	$x=0,$	$0\le j\le N,$
$(\psi_{xx})_{mj}=0,$	$\omega_{mj}-(\psi_{yy})_{mj}=0$	for	$x=x_{max},$	$0\le j\le N.$

4.4 Linearizing the Equations

We have nonlinear equations (4.14) and (4.15) with their boundary conditions, so we need to use a Newton linearization and work with correction terms G_{kj} and H_{kj} where

$$\begin{cases} \psi_{kj} &= \bar{\psi}_{kj} + G_{kj}, \\ \omega_{kj} &= \Omega_{kj} + H_{kj}, \end{cases} \tag{4.16}$$

such that $|G_{kj}|$, $|H_{kj}| \ll 1$ and $\bar{\psi}_{kj}$, Ω_{kj} are some initial guesses.

By substituting equations (4.16) into equations (4.14) and (4.15) and their boundary conditions, we obtain

$$\begin{aligned} &\left(\frac{dz}{dy}\right)\left(D_z\,\bar{\psi}\right)_{kj}\left(\frac{d\xi}{dx}\right)\frac{H_{k+1j}-H_{k-1j}}{2\Delta\xi}+\left(\frac{dz}{dy}\right)(D_zG)_{kj}\left(\frac{d\xi}{dx}\right)\\ &\frac{\Omega_{k+1j}-\Omega_{k-1j}}{2\Delta\xi}-\left(\frac{dz}{dy}\right)(D_zH)_{kj}\left(\frac{d\xi}{dx}\right)\frac{\bar{\psi}_{k+1j}-\bar{\psi}_{k-1j}}{2\Delta\xi}-\left(\frac{dz}{dy}\right)(D_z\Omega)_{kj}\\ &\left(\frac{d\xi}{dx}\right)\frac{G_{k+1j}-G_{k-1j}}{2\Delta\xi}-\frac{1}{Re}\left(\frac{d\xi}{dx}\right)^2\frac{H_{k+1j}-2H_{kj}+H_{k-1j}}{(\Delta\xi)^2}-\frac{1}{Re}\left(\frac{dz}{dy}\right)^2\\ &\left(D_z^2H\right)_{kj}-\frac{1}{Re}\left(\frac{d^2\xi}{dx^2}\right)\frac{H_{k+1j}-H_{k-1j}}{2\Delta\xi}-\frac{1}{Re}\left(\frac{d^2z}{dy^2}\right)(D_zH)_{kj}=RB_{kj}, \end{aligned} \tag{4.17}$$

where

$$\begin{aligned} RB_{kj} &= -\left(\frac{dz}{dy}\right)\left(D_z\,\bar{\psi}\right)_{kj}\left(\frac{d\xi}{dx}\right)\frac{\Omega_{k+1j}-\Omega_{k-1j}}{2\Delta\xi}+\left(\frac{dz}{dy}\right)(D_z\Omega)_{kj}\left(\frac{d\xi}{dx}\right)\\ &\quad\frac{\bar{\psi}_{k+1j}-\bar{\psi}_{k-1j}}{2\Delta\xi}+\frac{1}{Re}\left(\frac{d^2\xi}{dx^2}\right)\frac{\Omega_{k+1j}-\Omega_{k-1j}}{2\Delta\xi}+\frac{1}{Re}\left(\frac{d\xi}{dx}\right)^2\\ &\quad\frac{\Omega_{k+1j}-2\Omega_{kj}+\Omega_{k-1j}}{(\Delta\xi)^2}+\frac{1}{Re}\left(\frac{d^2z}{dy^2}\right)(D_z\Omega)_{kj}+\frac{1}{Re}\left(\frac{dz}{dy}\right)^2\left(D_z^2\Omega\right)_{kj}, \end{aligned} \tag{4.18}$$

we also have

$$\begin{aligned} &\left(\frac{d^2\xi}{dx^2}\right)\frac{G_{k+1j}-G_{k-1j}}{2\Delta\xi}+\left(\frac{d\xi}{dx}\right)^2\frac{G_{k+1j}-2G_{kj}+G_{k-1j}}{(\Delta\xi)^2}+\left(\frac{d^2z}{dy^2}\right)(D_zG)_{kj}\\ &+\left(\frac{dz}{dy}\right)^2\left(D_z^2G\right)_{kj}-H_{kj}=(RA)_{kj}, \end{aligned} \tag{4.19}$$

where

$$(RA)_{kj} = -\left(\frac{d^2\xi}{dx^2}\right)\frac{\bar{\psi}_{k+1j}-\bar{\psi}_{k-1j}}{2\Delta\xi}-\left(\frac{d\xi}{dx}\right)^2\frac{\bar{\psi}_{k+1j}-2\,\bar{\psi}_{kj}+\bar{\psi}_{k-1j}}{(\Delta\xi)^2} - \left(\frac{d^2z}{dy^2}\right)\left(D_z\,\bar{\psi}\right)_{kj}-\left(\frac{dz}{dy}\right)^2\left(D_z^2\,\bar{\psi}\right)_{kj}+\Omega_{kj}. \tag{4.20}$$

4.5 Solution of Discrete Equation

Let

$$\mathbf{T}_k=\begin{pmatrix} G_k \\ H_k \end{pmatrix} \qquad \& \qquad G_k=\begin{pmatrix} G_{k0} \\ G_{k1} \\ \vdots \\ G_{kN} \end{pmatrix} \qquad \& \qquad H_k=\begin{pmatrix} H_{k0} \\ H_{k1} \\ \vdots \\ H_{kN} \end{pmatrix}. \tag{4.21}$$

Below is the form of the linear system which we obtain after Newton linearization,

$$\mathbf{A}_k\mathbf{T}_{k-1}+\mathbf{B}_k\mathbf{T}_k+\mathbf{C}_k\mathbf{T}_{k+1}=\mathbf{R}_k \qquad 1\le k\le m, \tag{4.22}$$

where

$$\mathbf{A}_k=\begin{pmatrix} \mathbf{A}_1 & \mathbf{A}_2 \\ \mathbf{A}_3 & \mathbf{A}_4 \end{pmatrix},$$

$$\mathbf{B}_k=\begin{pmatrix} \mathbf{B}_1 & \mathbf{B}_2 \\ \mathbf{B}_3 & \mathbf{B}_4 \end{pmatrix},$$

$$\mathbf{C}_k=\begin{pmatrix} \mathbf{C}_1 & \mathbf{C}_2 \\ \mathbf{C}_3 & \mathbf{C}_4 \end{pmatrix},$$

$$\mathbf{R}_k=\begin{pmatrix} \mathbf{R}_1 \\ \mathbf{R}_2 \end{pmatrix}, \tag{4.23}$$

where (4.21) $\mathbf{T}_k$ is the vector of unknown streamfunction and vorticity corrections at each station $x = x_k$, with $\boldsymbol{\psi}_{kj}$, which is denoting the value of the streamfunction and Ω_{kj}, which is denoting the value of the vorticity at the point $x = x_k, y = y(z_j)$. Each entry in the vector $\mathbf{T}$ is a vector of size $(N+1) \times 1$. In x-direction the use of second order differences gives rise to the block tridiagonal structure in (4.22). In (4.22) each of the coefficient matrices is a dense matrix of size $2(N+1)$ by $2(N+1)$, stemming from the system (4.17) $\longrightarrow$ (4.20), enforced at the collocation points and all entries in these matrices are matrices of size $(N+1)$ by $(N+1)$. All the vectors $\mathbf{T}_k$ in the linear system (4.22) were solved by using a direct solver and utilizing the sparsity pattern of the block tridiagonal matrix. The result of the linear system (4.22), when written in matrix form is:

$$\mathbf{JT} = \mathbf{R}, \tag{4.24}$$

where

$$\mathbf{J} = \begin{bmatrix} \mathbf{B}_1 & \mathbf{C}_1 & & & & & & \\ \mathbf{A}_2 & \mathbf{B}_2 & \mathbf{C}_2 & & & & & \\ & \mathbf{A}_3 & \mathbf{B}_3 & \mathbf{C}_3 & & & & \\ & & \mathbf{A}_4 & \mathbf{B}_4 & \mathbf{C}_4 & & & \\ & & & \ddots & \ddots & \ddots & & \\ & & & & & \mathbf{A}_{m-1} & \mathbf{B}_{m-1} & \mathbf{C}_{m-1} \\ & & & & & & \mathbf{A}_m & \mathbf{B}_m \end{bmatrix}, \tag{4.25}$$

and

$\mathbf{T}$ is a vector of correction terms to be found,

$$\mathbf{T} = [\mathbf{T_1}, \mathbf{T_2}, \ldots, \mathbf{T_{m-1}}, \mathbf{T_m}]^T,$$

$$\mathbf{R} = [\mathbf{R_1}, \mathbf{R_2}, \ldots, \mathbf{R_{m-1}}, \mathbf{R_m}]^T.$$

4.6 The Boundary Conditions

The boundary conditions with Newton linearization become

$$\text{for} \quad y = 0, \qquad G_{k0} = -\bar{\psi}_{k0}, \qquad \left(\frac{dz}{dy}\right)(\mathbf{D_z}G)_{k0} = -\frac{dz}{dy}\mathbf{D_z}\bar{\psi}_{k0},$$

$$\text{for} \quad y = y_{max}, \quad \left(\frac{dz}{dy}\right)(\mathbf{D_z}G)_{kN} = -\frac{dz}{dy}\mathbf{D_z}\bar{\psi}_{kN} + 1 - \beta\hat{\omega}_s, \qquad H_{kN} = -\Omega_{kN},$$

$$\text{for} \quad x = 0, \qquad G_{1j} = -\bar{\psi}_{1j} + y_j, \qquad H_{1j} = -\Omega_{1j},$$

$$\text{for} \quad x = x_{max} \quad \begin{cases} \left(\frac{d^2\xi}{dx^2}\right)\frac{G_{mj}-G_{mj-1}}{\Delta\xi} + \left(\frac{d\xi}{dx}\right)^2\frac{G_{mj}-2G_{mj-1}+G_{mj-2}}{(\Delta\xi)^2} \\ = -\left(\frac{d^2\xi}{dx^2}\right)\frac{\bar{\psi}_{mj}-\bar{\psi}_{mj-1}}{\Delta\xi} - \left(\frac{d\xi}{dx}\right)^2\frac{\bar{\psi}_{mj}-2\bar{\psi}_{mj-1}+\bar{\psi}_{mj-2}}{(\Delta\xi)^2}, \\ H_{mj} - \left(\frac{d^2z}{dy^2}\right)(\mathbf{D_z}G)_{mj} - \left(\frac{dz}{dy}\right)^2\left(\mathbf{D_z}^2G\right)_{mj} \\ = -\Omega_{mj} + \left(\frac{d^2z}{dy^2}\right)\left(\mathbf{D_z}\bar{\psi}\right)_{mj} + \left(\frac{dz}{dy}\right)^2\left(\mathbf{D_z}^2\bar{\psi}\right)_{mj}. \end{cases}$$

As mentioned earlier in section (4.4) the x boundary condition is implemented through the establishment of the matrix equations of the form (4.22) for the cases $k = 1$ and $k = m$, but first, the y boundary conditions are included in the problem and the final form of the matrices in (4.22) are given for $2 \leq k \leq m-1$.

In the following, $(\mathbf{I})$ denotes an identity matrix and $(\mathbf{0})$ denotes a zero matrix each of size $(N+1)$ by $(N+\ 1)$.

Thus, the matrices for $2 \leq k \leq m-1$ are given by comparison with (4.19) and the boundary conditions,

$$(\mathbf{A1})_k = -\left(\frac{d^2\xi}{dx^2}\right)\frac{1}{2\Delta\xi}\mathbf{I} + \left(\frac{d\xi}{dx}\right)^2\frac{1}{\Delta\xi^2}\mathbf{I}, \tag{4.26}$$

and

$$\begin{aligned} \mathbf{A1}_k(0,:) &= \mathbf{0}, \\ \mathbf{A1}_k(N,:) &= \mathbf{0}. \end{aligned} \tag{4.27}$$

$$(\mathbf{A2})_k = \mathbf{0}. \tag{4.28}$$

$$(\mathbf{B1})_k = \left(\frac{d^2z}{dy^2}\right)(\mathbf{D_z}) + \left(\frac{dz}{dy}\right)^2(\mathbf{D_z^2}) - \left(\frac{d\xi}{dx}\right)^2\frac{2}{\Delta\xi^2}\mathbf{I}, \tag{4.29}$$

and

$$\begin{aligned}\mathbf{B1}_k(0,:) &= (1,0,\ldots,0),\\ \mathbf{B1}_k(N,:) &= \left(\frac{dz}{dy}\right)\mathbf{D_z}.\end{aligned} \tag{4.30}$$

$$(\mathbf{B2})_k = -\mathbf{I}, \tag{4.31}$$

and

$$\begin{aligned}\mathbf{B2}_k(0,:) &= \mathbf{0},\\ \mathbf{B2}_k(N,:) &= \mathbf{0}.\end{aligned} \tag{4.32}$$

$$(\mathbf{C1})_k = \left(\frac{d^2\xi}{dx^2}\right)\frac{1}{2\Delta\xi}\mathbf{I} + \left(\frac{d\xi}{dx}\right)^2\frac{1}{\Delta\xi^2}\mathbf{I}, \tag{4.33}$$

and

$$\begin{aligned}\mathbf{C1}_k(0,:) &= \mathbf{0},\\ \mathbf{C1}_k(N,:) &= \mathbf{0}.\end{aligned} \tag{4.34}$$

$$(\mathbf{C2})_k = \mathbf{0}. \tag{4.35}$$

$$(\mathbf{R1})_k = \begin{pmatrix} -\bar{\psi}_{k0} \\ (RA)_{kj} \\ -\frac{dz}{dy}\mathbf{D_z}\bar{\psi}_{kN} + 1 - \beta\hat{\omega}_s \end{pmatrix}.$$

Now, the matrices for $2 \leq k \leq m-1$ are given by comparison with (4.17) and the boundary conditions, where (diag(...)) denotes a diagonal matrix with the elements on the main diagonal shown in brackets below.

$$(\mathbf{A3})_k = \left(\frac{dz}{dy}\right) \text{diag}\left((\mathbf{D_z}\Omega)_{k,0}, (\mathbf{D_z}\Omega)_{k,1}, \ldots, (\mathbf{D_z}\Omega)_{k,j}, \ldots\right) \left(\frac{d\xi}{dx}\right) \frac{1}{2\Delta\xi}\mathbf{I}, \tag{4.36}$$

and

$$\begin{aligned} \mathbf{A3}_k(0,:) &= \mathbf{0}, \\ \mathbf{A3}_k(N,:) &= \mathbf{0}. \end{aligned} \tag{4.37}$$

$$\begin{aligned} (\mathbf{A4})_k = & -\left(\frac{dz}{dy}\right) \text{diag}\left(\left(\mathbf{D_z}\,\bar{\psi}\right)_{k,0}, \left(\mathbf{D_z}\,\bar{\psi}\right)_{k,1}, \ldots, \left(\mathbf{D_z}\,\bar{\psi}\right)_{k,j}, \ldots\right) \\ & \left(\frac{d\xi}{dx}\right) \frac{1}{2\Delta\xi}\mathbf{I} - \frac{1}{Re\Delta\xi^2}\left(\frac{d\xi}{dx}\right)^2 \mathbf{I} + \frac{1}{2Re\Delta\xi}\left(\frac{d^2\xi}{dx^2}\right)\mathbf{I}, \end{aligned} \tag{4.38}$$

and

$$\begin{aligned} \mathbf{A4}_k(0,:) &= \mathbf{0}, \\ \mathbf{A4}_k(N,:) &= \mathbf{0}. \end{aligned} \tag{4.39}$$

$$\begin{aligned} (\mathbf{B3})_k = & \left(\frac{d\xi}{dx}\right) \frac{1}{2\Delta\xi} \text{diag}\Big[(\Omega_{k+1,0} - \Omega_{k-1,0}), (\Omega_{k+1,1} - \Omega_{k-1,1}), \ldots, \\ & (\Omega_{k+1,j} - \Omega_{k-1,j}), \ldots \Big] \left(\frac{dz}{dy}\right) \mathbf{D_z}, \end{aligned} \tag{4.40}$$

and

$$\begin{aligned} \mathbf{B3}_k(0,:) &= \left(\frac{dz}{dy}\right) \mathbf{D_z}, \\ \mathbf{B3}_k(N,:) &= \mathbf{0}. \end{aligned} \tag{4.41}$$

$$\begin{aligned}(\mathbf{B4})_k &= -\left(\frac{d\xi}{dx}\right)\frac{1}{2\Delta\xi}\mathrm{diag}\Big[\left(\bar{\psi}_{k+1,0}-\bar{\psi}_{k-1,0}\right),\left(\bar{\psi}_{k+1,1}-\bar{\psi}_{k-1,1}\right),\ldots,\\ &\quad \left(\bar{\psi}_{k+1,j}-\bar{\psi}_{k-1,j}\right),\ldots\Big]\left(\frac{dz}{dy}\right)(\mathbf{D_z})+\frac{2}{Re\Delta x^2}\left(\frac{d\xi}{dx}\right)^2\mathbf{I}\\ &\quad -\frac{1}{Re}\left(\frac{dz}{dy}\right)^2(\mathbf{D_z^2})-\frac{1}{Re}\left(\frac{d^2z}{dy^2}\right)\mathbf{D_z},\end{aligned} \tag{4.42}$$

and

$$\begin{aligned}\mathbf{B4}_k(0,:) &= \mathbf{0},\\ \mathbf{B4}_k(N,:) &= (0,\ldots,0,1).\end{aligned} \tag{4.43}$$

$$(\mathbf{C3})_k = -\left(\frac{dz}{dy}\right)\mathrm{diag}\left((\mathbf{D_z}\Omega)_{k,0},(\mathbf{D_z}\Omega)_{k,1},\ldots,(\mathbf{D_z}\Omega)_{k,j},\ldots\right)\left(\frac{d\xi}{dx}\right)\frac{1}{2\Delta\xi}\mathbf{I}, \tag{4.44}$$

and

$$\begin{aligned}\mathbf{C3}_k(0,:) &= \mathbf{0},\\ \mathbf{C3}_k(N,:) &= \mathbf{0}.\end{aligned} \tag{4.45}$$

$$\begin{aligned}(\mathbf{C4})_k &= \left(\frac{dz}{dy}\right)\mathrm{diag}\left(\left(\mathbf{D_z}\,\bar{\psi}\right)_{k,0},\left(\mathbf{D_z}\,\bar{\psi}\right)_{k,1},\ldots,\left(\mathbf{D_z}\,\bar{\psi}\right)_{k,j},\ldots\right)\left(\frac{d\xi}{dx}\right)\\ &\quad \frac{1}{2\Delta\xi}\mathbf{I}-\frac{1}{Re\Delta\xi^2}\left(\frac{d\xi}{dx}\right)^2\mathbf{I}-\frac{1}{2Re\Delta\xi}\left(\frac{d^2\xi}{dx^2}\right)\mathbf{I},\end{aligned} \tag{4.46}$$

and

$$\begin{aligned}\mathbf{C4}_k(0,:) &= \mathbf{0},\\ \mathbf{C4}_k(N,:) &= \mathbf{0}.\end{aligned} \tag{4.47}$$

$$(\mathbf{R2})_k = \begin{pmatrix} -\left(\frac{dz}{dy}\right)\left(\mathbf{D_z}\ \bar{\psi}\right)_{k0} \\ RB_{kj} \\ -\Omega_{kN} \end{pmatrix}.$$

Now, the matrices for $K = 1$ are given by

$$\mathbf{A}_1\mathbf{T}_0 + \mathbf{B}_1\mathbf{T}_1 + \mathbf{C}_1\mathbf{T}_2 = \mathbf{R}_1, \tag{4.48}$$

where

$$\begin{aligned} \mathbf{A}_1 &= \mathbf{0}, \\ \mathbf{B1}_1 = \mathbf{B4}_1 &= \mathbf{I}, \\ \mathbf{C}_1 &= \mathbf{0}, \end{aligned} \tag{4.49}$$

and

$$\mathbf{R}_1 = \begin{pmatrix} -\bar{\psi}_{1j} + y_j \\ -\Omega_{1j} \end{pmatrix}.$$

Now, the matrices for $k = m$ are given by

$$\mathbf{D}_m\mathbf{T}_{m-2} + \mathbf{A}_m\mathbf{T}_{m-1} + \mathbf{B}_m\mathbf{T}_m = \mathbf{R}_m, \tag{4.50}$$

where

$$\begin{aligned} \mathbf{A1}_m &= -\left(\frac{d^2\xi}{dx^2}\right)\frac{1}{\Delta\xi} - \left(\frac{d\xi}{dx}\right)^2\frac{2}{\Delta\xi^2}, \\ \mathbf{B1}_m &= \left(\frac{d^2\xi}{dx^2}\right)\frac{1}{\Delta\xi} + \left(\frac{d\xi}{dx}\right)^2\frac{1}{\Delta\xi^2}, \\ \mathbf{B3}_m &= -\left(\frac{d^2z}{dy^2}\right)(\mathbf{D_z})_{mj} - \left(\frac{dz}{dy}\right)^2\left(\mathbf{D_z^2}\right)_{mj}, \\ \mathbf{B4}_m &= \mathbf{I}, \\ \mathbf{D1}_m &= \left(\frac{d\xi}{dx}\right)^2\frac{1}{\Delta\xi^2}, \end{aligned} \tag{4.51}$$

and

$$\mathbf{R}_m = \begin{pmatrix} -\left(\frac{d^2\xi}{dx^2}\right)\frac{\bar{\psi}_{mj}-\bar{\psi}_{mj-1}}{\Delta\xi} - \left(\frac{d\xi}{dx}\right)^2 \frac{\bar{\psi}_{mj}-2\bar{\psi}_{mj-1}+\bar{\psi}_{mj-2}}{(\Delta\xi)^2}, \\ -\Omega_{mj} + \left(\frac{d^2z}{dy^2}\right)\left(\mathbf{D_z}\bar{\psi}\right)_{mj} + \left(\frac{dz}{dy}\right)^2\left(\mathbf{D_z^2}\bar{\psi}\right)_{mj} \end{pmatrix}.$$

4.7 Results and Solutions

This section shows the results for the basic flow and bifurcations using different grid sizes, suction ratios β, and varying values for Re.

In the beginning, for calculating the Navier-Stokes equations, we used the Blasius solution in the inlet region as the initial condition. Here, for the finite Re outside the boundary layer, the flow will be slightly faster than the uniform flow speed of one. To calculate this slight difference we computed the flow from the initial Blasius solution, meaning, the inviscid solution without suction at $u = 1$, until we obtained a steady-state, adjusted Blasius solution. After that, we introduced a gradually increasing suction ratio β, until we arrived at its critical value when the flow separates.

The results obtained here in the basic flow give us an extremely sparse and large linear system, with the number of unknowns $2(N + 1)m$, while we observe good overall convergence to the steady solution, and the codes of second order finite differences in x-direction and Chebychev collocation in y-direction work well. Matlab and Fortran are used to solve the equations.

Note that all figures illustrating this particular problem show only the partial x-domain, while the full domain here in this chapter is [0.30].

Figure (4.3) shows the effect of an adverse pressure gradient produced by a suction port on the upper wall of a channel, which leads to the separation of a laminar boundary layer with consequent formation of a separation bubble on the lower wall. Here, $Re = 50000$, $N = 100$, $m = 501$, and $\beta = 0.0997$.

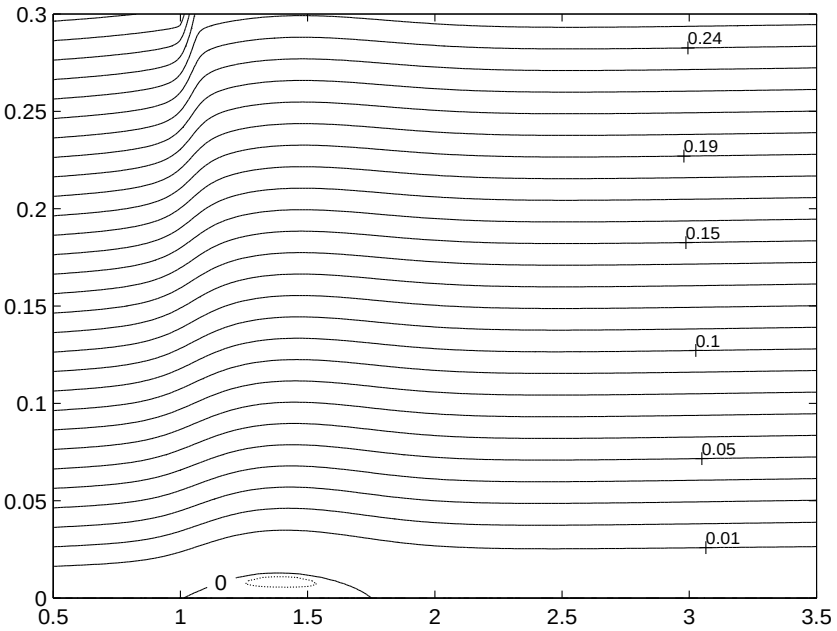

Figure 4.3: Streamline contour plots where $y_{max} = 0.3$, $Re = 50000$, $\beta = 0.0997$, $N = 100$ and $m = 501$. Solid line(-) for streamline level and dashed line(...) for separation bubble. Here contour levels are in intervals of (0.01).

Braun (2006) mentions that in marginal separation in a two dimensional boundary layer flow in a channel steady state solutions exist and admit of two branches of solutions as well as a turning point bifurcation. We note that in previous work with the two-dimensional boundary layer flow in a channel with suction on the upper wall, no one has calculated these branches and bifurcations. It is of interest that in this present study we have managed to calculate the two solution branches and turning point bifurcations for the first time, using the continuation algorithm described in the first chapter.

The plots of the parameter β and separation length (the distance between the separation point and the reattachment point) for different values of the Chebychev points N and finite difference points m in the y-direction and x-direction, respectively, and fixed value of $Re = 50000$, are shown in figures (4.4) and (4.5). These

plots illustrate the two branches of solutions, as well as turning point bifurcations which are similar to the ones discussed by Braun (2006). In marginal separation theory it is found that the steady state solutions also admit two branches of solutions in the vicinity of a critical parameter, as first shown by Ruban (1981) and Stewartson *et al.* (1982). According to the theoretical predictions described in Braun (2006) the theory predicts that the separation length $L_s = O\left((\beta - \beta_s)^{\frac{1}{2}}\right)$ as $\beta \to \beta_s^+$. The separation length is difficult to estimate correctly in the vicinity of β_s and this is one of the reasons why this behavior is not very apparent in figure (4.5). Taking even finer grids it is possible to reproduce this behavior, as seen for example in the work of Logue (2008) in a related context.

Figure (4.4) clearly shows grid independence for different values of N and fixed value of m, while there is a trend towards convergence for different values of m and fixed value of N in figure (4.5). Further branching diagrams and turning point bifurcations for different values of y_{max} are shown in figure (4.6). We see that as the value of y_{max} gets larger, the value of β, which is the starting point of the separation, also becomes larger.

In figure (4.7) we compare the two solutions on the upper and the lower branches, where figure (4.7.a) shows that on the lower branch the separation bubble for the solution is short, whereas in figure (4.7.b) we see a larger separation bubble on the upper branch. These results have been calculated using $Re = 50000$, $N = 100$, $m = 501$, and $\beta = 0.0997$.

From our results it is evident that for different values of N and m a turning point bifurcation occurs at critical value of the suction ratio β_c, as shown in table (4.1). Table (4.1) also shows extrapolated critical values for increasing m.

Computations were made for both, lower and upper branches, with different values for the total number of points m and N in x-direction and y-direction, respectively, in order to determine that our results are grid independent.

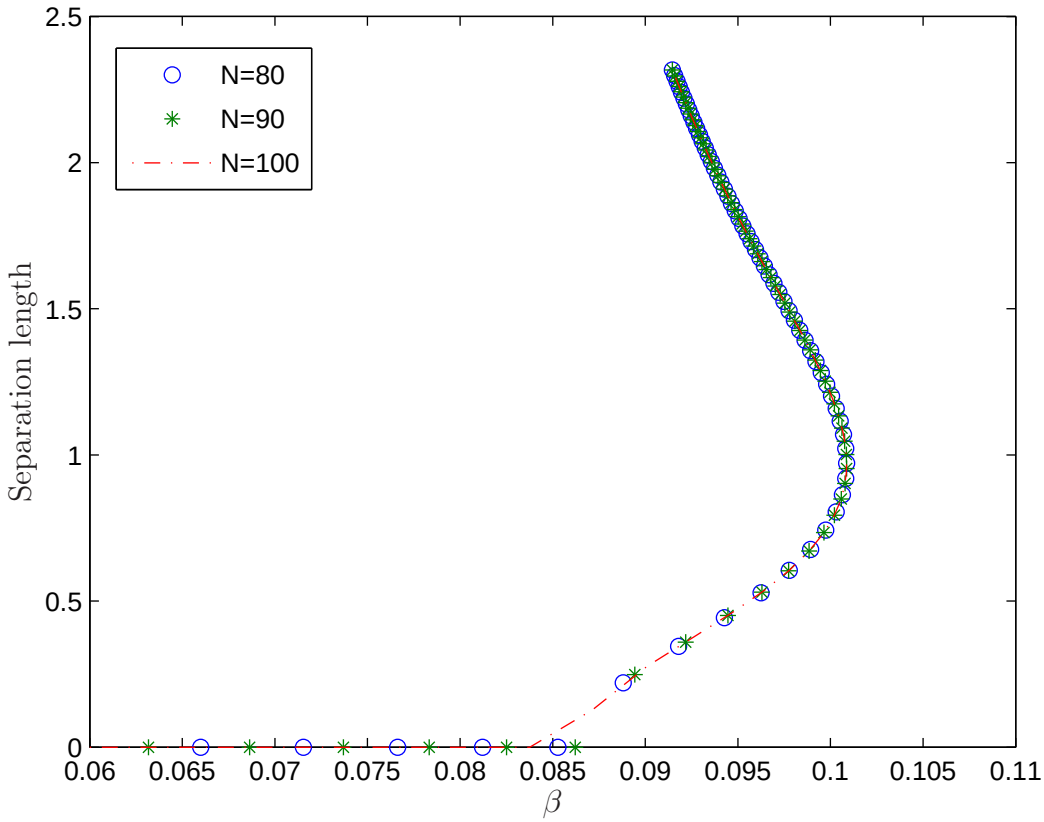

Figure 4.4: Tracking diagram of turning points obtained from different values of N and fixed value of $m = 501$, where $y_{max} = 0.3$ and $Re = 50000$.

Figures (4.8) and (4.9) show streamlines for different values for N and fixed values of $m = 100$, which shows us that our results are grid independent, with figure (4.8) illustrating the streamline for the first solution for the lower branch, and figure (4.9) illustrating the second solution for the upper branch. To give a clearer view we have plotted the velocity profile for different values of N and fixed values of m in figure (4.10).

We have the opposite setup in figures (4.11) and (4.12), where we have fixed value of $N = 100$ and different values for m, but for both branches of solutions the results are not grid independent and plotting the velocity profiles in figure (4.13) confirmed these results. Figures (4.11) and (4.13.a) show the results for

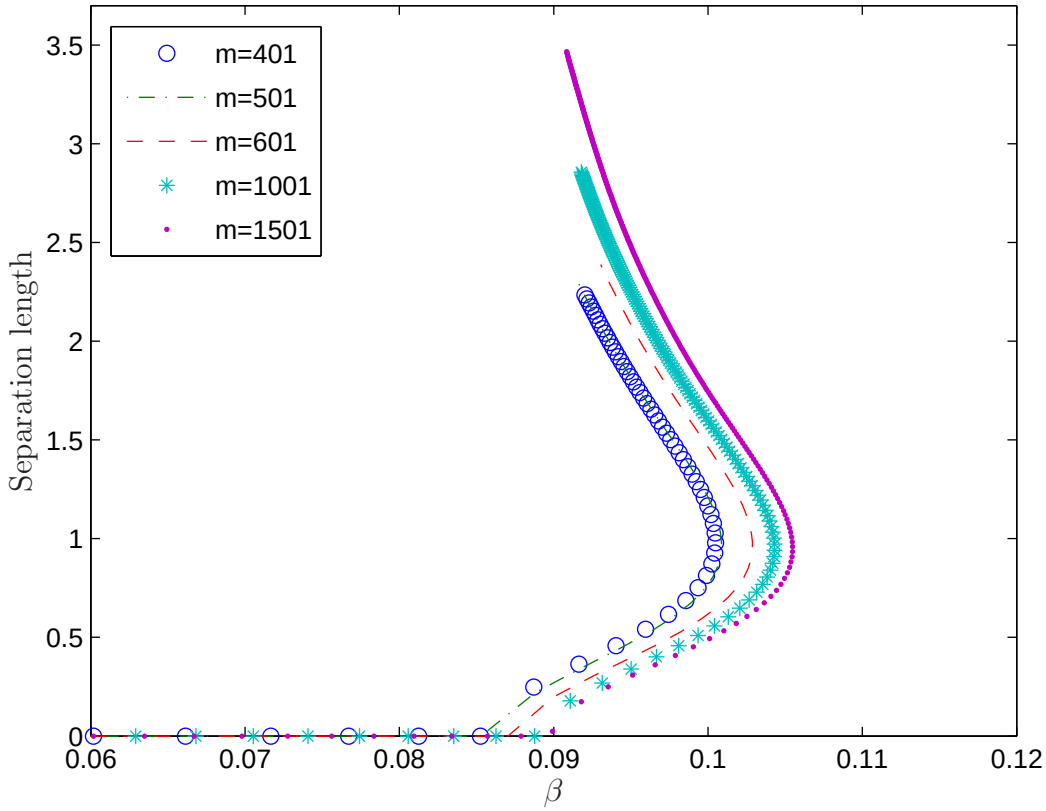

Figure 4.5: Tracking diagram of turning points obtained from different values of m and fixed value of $N = 100$, where $y_{max} = 0.3$ and $Re = 50000$.

the lower branch, while figures (4.12) and (4.13.b) show the results for the upper branch. All these results have been calculated using $Re = 50000$ and $\beta = 0.0997$.

As we calculate the results for the basic flow with different values of Re (table (4.2) and figure(4.14)) it becomes apparent that the flow starts to separate when suction ratio β reaches a critical value $\beta = \beta_s$. We observed as well that as the Reynolds number increases the critical suction ratio β_s, at which separation occurs, decreases.

From our calculations of the first solutions in the lower branch with varying values for the suction ratio β, we have observed that when the adverse pressure gradient is weak, as a direct result of the suction strength, the separated region

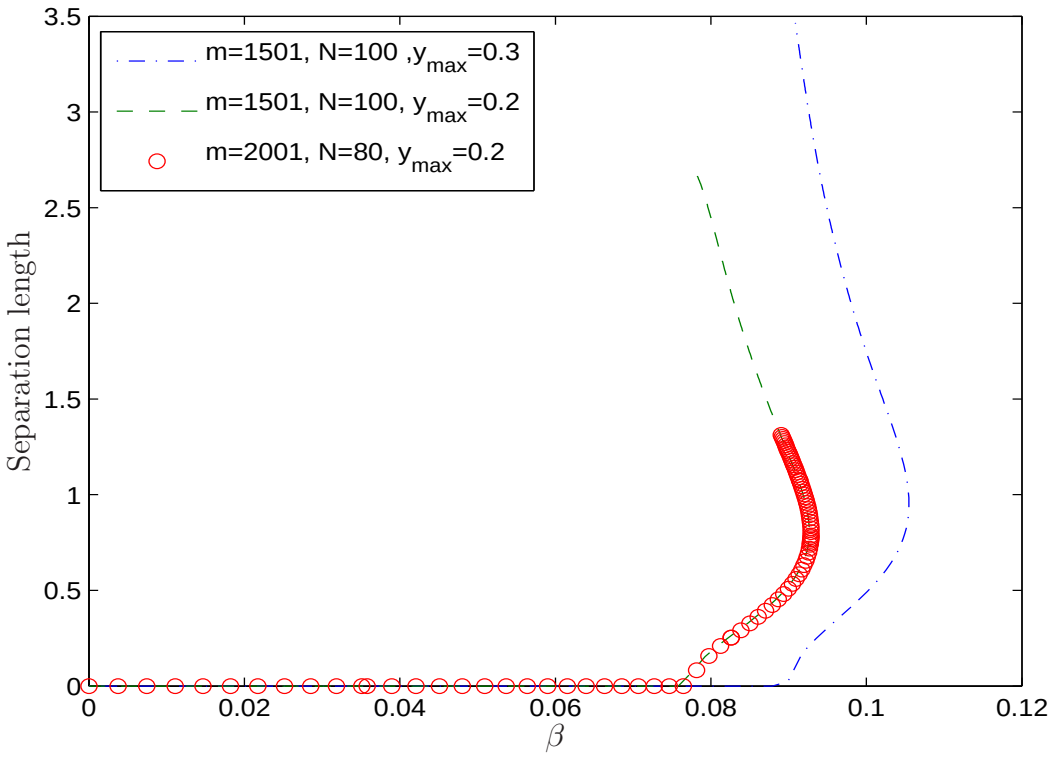

Figure 4.6: Tracking diagram of turning points obtained from different values of y_{max}, where $Re = 50000$ and $\beta = 0.0997$.

builds up into a steady, closed separation bubble. When suction increases corresponding to a stronger pressure gradient, the separated region lengthens, as seen in figure (4.15).

On the other hand, calculations of the second solutions in the upper branch with varying values for the suction ratio β, show that when suction decreases, the separated region length, as seen in figure(4.16). In both calculations, for the first and second set of solutions, we have been using 80 Chebychev points with 501 finite difference points, as well as Reynolds number $Re = 50000$.

Figures(4.17) and (4.18) detail the streamlines and the vorticity corresponding to the base flow for the first solution and second solution, respectively, for

	$N = 100$	$N = 90$	$N = 80$
m	β_c	β_c	β_c
401	0.100493		
501	0.100870	0.100870	0.100875
601	0.102879		
1001	0.104313		
1501	0.105479		
∞	0.106416		

Table 4.1: Comparison of critical values of the suction ratio β_c where the turning point bifurcation occurs, obtained from different values of m and N where $y_{max} = 0.3$ and $Re = 50000$.

	$m = 501$	$m = 1001$	$m = 1501$
Re	β_s	β_s	β_s
5000	0.11147	0.11163	0.10998
10000	0.11078	0.10745	0.10757
20000	0.10194	0.10019	0.10125
30000	0.09876	0.09846	0.09809
40000	0.09730	0.09619	0.09518
50000	0.09642	0.09501	0.09512
60000	0.09444	0.09437	0.09401
70000	0.09409	0.09398	0.09329
80000	0.09279	0.09259	0.09172

Table 4.2: Comparison of the critical values of suction ratio β_s when separation starts, and Re, for different grid sizes for $m = 501, 1001, 1501$ and $N = 100$ where $y_{max} = 0.3$.

$Re = 50000$, $\beta = 0.0997$, $N = 100$ and $m = 501$. The contours of streamlines in both solutions are smooth (figures (4.17.a) and (4.18).a), but we observe very small wiggles in the vorticity line in the first solution on the lower branch (figure(4.17.b)), which increase slightly in the second solution on the upper branch, (figure (4.18.b)). Since these wiggles are relatively small they do not have a determining effect on the solutions and if we minimize the grid size further they may disappear.

Table (4.3) shows the relationship between the values of m and the corresponding highest values of Re, which are useful in our calculations, where we can see that the value of Re increases proportionately to the increase in the number of grid points m. Therefore, to calculate with higher Reynolds numbers Re than those we used, one would have to increase the number of grid points m, because we found that in computations with Re higher than those shown in table (4.3), our method is no longer convergent in basic flow.

m	Re
501	≈ 55000
1001	≈ 74000
1501	≈ 81000

Table 4.3: Comparison of grid points m and Re, for $y_{max} = 0.3$, $N = 100$ and $\beta = 0.0997$.

Figures (4.19) and (4.20) illustrate the wall pressure for the lower and upper branch, respectively. It is evident that the pressure curve rises until it approaches the separation point, where it becomes constant until the reattachment point, where pressure increases slightly until it becomes constant again downstream. In figure (4.20) the peak in the pressure curve resulting from the large separation bubble on the upper branch is significant, while we see a negligible rise in the pressure curve in figure (4.19), where the separation bubble on the lower branch is short. Past experiments by Gaster (1966) showed that the rising pressure coefficient curve becomes constant, corresponding to the region of the separation bubble, followed by a rise in magnitude downstream past the reattachment point.

Wall skin friction (τ) where ($\tau = \psi_{yy}$) at $y = 0$ for the lower and upper branches is illustrated in figure (4.21), where we see the curve of the skin friction remaining constant downstream, except for a downturn in the region of the separation bubble. The relatively small size of the downturn in figures (4.21.

a,b) is characteristic of the lower branch, where the separation bubble is short, while on the upper branch, where the separation bubble is large, the downturn is slightly deeper, see figures (4.21. c,d). More wall skin friction features (τ) where ($\tau = \frac{\psi_{yy}}{\sqrt{\frac{Re}{x}}}$) at $y = 0$, are shown in figure (4.22), where we see in figure (4.22 a, b), in the separation region on the lower branch a sharp initial downturn, followed immediately by an equally abrupt ascent until the skin friction becomes constant downstream in the x-direction. In figure (4.22 c, d) for the upper branch we see a similar feature, but at a greater magnitude corresponding to the larger separation bubble.

Multiple wall skin friction curves for different values of β are shown in figure (4.23). It is evident that the first curve, where $\beta = 0.0783$ is less than critical value of the suction ratio $\beta_s = 0.0951$, does not descend below zero, while with increasing values of beta, above β_s, the wall skin friction curve descends to below zero.

Figure (4.24) shows plotting of the wall skin friction at $x = 1.5$ with different values of β. This figure clearly illustrates the two branches of solutions, the upper and the lower branch, as well as the turning point bifurcation. Our result in this plotting is in some agreement with the plot by Braun (2006) in his bifurcation analysis. In Braun's figure 25 (b) there are four multiple solutions in some interval, while in another interval showed only two solutions. In our work we have found only two solutions.

From this section it has become evident that the basic flow results are grid independent for N but not quite for m. The importance of our work lies in the fact that we are the first to calculate two solutions and the turning point bifurcation in this particular problem. In the next section we will discuss the linear stability of the solution around the turning point.

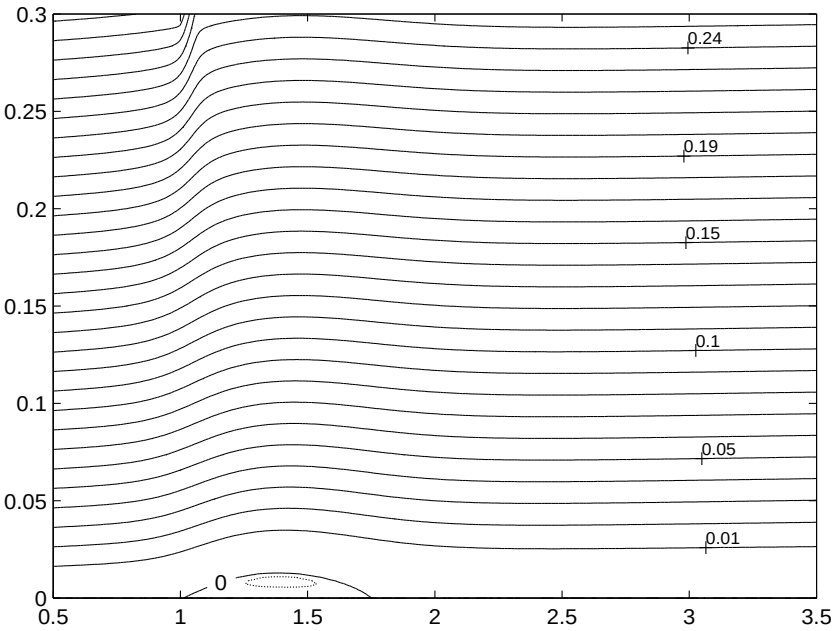

(a) Lower branch

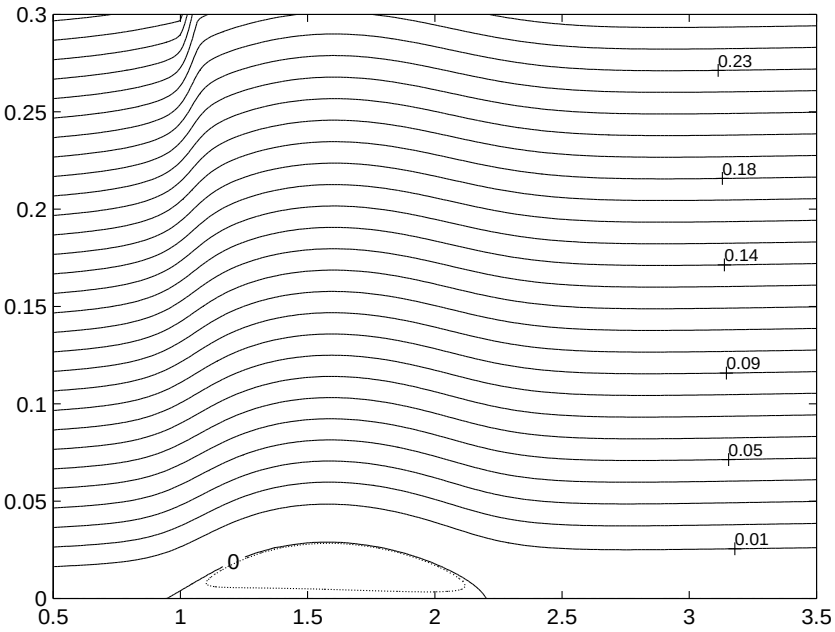

(b) Upper branch

Figure 4.7: Streamline contour plots for lower and upper branches where $y_{max} = 0.3$, $Re = 50000$, $\beta = 0.0997$, $N = 100$ and $m = 501$. Solid line(-) for streamline level and dashed line(...) for separation bubble. Here contour levels are in intervals of (0.01).

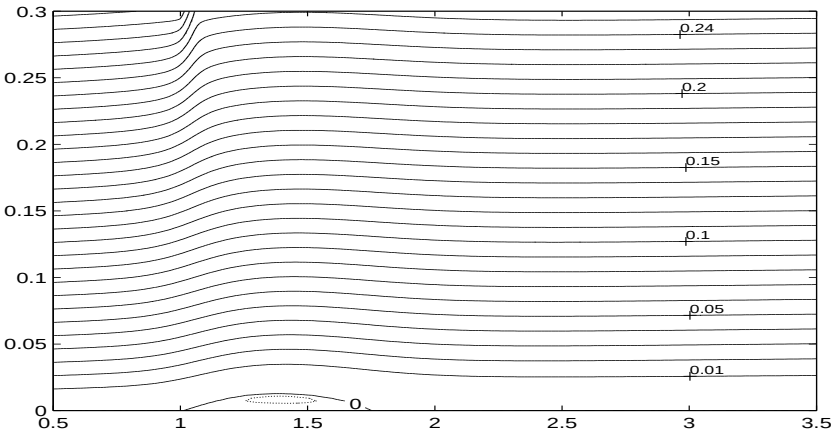

(a) $N = 80$

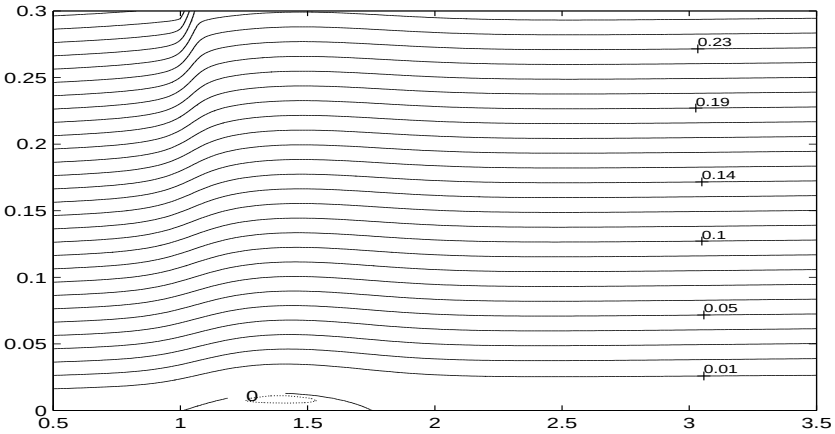

(b) $N = 90$

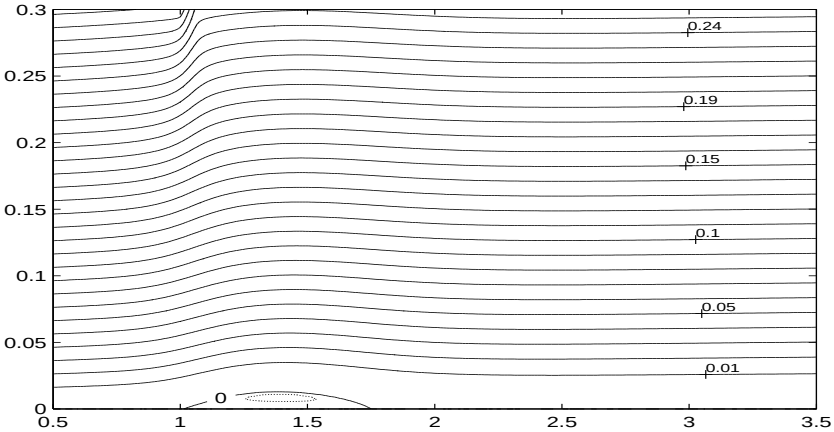

(c) $N = 100$

Figure 4.8: Streamline contour plots (lower branch) for different grid sizes for $N = 80, 90, 100$ and $m = 501$, where $y_{max} = 0.3$, $Re = 50000$ and $\beta = 0.0997$. Solid line(-) for streamline level and dashed line(...) for separation bubble. Here contour levels are in intervals of (0.01).

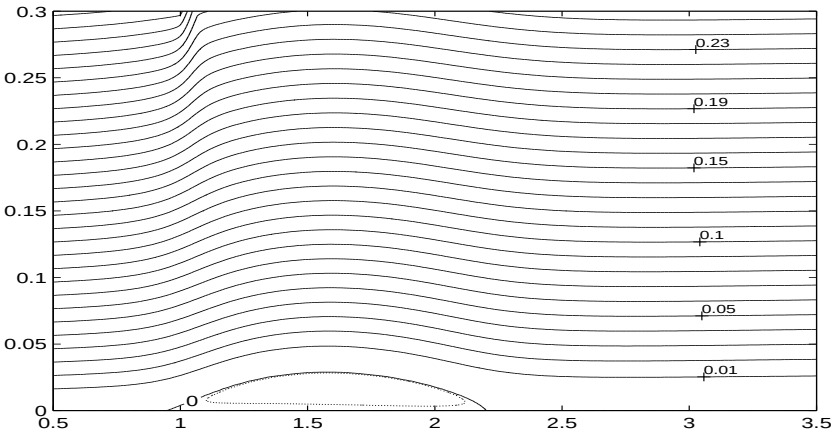

(a) $N = 80$

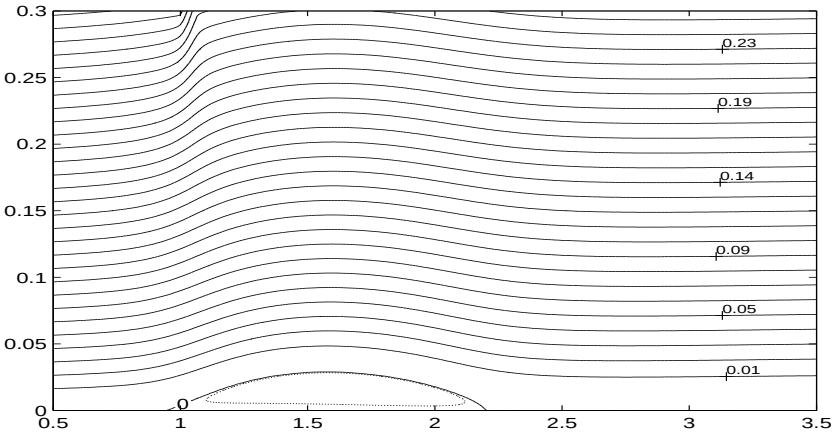

(b) $N = 90$

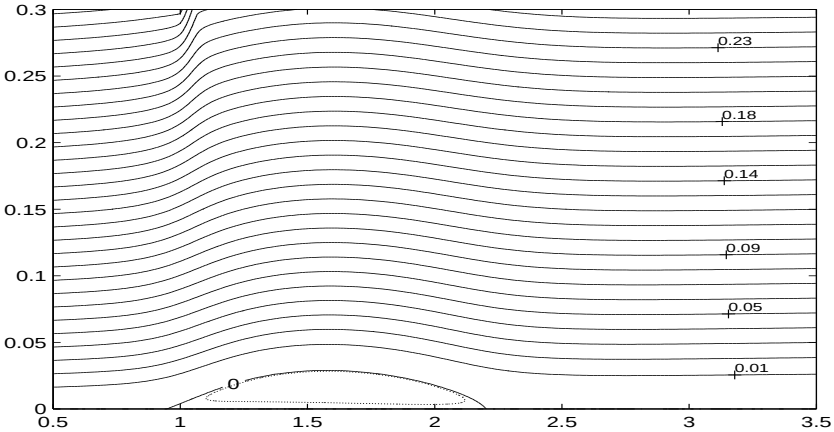

(c) $N = 100$

Figure 4.9: Streamline contour plots (upper branch) for different grid sizes for $N = 80, 90, 100$ and $m = 501$, where $y_{max} = 0.3$, $Re = 50000$ and $\beta = 0.0997$. Solid line(-) for streamline level and dashed line(...) for separation bubble. Here contour levels are in intervals of (0.01).

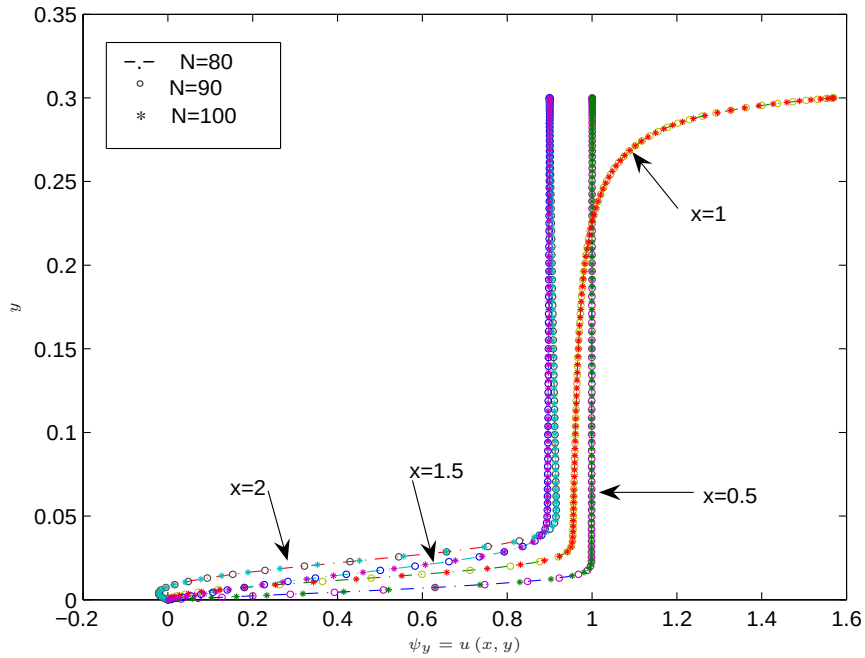

(a) Lower branch

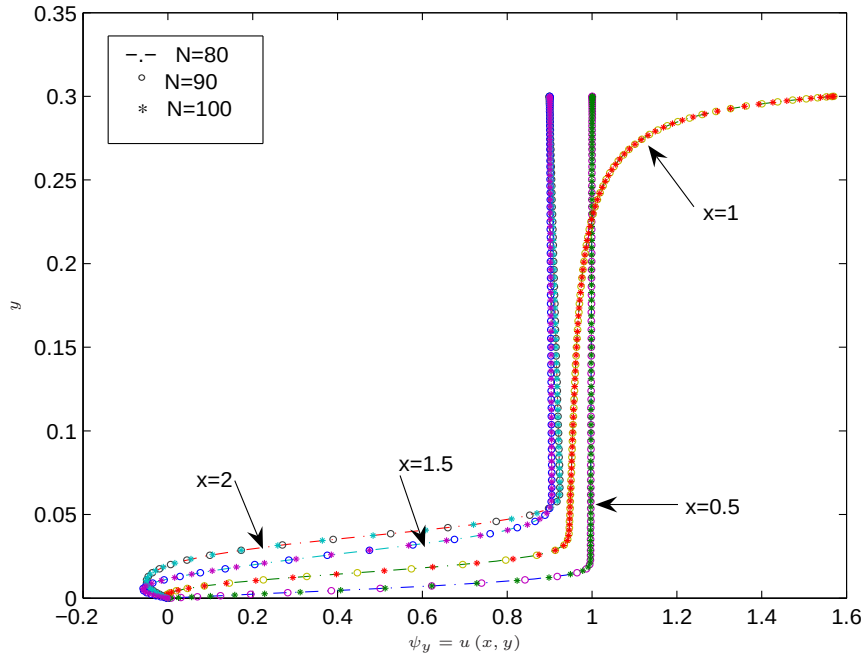

(b) Upper branch

Figure 4.10: Plot showing velocity profile for lower branch and upper branch at $y_{max} = 0.3$, $Re = 50000$, $\beta = 0.0997$ and different grid sizes for $N = 80, 90, 100$, and $m = 501$.

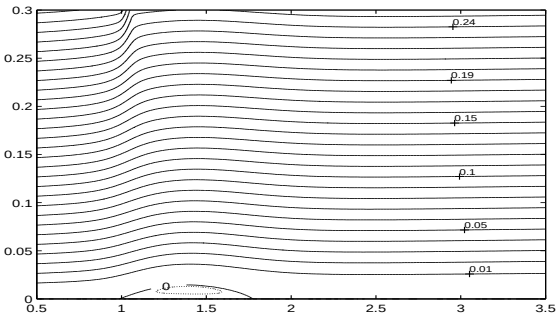

(a) $m = 401$

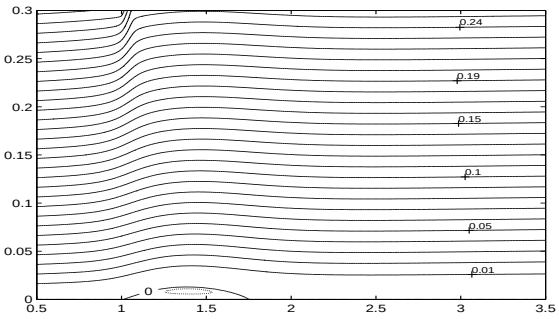

(b) $m = 501$

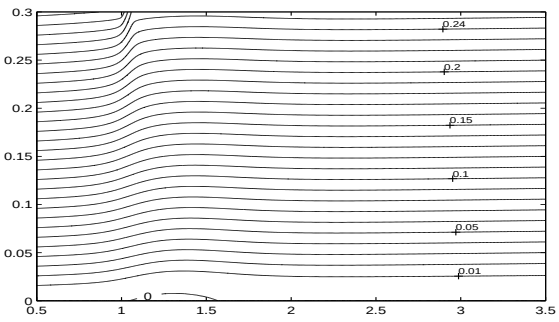

(c) $m = 1001$

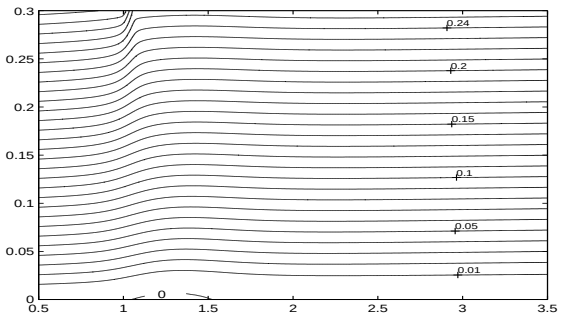

(d) $m = 1501$

Figure 4.11: Streamline contour plots (lower branch) for different grid sizes for $m = 401, 501, 1001, 1501$ and $N = 100$, where $y_{max} = 0.3$, $Re = 50000$ and $\beta = 0.0997$. Solid line(-) for streamline level and dashed line(...) for separation bubble. Here contour levels are in intervals of (0.01).

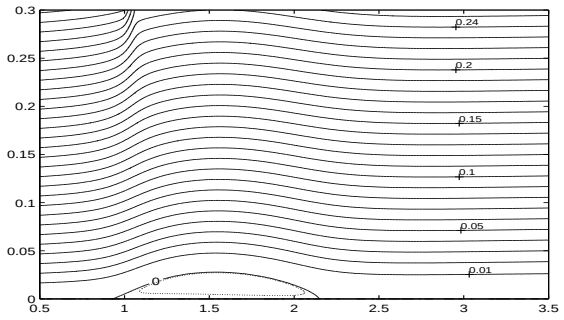

(a) $m = 401$

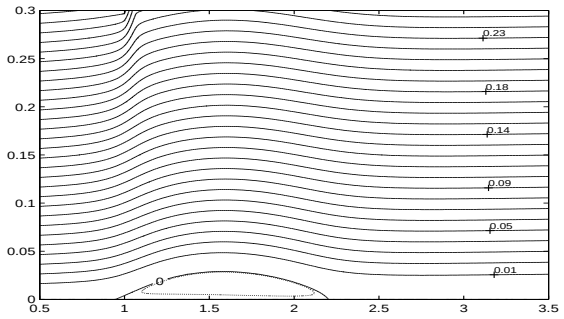

(b) $m = 501$

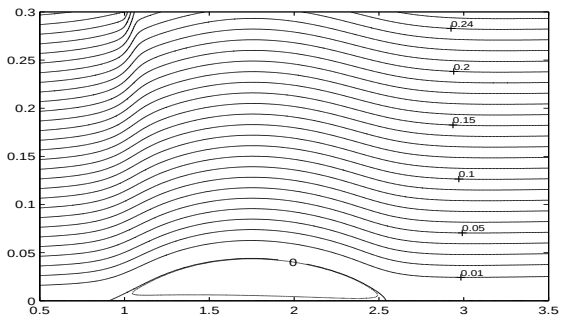

(c) $m = 1001$

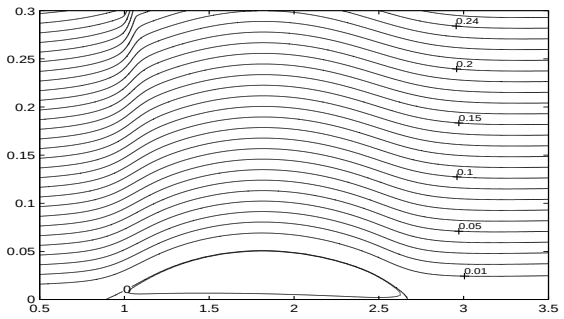

(d) $m = 1501$

Figure 4.12: Streamline contour plots (upper branch) for different grid sizes for $m = 401, 501, 1001, 1501$ and $N = 100$, where $Re = 50000$, $y_{max} = 0.3$ and $\beta = 0.0997$. Solid line(-) for streamline level and dashed line(...) for separation bubble. Here contour levels are in intervals of (0.01).

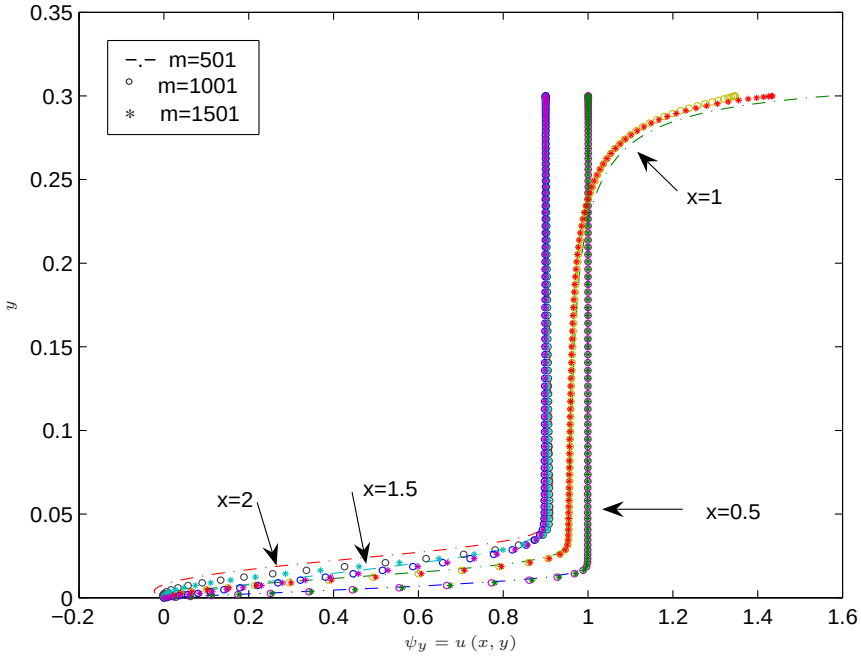

(a) Lower branch

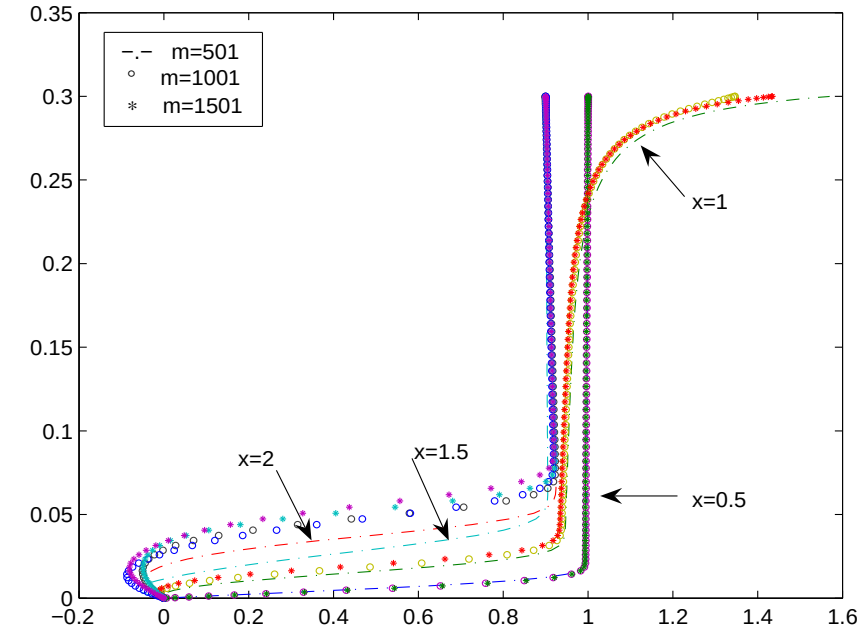

(b) Upper branch

Figure 4.13: Plot showing velocity profile for lower and upper branches at $y_{max} = 0.3$, $Re = 50000$ and $\beta = 0.0997$, and different grid sizes for $m = 501, 1001, 1501$ and $N = 100$.

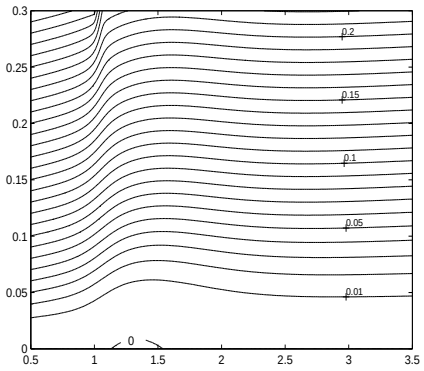

(a) $Re = 5000$, $\beta = 0.11001$

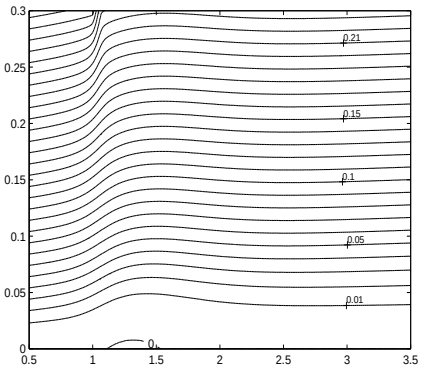

(b) $Re = 10000$, $\beta = 0.10618$

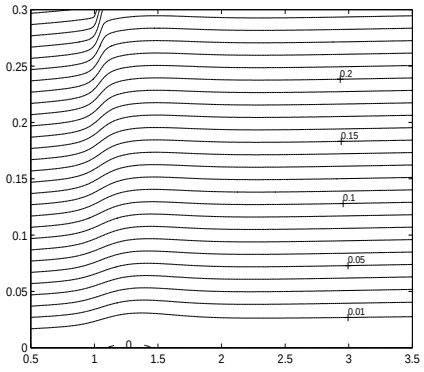

(c) $Re = 40000$, $\beta = 0.09385$

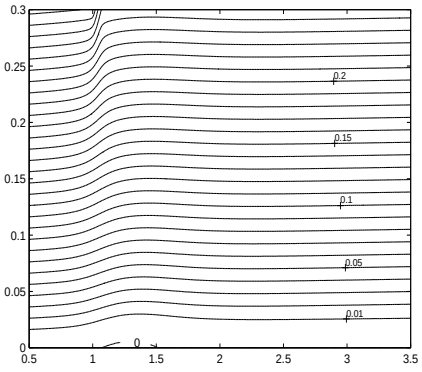

(d) $Re = 50000$, $\beta = 0.09180$

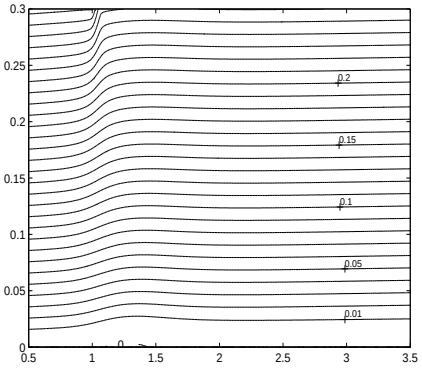

(e) $Re = 60000$, $\beta = 0.09046$

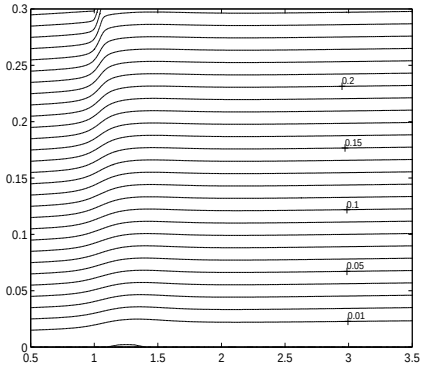

(f) $Re = 80000$, $\beta = 0.08680$

Figure 4.14: Streamline contour plots for $y_{max} = 0.3$, $N = 80$, $m = 501$, different Reynolds numbers Re and the various critical suction ratios β_s. Here contour levels are in intervals of (0.01).

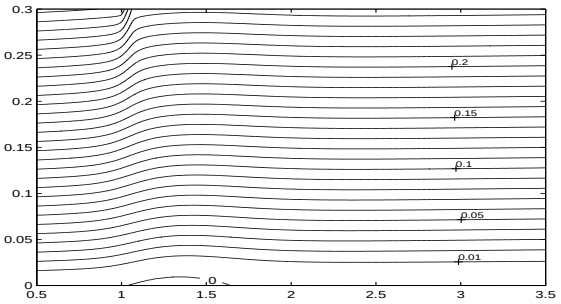

(a) $\beta = 0.09777$

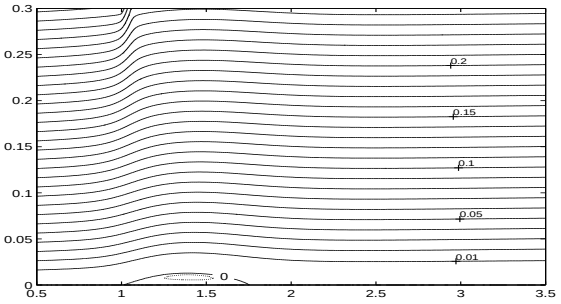

(b) $\beta = 0.09974$

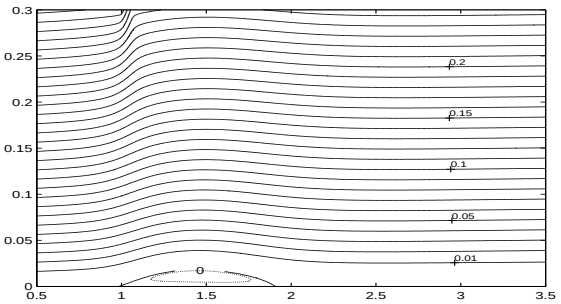

(c) $\beta = 0.10082$

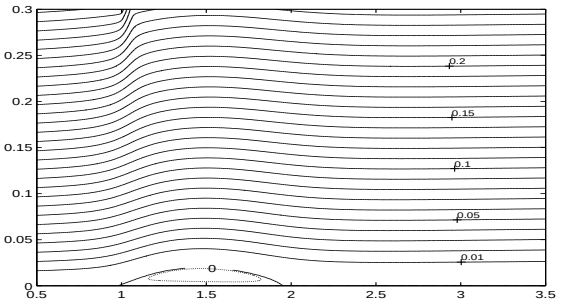

(d) $\beta = 0.10087$

Figure 4.15: Streamline contour plots for lower branch at $y_{max} = 0.3$, $Re = 50000$, $N = 80$, $m = 501$, and different values of β. Solid line(-) for streamline level and dashed line(...) for separation bubble. Here contour levels are in intervals of (0.01).

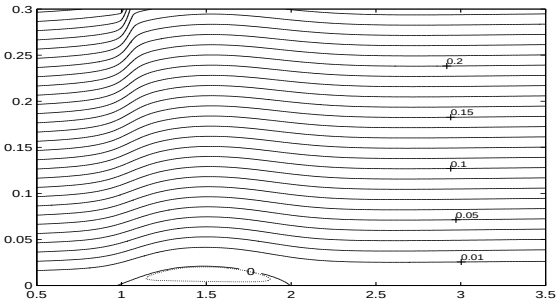

(a) $\beta = 0.10082$

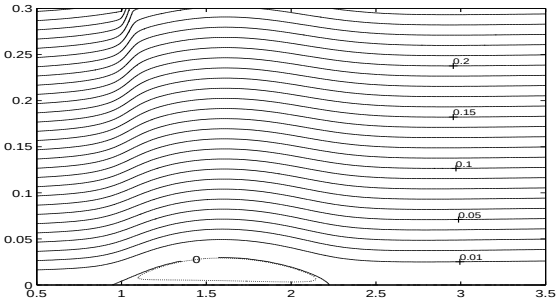

(b) $\beta = 0.09950$

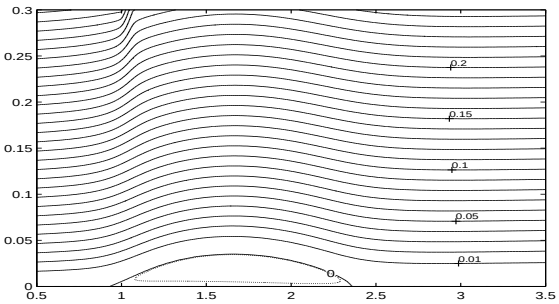

(c) $\beta = 0.09833$

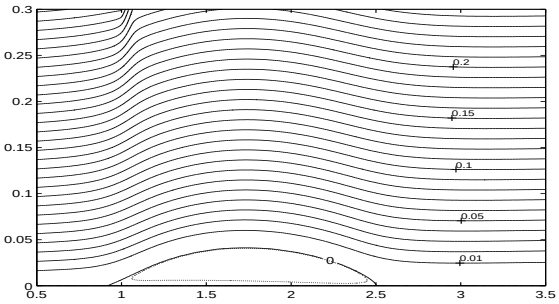

(d) $\beta = 0.09694$

Figure 4.16: Streamline contour plots for upper branch at $y_{max} = 0.3$, $Re = 50000$, $N = 80$, $m = 501$ and different values of β. Solid line(-) for streamline level and dashed line(...) for separation bubble. Here contour levels are in intervals of (0.01).

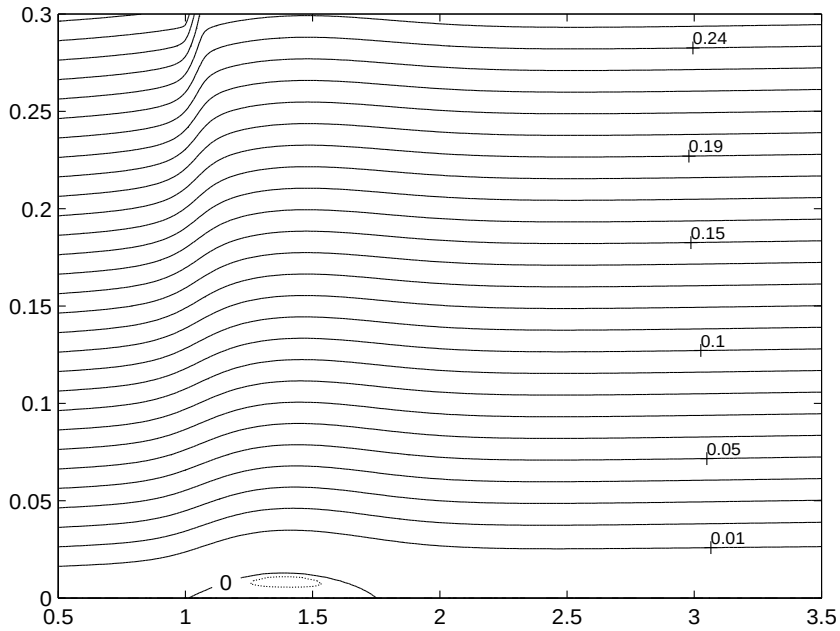

(a) Streamlines

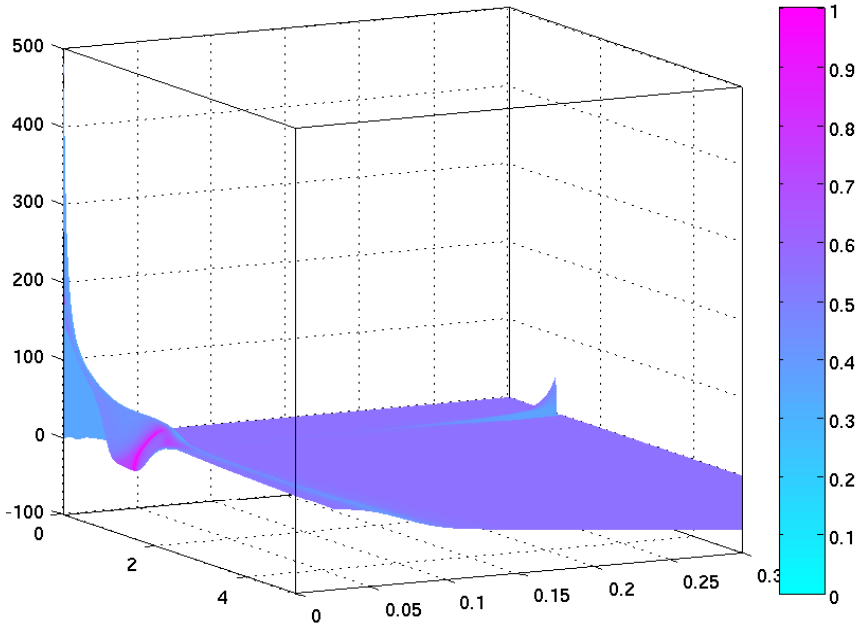

(b) Vorticity

Figure 4.17: Plot showing streamlines and vorticity for lower branch at $y_{max} = 0.3$, $Re = 50000$, $\beta = 0.0997$, $m = 501$ and $N = 100$.

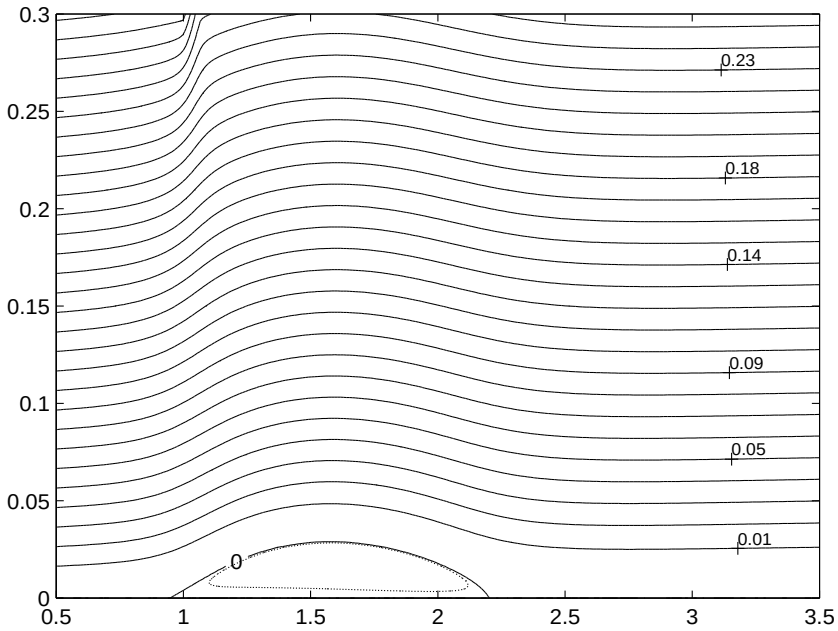

(a) Streamlines

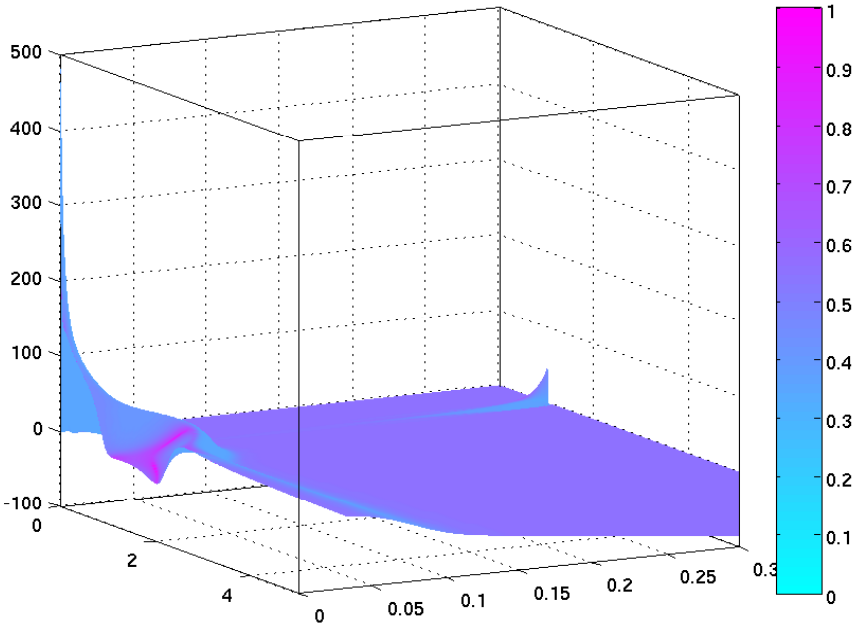

(b) Vorticity

Figure 4.18: Plot showing streamlines and vorticity for upper branch at $y_{max} = 0.3$, $Re = 50000$, $\beta = 0.0997$, $m = 501$ and $N = 100$.

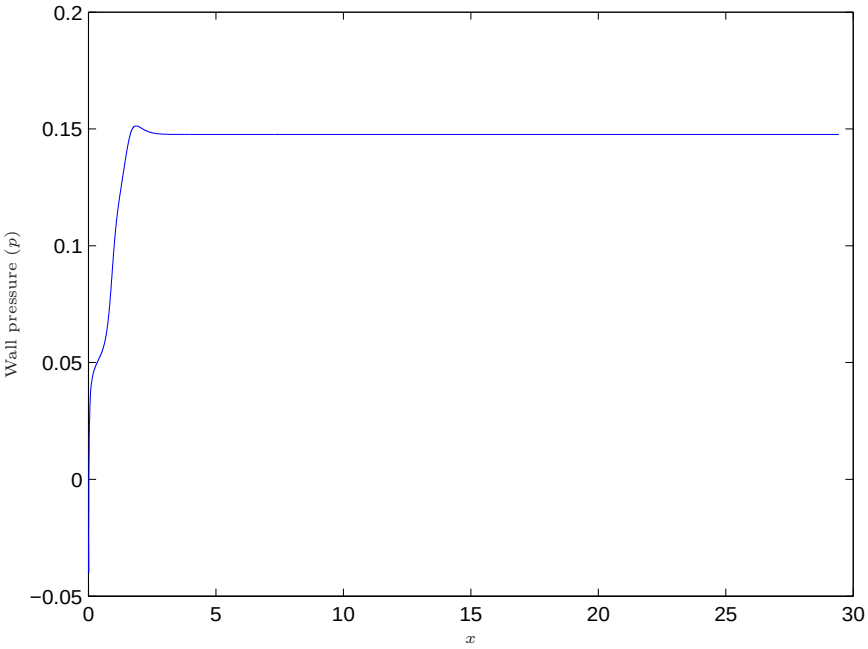

(a) Wall pressure for lower branch

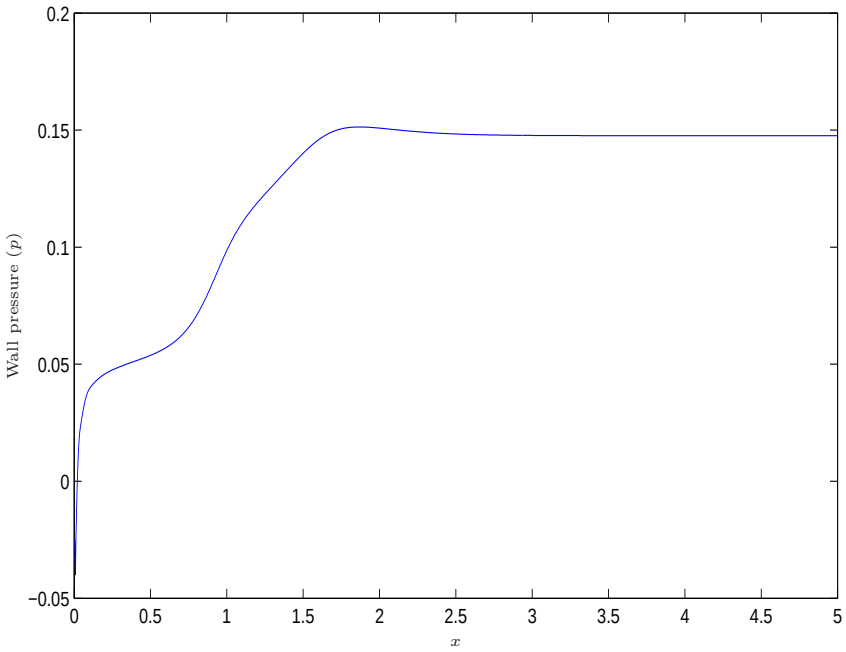

(b) Snapshot of the figure above

Figure 4.19: Plot showing wall pressure for lower branch at $y_{max} = 0.3$, $Re = 50000$, $\beta = 0.0997$, and grid size $m = 1501$ and $N = 100$.

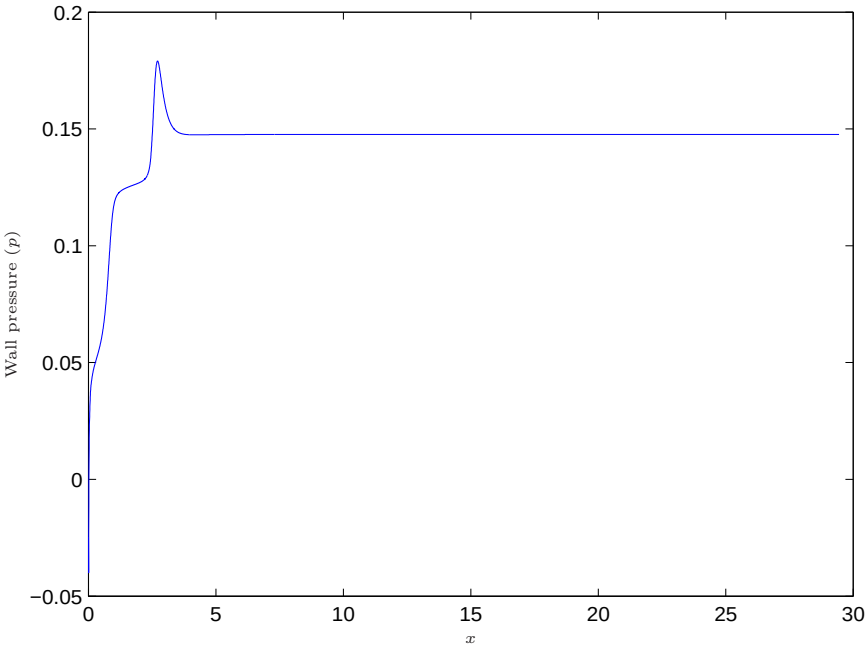

(a) Wall pressure for upper branch

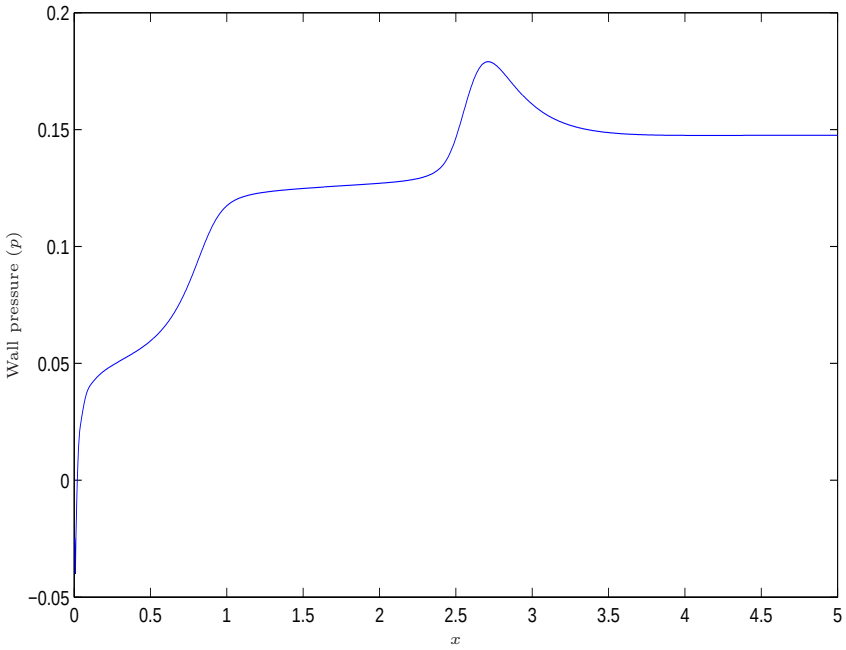

(b) Snapshot of the figure above

Figure 4.20: Plot showing wall pressure for upper branch at $y_{max} = 0.3$, $Re = 50000$, $\beta = 0.0997$, and grid size $m = 1501$ and $N = 100$.

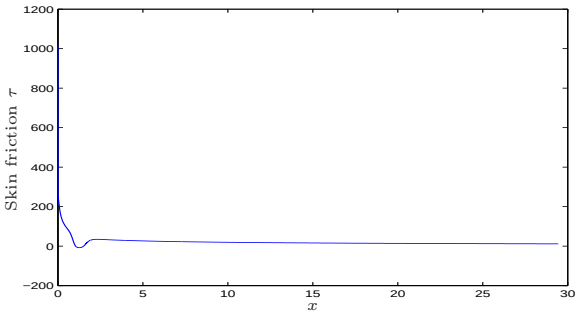

(a) Wall skin friction for lower branch

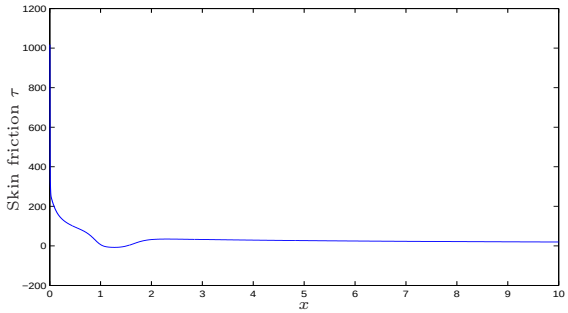

(b) Snapshot of the figure above

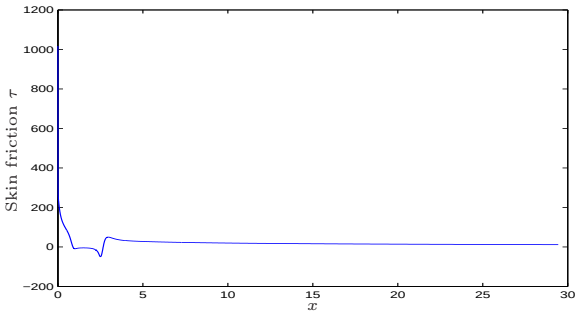

(c) Wall skin friction for upper branch

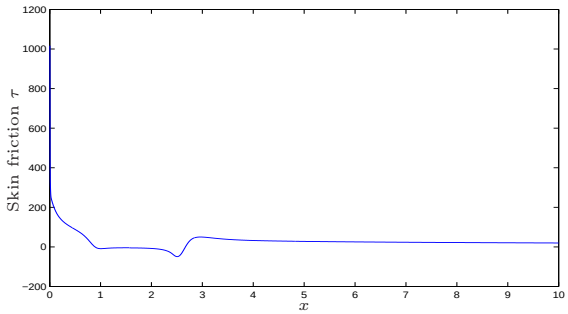

(d) Snapshot of the figure above

Figure 4.21: Plot showing wall skin friction τ where $\tau = \psi_{yy}$ at $y = 0$ for lower and upper branches at $y_{max} = 0.3$, $Re = 50000$, $\beta = 0.0997$, and grid size $m = 1501$ and $N = 100$.

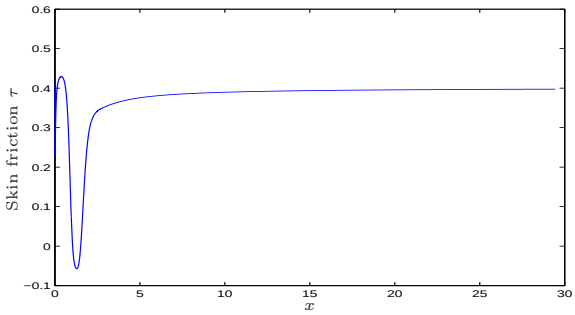

(a) Wall skin friction for lower branch

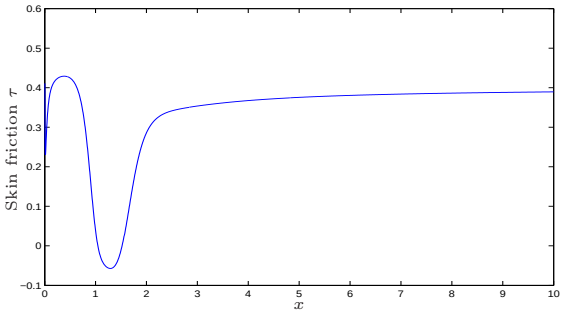

(b) Snapshot of the figure above

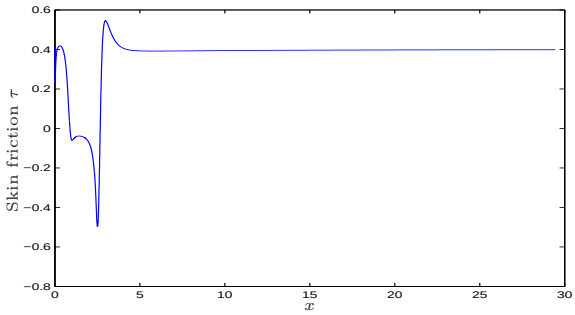

(c) Wall skin friction for upper branch

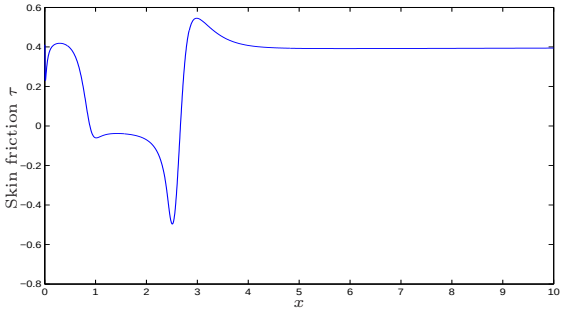

(d) Snapshot of the figure above

Figure 4.22: Plot showing wall skin friction τ where $\tau = \frac{\psi_{yy}}{\sqrt{\frac{Re}{x}}}$ at $y = 0$ for lower and upper branches at $y_{max} = 0.3$, $Re = 50000$, $\beta = 0.0997$, and grid size $m = 1501$ and $N = 100$.

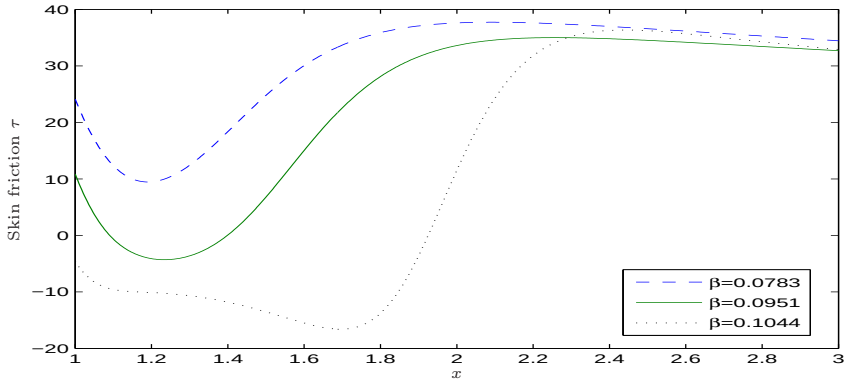

Figure 4.23: Plot showing wall skin friction τ where $\tau = \psi_{yy}$ at $y = 0$ for different values of β where $y_{max} = 0.3$, $Re = 50000$, and grid size $m = 1501$ and $N = 100$.

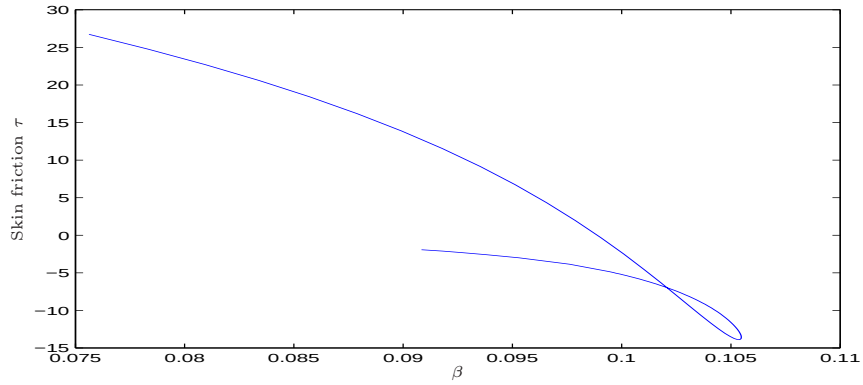

(a) Wall skin friction at $x = 1.5$

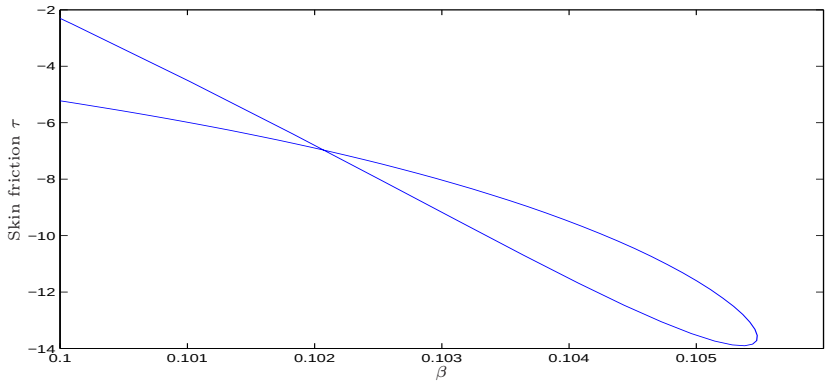

(b) Snapshot of the figure above

Figure 4.24: Plot showing wall skin friction τ where $\tau = \psi_{yy}$ at $y = 0$ and $x = 1.5$ where $y_{max} = 0.3$, $Re = 50000$, $\beta = 0.0997$, and grid size $m = 1501$ and $N = 100$.

4.8 Stability of Flow through a Channel with Suction

The study of the stability of a two-dimensional boundary layer flow in a channel with a suction by solving Navier-Stokes equations has been the subject of many research projects in recent times. In these studies different numerical methods have been used to analyze the stability of the flow. We have discussed some of these works in the literature review in chapter 2.

In this section the primary focus is on analysis and calculation of the stability of the flow through a channel with suction and the investigation of bifurcations occurring in separated flows at large Reynolds numbers, using global stability analysis.

The method which we have used here to analyze the stability of a stationary solution is the one employed by Boppana (2007), where the unsteady Navier-Stokes equations which govern the flow are linearized in the neighborhood of the stationary solution and, to determine the stability, the eigenvalues of the resulting large matrix are computed. This method is called the global stability analysis and has never been used to analyze stability in this particular problem, but is being applied in the present work for the first time.

Throughout our work with global stability analysis to determine the stability of the flow, we have chosen to use ARPACK software which computed the smallest magnitude eigenvalues and eigenvectors of the system. ARPACK is an abbreviation for ARnoldi PACKage, which is a collection of Fortran77 subroutines created to solve large scale eigenvalue problems. The technique called the Arnoldi process is more suitable for large matrices and is used in approximating a number of eigenvalues and corresponding eigenvectors of a general $(n \times n)$ matrix. ARPACK software is designed to enable calculation of a number (say, k) of

eigenvalues of a large structured matrix J, using $n \cdot O(k) + O(k^2)$ storage. The k eigenvalues with, for example, largest real part or largest magnitude and the corresponding eigenvectors are specified by the user. To solve generalized eigenvalue problems ARPACK is the specialized software appropriate to the task. For more detailed information on ARPACK, see Lehoucq *et al.* (1997).

The work on calculations and analyses of stability in this section is dependent on computations and results which we have obtained previously, when working with the basic flow.

In the following sections we will show the particularities of the numerical technique used to analyze global stability of flow in different configurations, as well as present the results.

4.8.1 Flow Stability Analysis

The form of unsteady Navier-Stokes equations in stream function ψ and vorticity ω is given as,

$$\omega_t + \psi_y \omega_x - \psi_x \omega_y = \frac{1}{Re}(\omega_{xx} + \omega_{yy}), \tag{4.52}$$

$$\omega = (\psi_{xx} + \psi_{yy}). \tag{4.53}$$

To begin with, we suppose that the solutions of the equations (4.52) and (4.53) for the basic steady flow with perturbations can be expressed as

$$\psi = \widehat{\psi}(x,y) + \delta\vec{\psi}(x,y,t), \tag{4.54}$$

$$\omega = \widehat{\omega}(x,y) + \delta\vec{\omega}(x,y,t). \tag{4.55}$$

Here we let the steady, basic flow which satisfies equations (4.52) and (4.53) be $\widehat{\psi}(x,y)$ and $\widehat{\omega}(x,y)$ and its perturbations are $\vec{\psi}(x,y,t)$ and $\vec{\omega}(x,y,t)$, where the value of δ is supposed to be small.

To determine whether the perturbations increase or decrease in time we employ the following procedure:

First: we have computed the steady basic flow or stationary solution, which we have calculated in the previous section.

Second: The perturbation components of the above system are determined by solving the form of the Navier-Stokes equations that result from substituting these quantities (4.54) and (4.55) into equations (4.52) and (4.53), and subtracting out the basic flow equations.

Third: We then linearized the resulting equations for small perturbations by neglecting terms of $O(\delta^2)$.

Fourth: Values for the temporal evolution of $\vec{\psi}$ and $\vec{\omega}$ are thus found from normal modes and hence the perturbations can be decomposed into a normal mode form proportional to $e^{-\lambda t}$.

Therefore, the perturbations may be assumed to be of the form:

$$\vec{\psi}(x,y,t) = \widetilde{\psi}(x,y)\, e^{-\lambda t}, \tag{4.56}$$

$$\vec{\omega}(x,y,t) = \widetilde{\omega}(x,y)\, e^{-\lambda t}. \tag{4.57}$$

Now, by substituting equations (4.56) and (4.57) into equation (4.54) and (4.55) and then substituting the result into equations (4.52) and (4.53) we obtain,

$$\begin{aligned} \lambda\delta\widetilde{\omega}e^{-\lambda t} &+ \left(\widehat{\psi}_y + \delta\widetilde{\psi}_y e^{-\lambda t}\right)\left(\widehat{\omega}_x + \delta\widetilde{\omega}_x e^{-\lambda t}\right) - \left(\widehat{\psi}_x + \delta\widetilde{\psi}_x e^{-\lambda t}\right)\left(\widehat{\omega}_y + \delta\widetilde{\omega}_y e^{-\lambda t}\right) \\ &= \frac{1}{Re}\left(\widehat{\omega}_{xx} + \delta\widetilde{\omega}_{xx}e^{-\lambda t} + \widehat{\omega}_{yy} + \delta\widetilde{\omega}_{yy}e^{-\lambda t}\right), \end{aligned} \tag{4.58}$$

$$\widehat{\omega} + \delta\widetilde{\omega}e^{-\lambda t} = \widehat{\psi}_{xx} + \delta\widetilde{\psi}_{xx}e^{-\lambda t} + \widehat{\psi}_{yy} + \delta\widetilde{\psi}_{yy}e^{-\lambda t}. \tag{4.59}$$

Then, by subtracting out the basic-flow equations we obtain:

First: a steady system of equations,

$$\widehat{\psi}_y\widehat{\omega}_x - \widehat{\psi}_x\widehat{\omega}_y = \frac{1}{Re}\left(\widehat{\omega}_{xx} + \widehat{\omega}_{yy}\right), \tag{4.60}$$

$$\widehat{\omega} = \left(\widehat{\psi}_{xx} + \widehat{\psi}_{yy}\right), \tag{4.61}$$

with the boundary conditions,

$$\begin{array}{llllll}
\widehat{\psi} = 0, & \widehat{\psi}_y = 0 & \text{for} & y = 0, & 0 \le x \le x_{max}, \\
\widehat{\psi}_y = 1 - \beta\hat{\psi}_s, & \widehat{\omega} = 0 & \text{for} & y = y_{max}, & 0 \le x \le x_{max}, \\
\widehat{\psi} = y, & \widehat{\omega} = 0 & \text{for} & x = 0, & 0 \le y \le y_{max}, \\
\widehat{\psi}_{xx} = 0, & \widehat{\omega} - \widehat{\psi}_{yy} = 0 & \text{for} & x = x_{max}, & 0 \le y \le y_{max}.
\end{array}$$

The above steady system of equations with their boundary conditions is identical to the one we worked with in the previous section, except that we replaced ψ and ω with $\widehat{\psi}$ and $\widehat{\omega}$.

Second: the linear stability equations

$$\lambda\widetilde{\omega} + \widehat{\psi}_y\widetilde{\omega}_x + \widetilde{\psi}_y\widehat{\omega}_x - \widehat{\psi}_x\widetilde{\omega}_y - \widetilde{\psi}_x\widehat{\omega}_y = \frac{1}{Re}\left(\widetilde{\omega}_{xx} + \widetilde{\omega}_{yy}\right), \tag{4.62}$$

$$\widetilde{\omega} = \left(\widetilde{\psi}_{xx} + \widetilde{\psi}_{yy}\right), \tag{4.63}$$

with homogenous boundary conditions,

$$\begin{cases}
\widetilde{\psi} = 0 \quad \text{and} \quad \widetilde{\psi}_y = 0 & \text{for,} \quad y = 0, \quad 0 \le x \le x_{max}, \\
\widetilde{\psi}_y = 0 \quad \text{and} \quad \widetilde{\omega} = 0 & \text{for,} \quad y = y_{max}, \quad 0 \le x \le x_{max}, \\
\widetilde{\psi} = 0 \quad \text{and} \quad \widetilde{\omega} = 0 & \text{for,} \quad x = 0, \quad 0 \le y \le y_{max}, \\
\widetilde{\psi}_{xx} = 0 \quad \text{and} \quad \widetilde{\omega} - \widetilde{\psi}_{yy} = 0 & \text{for,} \quad x = x_{max}, \quad 0 \le y \le y_{max}.
\end{cases}$$

To find $\widetilde{\psi}$, $\widetilde{\omega}$ and λ for different Re, β and grid sizes we have already solved equations (4.60) and (4.61) with their boundary conditions for $\widehat{\psi}$ and $\widehat{\omega}$ in the previous section, and when we used this stationary solution to feed into equations

(4.62) and (4.63) and by using functions $y = f(z)$ and $x = f(\xi)$ where,

$$\frac{d}{dy} = \frac{dz}{dy}\frac{d}{dz} \qquad \text{and} \qquad \frac{d}{dx} = \frac{d\xi}{dx}\frac{d}{d\xi},$$

we also have,

$$\frac{d^2}{dy^2} = \frac{d^2z}{dy^2}\frac{d}{dz} + \left(\frac{dz}{dy}\right)^2 \frac{d^2}{dz^2} \qquad \text{and} \qquad \frac{d^2}{dx^2} = \frac{d^2\xi}{dx^2}\frac{d}{d\xi} + \left(\frac{d\xi}{dx}\right)^2 \frac{d^2}{d\xi^2},$$

we got the following discrete equation:

$$\begin{aligned}
&\left(\frac{dz}{dy}\right)\left(D_z\widehat{\psi}\right)_{kj}\left(\frac{d\xi}{dx}\right)\frac{\widetilde{\omega}_{k+1j} - \widetilde{\omega}_{k-1j}}{2\Delta\xi} + \left(\frac{dz}{dy}\right)\left(D_z\widetilde{\psi}\right)_{kj}\left(\frac{d\xi}{dx}\right)\frac{\widehat{\omega}_{k+1j} - \widehat{\omega}_{k-1j}}{2\Delta\xi} \\
&- \left(\frac{dz}{dy}\right)\left(D_z\widetilde{\omega}\right)_{kj}\left(\frac{d\xi}{dx}\right)\frac{\widehat{\psi}_{k+1j} - \widehat{\psi}_{k-1j}}{2\Delta\xi} - \left(\frac{dz}{dy}\right)\left(D_z\widehat{\omega}\right)_{kj}\left(\frac{d\xi}{dx}\right)\frac{\widetilde{\psi}_{k+1j} - \widetilde{\psi}_{k-1j}}{2\Delta\xi} \\
&= \frac{1}{Re}\left(\frac{d^2\xi}{dx^2}\right)\frac{\widetilde{\omega}_{k+1j} - \widetilde{\omega}_{k-1j}}{2\Delta\xi} + \frac{1}{Re}\left(\frac{d\xi}{dx}\right)^2\frac{\widetilde{\omega}_{k+1j} - 2\widetilde{\omega}_{kj} + \widetilde{\omega}_{k-1j}}{(\Delta\xi)^2} \\
&+ \frac{1}{Re}\left(\frac{d^2z}{dy^2}\right)\left(D_z\widetilde{\omega}\right)_{kj} + \frac{1}{Re}\left(\frac{dz}{dy}\right)^2\left(D_z^2\widetilde{\omega}\right)_{kj} - \lambda\widetilde{\omega}_{kj},
\end{aligned} \tag{4.64}$$

and

$$\begin{aligned}
&\widetilde{\omega}_{kj} = \left(\frac{d^2\xi}{dx^2}\right)\frac{\widetilde{\psi}_{k+1j} - \widetilde{\psi}_{k-1j}}{2\Delta\xi} + \left(\frac{d\xi}{dx}\right)^2\frac{\widetilde{\psi}_{k+1j} - 2\widetilde{\psi}_{kj} + \widetilde{\psi}_{k-1j}}{(\Delta\xi)^2} + \\
&\left(\frac{d^2z}{dy^2}\right)\left(D_z\widetilde{\psi}\right)_{kj} + \left(\frac{dz}{dy}\right)^2\left(D_z^2\widetilde{\psi}\right)_{kj}, \\
&1 \le k \le m \qquad \textit{and} \qquad 0 \le j \le N.
\end{aligned} \tag{4.65}$$

The stability equations above with their boundary condition can be written in the form of the general linear system,

$$\bar{\mathbf{A}}_k\bar{\mathbf{T}}_{k-1} + \bar{\mathbf{B}}_k\bar{\mathbf{T}}_k + \bar{\mathbf{C}}_k\bar{\mathbf{T}}_{k+1} = \lambda\bar{\mathbf{R}}_k\bar{\mathbf{T}}_k \qquad 1 \le k \le m. \tag{4.66}$$

All the matrices $\bar{\mathbf{A}}_k$, $\bar{\mathbf{B}}_k$ and $\bar{\mathbf{C}}_k$ which we have written in the linear system above are similar to the matrices $\mathbf{A_k}$, $\mathbf{B}_k$ and $\mathbf{C}_k$ which we have obtained before in the previous section, in the linearization, with the exception of $\bar{\psi}$ and Ω which have to be replaced by $\widehat{\omega}$ and $\widehat{\psi}$.

In addition, the vectors $\bar{\mathbf{R}}$ here are different,

$$\left(\bar{\mathbf{R}}\right)_k = \mathbf{0}. \tag{4.67}$$

Here, the form of the general linear system (4.66) can be expressed in the form of a generalized eigenvalue problem given by,

$$\bar{\mathbf{J}}\bar{\mathbf{T}} = \lambda\bar{\mathbf{R}}\bar{\mathbf{T}}, \tag{4.68}$$

where

$$\bar{\mathbf{T}} = \left[\bar{\mathbf{T}}_\mathbf{1}, \bar{\mathbf{T}}_\mathbf{2}, \ldots, \bar{\mathbf{T}}_{\mathbf{m-1}}, \bar{\mathbf{T}}_\mathbf{m}\right]^T,$$

$$\bar{\mathbf{R}} = \begin{bmatrix} \bar{\mathbf{R}}_\mathbf{1} & & & & & & \\ & \bar{\mathbf{R}}_\mathbf{2} & & & & & \\ & & \bar{\mathbf{R}}_\mathbf{3} & & & & \\ & & & \ddots & & & \\ & & & & \bar{\mathbf{R}}_{\mathbf{m-1}} & & \\ & & & & & \bar{\mathbf{R}}_\mathbf{m} \end{bmatrix}, \tag{4.69}$$

and

$$\mathbf{J} = \begin{bmatrix} \bar{\mathbf{B}}_\mathbf{1} & \bar{\mathbf{C}}_\mathbf{1} & & & & & & \\ \bar{\mathbf{A}}_\mathbf{2} & \bar{\mathbf{B}}_\mathbf{2} & \bar{\mathbf{C}}_\mathbf{2} & & & & & \\ & \bar{\mathbf{A}}_\mathbf{3} & \bar{\mathbf{B}}_\mathbf{3} & \bar{\mathbf{C}}_\mathbf{3} & & & & \\ & & \bar{\mathbf{A}}_\mathbf{4} & \bar{\mathbf{B}}_\mathbf{4} & \bar{\mathbf{C}}_\mathbf{4} & & & \\ & & & \ddots & \ddots & \ddots & & \\ & & & & & \bar{\mathbf{A}}_{\mathbf{m-1}} & \bar{\mathbf{B}}_{\mathbf{m-1}} & \bar{\mathbf{C}}_{\mathbf{m-1}} \\ & & & & & & \bar{\mathbf{A}}_\mathbf{m} & \bar{\mathbf{B}}_\mathbf{m} \end{bmatrix}. \tag{4.70}$$

Finally, to obtain eigenvalues λ and eigenvectors $\bar{\mathbf{T}}$ we solve the generalized eigenvalue problem (4.68) using ARPACK.

4.8.2 Results of Global Stability Analysis

Here we will discuss in detail the results we have obtained through our work with global stability analysis to determine the stability of the flow through a channel.

In the system we have formulated the eigenvalue can be real or complex. Therefore, to determine the stability of the flow we have to calculate the eigenvalue and determine if the smallest magnitude of the real part of eigenvalue is positive or negative. Thus,

1-The flow will be temporally unstable with growing perturbation, if the real part of the eigenvalue is negative.

2- The flow will be temporally stable with decreasing perturbation if the real part of the eigenvalue is positive.

3-The flow will be marginally stable if the real part of the eigenvalue equals zero, but the imaginary part has any value other than zero.

4-An exchange of stabilities takes place when both parts of the eigenvalue, real and imaginary, have values which equal zero.

From calculating the results for the basic flow we have observed that there are two solutions, one in the lower branch and the other in the upper branch, as well as a turning point. Here, by calculating the global stability result, we have determined that the first solution on the lower branch is stable, while, after the turning point bifurcation, the second solution on the upper branch is unstable. At the turning point bifurcations these changing stabilities are not unusual, but for this particular flow a turning point bifurcation has been discovered here for the first time.

In the global stability calculations for the two solutions the values of the real eigenvalues move along the real axis towards the origin approaching the turning point. The first solution figure (4.25.a) shows that the real part of the

eigenvalues does not change signs meaning does not crossing the imaginary axis, which indicates that the short bubble branch is stable, while the second solution figure(4.25.b) shows the real part of the eigenvalue spectrum as well as the changing signs of the real eigenvalue which indicates that the long bubble branch is unstable. The changing signs in the eigenvalue spectrum as we move from the lower solution branch to the upper solution branch further confirm the presence of the turning point.

Throughout our computations the solutions have been calculated for both branches with various values for the different parameters.

In the beginning, using various domain checks in order to check convergence, we determined that the result is grid independent for different values of N, where $m = 501$ is fixed for both, the stable solution in the lower branch (figure (4.26.a)), as well as the unstable solution in the upper branch (figure (4.26.b)).

On the other hand, for both, the stable and unstable solutions, results are not grid independent, although we observe a slow trend towards it, when using different numbers of Chebychev points, $m = 401$, $m = 501$, $m = 1001$, and $m = 1501$, while the number of finite difference points remains fixed at $N = 100$, as shown in figure (4.27.a) for the stable solution and figure (4.27.b) for the unstable solution. The figure (4.27) shows that for the lower branch the number of eigenvalues changes most.

In the previous section we have expressed the general linear system(4.66) in the form of the generalized eigenvalue problem,

$$\bar{\mathbf{J}}\bar{\mathbf{T}} = \lambda\bar{\mathbf{R}}\bar{\mathbf{T}}. \tag{4.71}$$

In this system, to ensure that ARPACK would not miss any unstable modes with a large imaginary part, we have generated many more eigenvalues than needed because ARPACK cannot specify that the smallest real part be calculated,

but only the smallest magnitude complex number. Figure (4.28.a) shows that when we generate 200, 400 and 600 eigenvalues to determine the critical eigenvalue for the stable solution, all the numbers of eigenvalues (nev) generated give the same smallest real part. Working with the unstable solution we obtain the same result as in the stable solution, as exhibited in figure(4.28.b).

Figures (4.29.a) and (4.29.b) show the results of our computations for the eigenvalues with different values of σ in the stable and unstable solutions respectively, to be convergent, where σ is a shift in spectral transformation (ARPACK).

All these computations have been made using the same Re, β and grid size, which typically took the values, 50000, 0.0997 and $N = 100$, $m = 501$, respectively.

To check for grid convergence for different values of (nev) and σ, all the results have been calculated using three different grid sizes, 501, 1001 and 1501, finite difference points with 100 Chebychev points. Increasing the value of finite difference points had no effect on grid independence and results have been found to be convergent.

Figures (4.30.a) and (4.30.b) illustrate that for typically 1501 finite difference points and 100 Chebychev points the flow is about to undergo another kind of bifurcation, a Hopf bifurcation. In both, the stable and unstable solutions, the eigenvalues of the Hopf bifurcation tend to zero, but do not cross the imaginary axis. But in the unstable solution at the largest separated region of our calculations for these high gradients, where $Re = 50000$ and $\beta = 0.0908$, we observe that the eigenvalues of the Hopf bifurcation cross the imaginary axis with the eigenvalue of the turning point bifurcation which we have calculated previously, see figure (4.31).

As explained earlier, in the formulation of our system a stable mode is indicated by a positive real part of the eigenvalue, while a negative real part of the

eigenvalue shows an unstable mode. For these computations we used ARPACK, to calculate eigenvalues as well as the corresponding eigenvectors.

In the first solution on the lower branch the channel flow is linearly stable within the range of computed Re. These results are shown in figure (4.32) and this figure shows the comparison between increasing values of Re and the smallest real part of the eigenvalue $\Re(\lambda_s)$, with varying values for β. From this figure (4.32) and table (4.4) we see that when we increase the value of the Re, the smallest critical real part of eigenvalue $\Re(\lambda_s)$ is positive and decreases very close to zero. For the unstable solution, figure (4.33) and table (4.5) illustrates that with increasing value of Re, the smallest critical real part of eigenvalue is negative and crosses the imaginary axis. The grid size we use here in this computation is $N = 100$, $m = 1501$.

	$\beta = 0.0997$	$\beta = 0.1$
Re	$\Re(\lambda_s)$	$\Re(\lambda_s)$
1000	0.36548E+00	0.36459E+00
5000	0.22437E+00	0.22432E+00
10000	0.15788E+00	0.15785E+00
20000	0.12121E+00	0.12119E+00
30000	0.99102E-01	0.99083E-01
40000	0.88420E-01	0.88399E-01
50000	0.83138E-01	0.83114E-01
60000	0.80763E-01	0.80735E-01
70000	0.73678E-01	0.65652E-01
80000	0.26100E-01	0.52364E-02

Table 4.4: Comparison of Re and the smallest real part of the eigenvalue $\Re(\lambda_s)$ for lower branch solution, with different values for β at $y_{max} = 0.3$, $N = 100$ and $m = 1501$.

The figures (4.34) show contour plots of the real part of the eigenfunction for the disturbance streamfunction for various grid sizes, on the unstable branch with $Re = 50000$, $N = 100$ and $\beta = 0.0997$. Note that since the eigenvalue is real, the imaginary part of the eigenfunction can be taken to be zero. The

	$\beta = 0.0997$	$\beta = 0.1$
Re	$\Re(\lambda_s)$	$\Re(\lambda_s)$
37000	-0.15326E-01	-0.15681E-01
40000	-0.16542E-01	-0.16847E-01
45000	-0.18778E-01	-0.19356E-01
50000	-0.21961E-01	-0.22628E-01
55000	-0.24996E-01	-0.25556E-01
60000	-0.27356E-01	-0.27683E-01
65000	-0.28713E-01	-0.28635E-01
70000	-0.28613E-01	-0.27813E-01
75000	-0.26118E-01	-0.23733E-01
80000	-0.17888E-01	-0.48057E-02

Table 4.5: Comparison of Re and the smallest real part of the eigenvalue $\Re(\lambda_s)$ for upper branch solution with different values for β at $y_{max} = 0.3$, $N = 100$ and $m = 1501$.

eigenfunction is normalised so that the maximum value is unity in the region $0 < x < 20$. The contour plots in figures (4.34) show that the the eigenvector is converged for different grid sizes in the region shown. Note that the calculated imaginary part of the eigenfunction was not zero but exhibited an oscillation, but with zero mean, for any fixed y value. This is an indication of numerical errors, which we speculate would be reduced by appropriate choice of grid sizes, and using different boundary conditions at the outlet boundary. It was not feasible to conduct these investigations because of insufficient computational resources.

The global stability results that have been presented in this section are shown to be linearly stable in the first solution on the lower branch and unstable in the second solution of the upper branch, while the change from stable to unstable, as we move from the lower to the upper branch of the solutions, further confirms the presence of the turning point. To confirm the results of the global stability analysis and to get accurate values for the critical parameters of stability loss we use linear temporal simulations of the unsteady equations as discussed in the following section.

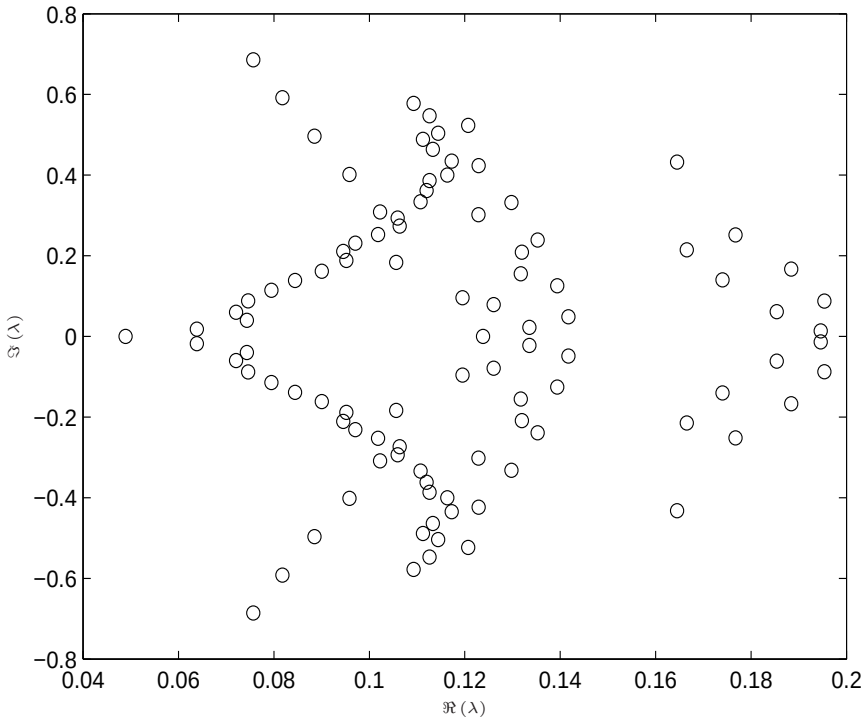

(a) Lower branch

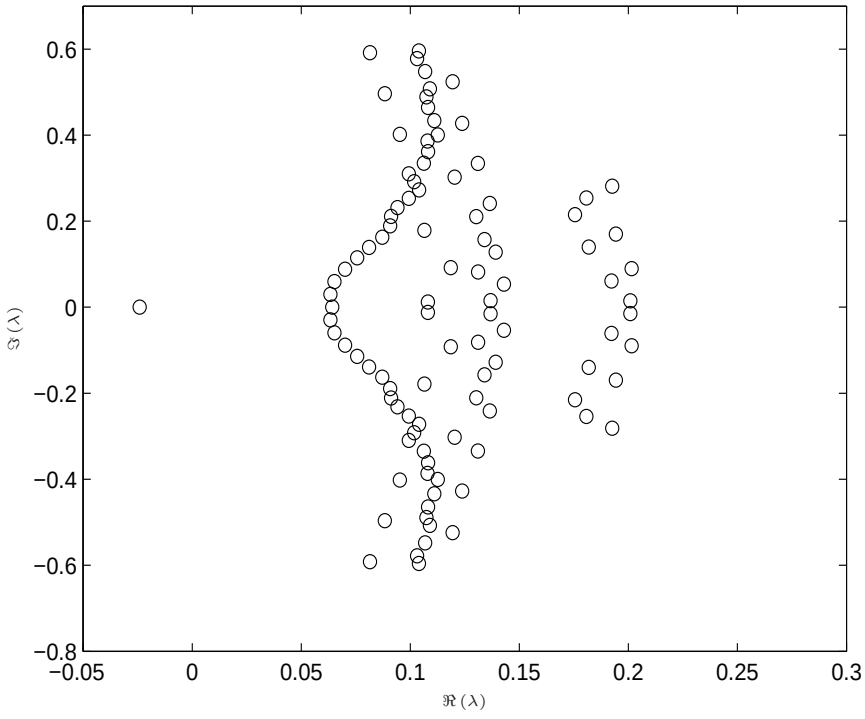

(b) Upper branch

Figure 4.25: Plot showing eigenvalues for two solutions, lower and upper branches at $y_{max} = 0.3$, $Re = 50000$, $\beta = 0.0997$, $N = 100$ and $m = 501$.

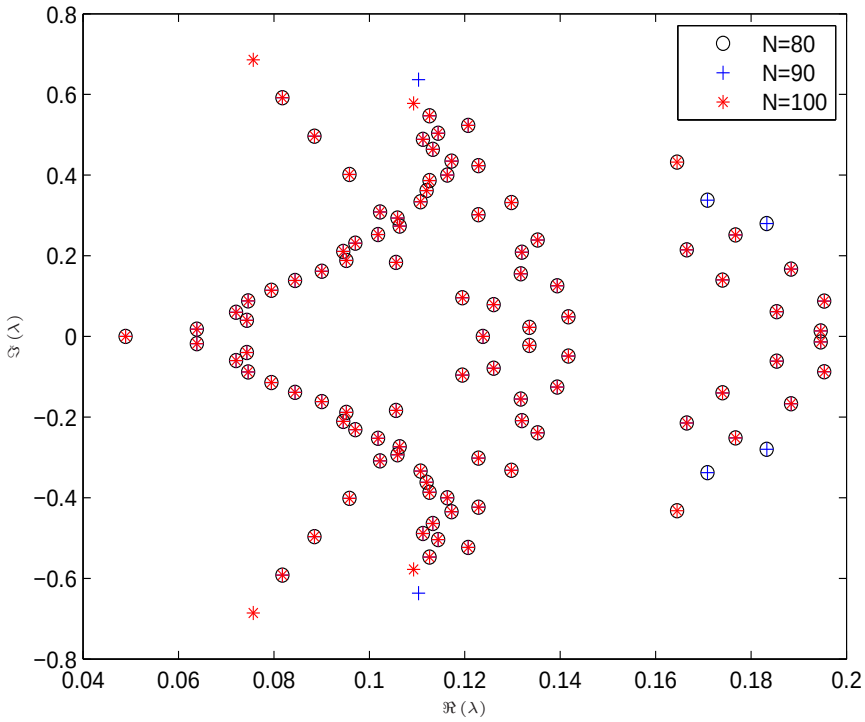

(a) Lower branch

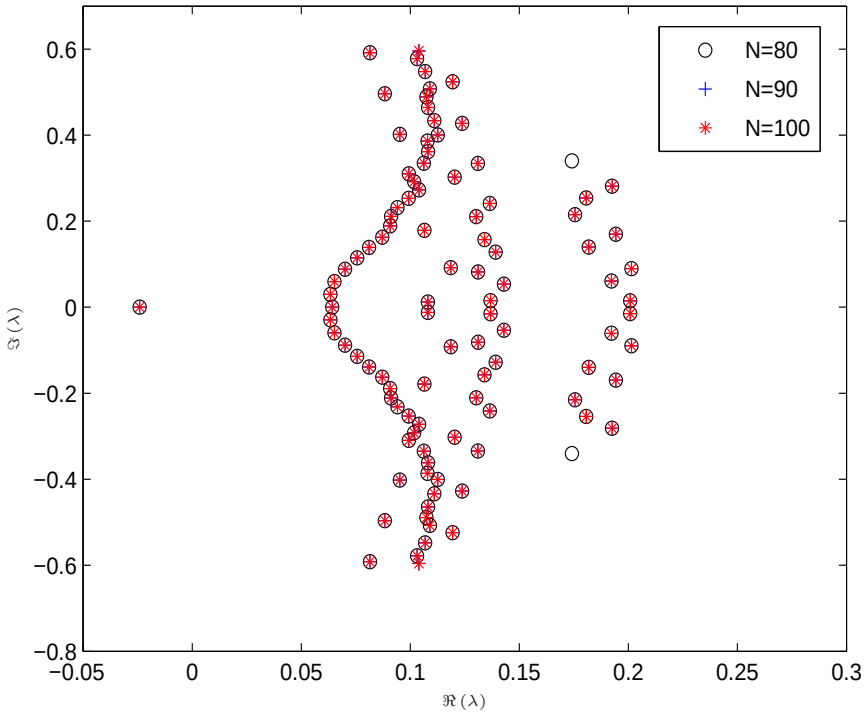

(b) Upper branch

Figure 4.26: Plot showing eigenvalues for two solutions, lower and upper branches at $y_{max} = 0.3$, $Re = 50000$, $\beta = 0.0997$ and different grid sizes for $N = 80, 90, 100$ and $m = 501$.

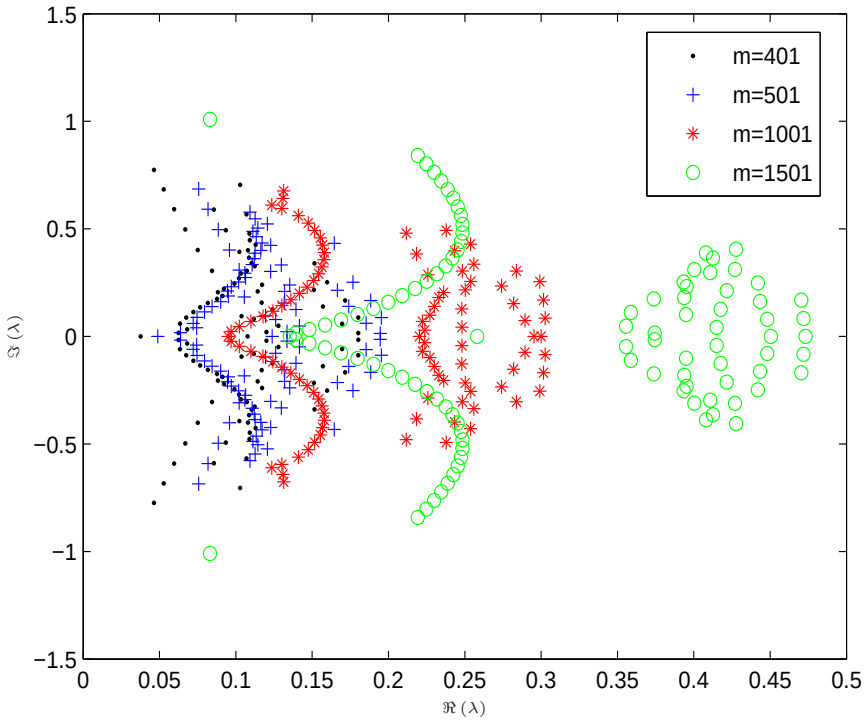

(a) Lower branch

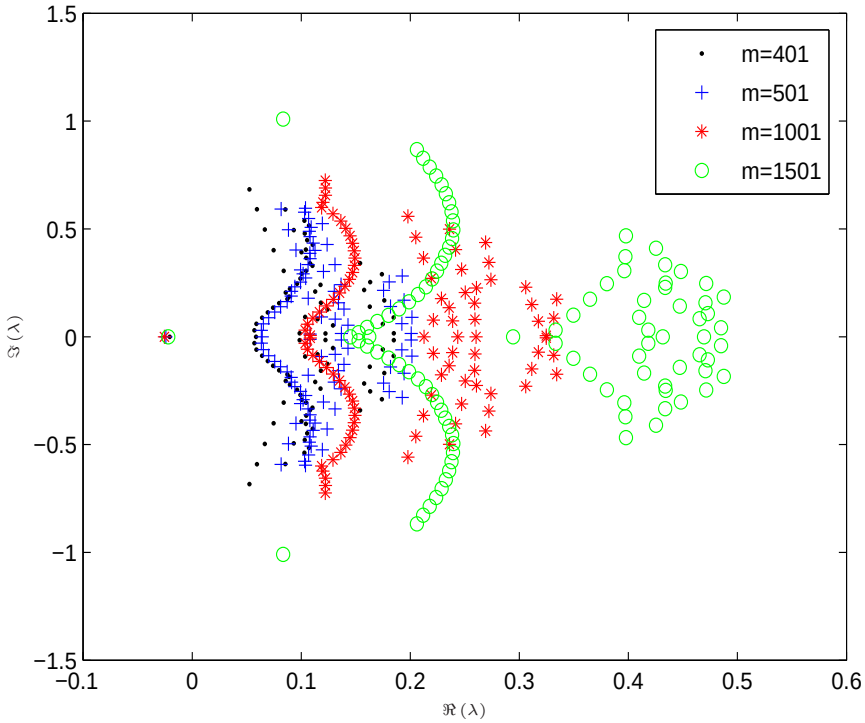

(b) Upper branch

Figure 4.27: Plot showing eigenvalues for two solutions, lower and upper branches at $y_{max} = 0.3$, $Re = 50000$, $\beta = 0.0997$ and different grid sizes for $m = 401, 501, 1001, 1501$ and $N = 100$.

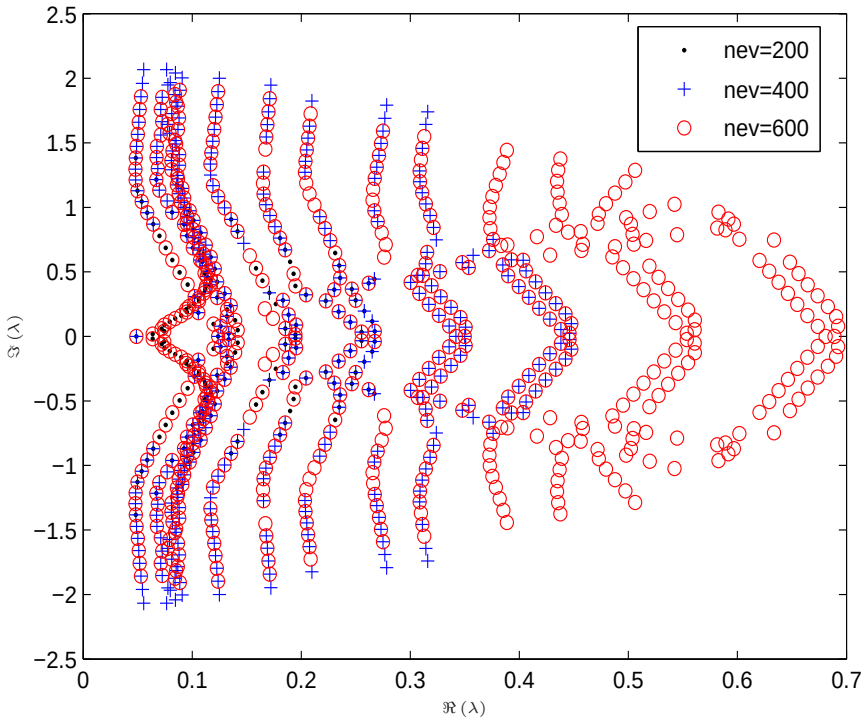

(a) Lower branch

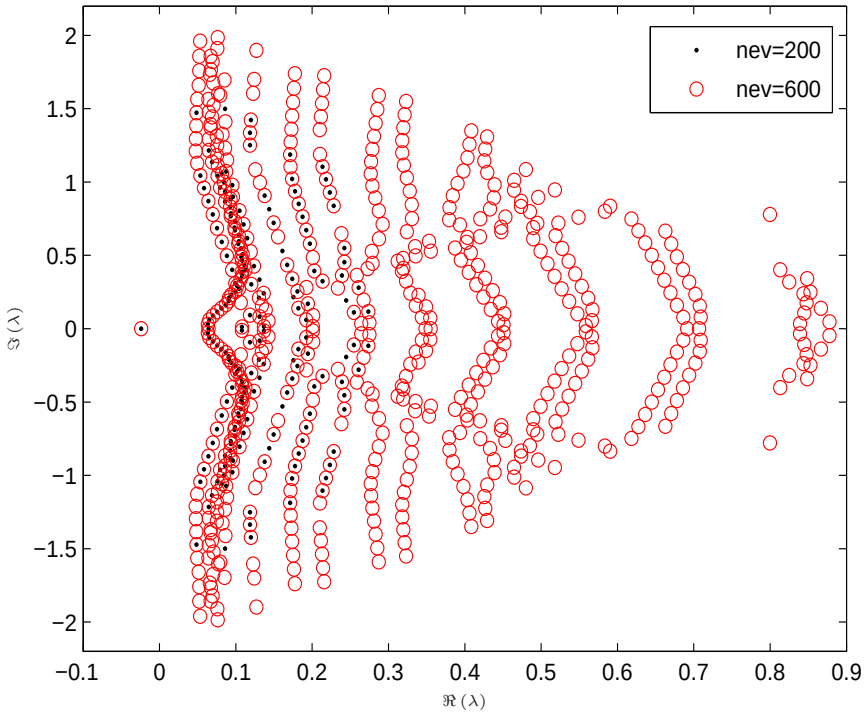

(b) Upper branch

Figure 4.28: Plot showing the different number of eigenvalues for two solutions, lower and upper branches at $y_{max} = 0.3$, $Re = 50000$, $\beta = 0.0997$, $m = 501$ and $N = 100$.

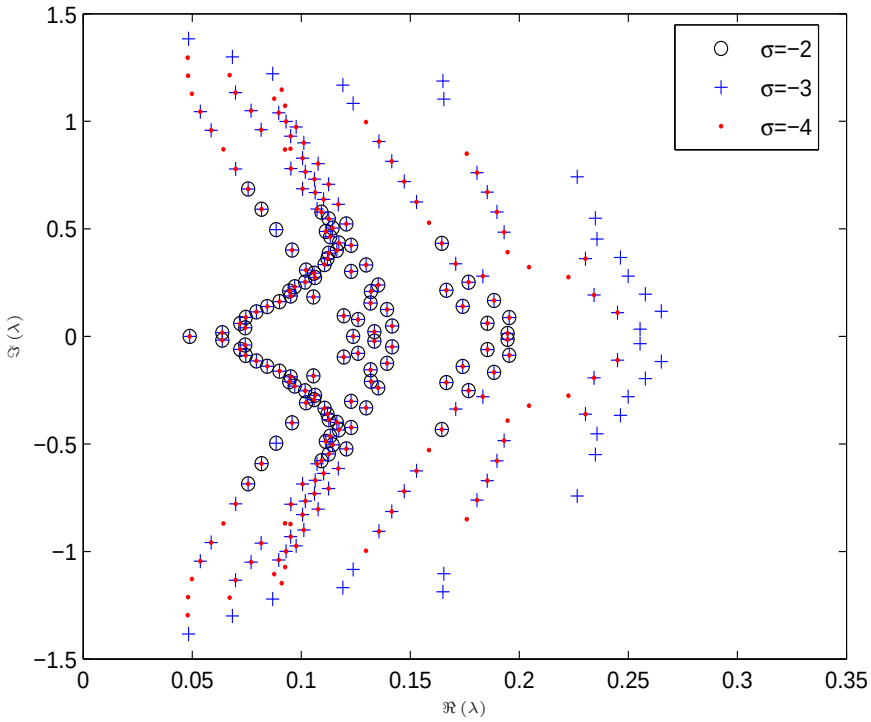

(a) Lower branch

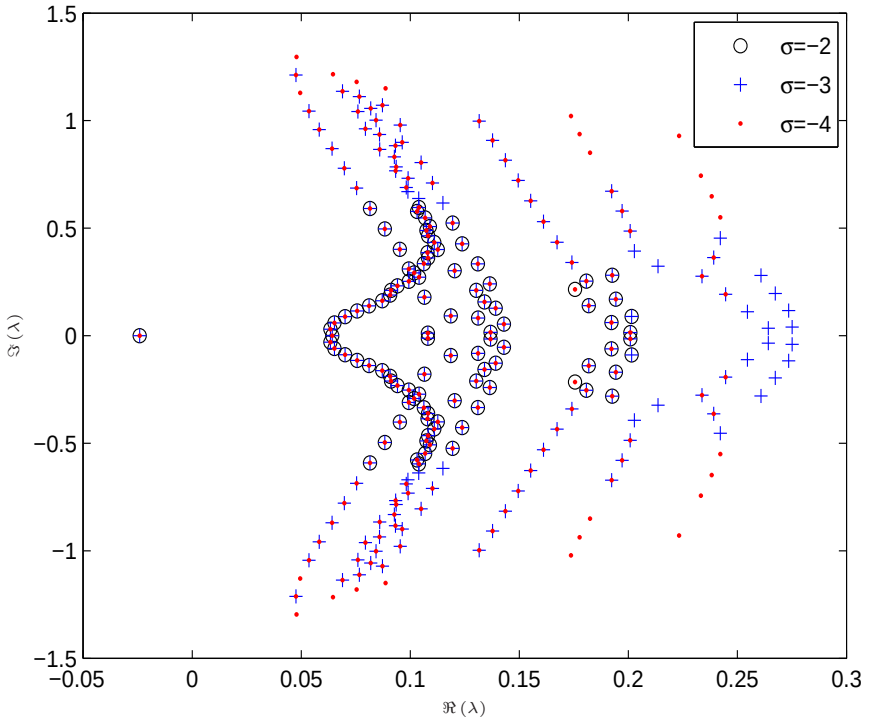

(b) Upper branch

Figure 4.29: Plot showing the eigenvalues with varying shift-σ for two solutions, lower and upper branches, at $y_{max} = 0.3$, $Re = 50000$, $\beta = 0.0997$, $m = 501$ and $N = 100$.

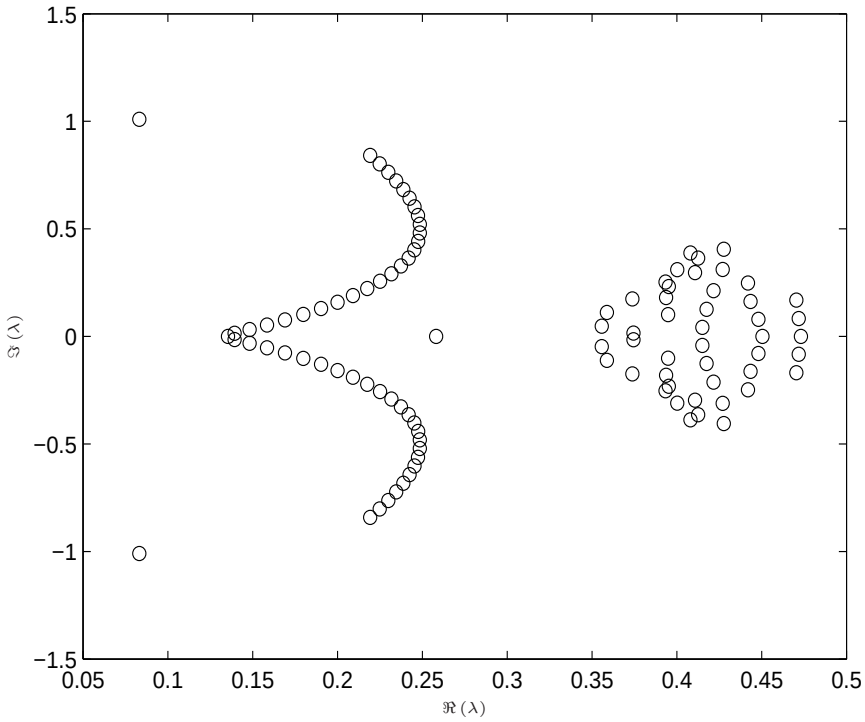

(a) Stable solution

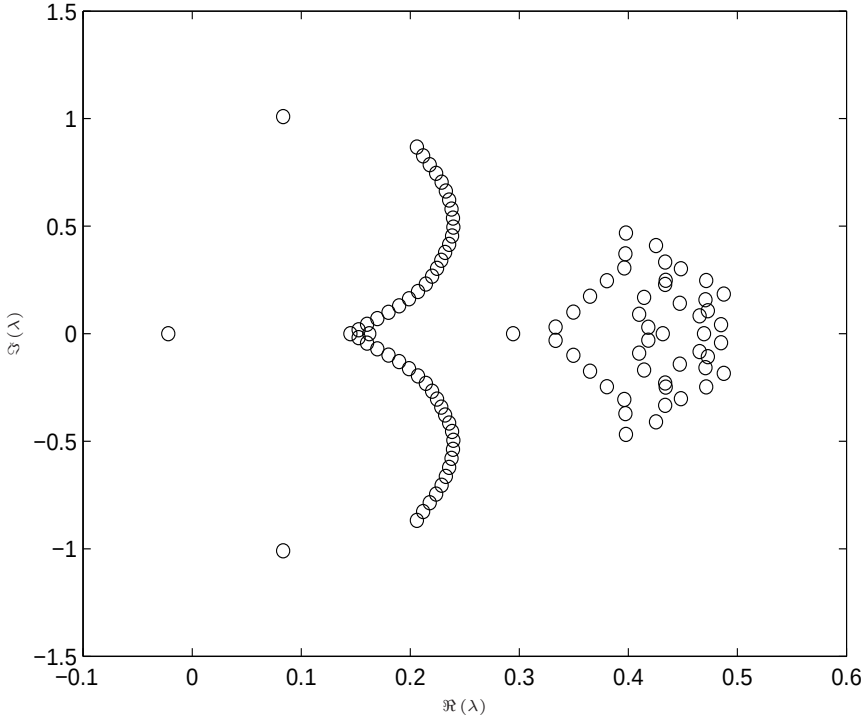

(b) Unstable solution

Figure 4.30: Plot showing eigenvalues for two solutions, stable and unstable, at $y_{max} = 0.3$, $Re = 50000$, $\beta = 0.0997$, $N = 100$ and $m = 1501$.

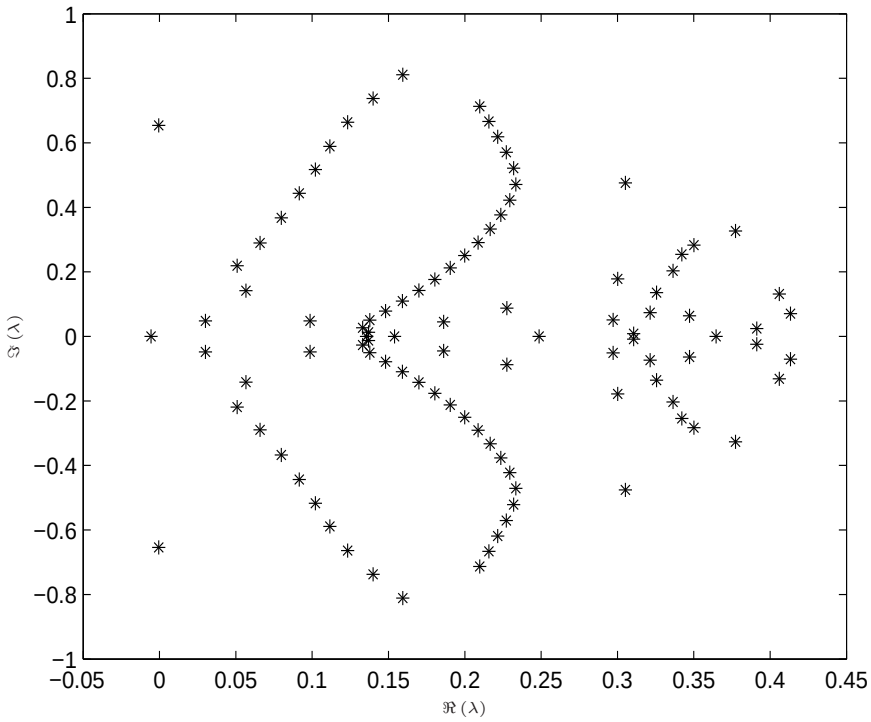

(a) Eigenvalues

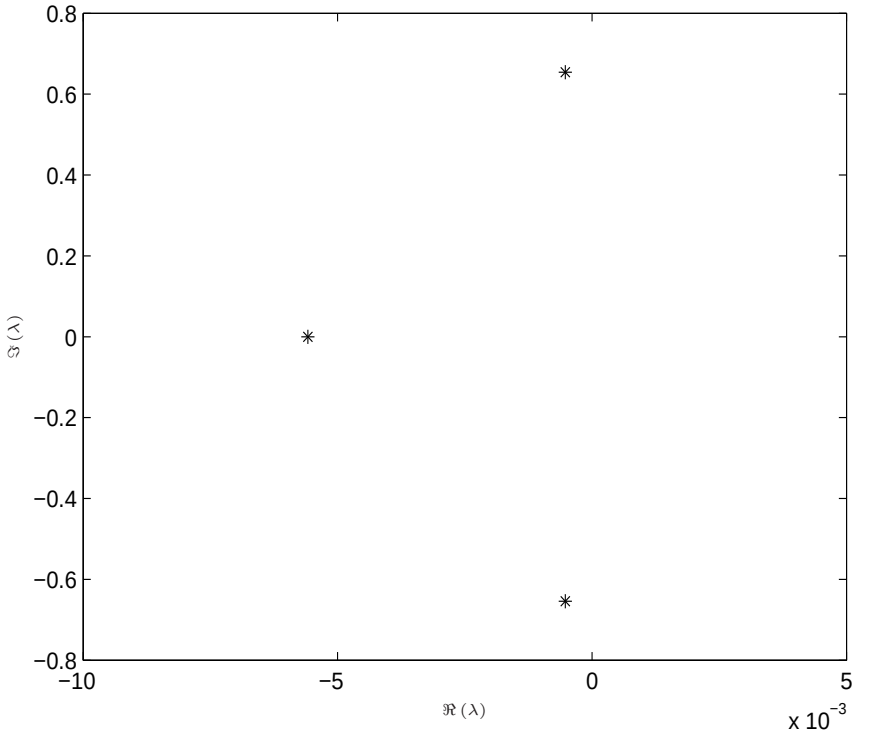

(b) Diagram of eigenvalues crossing the imaginary axis

Figure 4.31: Plot showing eigenvalues for unstable solution at the largest separated region where $y_{max} = 0.3$, $Re = 50000$, $\beta = 0.0908$, $N = 100$ and $m = 1501$.

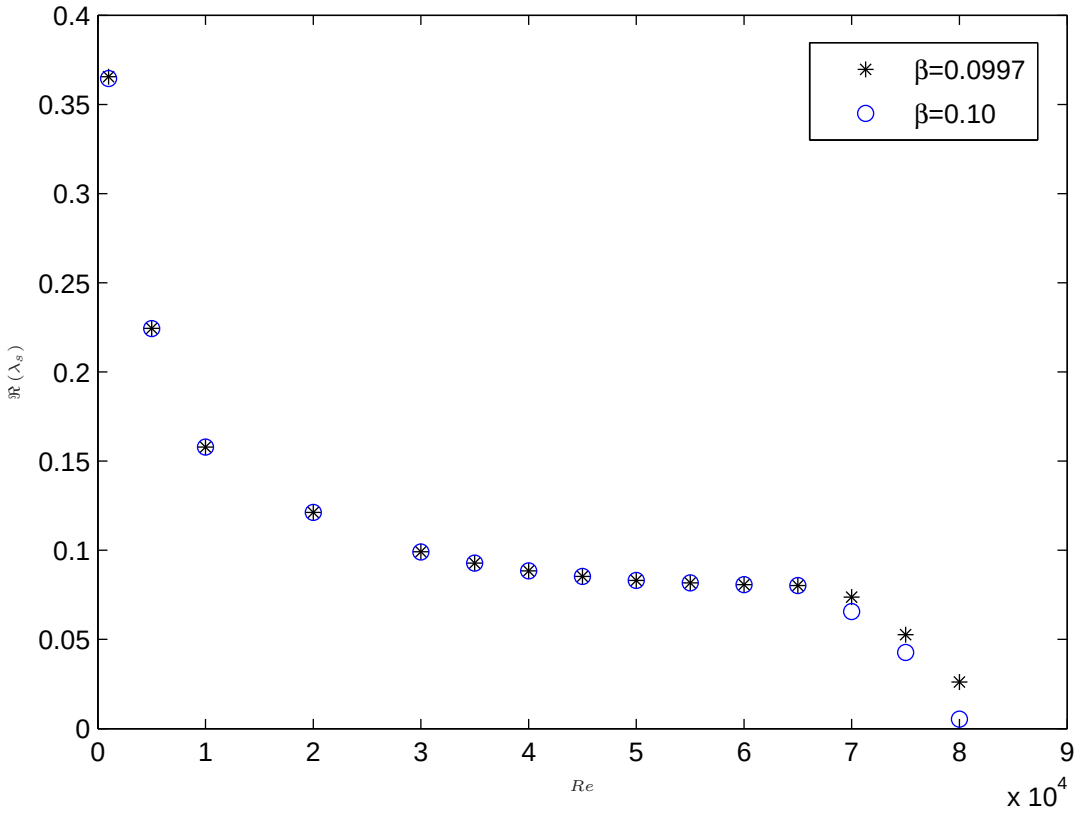

Figure 4.32: Comparison between increasing values of Re and the smallest real part of the eigenvalue $\Re(\lambda_s)$ for lower branch solution, with varying values for β at $y_{max} = 0.3$, $N = 100$ and $m = 1501$.

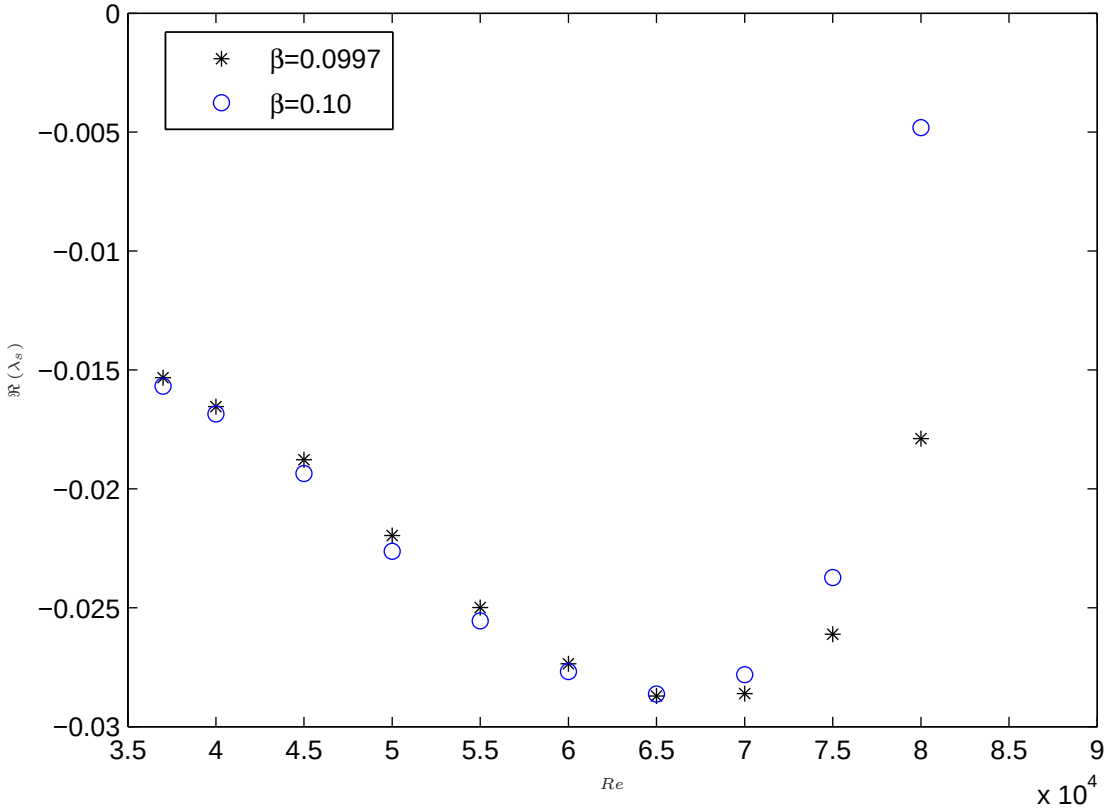

Figure 4.33: Comparison between increasing values of Re and the smallest real part of the eigenvalue $\Re(\lambda_s)$ for upper branch solution, with varying values for β at $y_{max} = 0.3$, $N = 100$ and $m = 1501$.

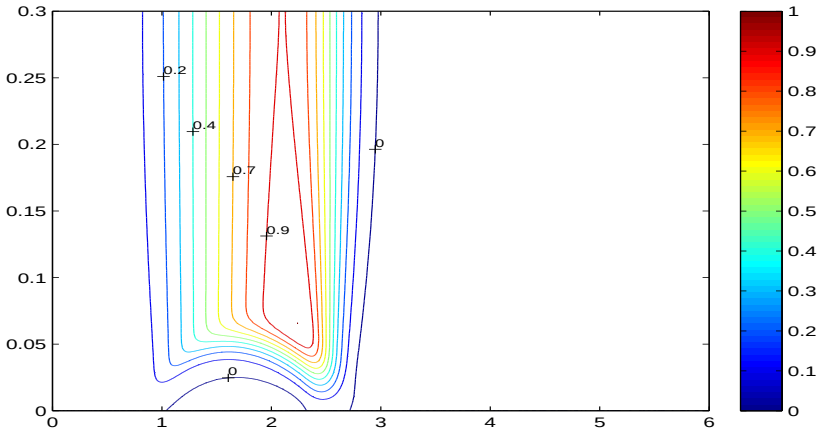

(a) $\Re\left(\widetilde{\psi}\right)$ where $m = 1001$

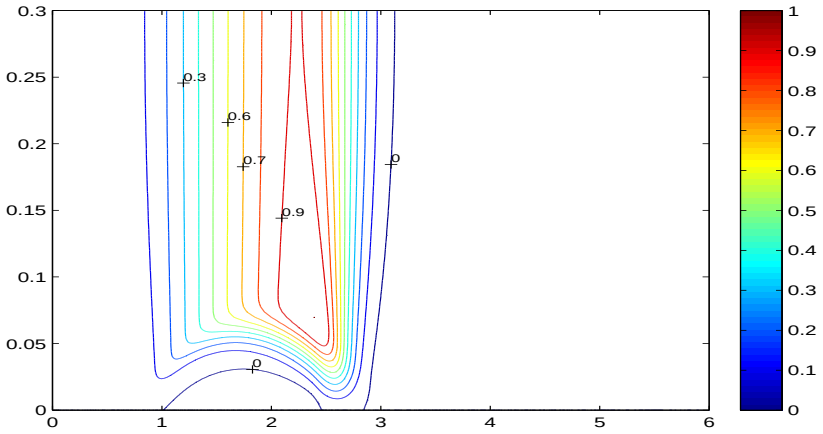

(b) $\Re\left(\widetilde{\psi}\right)$ where $m = 1501$

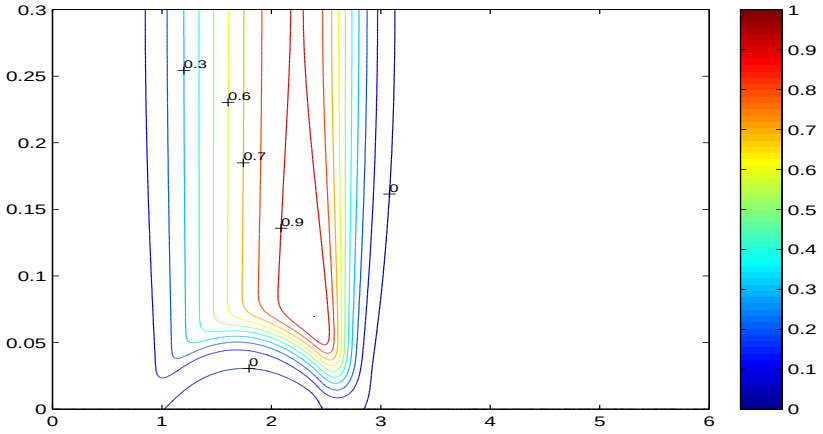

(c) $\Re\left(\widetilde{\psi}\right)$ where $m = 2001$

Figure 4.34: Contour plots of the real part of the stream function eigenvector for unstable solution, where $y_{max} = 0.3$, $Re = 50000$, $\beta = 0.0997$, $N = 100$ and different $m = 1001, 1501, 2001$.

4.9 Linear Temporal Simulation

In this section we apply linear temporal simulation to investigate the stability of the channel flow, using the linearized unsteady Navier-Stokes equations describing the flow. We will verify that our results are numerically stable by performing a stability test, using $Re = 50000$, $\beta = 0.0997$, $N = 100$ and $m = 501$.

4.9.1 Verifying Numerical Stability

The form of the incompressible, unsteady Navier-Stokes equations in stream function ψ and vorticity ω in the channel flow is given as,

$$\omega_t + \psi_y \omega_x - \psi_x \omega_y = \frac{1}{Re}\left(\omega_{xx} + \omega_{yy}\right), \tag{4.72}$$

$$\omega = \left(\psi_{xx} + \psi_{yy}\right), \tag{4.73}$$

with boundary conditions,

$$\begin{array}{llllll} \psi = 0, & \psi_y = 0 & \text{for} & y = 0, & 0 \le x \le x_{max}, \\ \psi_y = 1 - \beta\hat{\psi}_s, & \omega = 0 & \text{for} & y = y_{max}, & 0 \le x \le x_{max}, \\ \psi = y, & \omega = 0 & \text{for} & x = 0, & 0 \le y \le y_{max}, \\ \psi_{xx} = 0, & \omega - \psi_{yy} = 0 & \text{for} & x = x_{max}, & 0 \le y \le y_{max}. \end{array}$$

Assuming the total flow to be separated into a basic flow and a perturbed flow we get:

$$\psi = \widehat{\psi}\left(x, y\right) + \delta\vec{\psi}\left(x, y, t\right), \tag{4.74}$$

$$\omega = \widehat{\omega}\left(x, y\right) + \delta\vec{\omega}\left(x, y, t\right). \tag{4.75}$$

where ψ and ω are total flow, $\widehat{\psi}$ and $\widehat{\omega}$ denote the basic flow, perturbed flow is expressed as variables with a bar, and δ is a small number ($\delta \ll 1$).

By substituting equations (4.74) and (4.75) into equations (4.72) and (4.73) and neglecting terms of $O\left(\delta^2\right)$ we obtain,

First, a steady system of equations

$$\widehat{\psi}_y\widehat{\omega}_x - \widehat{\psi}_x\widehat{\omega}_y = \frac{1}{Re}\left(\widehat{\omega}_{xx} + \widehat{\omega}_{yy}\right), \tag{4.76}$$

$$\widehat{\omega} = \left(\widehat{\psi}_{xx} + \widehat{\psi}_{yy}\right). \tag{4.77}$$

Second, the stability equations

$$\widehat{\omega}_t + \widehat{\psi}_y\vec{\omega}_x + \vec{\psi}_y\widehat{\omega}_x - \widehat{\psi}_x\vec{\omega}_y - \vec{\psi}_x\widehat{\omega}_y = \frac{1}{Re}\left(\vec{\omega}_{xx} + \vec{\omega}_{yy}\right), \tag{4.78}$$

$$\vec{\omega} = \left(\vec{\psi}_{xx} + \vec{\psi}_{yy}\right). \tag{4.79}$$

From equations (4.78) and (4.79) we can see that $\vec{\omega}$ and $\vec{\psi}$ have a trivial solution, meaning that these equations are homogeneous. Because the values of $\vec{\omega}$ and $\vec{\psi}$ must be very small in order to obtain a numerically stable solution for equations (4.78) and (4.79), we are going to use relations (4.74) and (4.75) to change the equations (4.78) and (4.79) from homogeneous to non-homogeneous equations by substituting $\vec{\omega} = \omega - \widehat{\omega}$ and $\vec{\psi} = \psi - \widehat{\psi}$ into (4.78) and (4.79) arriving at,

$$\begin{aligned}\omega_t + \widehat{\psi}_y\omega_x + \psi_y\widehat{\omega}_x &- \widehat{\psi}_x\omega_y - \psi_x\widehat{\omega}_y - \frac{1}{Re}\left(\omega_{xx} + \omega_{yy}\right) \\ &= 2\left(\widehat{\psi}_y\widehat{\omega}_x - \widehat{\psi}_x\widehat{\omega}_y\right) - \frac{1}{Re}\left(\widehat{\omega}_{xx} + \widehat{\omega}_{yy}\right), \qquad (4.80)\\ \omega - \left(\psi_{xx} + \psi_{yy}\right) &= \widehat{\omega} - \left(\widehat{\psi}_{xx} + \widehat{\psi}_{yy}\right). \qquad (4.81)\end{aligned}$$

By substituting the steady system of equations (4.76) and (4.77) into equations (4.80) and (4.81) we obtain the following equations. These equations with their corresponding boundary conditions are solved for ω and ψ.

$$\omega_t + \widehat{\psi}_y\omega_x + \psi_y\widehat{\omega}_x - \widehat{\psi}_x\omega_y - \psi_x\widehat{\omega}_y - \frac{1}{Re}\left(\omega_{xx} + \omega_{yy}\right) = \widehat{\psi}_y\widehat{\omega}_x - \widehat{\psi}_x\widehat{\omega}_y \tag{4.82}$$

$$\omega - \left(\psi_{xx} + \psi_{yy}\right) = 0. \tag{4.83}$$

Again, as in previous sections, by using functions $y = f(z)$ and $x = f(\xi)$ where,

$$\frac{d}{dy} = \frac{dz}{dy}\frac{d}{dz} \qquad \text{and} \qquad \frac{d}{dx} = \frac{d\xi}{dx}\frac{d}{d\xi},$$

we also have,

$$\frac{d^2}{dy^2} = \frac{d^2z}{dy^2}\frac{d}{dz} + \left(\frac{dz}{dy}\right)^2\frac{d^2}{dz^2} \qquad \text{and} \qquad \frac{d^2}{dx^2} = \frac{d^2\xi}{dx^2}\frac{d}{d\xi} + \left(\frac{d\xi}{dx}\right)^2\frac{d^2}{d\xi^2},$$

we got the following equations:

$$\begin{aligned}
&\omega_t + \left[\frac{dz}{dy}\frac{d\widehat{\psi}}{dz}\right]\left[\frac{d\xi}{dx}\frac{d\omega}{d\xi}\right] + \left[\frac{dz}{dy}\frac{d\psi}{dz}\right]\left[\frac{d\xi}{dx}\frac{d\widehat{\omega}}{d\xi}\right] - \left[\frac{d\xi}{dx}\frac{d\widehat{\psi}}{d\xi}\right]\left[\frac{dz}{dy}\frac{d\omega}{dz}\right] \\
&- \left[\frac{d\xi}{dx}\frac{d\psi}{d\xi}\right]\left[\frac{dz}{dy}\frac{d\widehat{\omega}}{dz}\right] - \frac{1}{Re}\left[\frac{d^2\xi}{dx^2}\frac{d\omega}{d\xi} + \left(\frac{d\xi}{dx}\right)^2\frac{d^2\omega}{d\xi^2} + \frac{d^2z}{dy^2}\frac{d\omega}{dz}\right. \\
&\left. + \left(\frac{dz}{dy}\right)^2\frac{d^2\omega}{dz^2}\right] = \left[\frac{dz}{dy}\frac{d\widehat{\psi}}{dz}\right]\left[\frac{d\xi}{dx}\frac{d\widehat{\omega}}{d\xi}\right] - \left[\frac{d\xi}{dx}\frac{d\widehat{\psi}}{d\xi}\right]\left[\frac{dz}{dy}\frac{d\widehat{\omega}}{dz}\right], \qquad (4.84)
\end{aligned}$$

and

$$\omega - \left[\frac{d^2\xi}{dx^2}\frac{d\psi}{d\xi} + \left(\frac{d\xi}{dx}\right)^2\frac{d^2\psi}{d\xi^2} + \frac{d^2z}{dy^2}\frac{d\psi}{dz} + \left(\frac{dz}{dy}\right)^2\frac{d^2\psi}{dz^2}\right] = 0. \qquad (4.85)$$

To develop the above equations in time, a first order backward difference method is used to discretize the term for the time derivative which is illustrated by the first term in the following scheme.

$$\begin{aligned}
&\frac{\omega^{p+1} - \omega^p}{\Delta t} + \left(\frac{dz}{dy}\right)\left(D_z\widehat{\psi}\right)_{kj}\left(\frac{d\xi}{dx}\right)\frac{\omega^{p+1}_{k+1j} - \omega^{p+1}_{k-1j}}{2\Delta\xi} + \left(\frac{dz}{dy}\right)\left(D_z\psi^{p+1}\right)_{kj} \\
&\left(\frac{d\xi}{dx}\right)\frac{\widehat{\omega}_{k+1j} - \widehat{\omega}_{k-1j}}{2\Delta\xi} - \left(\frac{dz}{dy}\right)\left(D_z\omega^{p+1}\right)_{kj}\left(\frac{d\xi}{dx}\right)\frac{\widehat{\psi}_{k+1j} - \widehat{\psi}_{k-1j}}{2\Delta\xi} \\
&- \left(\frac{dz}{dy}\right)\left(D_z\widehat{\omega}\right)_{kj}\left(\frac{d\xi}{dx}\right)\frac{\psi^{p+1}_{k+1j} - \psi^{p+1}_{k-1j}}{2\Delta\xi} - \frac{1}{Re}\left(\frac{d^2\xi}{dx^2}\right)\frac{\omega^{p+1}_{k+1j} - \omega^{p+1}_{k-1j}}{2\Delta\xi} \\
&-\frac{1}{Re}\left(\frac{d\xi}{dx}\right)^2\frac{\omega^{p+1}_{k+1j} - 2\omega^{p+1}_{kj} + \omega^{p+1}_{k-1j}}{(\Delta\xi)^2} - \frac{1}{Re}\left(\frac{d^2z}{dy^2}\right)\left(D_z\omega^{p+1}\right)_{kj} \\
&-\frac{1}{Re}\left(\frac{dz}{dy}\right)^2\left(D_z^2\omega^{p+1}\right)_{kj} = \left(\frac{dz}{dy}\right)\left(D_z\widehat{\psi}\right)_{kj}\left(\frac{d\xi}{dx}\right)\frac{\widehat{\omega}_{k+1j} - \widehat{\omega}_{k-1j}}{2\Delta\xi} \\
&- \left(\frac{dz}{dy}\right)\left(D_z\widehat{\omega}\right)_{kj}\left(\frac{d\xi}{dx}\right)\frac{\widehat{\psi}_{k+1j} - \widehat{\psi}_{k-1j}}{2\Delta\xi}, \qquad (4.86)
\end{aligned}$$

and

$$\omega_{kj}^{p+1} - \left(\frac{d^2\xi}{dx^2}\right)\frac{\psi_{k+1j}^{p+1} - \psi_{k-1j}^{p+1}}{2\Delta\xi} - \left(\frac{d\xi}{dx}\right)^2 \frac{\psi_{k+1j}^{p+1} - 2\psi_{kj}^{p+1} + \psi_{k-1j}^{p+1}}{(\Delta\xi)^2}$$
$$- \left(\frac{d^2z}{dy^2}\right)\left(D_z\psi^{p+1}\right)_{kj} - \left(\frac{dz}{dy}\right)^2\left(D_z^2\psi^{p+1}\right)_{kj} = 0,$$
$$1 \le k \le m \qquad and \qquad 0 \le j \le N, \qquad (4.87)$$

where Δt is the time step and superscript p denotes variables from the previous time levels, while $p+1$ denotes variables from the present time levels.

The above schemes (4.86) and (4.87) have been discretized by using the Chebychev collocation combined with second order central difference in y-direction and x-direction, respectively, as previously described in section 4.3.

These equations (4.86) and (4.87) with their boundary conditions can be written in the form of a general linear system,

$$\tilde{\mathbf{J}}\tilde{\mathbf{\Phi}} = \tilde{\mathbf{R}}, \qquad (4.88)$$

where $\tilde{\mathbf{\Phi}}$ is the vector of the unknown streamfunction and vorticity is expressed as,

$$\tilde{\mathbf{\Phi}} = \begin{pmatrix} \psi^{p+1} \\ \omega^{p+1} \end{pmatrix} \qquad (4.89)$$

and the block tridiagonal matrix $\tilde{\mathbf{J}}$ which has been written in the linear system above is similar to the block tridiagonal matrix $\mathbf{J}$ which we have obtained before in section (4.5), while additional terms arise from the unsteady term and are easily incorporated into the solve. The vector $\tilde{\mathbf{\Phi}}$ in the linear system (4.88) was solved by using a direct solver and utilizing the sparsity pattern of the block tridiagonal matrix.

Figures (4.42) and (4.43) demonstrate the maximum values of $\vec{\psi}$ $\left(\vec{\psi}_{max}\right)$ and $\vec{\omega}$ $(\vec{\omega}_{max})$ at each time step for the whole time range (t) respectively and affirm

that the numerical method is stable. The maximum values for $\vec{\psi}$ and $\vec{\omega}$ were obtained by subtracting the base flow from the total flow.

Following, we will discuss the simulation employing the numerical method which has been proven to be stable from the results of the previous computations.

The equations below are the governing equations for the channel flow, followed by the boundary conditions

$$\omega_t + \widehat{\psi}_y\omega_x + \psi_y\widehat{\omega}_x - \widehat{\psi}_x\omega_y - \psi_x\widehat{\omega}_y - \frac{1}{Re}\left(\omega_{xx} + \omega_{yy}\right) = \widehat{\psi}_y\widehat{\omega}_x - \widehat{\psi}_x\widehat{\omega}_y \quad (4.90)$$

$$\omega - \left(\psi_{xx} + \psi_{yy}\right) = 0. \quad (4.91)$$

$$\begin{array}{llllll} \psi = f(x,t), & \psi_y = 0 & \text{for} & y = 0, & 0 \le x \le x_{max}, \\ \psi_y = 1 - \beta\hat{\psi}_s, & \omega = 0 & \text{for} & y = y_{max}, & 0 \le x \le x_{max}, \\ \psi = y, & \omega = 0 & \text{for} & x = 0, & 0 \le y \le y_{max}, \\ \psi_{xx} = 0, & \omega - \psi_{yy} = 0 & \text{for} & x = x_{max}, & 0 \le y \le y_{max}. \end{array}$$

where

$$f(x,t) = \left[e^{-20(x-1.5)^2}\right]\left[e^{-50(t-1)^2/\left(1000\sqrt{\pi}\right)}\right]$$

Here, we investigate the effects on the above flow of the introduction of a source of perturbation, i.e. a change in the boundary conditions at the wall, as well as the development of this perturbation as time increases. We are using the same simulation method as Boppana (2007).

The equation(4.90) we arrived at previously, can be expressed as,

$$\omega_t + \underbrace{\widehat{\psi}_y\omega_x + \psi_y\widehat{\omega}_x - \widehat{\psi}_x\omega_y - \psi_x\widehat{\omega}_y - \frac{1}{Re}\left(\omega_{xx} + \omega_{yy}\right)}_{V} = \widehat{\psi}_y\widehat{\omega}_x - \widehat{\psi}_x\widehat{\omega}_y \quad (4.92)$$

In the segment below we will discretize the time derivative term.

1- The first time step.

Here, we use the Crank-Nicholson scheme, where equation (4.92) becomes,

$$\frac{\omega^{p+1}-\omega^{p}}{\Delta t}+\frac{V^{p+1}+V^{p}}{2}=\widehat{\psi}_{y}\widehat{\omega}_{x}-\widehat{\psi}_{x}\widehat{\omega}_{y}.$$

$\Longrightarrow$

$$\frac{2}{\Delta t}\omega^{p+1}+V^{p+1}=\frac{2}{\Delta t}\omega^{p}-V^{p}+\widehat{\psi}_{y}\widehat{\omega}_{x}-\widehat{\psi}_{x}\widehat{\omega}_{y}. \tag{4.93}$$

In our computations, the value for the time levels starts at $p=0$, then we obtain $\psi^{(0)}$ and $\omega^{(0)}$ from the basic flow, while we obtain $\psi^{(1)}$ and $\omega^{(1)}$ when we solve equations (4.91) and (4.93) with the corresponding boundary condition.

2- The second time step and later.

We use here a second order backward difference scheme, where equation (4.92) becomes,

$$\frac{1}{\Delta t}\left(\frac{3}{2}\omega^{p+2}-2\omega^{p+1}+\frac{1}{2}\omega^{p}\right)+V^{p+2}=\widehat{\psi}_{y}\widehat{\omega}_{x}-\widehat{\psi}_{x}\widehat{\omega}_{y}.$$

$\Longrightarrow$

$$\frac{3}{2\Delta t}\omega^{p+2}+V^{p+2}=\frac{4\omega^{p+1}-\omega^{p}}{2\Delta t}+\widehat{\psi}_{y}\widehat{\omega}_{x}-\widehat{\psi}_{x}\widehat{\omega}_{y}. \tag{4.94}$$

After obtaining the solution for two time levels from the first time step above, we can therefore obtain ψ^{p+2} and ω^{p+2} by solving equations (4.91) and (4.94) with corresponding boundary conditions.

4.9.2 Results of the Simulation

In the linear temporal simulation to track the convergence to an asymptotic state we use the horizontal velocity (u) at a randomly chosen node $(x,y)=(0.1,1.4)$, where, typically, we use $Re=50000$, $\beta=0.0997$ and $\Delta t=0.025$, in calculating our results.

Figure (4.35.a) illustrates that the first solution on the lower branch is stable, where $t = 300$, whereas the second solution on the upper branch is unstable, where $t = 1000$, as shown in figure (4.35.b). After performing various grid size checks with increasing accuracy for Chebychev points (N) in y-direction, as well as varying finite difference points (m) in x-direction, the solutions on the lower and upper branches remain the same. See figure (4.36) for different N and figure (4.37) for different m.

In the first solution on the lower branch, at each time interval and for each of the three different time steps used, $\Delta(t) = 0.025, 0.0125$ and 0.05, when we compute the value of (u), the results are graphically similar and grid independent, as presented in figure (4.38). Figure (4.38.a) shows the full time range (t), while figure (4.38.b) shows the time range (t) truncated. From these results we chose $\Delta(t) = 0.025$ as the most suitable and least time-consuming one for our calculations. At the same time, in the second solution on the upper branch our computations give us identical results, see figure (4.39.a) and figure (4.39.b) for the whole range of (t) and truncated (t), respectively.

As mentioned in section (4.8.2) on results of global stability analysis, the second solution on the upper branch is unstable. Here in the linear simulation the velocity (u) has the form:

$$u(x, y, t) = e^{kt} f(x_0, y_0). \tag{4.95}$$

To confirm our results in the global stability, the value of (k) in the equation (4.95) should agree with the smallest real part of the eigenvalue $\Re(\lambda_s)$ in the global stability after a long time. From the simulation the growth rate k was estimated via

$$k = \frac{G_t(t)}{G(t)} \simeq \frac{G(t + \Delta t) - G(t - \Delta t)}{2G(t)},$$

with various measures taken for $G(t)$. In the figure (4.40) results are shown with

$$G(t) = \left(\int \int u^2 dxdy \right)^{\frac{1}{2}},$$

with the integral taken over the whole domain and approximated unmerically using a trapezoidal rule. From figure (4.40) it is evident that the value of (k) is very close to the predicted value of $\Re(\lambda_s)$ for various m which means that the results of the linear temporal simulation in the unstable solution on the upper branch are in excellent agreement with the smallest real part of the eigenvalue obtained from the global stability analysis of the second solution. Other measures, for example taking $G(t) = u(x_0, y_0, t)$, gave similar results, with the mean value of k in good agreement with the predicted values. In the figure (4.40) some oscillation can be seen in k, and with other measures these were large.

Further confirmation of the agreement can be seen in the contour plot of the perturbation streamfunction shown in figure (4.41) taken at time $t = 199.9$. This can be compared with the contour of the eigenvector shown in figure (4.34)

4.10 Conclusions

The numerical technique employed to calculate a two dimensional boundary layer flow in a channel with a suction port on the upper wall, which involves Chebychev collocation in one direction, combined with finite differences in the other direction, proved to be adequate and gave good results.

Investigating the formation of a laminar separation bubble on the lower wall of a channel with a suction profile on the upper wall, we find that the size of the bubble depends on the strength of the adverse pressure gradient.

Of interest here is that for the first time in this particular problem we discovered two solutions as well as a turning point as the solutions move from the the

lower to the upper branch. Characteristic for the flow on the lower, first solution branch is a short separation bubble, while we have a larger separation bubble on the second solution upper branch.

In the basic flow, our computations for both solutions obtained good results and showed these results to be grid independent of m for any given values of N, but in the opposite case, when N is fixed and for different values of m, results tend towards convergence.

The length of the separation bubble depends on the suction ratio β which in turn depends on the value of the Reynolds numbers. This means that in the first solution on the lower branch the separation bubble becomes larger when the suction ratio increases as a result of the decrease in the value of the Reynolds number Re. While in the second solution on the upper branch the separation bubble becomes larger when the suction ratio decreases as a result of the increase in the value of the Reynolds number Re.

The global stability and linear temporal simulation results both indicate that the first solution on the lower branch is stable, while the second solution on the upper branch is unstable. In addition, computations for various grid checks confirmed for both, stable and unstable solutions, that the result is grid independent for different values of N, but not quite convergent for different values of m. In the global stability analysis the smallest real part of the eigenvalue approaches and crosses the imaginary axis as it moves from the lower, stable solution branch to the upper unstable solution branch and confirms the presence of the turning point. In linear temporal simulation we obtain that the results are convergent for varying values of $\Delta(t)$ in the two solutions.

Comparison between the value of the smallest real part of the eigenvalue which we obtained from the global stability analysis in the unstable solution on the upper branch and the results of linear temporal simulation were good

agreement.

4.11 Comparison of Results with Literature

This current study, to the best of our knowledge, is the first work to calculate two solution branches and the turning point bifurcation in the two dimensional boundary layer flow in a channel with a suction on the upper wall. To investigate the stability of the flow the global stability analysis has been applied in this particular problem for the first time as well. Consequently, comparisons of our computational results to the results of previous works which we have discussed in the literature review in chapter 2, are limited.

In the computations of incompressible Navier-Stokes equations of Pauley *et al.* (1990), Hsiao & Pauley (1994), Alam & Sandham (2000) and Cassel *et al.* (2007), as well as in our work, the Blasius boundary layer solution was used at the inlet of the computational domain, while the boundary conditions we used here are different from theirs.

Similar behaviour in the response of the separation bubble to an increase in the adverse pressure gradient was found in the study of Pauley *et al.* (1990) and our computations. Increased suction produced a lengthening of the separated region. In their work the separation bubble remained steady until the critical value of suction strength $S = 0.12$, which marks the onset of unsteady separation. When they investigated the timestep independence of the solution they used two different timesteps $\Delta T = 0.005$ and $\Delta T = 0.0025$. They obtained that the two step sizes for flow velocities and shedding frequencies differed by at most 0.5%, while in the two solutions we obtained when we computed the velocity u for three different time steps $\Delta(t) = 0.025, 0.0125$ and 0.05, our results were grid independent.

Hsiao & Pauley (1994), quite opposite to our findings, did not obtain a stable solution of laminar flow at high Reynolds numbers for their full Navier-Stokes computation, although they used the same geometry as we did, but with a different value for channel height $H = 0.2096$. In their computation, when separation occurred at high suction strength, the boundary layer became unstable near the reattachment point. This differs from our result which produced two solutions, one stable and the other unstable.

In comparing our results with Alam & Sandham (2000) we are in agreement with their description in the three-dimensional case study of the separation bubble as being located in the region of the strongest adverse pressure gradient, as well as their finding that a stronger suction resulting in a stronger adverse pressure gradient produces a longer bubble. In their work in three dimensions with numerical stability, they classified their simulated bubbles as convectively unstable, meaning spatially unstable, while we observed in our work with global stability analysis that in the first solution the short bubble is stable, whereas the long bubble in the second solution is unstable.

Comparing our study with Cassel *et al.* (2007), we show a schematic comparison in table (4.6) between our results for the critical suction ratio when flow starts to separate at different Reynolds numbers and those given by Cassel. Although our boundary conditions are different from those used by Cassel it becomes evident from this table that the same effect we observed in our study has been observed by Cassel, i.e., that when we increase the value of the Reynolds number the critical suction ratio decreases. We can also see that while we use the same values for Reynolds numbers our values for critical suction ratios are smaller than those used by Cassel. We note that the channel height Cassel worked with is $H \leq 0.25$, while the channel height we worked with is $H = 0.3$. Similarities

in our results can also be observed in their mention of a steady recirculation region in the steady Navier-Stokes solutions of a channel flow with suction, where they describe the effect of a suction slot in the upper wall on the formation of a recirculation region in the lower wall.

	Cassel study	This study
Re	(β_s)	(β_s)
5000	0.205	0.111
10000	0.170	0.110
20000	0.134	0.101
50000	0.105	0.096

Table 4.6: Comparison of the critical values of suction ratio β_s and Re, for Cassel study and this study.

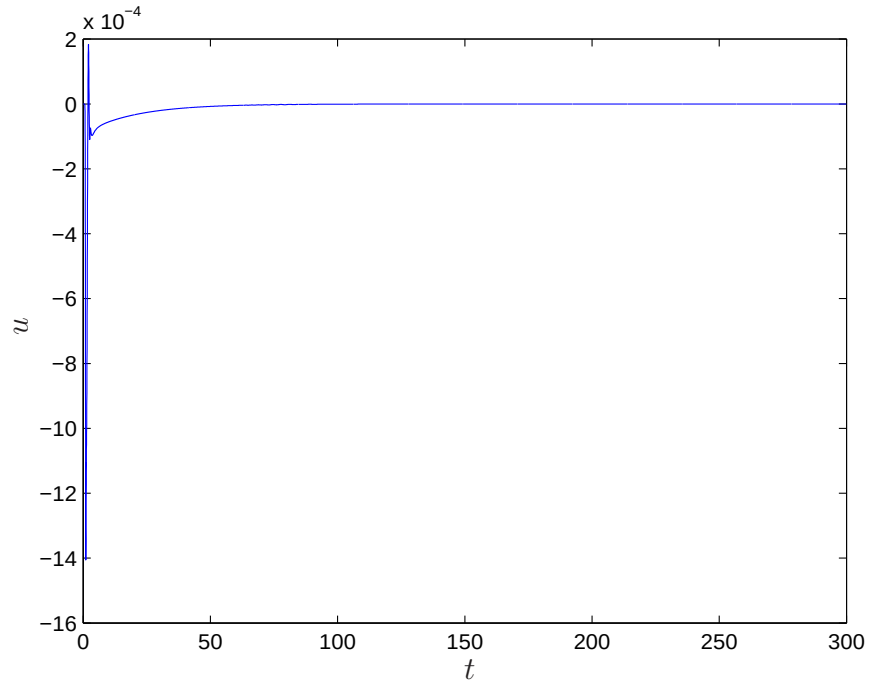

(a) Lower branch

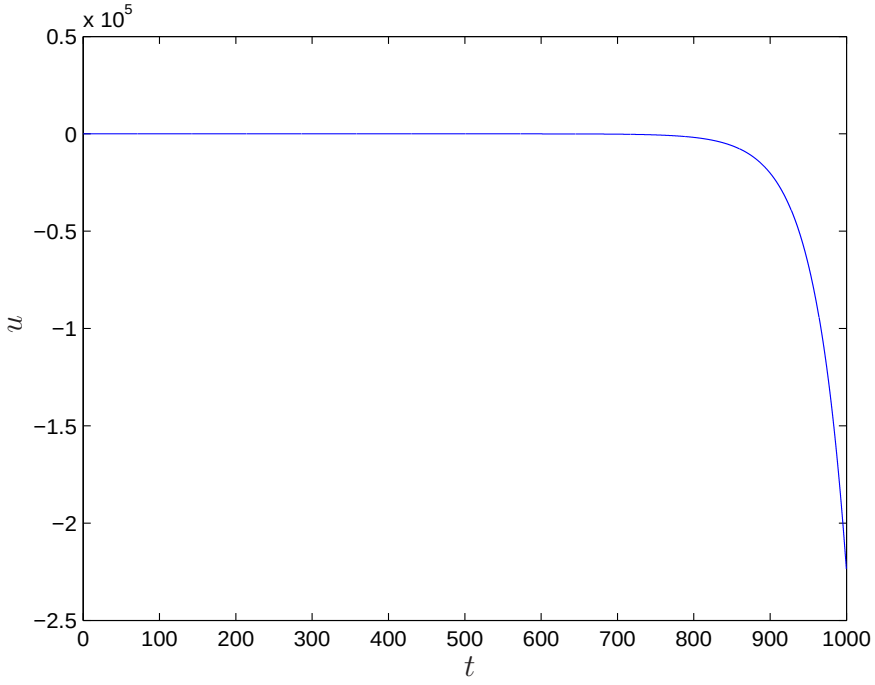

(b) Upper branch

Figure 4.35: Plot showing $u(0.1, 1.4, t)$ evolving with time t for two solutions lower and upper branches at $y_{max} = 0.3$, $Re = 50000$, $\beta = 0.0997$, $N = 100$ and $m = 501$.

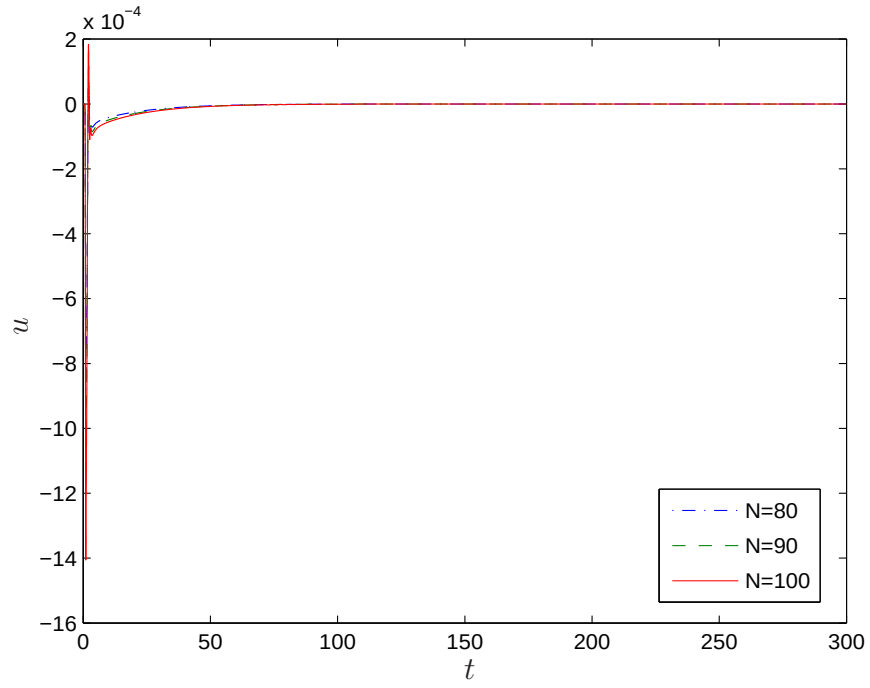

(a) Lower branch

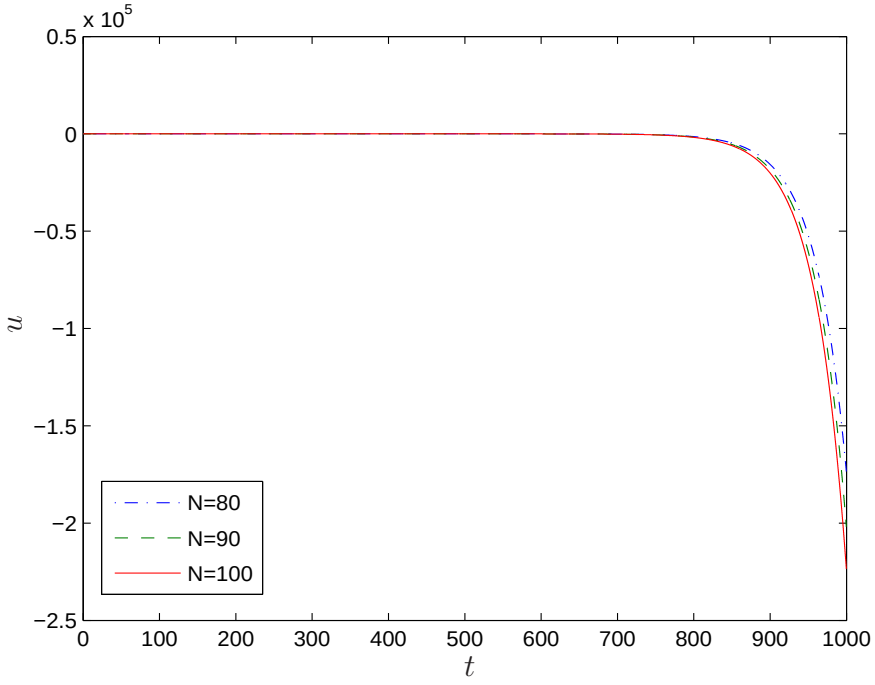

(b) Upper branch

Figure 4.36: Plot showing $u(0.1, 1.4, t)$ evolving with time t for two solutions, lower and upper branches, at different grid sizes for $N = 80, 90, 100$ and $m = 501$, where $y_{max} = 0.3$, $Re = 50000$, $\beta = 0.0997$.

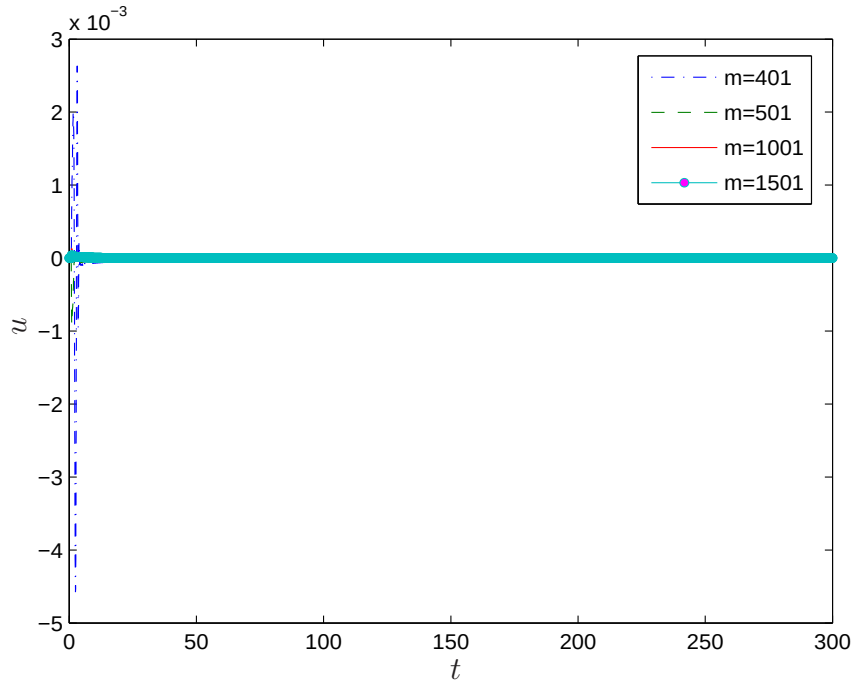

(a) Lower branch

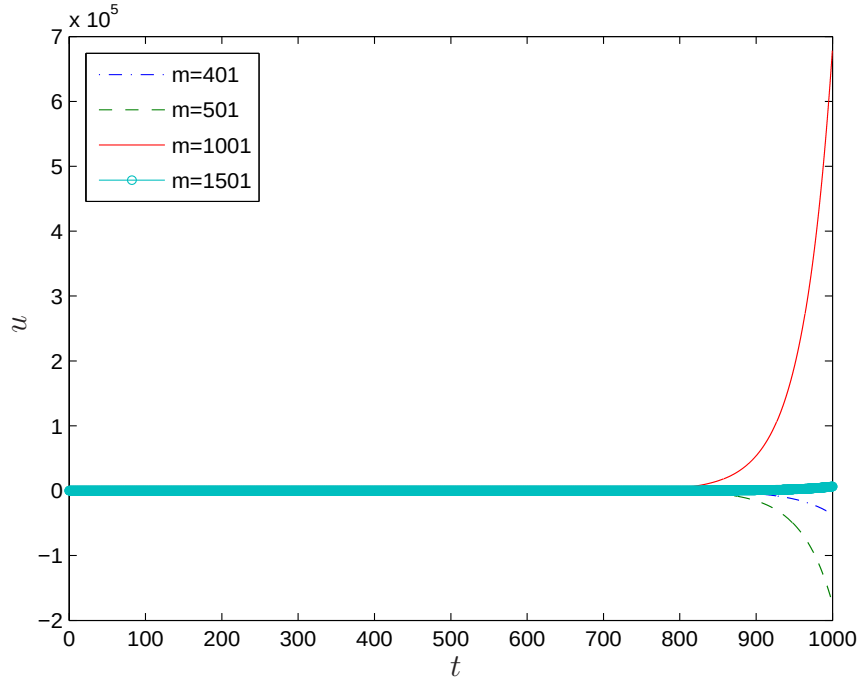

(b) Upper branch

Figure 4.37: Plot showing $u(0.1, 1.4, t)$ evolving with time t for two solutions, lower and upper branches, at different grid sizes for $m = 401, 501, 1001, 1501$ and $N = 100$ where $y_{max} = 0.3$, $Re = 50000$, $\beta = 0.0997$.

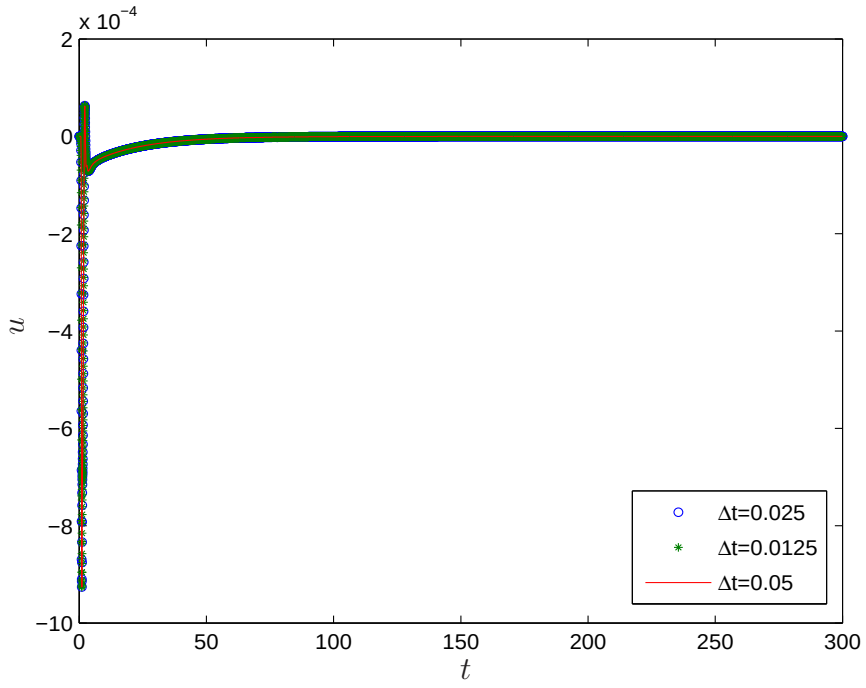

(a) Lower branch

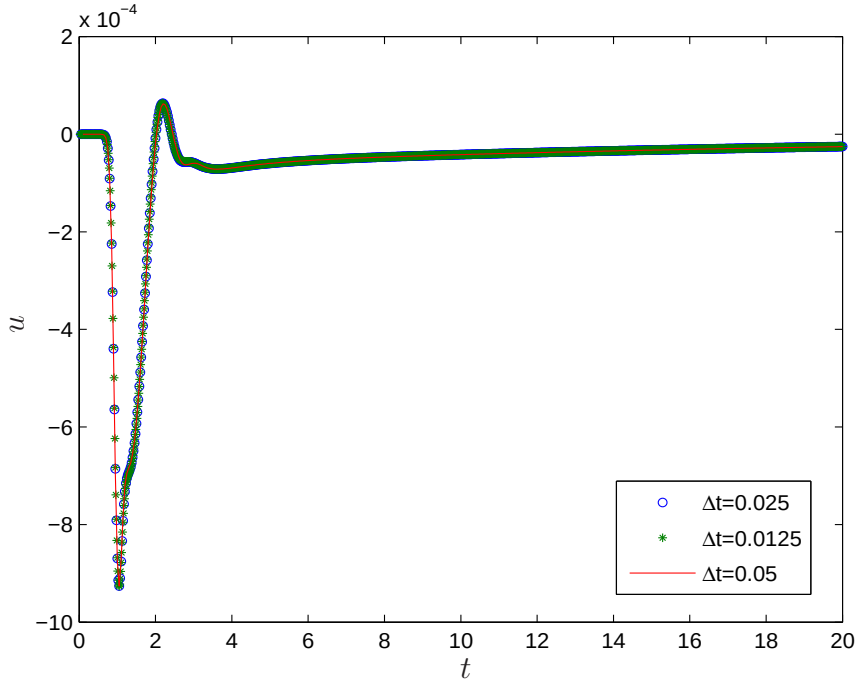

(b) Detailed view of the same signal

Figure 4.38: Plot showing $u(0.1, 1.4, t)$ evolving with time t for lower branch at different time steps $\Delta(t)$, where $y_{max} = 0.3$, $Re = 50000$, $\beta = 0.0997$, $m = 501$ and $N = 80$.

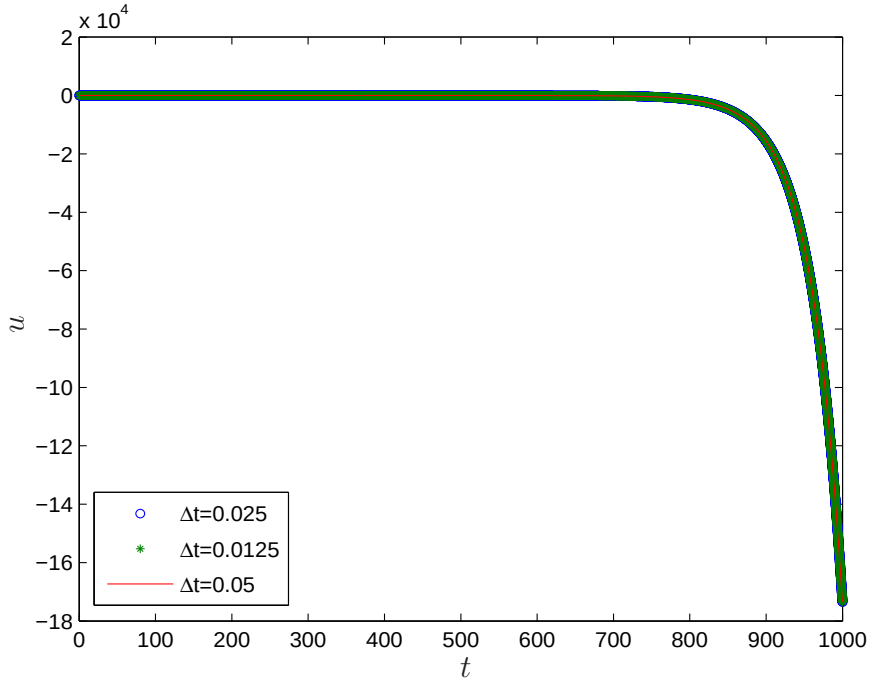

(a) Upper branch

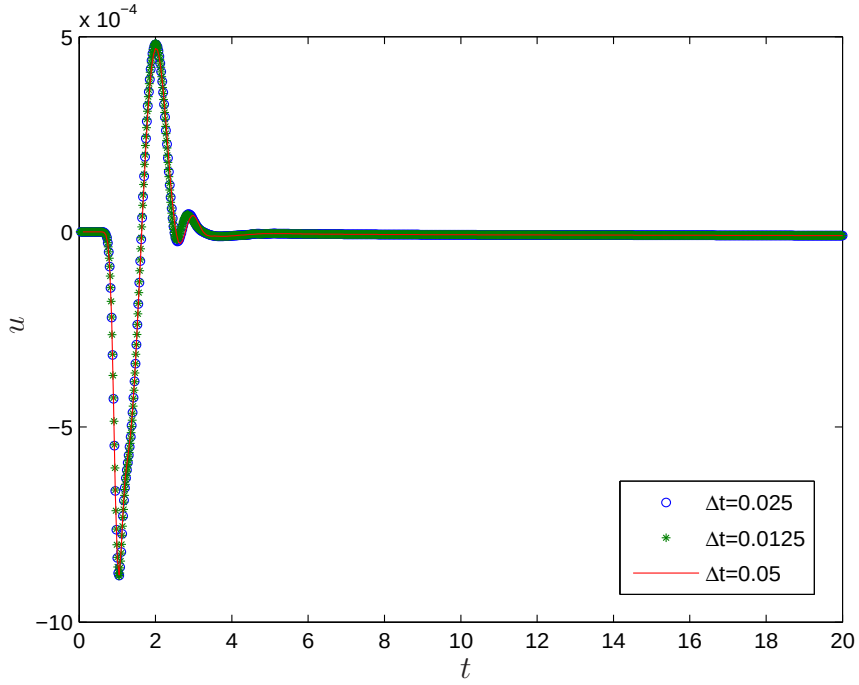

(b) Detailed view of the same signal

Figure 4.39: Plot showing $u(0.1, 1.4, t)$ evolving with time t for the upper branch for different time steps $\Delta(t)$ where $y_{max} = 0.3$, $Re = 50000$, $\beta = 0.0997$, $m = 501$ and $N = 80$.

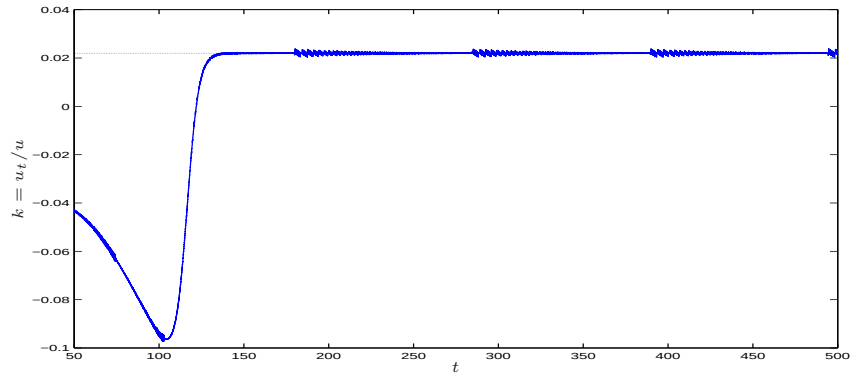

(a) k calculated numerically as compared with the smallest real part of the eigenvalue ($\Re(\lambda_s) \approx -0.021961$) where m=1501

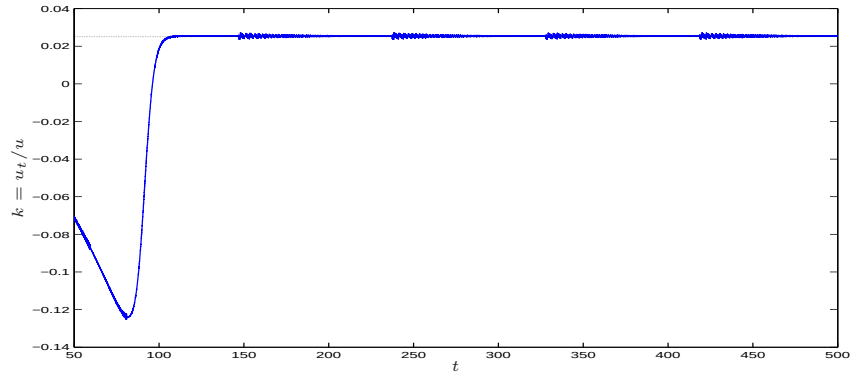

(b) k calculated numerically as compared with the smallest real part of the eigenvalue ($\Re(\lambda_s) \approx -0.025407$) where m=1001

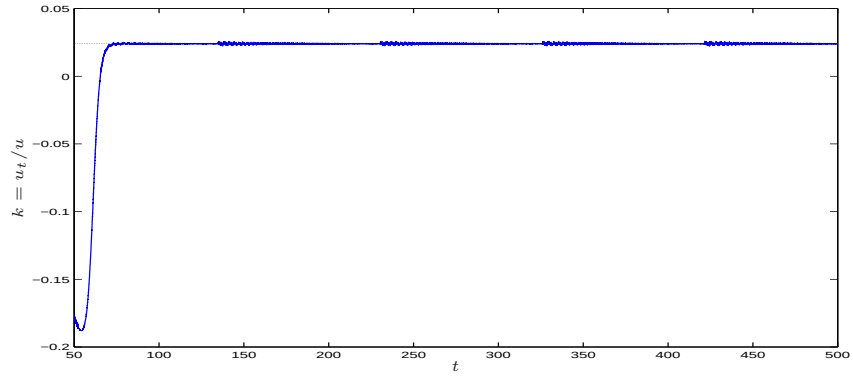

(c) k calculated numerically as compared with the smallest real part of the eigenvalue ($\Re(\lambda_s) \approx -0.024085$) where m=501

Figure 4.40: Plot showing k evolving with time t for the upper branch as compared with the predicted smallest real part of the eigenvalue ($\Re(\lambda_s)$) for different m, where $y_{max} = 0.3$ $Re = 50000$, $\beta = 0.0997$, and $N = 100$. The dashed line shows the smallest real part of the eigenvalue as predicted from the global stability analysis.

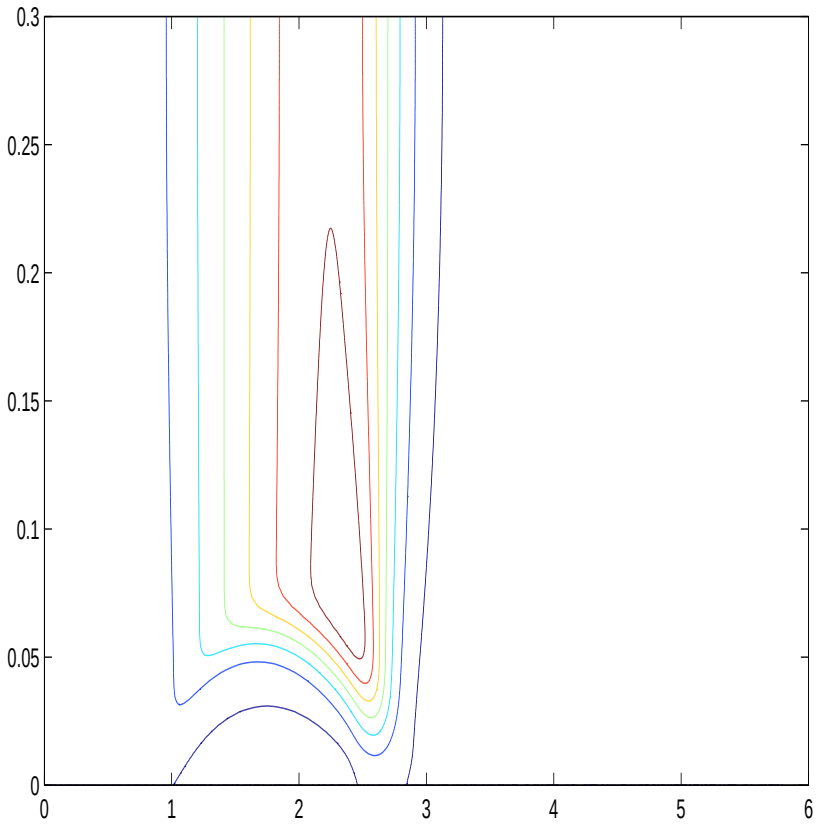

Figure 4.41: Plot showing the perturbations streamfunction with time $t = 199.9$ at $y_{max} = 0.3$, $Re = 50000$, $\beta = 0.0997$, $N = 100$ and $m = 1501$.

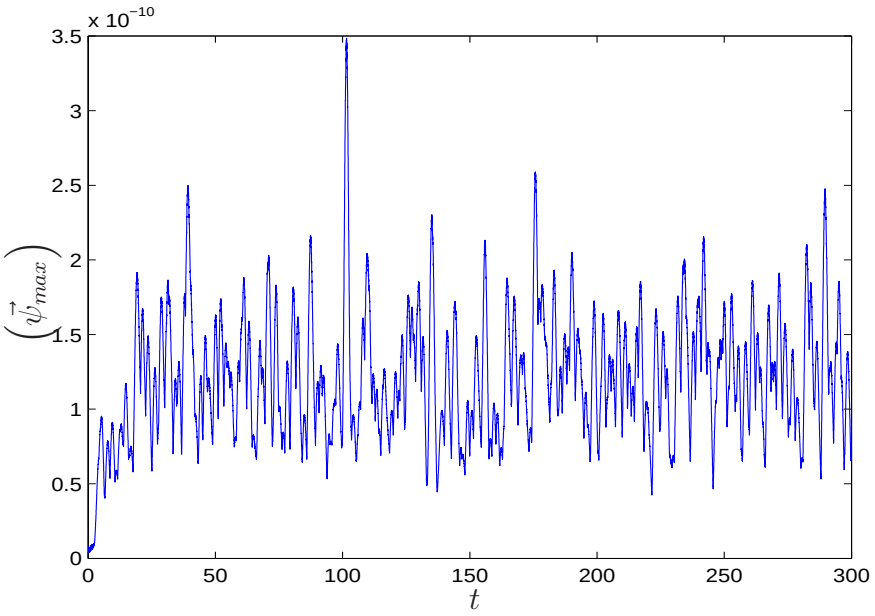

Figure 4.42: Plot showing the perturbations with time t at $y_{max} = 0.3$, $Re = 50000$, $\beta = 0.0997$, $N = 100$ and $m = 501$.

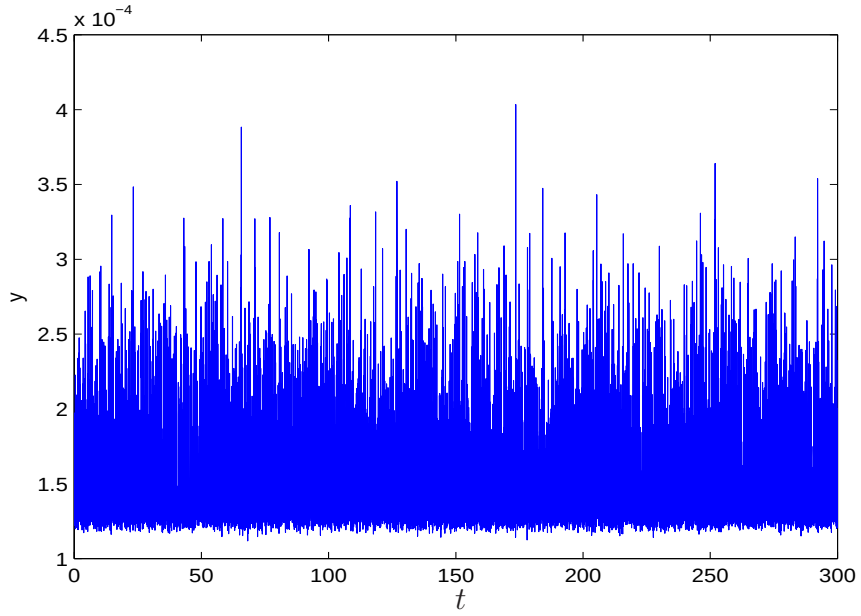

Figure 4.43: Plot showing the perturbations with time t at $y_{max} = 0.3$, $Re = 50000$, $\beta = 0.0997$, $N = 100$ and $m = 501$.

Chapter 5

Different Boundary Conditions in Two-Dimensional Boundary Layer Flow in a Channel with Suction on the Upper Wall

5.1 Introduction

In this chapter we study a two-dimensional boundary layer flow in a channel with a suction on the upper wall, as we have done in the previous chapter, where we have obtained satisfactory results, meaning two solutions on the upper and lower branches respectively, as well as a turning point. Here, we solve the same steady Navier-Stokes equations, but with different boundary conditions, in order to check for changes in the solutions when we introduce slight differences in the boundary conditions, as well as to determine which boundary conditions can be useful for working with this problem. The predominant differences in the boundary conditions we worked with in the previous chapter and those used in

the three cases treated in this chapter, are located on the upper wall.

Here we discuss the study of these various different boundary conditions in the three cases below.

The first boundary condition which is discussed in case 1 shows itself to be only partially useful in our work, as explained later in this chapter.

Case 2 is mainly a discussion of the results we obtained when we worked with a variation in the boundary condition used in case 1. This variation was very slight and located in the upper wall only, but yielded several different results.

The boundary condition described in case 3 is similar to that studied by Alam & Sandham (2000) but it proves to be not suitable for solving our problem for reasons given later in the following section.

Below we show the different boundary conditions of cases 1 to 3 and in the next section we will discuss each case separately.

The boundary conditions for case 1 are as follows:

$$
\begin{array}{lll}
\psi = 0, & \psi_y = 0 & \text{for} \quad y = 0, \\
\psi = \beta\hat{\psi}_s + y_{max}, & \omega = \beta\hat{\omega}_s & \text{for} \quad y = y_{max}, \\
\psi = y, & \omega = 0 & \text{for} \quad x = 0, \\
\psi = \frac{y_{max}}{2}(1-\beta)\left(\frac{y}{y_{max}}\right)^2\left(3-\frac{y}{y_{max}}\right), & \omega = \frac{3}{y_{max}}(1-\beta)\left(1-\frac{y}{y_{max}}\right) & \text{for} \quad x = x_{max}.
\end{array}
$$

Case 2 is the outcome of our work with case 1, all the boundary conditions being identical, except for a small variation in the boundary condition of the upper wall, which is as follows:

$$
\begin{array}{lll}
\psi = 0, & \psi_y = 0 & \text{for} \quad y = 0, \\
\psi = \beta\hat{\psi}_s + y_{max}, & \psi_{yy} = 0 & \text{for} \quad y = y_{max}, \\
\psi = y, & \omega = 0 & \text{for} \quad x = 0, \\
\psi = \frac{y_{max}}{2}(1-\beta)\left(\frac{y}{y_{max}}\right)^2\left(3-\frac{y}{y_{max}}\right), & \omega = \frac{3}{y_{max}}(1-\beta)\left(1-\frac{y}{y_{max}}\right) & \text{for} \quad x = x_{max}.
\end{array}
$$

Finally, the boundary conditions in case 3 which are similar to the study by Alam & Sandham (2000) are completely different from those in case 1 and 2, as seen below:

$$\begin{array}{llllll} \psi = \psi_b & \& & \omega = \omega_b & \text{for} & x = 0, & 0 \le y \le y_{max}, \\ \psi_{xx} = 0 & \& & \omega = \psi_{yy} & \text{for} & x = x_{max}\ , & 0 \le y \le y_{max}, \\ \psi = 0 & \& & \psi_y = 0 & \text{for} & y = 0, & 0 \le x \le x_{max}, \\ \psi_y = 1 & \& & \psi = y - S(x) & \text{for} & y = y_{max}, & 0 \le x \le x_{max}. \end{array}$$

In the following sections we will show the results of the calculations of the channel flow for these three cases, using the same problem formulation and numerical method already discussed extensively in chapter 4 and summarized in the section below.

5.2 Problem Formulation and Numerical Solution Procedure

The problem consists of a flow through a channel with a suction port and an adjustable adverse pressure gradient on the upper wall leading to corresponding changes in the separation conditions in the laminar boundary layer on the lower wall.

We have written and solved the governing, non-dimensional, steady-state, 2-D, incompressible Navier-Stokes equations in terms of streamfunction (ψ) and vorticity (ω) formulation as,

$$\psi_y \omega_x - \psi_x \omega_y = \frac{1}{Re} \left(\omega_{xx} + \omega_{yy} \right), \tag{5.1}$$

$$\omega = \left(\psi_{xx} + \psi_{yy} \right). \tag{5.2}$$

The Reynolds number here is given by $Re = \frac{UL}{\nu}$, while L is the characteristic

entrance length, and the inlet velocity is U, with ν being the kinematic viscosity of the fluid.

In the numerical techniques employed here we solved the incompressible Navier-Stokes equation first by transforming, then discretizing the domain, using the Chebychev collocation in the y-direction domain combined with the finite difference method for the first and second derivative on a non-uniform grid in the x-direction. As in chapter 4, we use Newton linearization and correction terms to linearize the equations. We solve the matrix which resulted from the discretization through the combined use of Newton linearization with a direct solver in order to solve the vorticity streamfunction form of the equation.

5.3 Case 1

The boundary conditions for the flow in this case, which are given below, differ from those used in chapter 4 at $y = y_{max}$ and $x = x_{max}$, while the values for y_{max} and b_s are changed as well (see Figure 5.1).

$$\begin{array}{lll}
\psi = 0, & \psi_y = 0 & \text{for} \quad y = 0, \\
\psi = \beta\hat{\psi}_s + y_{max}, & \omega = \beta\hat{\omega}_s & \text{for} \quad y = y_{max}, \\
\psi = y, & \omega = 0 & \text{for} \quad x = 0, \\
\psi = \frac{y_{max}}{2}(1-\beta)\left(\frac{y}{y_{max}}\right)^2\left(3-\frac{y}{y_{max}}\right), & \omega = \frac{3}{y_{max}}(1-\beta)\left(1-\frac{y}{y_{max}}\right) & \text{for} \quad x \to \infty,
\end{array}$$

where β is the suction ratio (control size),

y_{max} is channel height which equals 0.25,

$\hat{\psi}_s$ is a function defined as

$$\hat{\psi}_s = \frac{1}{2}\left[erf\left(-\sqrt{b_s}\,(x-1)\right)-1\right]y_{max},$$

$\hat{\omega}_s$ is a function defined as

$$\hat{\omega}_s = 2y_{max}\frac{\left(b_s^{\frac{3}{2}}\right)}{\sqrt{\pi}}\left[x-1\right]e^{-b_s[x-1]^2},$$

and b_s is the set equal to 500.

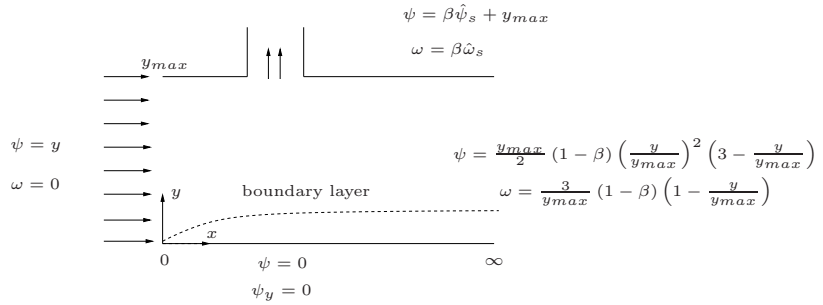

Figure 5.1: Sketch of channel with suction with boundary conditions for case 1.

The equations with the boundary condition have to be solved to obtain ψ and ω. The computational details for the matrices which describe the equations with the above boundary conditions are given in Appendix B.

5.3.1 Case 1: Results and Solutions

The initial condition used here for calculating the Navier-Stokes equations is the Blasius solution. In the present study the effect of an adverse pressure gradient produced by a suction port on the upper wall of a channel leads to the development of a separation bubble on the lower wall.

Results are described for different grid sizes, different values of Re and suction ratios β.

Working with a large, sparse linear system where the number of unknowns is $2(N+1)m$, we observe a good convergence to the steady solution, with the codes of second order finite differences in x-direction and Chebychev collocation in y-direction converging very well. The number of Chebychev points and finite difference points used here is $N = 90$ and $m = 501$, respectively, with $Re = 10000$.

In order to determine that our results are grid independent, computations were made for different values of the total number of points m and N in x-direction and y-direction, respectively.

The first computations with $Re = 10000$ are shown in figures (5.2) and (5.3). In figure (5.2) streamlines are plotted for different values for N and fixed value of m, while in figure (5.3) we have the opposite setup, meaning we have fixed value of N and different values for m. From these figures we can observe that the results are grid independent. We have plotted the velocity profile for different values of N and fixed m in figures (5.4).

The second computations with $Re = 15000$ are seen here in figures (5.5) and (5.6). In figure (5.5) streamline is plotted for different values for m and fixed value of N, but in figure (5.6) we have fixed value of m and use different values for N. The velocity profile plot shown in figure (5.7), also shows that our results are grid independent.

As shown below, in table (5.1) and figure (5.8), after testing many different values of Reynolds numbers Re we found that the critical suction ratio β_s at which separation occurs, decreases as the Reynolds number increases. (see table 5.1). Another visualisation of the same effect is seen in figure (5.9), where we observe that at fixed value of $\beta = 0.219$, but with increasing values of the Reynolds number Re, the separation bubble increases in length.

From our calculations with different values for the suction ratio and Reynolds number we have observed that when the adverse pressure gradient which is the direct result of the suction strength, is weak, the separated region builds up into a steady, closed separation bubble. When we increase suction corresponding to a stronger pressure gradient the separated region lengthens, as seen in figure (5.10) at fixed Reynolds number $Re = 10000$ and fixed grid size $N = 100$, $m = 501$.

Figure (5.11.a) shows the plot of the wall pressure for the whole domain, while

Re	β_s
5000	0.205
7000	0.18
10000	0.165
15000	0.15
20000	0.134
30000	0.125
40000	0.119
50000	0.109
60000	0.107
80000	0.100
100000	0.095

Table 5.1: Comparison of the critical values of β_s, and Re, for $N = 80$, $m = 501$, $a_g = 1$ and $b_s = 500$ in (case 1).

figure (5.11.b) shows the wall pressure plot for the partial domain. It is evident that after the initial event the pressure decreases in the x-direction, whereas, in chapter 4 we observed that the pressure, after initial developments related to the separation bubble, becomes constant. This difference in the wall pressure solutions is the result of a slight difference between the boundary conditions in the two cases.

Our computations for the basic flow in this case gave us good results which allow us to further investigate the stability of the separated flow. But results here allowed for only one solution, while we obtained two solutions and the turning point bifurcation in chapter 4, due to the slight difference in boundary conditions from chapter 4, which we introduced here.

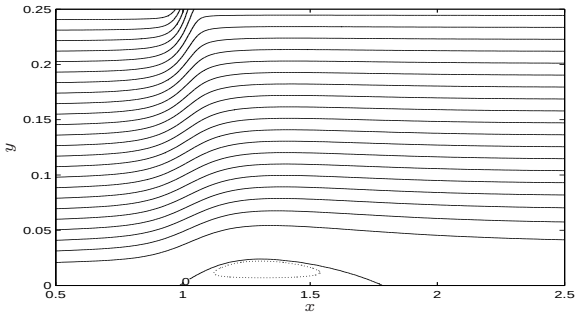

(a) N=80, m=501

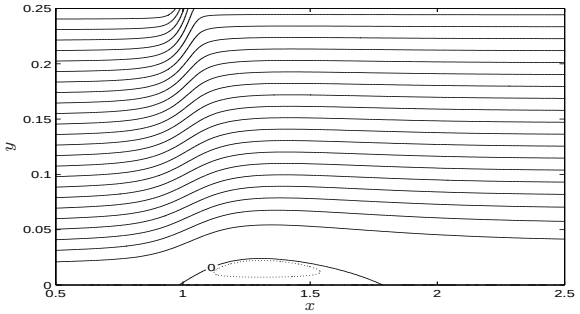

(b) N=90, m=501

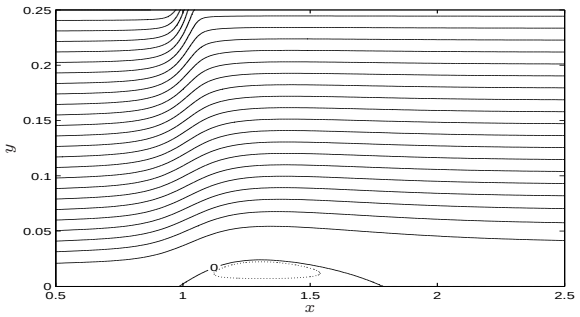

(c) N=100, m=501

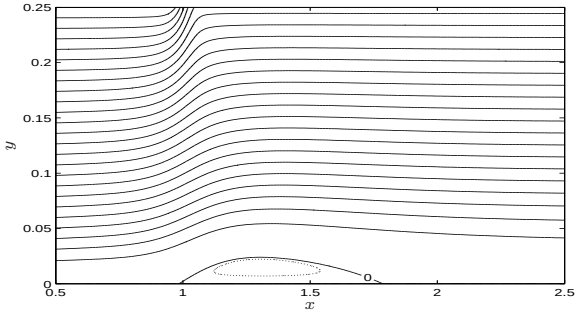

(d) N=110, m=501

Figure 5.2: Streamline contour plots (case 1) for $R = 10000$, $\beta = 0.219$, $a_g = 1$, $b_s = 500$ and different grid sizes for $N = 80, 90, 100, 110$ and $m = 501$. Solid line(-) for streamline level and dashed line(...) for separation bubble. Here contour levels are in intervals of (0.01).

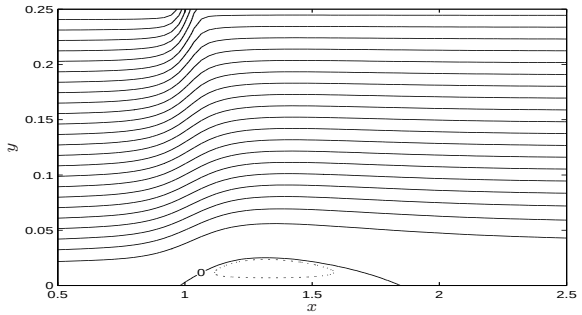

(a) N=80, m=201

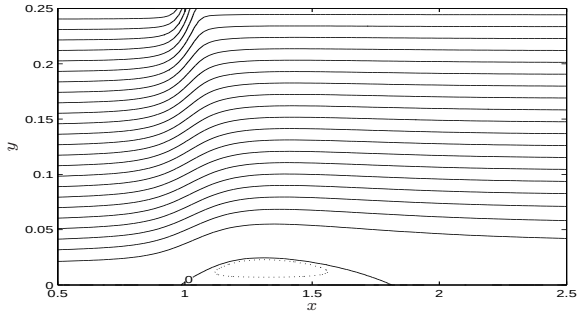

(b) N=80, m=301

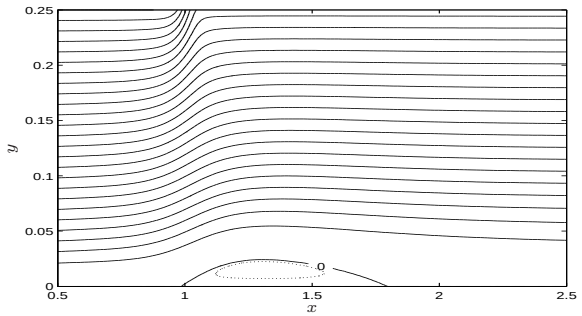

(c) N=80, m=401

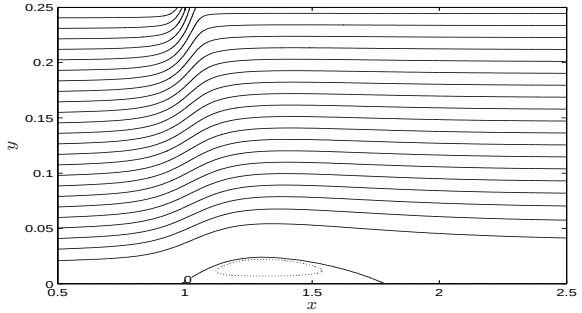

(d) N=80, m=501

Figure 5.3: Streamline contour plots (case 1) for $R = 10000$, $\beta = 0.219$, $a_g = 1$, $b_s = 500$ and different grid sizes for $m = 201, 301, 401, 501$ and $N = 80$. Solid line(-) for streamline level and dashed line(...) for separation bubble. Here contour levels are in intervals of (0.01).

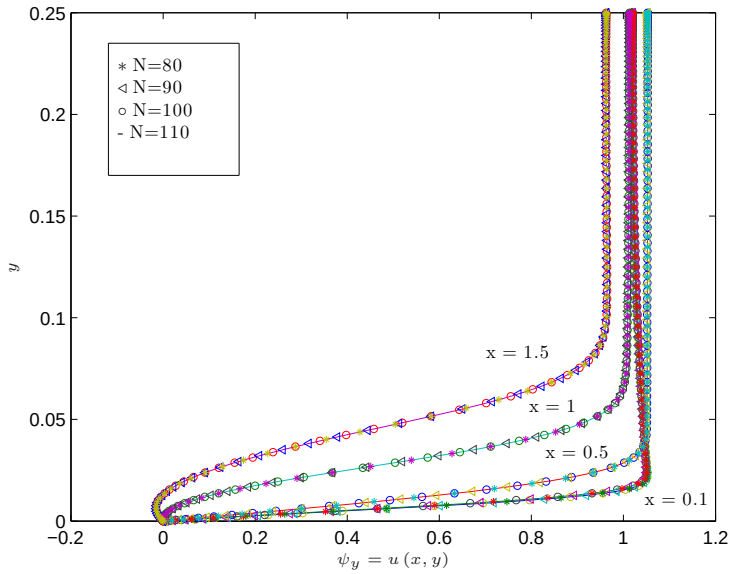

Figure 5.4: Plot showing velocity profile (case 1) at $R = 10000$, $\beta = 0.219$, $a_g = 1$, $b_s = 500$ and different grid sizes for $N = 80, 90, 100, 110$ and $m = 501$.

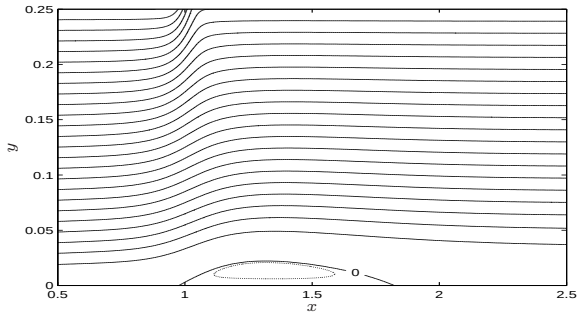

(a) N=100, m=801

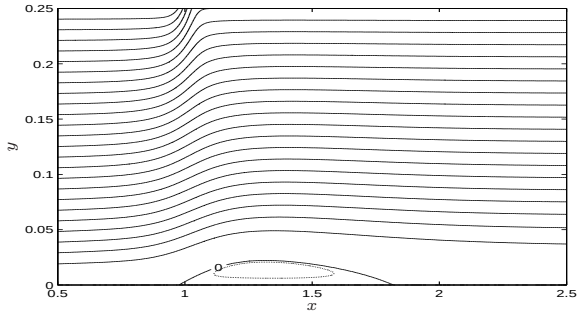

(b) N=100, m=901

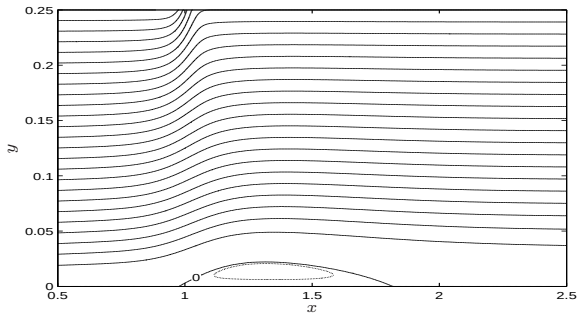

(c) N=100, m=1001

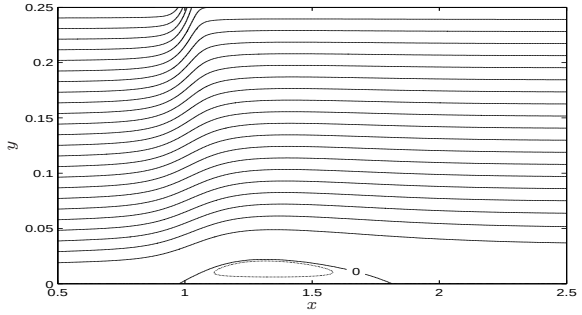

(d) N=100, m=1101

Figure 5.5: Streamline contour plots (case 1) for $R = 15000$, $\beta = 0.2$, $a_g = 1$, $b_s = 500$ and different grid sizes for $m = 801, 901, 1001, 1101$ and $N = 100$. Solid line(-) for streamline level and dashed line(...) for separation bubble. Here contour levels are in intervals of (0.01).

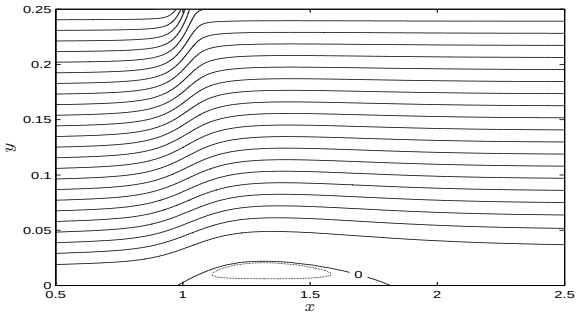

(a) N=80, m=1001

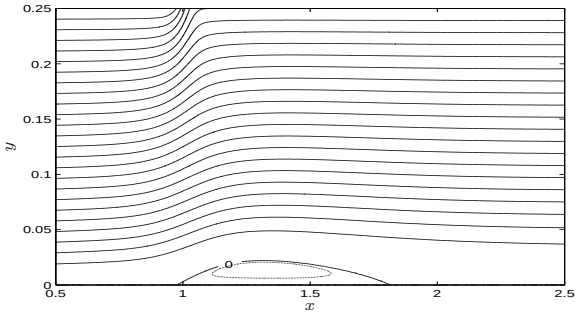

(b) N=90, m=1001

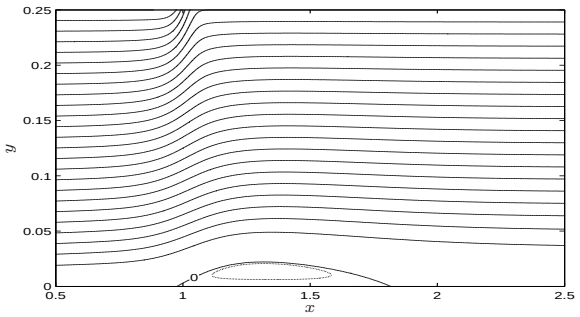

(c) N=100, m=1001

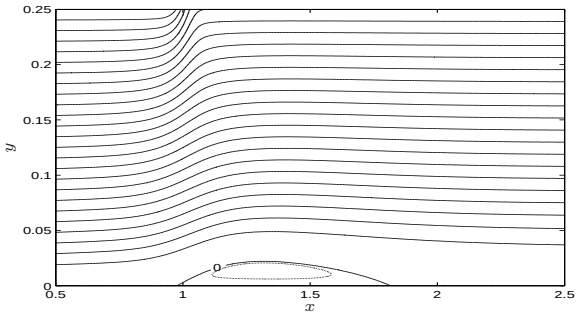

(d) N=110, m=1001

Figure 5.6: Streamline contour plots (case 1) for $R = 15000$, $\beta = 0.2$, $a_g = 1$, $b_s = 500$ and different grid sizes for $N = 80, 90, 100, 110$ and $m = 1001$. Solid line(-) for streamline level and dashed line(...) for separation bubble. Here contour levels are in intervals of (0.01).

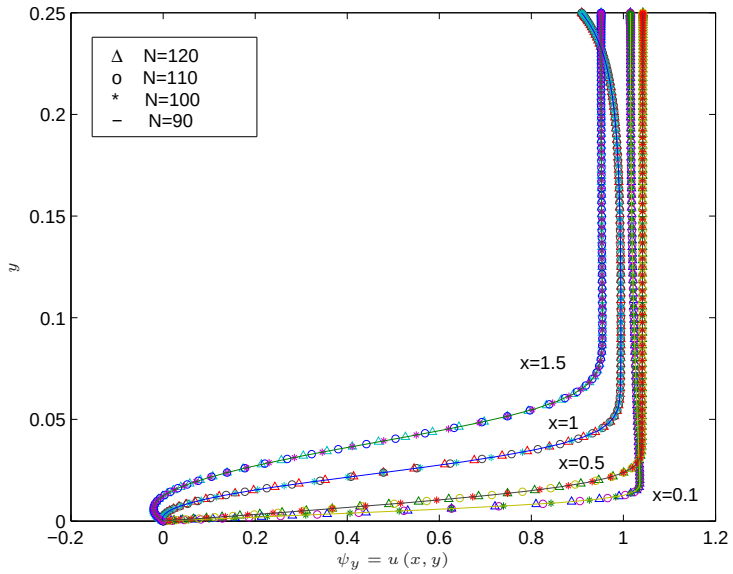

Figure 5.7: Plot showing velocity profile (case 1) at $R = 15000$, $\beta = 0.2$, $a_g = 1$, $b_s = 500$ and different grid sizes for $N = 90, 100, 110, 120$ and $m = 1001$.

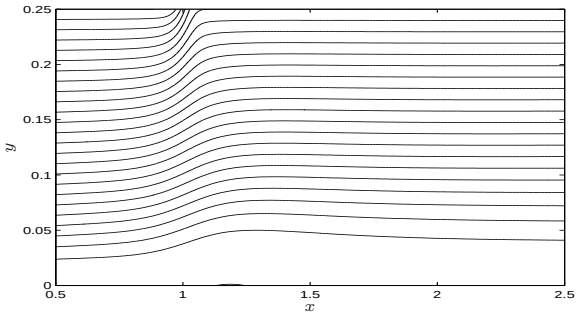

(a) $Re = 5000$, $\beta = 0.2$

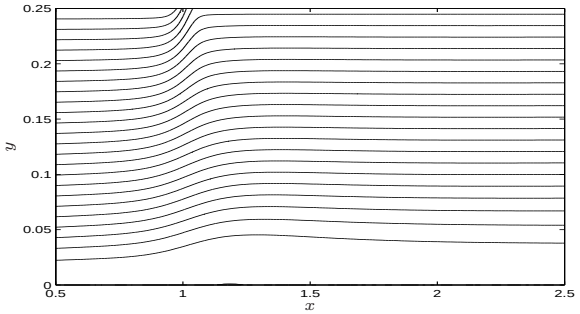

(b) $Re = 7000$, $\beta = 0.18$

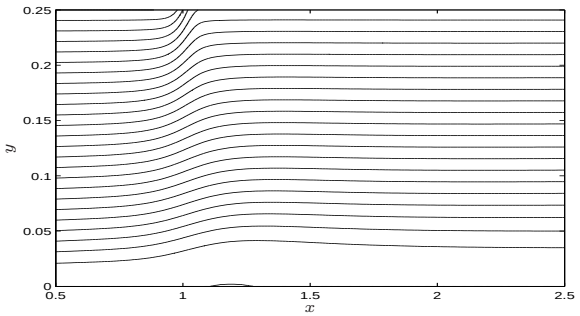

(c) $Re = 10000$, $\beta = 0.165$

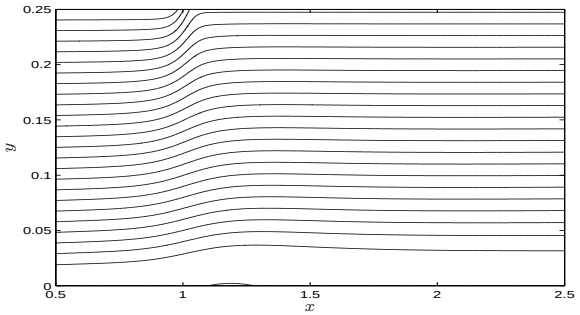

(d) $Re = 15000$, $\beta = 0.15$

Figure 5.8: Streamline contour plots (case 1) for $N = 80$, $m = 501$, $a_g = 1$, $b_s = 500$, different Reynolds numbers $Re = 5000, 7000, 10000, 15000$ and the various critical suction ratios β_s. Solid line(-) for streamline level and dashed line(...) for separation bubble. Here contour levels are in intervals of (0.01).

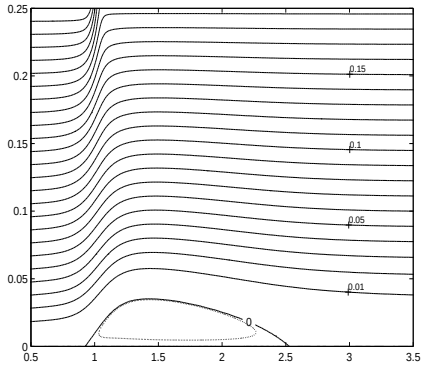

(a) $Re = 20000$

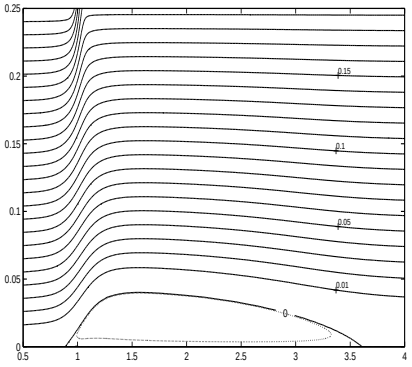

(b) $Re = 40000$

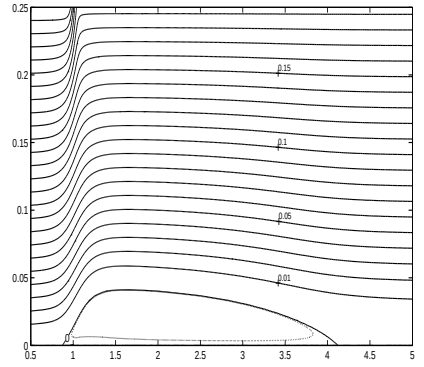

(c) $Re = 50000$

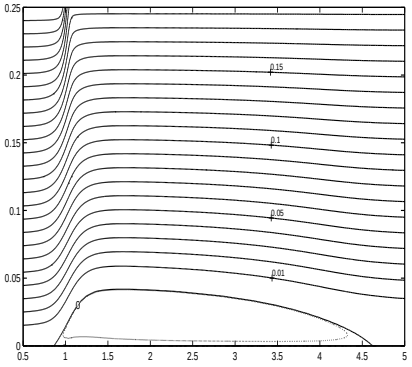

(d) $Re = 60000$

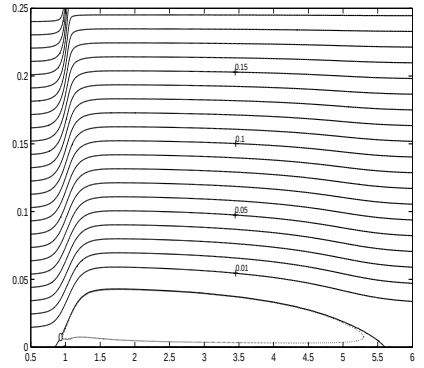

(e) $Re = 80000$

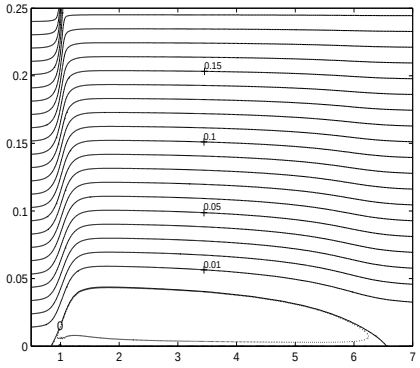

(f) $Re = 100000$

Figure 5.9: Streamline contour plots (case 1) for $N = 80$, $m = 501$, $\beta = 0.219$, $a_g = 1$, $b_s = 500$ and different values of Re. Solid line(-) for streamline level and dashed line(...) for separation bubble. Here contour levels are in intervals of (0.01).

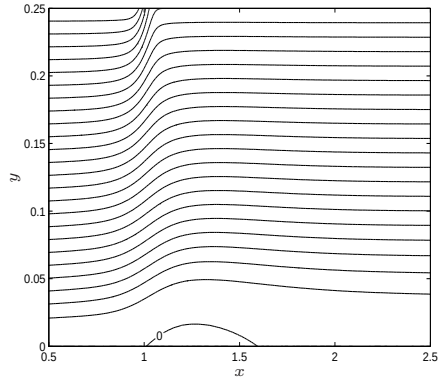

(a) $\beta = 0.2$

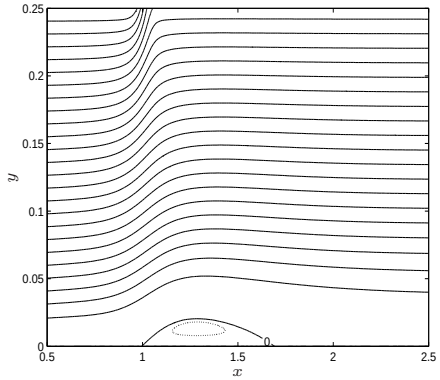

(b) $\beta = 0.21$

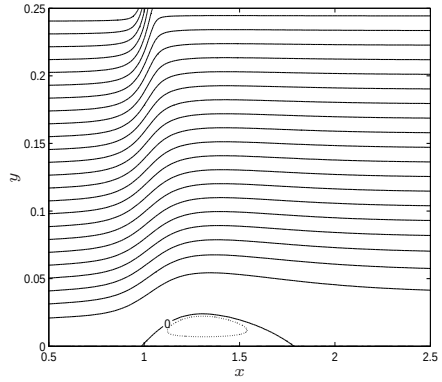

(c) $\beta = 0.219$

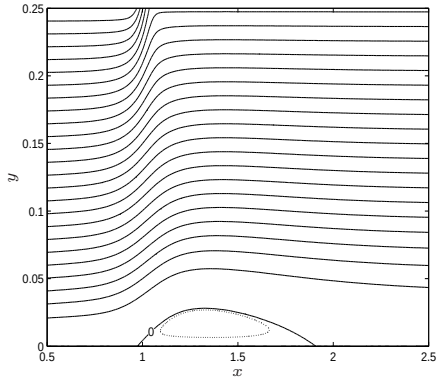

(d) $\beta = 0.23$

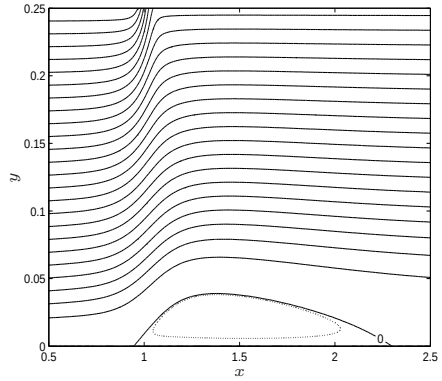

(e) $\beta = 0.26$

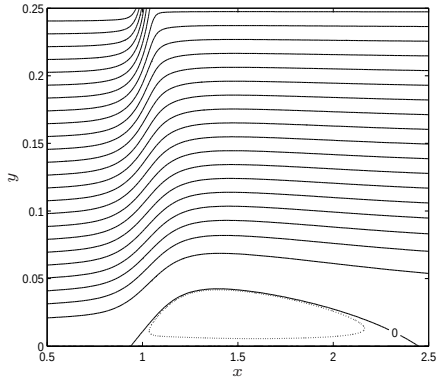

(f) $\beta = 0.27$

Figure 5.10: Streamline contour plots (case 1) for $R = 10000$, $N = 100$, $m = 501$, $a_g = 1$, $b_s = 500$ and different values of β. Solid line(-) for streamline level and dashed line(...) for separation bubble. Here contour levels are in intervals of (0.01).

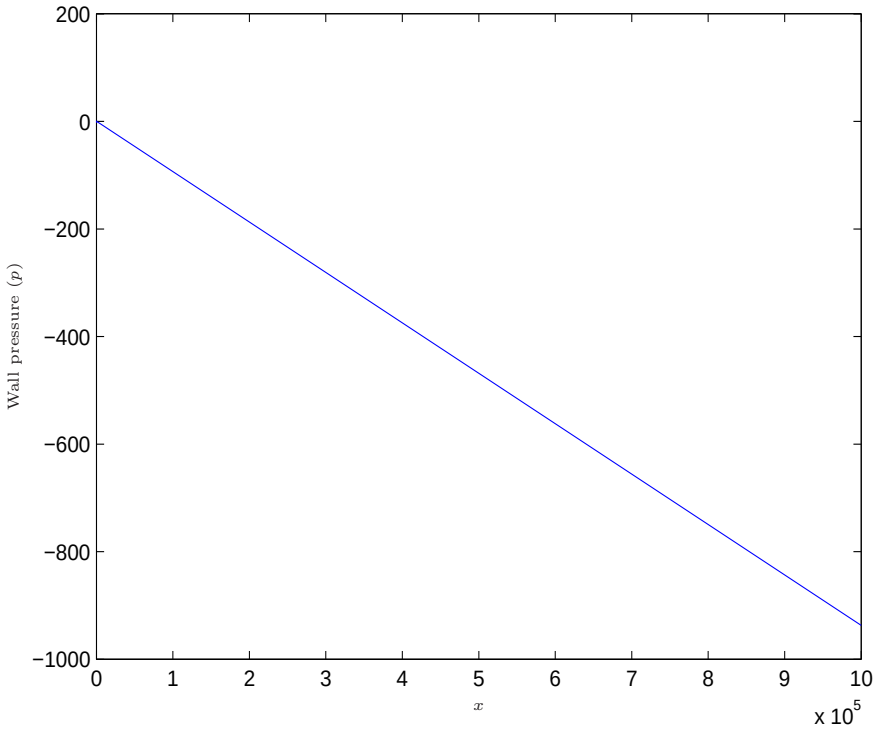

(a) Wall pressure for the whole domain

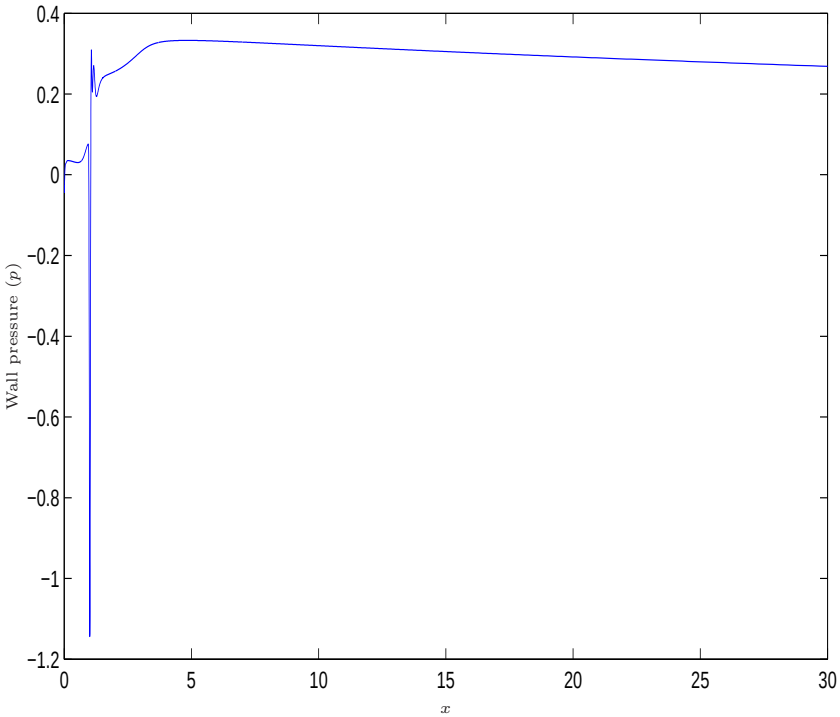

(b) Snapshot of the wall pressure for the partial domain

Figure 5.11: Plot of wall pressure (p) for case 1 where $R = 40000$, $\beta = 0.219$ and grid sizes $N = 80$ and $m = 1501$.

5.4 Case 2

While in the results from case 1 in equation (4.7), we used the value of $a_g = 1$, here in case 2, when we studied the problem with a different boundary condition in the upper wall, by replacing $\omega = \beta\hat{\omega}_s$ with $\psi_{yy} = 0$, where $b_s = 5000$, we also changed the value for a_g from $a_g = 1$ in case 1, to $a_g = 0.1$ in case 2, because we wanted to increase the number of points close to the lower wall over the number of points close to the upper wall. In fact, equation(4.7) shows that a_g influences the distribution of Chebychev points, meaning the value of $a_g = 1$ corresponds to standard Chebychev points, while, when a_g is smaller than this, it means more points in the lower boundary near $y = 0$ than in the upper boundary. Working with these changes we obtained several results which we will discuss further below.

In case 2 we performed many grid checks for different values of m and$N$ to confirm that our results are grid independent, as shown in figures (5.12), where we have a fixed value for m and N is variable, and figure (5.13), where m is variable and N is fixed, with $Re = 10000$. Furthermore, an additional clarification of grid independence is furnished by the velocity profile plot for different values of N and fixed m, as shown in figure (5.14). In figure (5.13), for instance, we can see the appearance of a minute bubble situated at $x = 1$ which is closely followed by the much larger main bubble.

We tested many different values of Reynolds number Re in case 2 and we obtained the same results as in case 1, namely that when we increase the value of the Reynolds number the critical suction ratio β_s decreases. See figure (5.15) and table (5.2).

We worked with different values for suction strength at fixed Reynolds number $Re = 10000$ with grid size $N = 100$ and $m = 501$ and we observed that as we increase the adverse pressure gradient the separation bubble lengthens in direct

Re	β_s
5000	0.2
7000	0.18
10000	0.165
15000	0.15

Table 5.2: Comparison of the critical values of β_s, and Re (case 2), for $N = 80$, $m = 501$, $a_g = 0.1$ and $b_s = 5000$.

proportion to the strength of the suction, confirming our results in case 1. This is illustrated clearly in figures (5.16) where $a_g = 0.1$ and $b_s = 5000$.

As an additional check from equation (5.2),

$$\omega = (\psi_{xx} + \psi_{yy}), \tag{5.3}$$

and with our boundary condition on $y = 0$, $\psi = 0$ substituted into the above we arrive at,

$$\omega = \psi_{yy}, \qquad on \qquad y = 0. \tag{5.4}$$

That means we should get the same plot for ω and ψ_{yy}, but in this present study we arrived at below that there was a large difference in computed values of ω and ψ_{yy}. This led us to test the values of the parameters a_g and b_s as well as the different boundary conditions in the upper wall in cases 1 and 2 to find out where this problem originates. In the following paragraphs we give a detailed description of these tests as well as a comparison of the results.

Figures (5.17) and (5.18) show us the comparison between ω and ψ_{yy} for cases 2 and 1 with different grid sizes, when $Re = 10000$ and $\beta = 0.219$. Figures (5.19) and (5.20) show the comparison of the range of errors between ω and ψ_{yy} in cases 2 and 1, when we subtract ω from ψ_{yy}, with different grid sizes, and the same Re and β. From these figures we observed that in case 1, when we increase the

number of points in the y-direction, the range of error decreases (figure 5.20), whereas in case 2, with the same increase in points in the y-direction, the range of error increases (figure 5.19). This happens because the value of a_g in case 1 is $a_g = 1$, but the value of a_g in case 2 is $a_g = 0.1$.

In addition, figures (5.21) and (5.22) illustrate the result of our work in both cases, 1 and 2, where $\beta = 0.2$, when we exchanged the values of the parameter $a_g = 0.1$ for $a_g = 1$ and vice versa, with fixed b_s and the boundary conditions in the upper wall. We obtain that the range of error between ω and ψ_{yy} increases when we change the value of a_g from $a_g = 1$ to $a_g = 0.1$.

Figures (5.23) and (5.24) show the result of testing two different values of b_s, 5000 and 500 for both cases, 1 and 2, with fixed values for parameter a_g and the boundary condition in the upper wall. We observe from these results that when we change the value of b_s the resulting range of error is not very significant. For the most suitable results it is preferable to work with the value $b_s = 500$ rather than $b_s = 5000$.

While the boundary conditions in the upper wall are different, the figures (5.25) which illustrate the comparison between ψ_{yy} and ω and figure (5.26) which shows streamline plotting, clearly demonstrate agreement between cases 1 and 2 when we fixed the parameter $a_g = 1$ and $b_s = 500$, with $R = 10000$, $\beta = 0.2$ and grid sizes $N = 90$ and $m = 501$.

In figures (5.27) we show that the range of error, when we fix the parameter $a_g = 1$ and $b_s = 500$ with $R = 10000$, $\beta = 0.2$ and grid sizes $N = 90$ and $m = 501$, is smaller in case 1 than in case 2.

Finally, we have established that the source of the error is to do with the value of the parameter a_g. When we change a_g it means more points on the lower wall which leads to less resolution at the upper wall, whereas our results show that we also need resolution at the upper wall near the suction slot. Likewise,

the boundary condition in the upper wall $\omega = \beta\hat{\omega}_s$ in case 1, has been proven to be more suitable for our problem than $\psi_{yy} = 0$ in case 2, because the range of error between ψ_{yy} and ω for case 1 is less than that in case 2. While we worked with the boundary conditions in chapter 4 we also tested the values of ψ_{yy}, and ω and we observed that the range of error is very small, much smaller than in case 1, see figure (5.28). Figure (5.28. a) shows a comparison between ψ_{yy} and ω, while figure (5.28. b) shows the range of error.

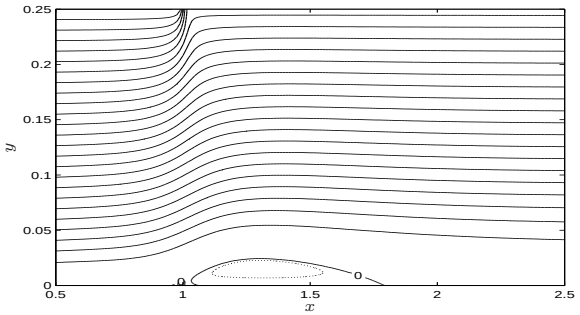

(a) N=80, m=501

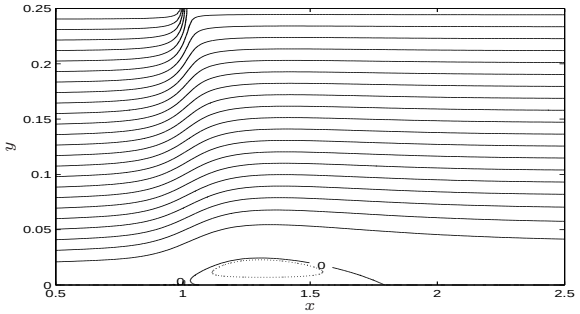

(b) N=90, m=501

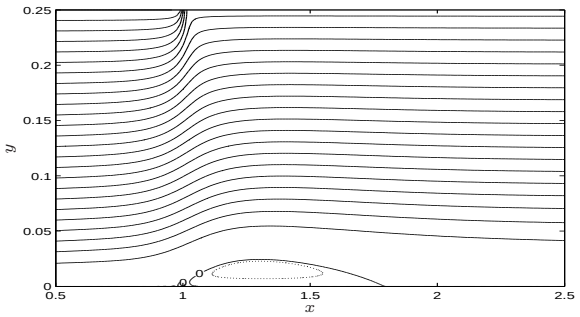

(c) N=100, m=501

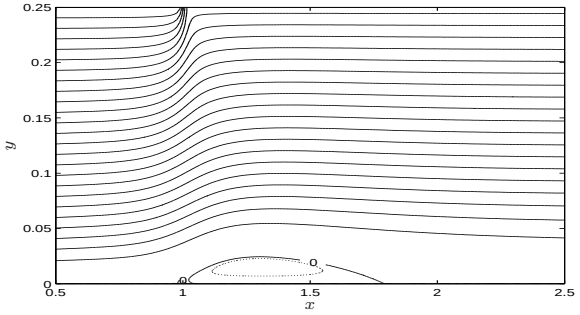

(d) N=110, m=501

Figure 5.12: Streamline contour plots (case 2) for $R = 10000$, $\beta = 0.219$, $a_g = 0.1$, $b_s = 5000$ and different grid sizes for $N = 80, 90, 100, 110$ and $m = 501$. Solid line(-) for streamline level and dashed line(...) for separation bubble. Here contour levels are in intervals of (0.01).

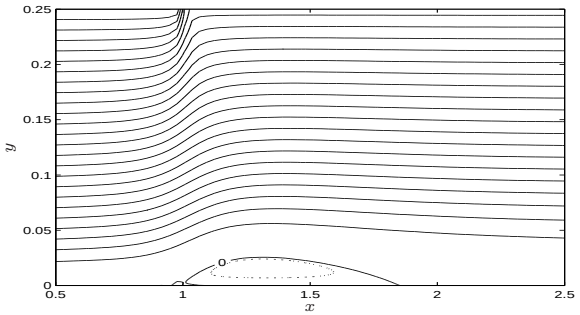

(a) N=80, m=201

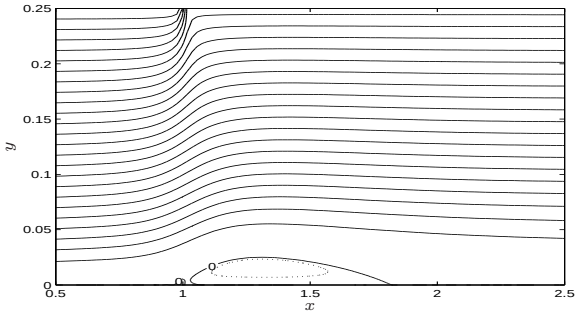

(b) N=80, m=301

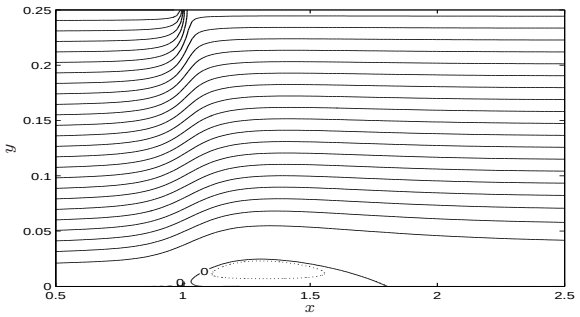

(c) N=80, m=401

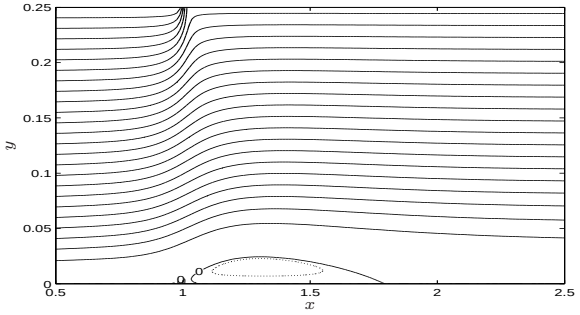

(d) N=80, m=501

Figure 5.13: Streamline contour plots (case 2) for $R = 10000$, $\beta = 0.219$, $a_g = 0.1$, $b_s = 5000$ and different grid sizes for $m = 201, 301, 401, 501$ and $N = 80$. Solid line(-) for streamline level and dashed line(...) for separation bubble. Here contour levels are in intervals of (0.01).

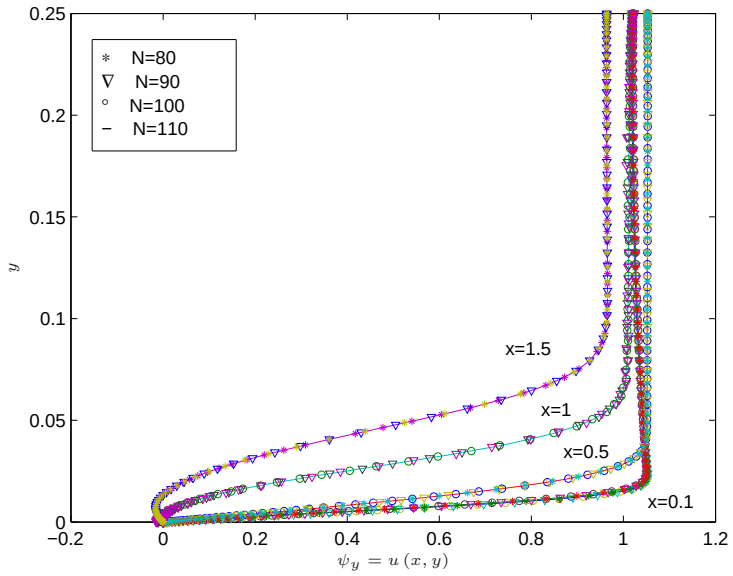

Figure 5.14: Plot showing velocity profile (case 2) at $R = 10000$, $\beta = 0.219$, $a_g = 0.1$, $b_s = 5000$ and different grid sizes for N and $m = 501$

.

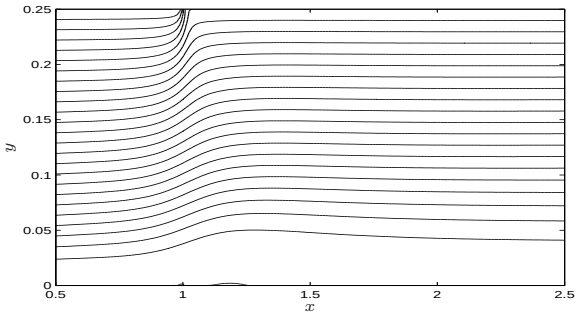

(a) $Re = 5000$, $\beta_s = 0.2$

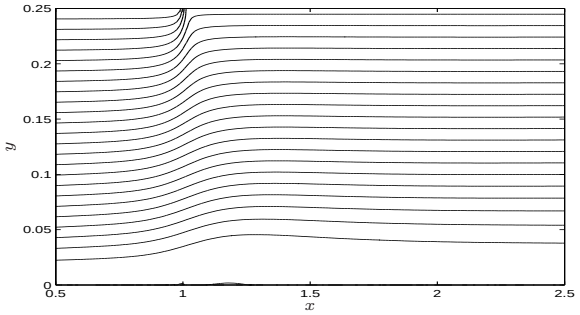

(b) $Re = 7000$, $\beta_s = 0.18$

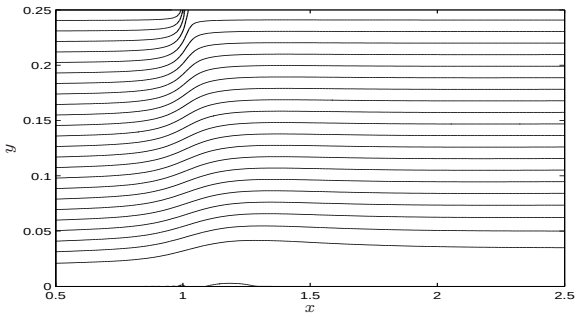

(c) $Re = 10000$, $\beta_s = 0.165$

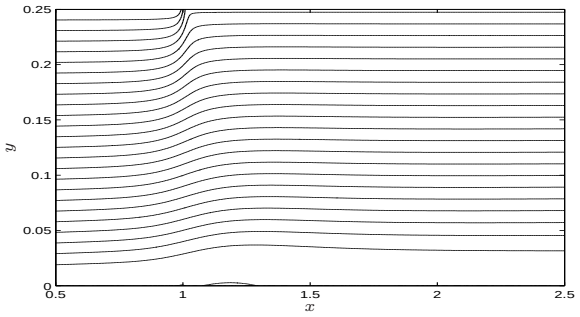

(d) $Re = 15000$, $\beta_s = 0.15$

Figure 5.15: Streamline contour plots (case 2) for $N = 80$, $m = 501$, $a_g = 0.1$, $b_s = 5000$, different Reynolds numbers $Re = 5000, 7000, 10000, 15000$, and the various critical suction ratios β_s. Solid line(-) for streamline level and dashed line(...) for separation bubble. Here contour levels are in intervals of (0.01).

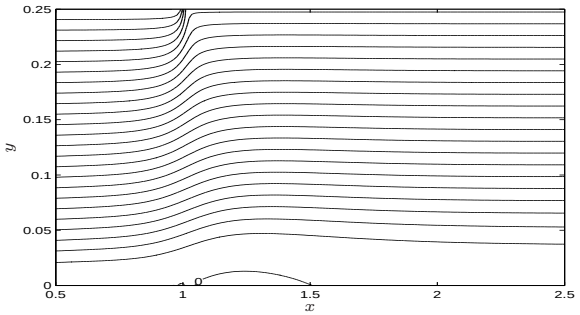

(a) $\beta = 0.19$

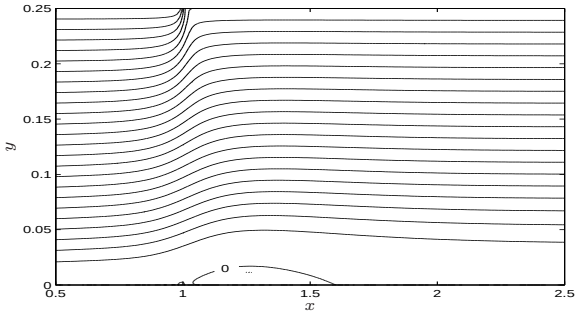

(b) $\beta = 0.2$

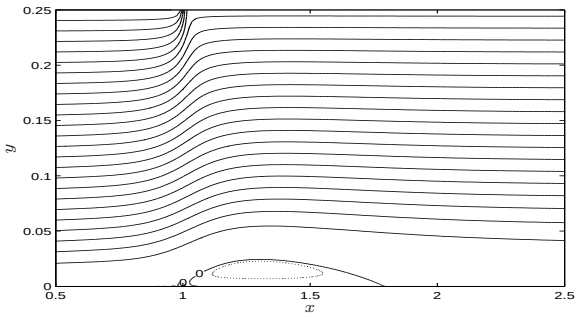

(c) $\beta = 0.219$

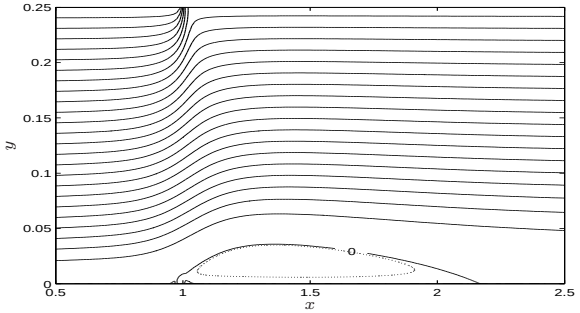

(d) $\beta = 0.25$

Figure 5.16: Streamline contour plots (case 2) for $R = 10000$, $N = 100$, $m = 501$, $a_g = 0.1$, $b_s = 5000$ and different values of β. Solid line(-) for streamline level and dashed line(...) for separation bubble. Here contour levels are in intervals of (0.01).

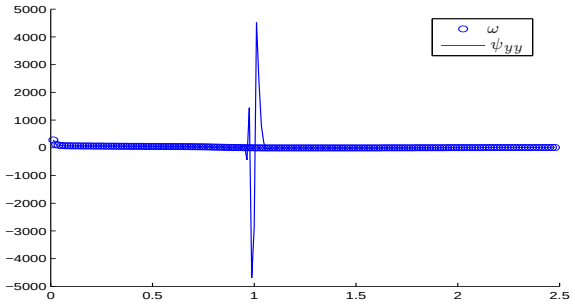

(a) N=110, m=501

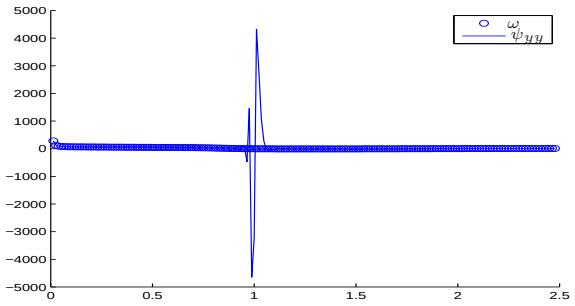

(b) N=100, m=501

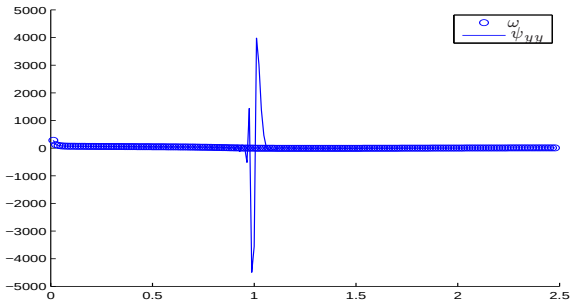

(c) N=90, m=501

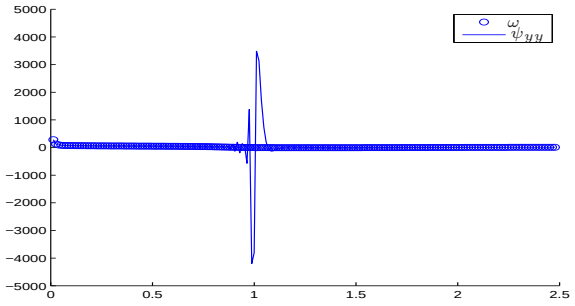

(d) N=80, m=501

Figure 5.17: Comparison of ψ_{yy} and ω for case 2 where $b_s = 5000$, $a_g = 0.1$, $R = 10000$, $\beta = 0.219$, and different grid sizes for $N = 110, 100, 90, 80$ and $m = 501$.

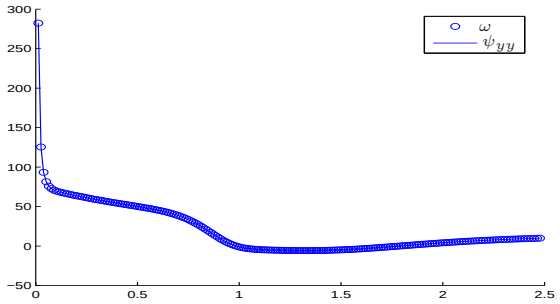

(a) N=110, m=501

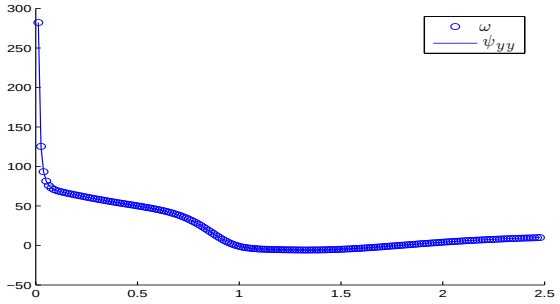

(b) N=100, m=501

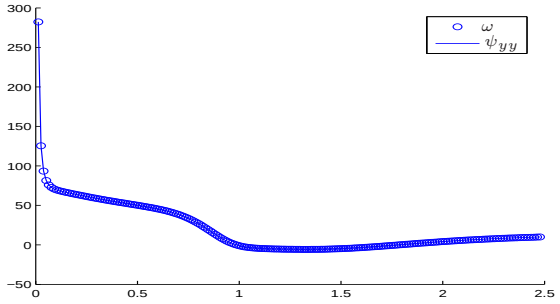

(c) N=90, m=501

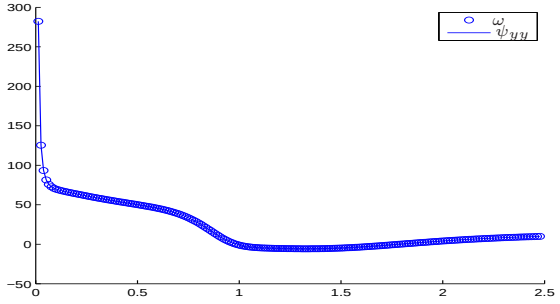

(d) N=80, m=501

Figure 5.18: Comparison of ψ_{yy} and ω for case 1 where $b_s = 500$, $a_g = 1$, $R = 10000$, $\beta = 0.219$ and different grid sizes for $N = 110, 100, 90, 80$ and $m = 501$.

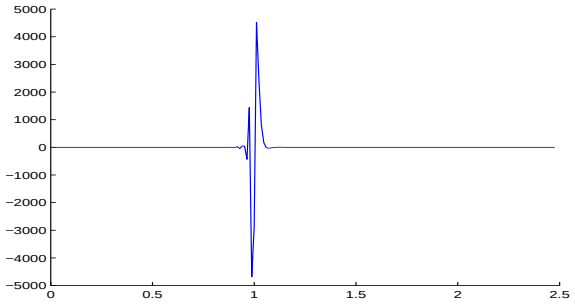

(a) N=110, m=501

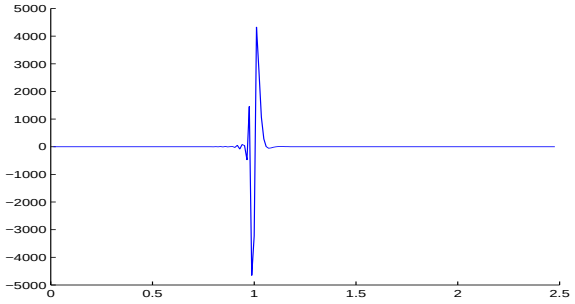

(b) N=100, m=501

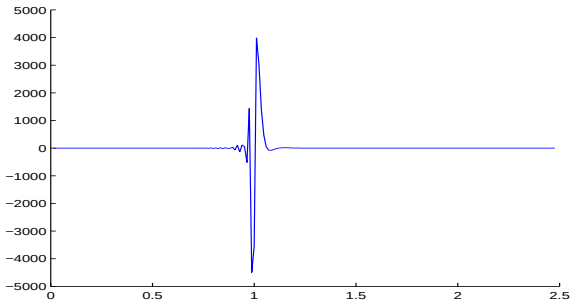

(c) N=90, m=501

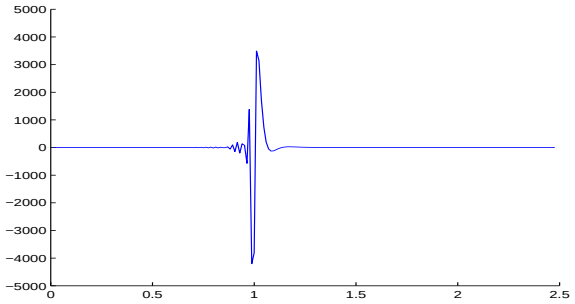

(d) N=80, m=501

Figure 5.19: Comparison of the errors between ψ_{yy} and ω for case 2 where $b_s = 5000$, $a_g = 0.1$, $R = 10000$, $\beta = 0.219$, and different grid sizes for $N = 110, 100, 90, 80$ and $m = 501$.

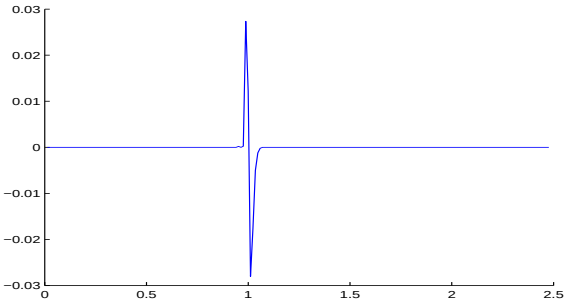

(a) N=110, m=501

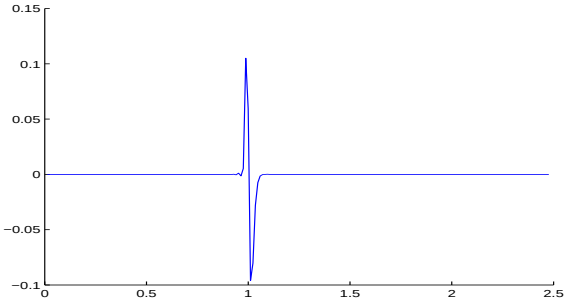

(b) N=100, m=501

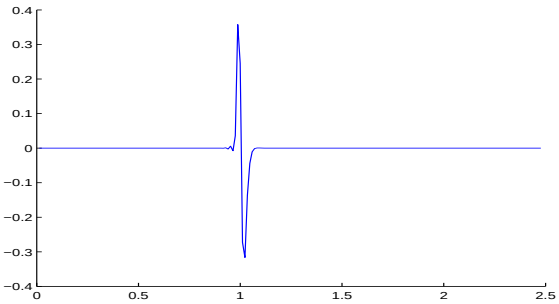

(c) N=90, m=501

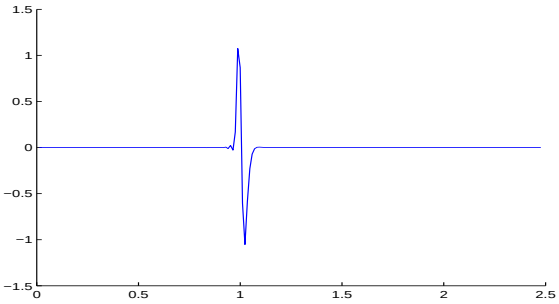

(d) N=80, m=501

Figure 5.20: Comparison of the errors between ψ_{yy} and ω for case 1 where $b_s = 500$, $a_g = 1$, $R = 10000$, $\beta = 0.219$ and different grid sizes for $N = 110, 100, 90, 80$ and $m = 501$.

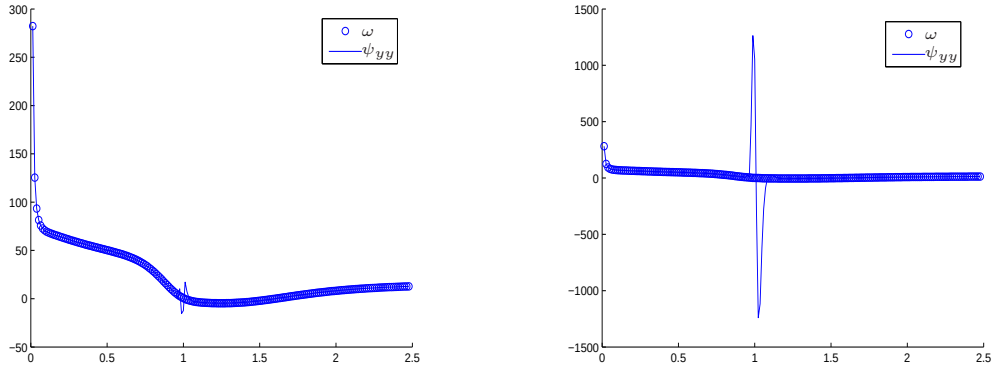

(a) Case 2 where $b_s = 5000$ and $a_g = 1$ (b) Case 1 where $b_s = 500$ and $a_g = 0.1$

Figure 5.21: Comparison of ψ_{yy} and ω for case 1 and case 2 by interchanging the values for parameter $a_g = 0.1$ and $a_g = 1$, where $R = 10000$, $\beta = 0.2$ and grid sizes $N = 90$ and $m = 501$.

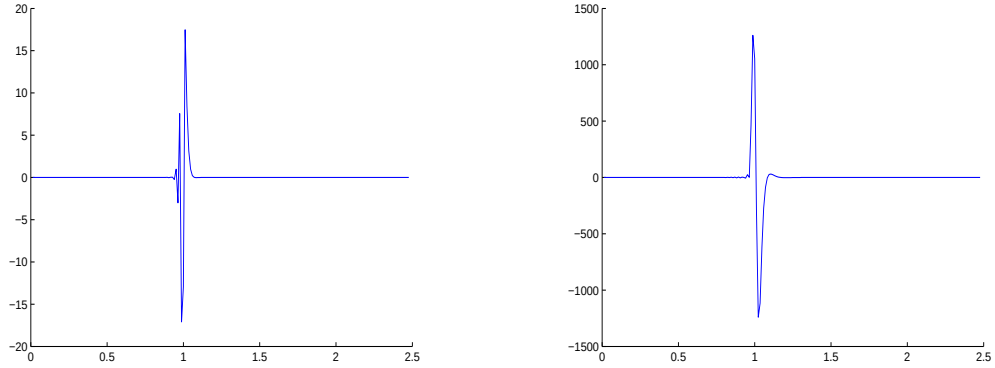

(a) Case 2 where $b_s = 5000$ and $a_g = 1$ (b) Case 1 where $b_s = 500$ and $a_g = 0.1$

Figure 5.22: Comparison of the errors between ψ_{yy} and ω for case 1 and case 2 by interchanging the values for parameter $a_g = 0.1$ and $a_g = 1$, where $R = 10000$, $\beta = 0.2$ and grid sizes $N = 90$ and $m = 501$.

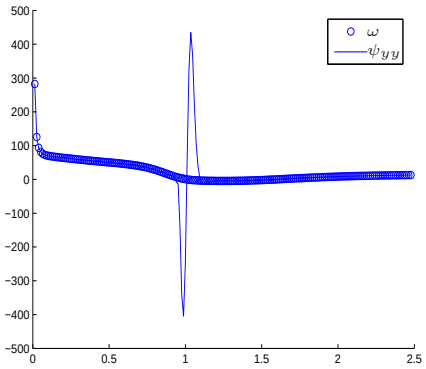

(a) Case 2 where $b_s = 500$ and $a_g = 0.1$

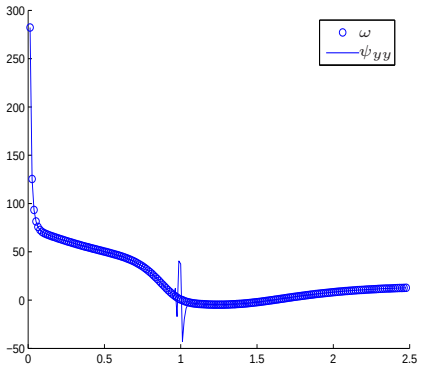

(b) Case 1 where $b_s = 5000$ and $a_g = 1$

Figure 5.23: Comparison of ψ_{yy} and ω for case 1 and case 2 by interchanging the values for $b_s = 5000$ and $b_s = 500$, where $R = 10000$, $\beta = 0.2$ and grid sizes $N = 90$ and $m = 501$

.

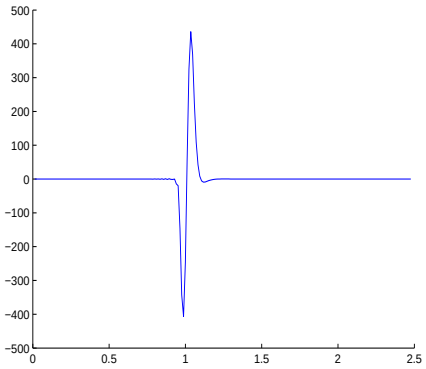

(a) Case 2 where $b_s = 500$ and $a_g = 0.1$

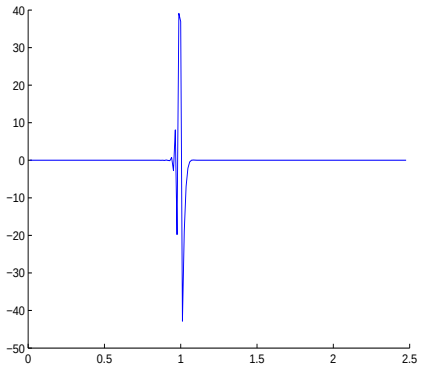

(b) Case 1 where $b_s = 5000$ and $a_g = 1$

Figure 5.24: Comparison of the errors between ψ_{yy} and ω for case 1 and case 2 by interchanging the values for $b_s = 5000$ and $b_s = 500$, where $R = 10000$, $\beta = 0.2$ and grid sizes $N = 90$ and $m = 501$.

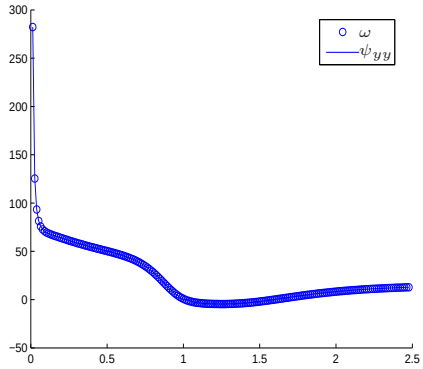

(a) Case 2 where $b_s = 500$ and $a_g = 1$

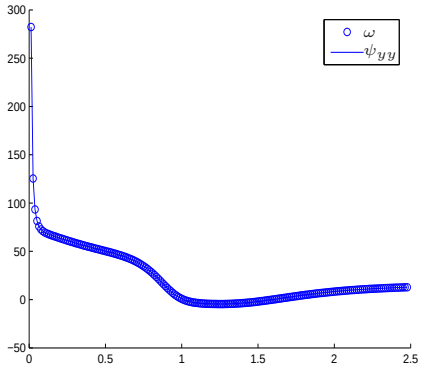

(b) Case 1 where $b_s = 500$ and $a_g = 1$

Figure 5.25: Comparison of ψ_{yy} and ω for case 1 and case 2 by fixing the parameter $a_g = 1$ and $b_s = 500$, where $R = 10000$, $\beta = 0.2$ and grid sizes $N = 90$ and $m = 501$.

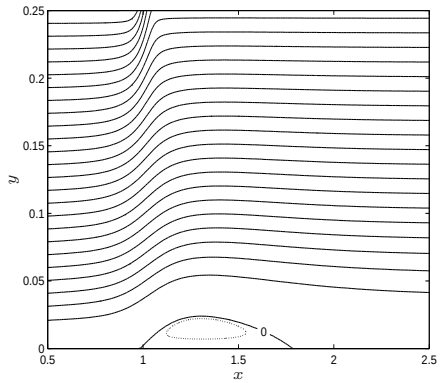

(a) Case 2 where $b_s = 500$ and $a_g = 1$

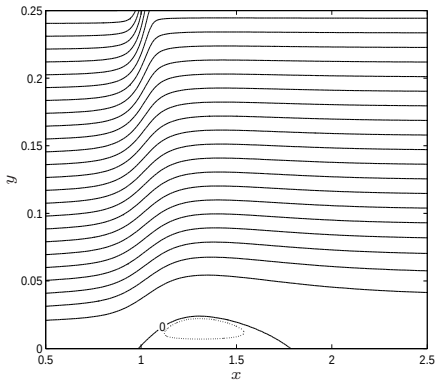

(b) Case 1 where $b_s = 500$ and $a_g = 1$

Figure 5.26: Streamline contour plots for case 1 and case 2 by fixing the parameter $a_g = 1$ and $b_s = 500$, where $R = 10000$, $\beta = 0.219$ and grid sizes $N = 90$ and $m = 501$. Solid line(-) for streamline level and dashed line(...) for separation bubble. Here contour levels are in intervals of (0.01).

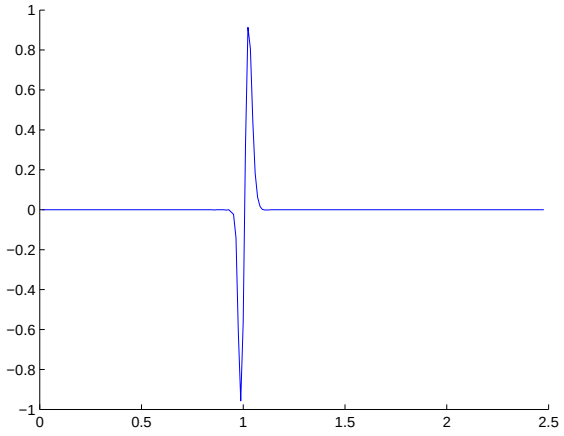

(a) Case 2 where $b_s = 500$ and $a_g = 1$

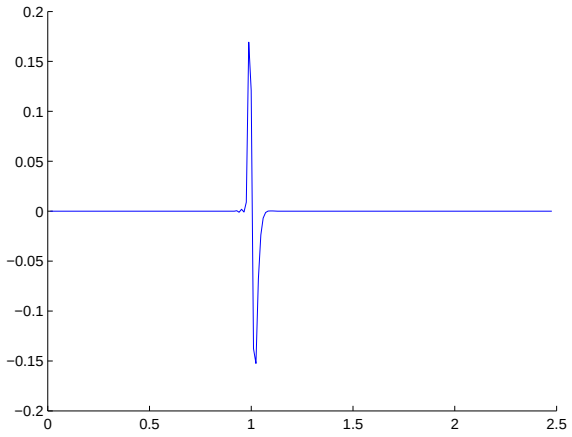

(b) Case 1 where $b_s = 500$ and $a_g = 1$

Figure 5.27: Comparison of case 1 and case 2 for ranges of error between ψ_{yy} and ω by fixing the parameter $a_g = 1$ and $b_s = 500$, where $R = 10000$, $\beta = 0.2$ and grid sizes $N = 90$ and $m = 501$.

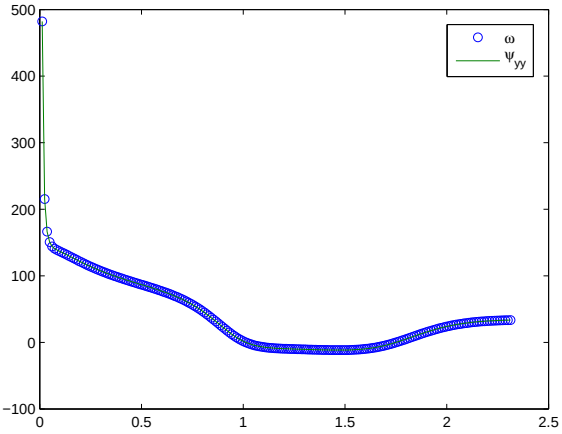

(a) Comparison of ψ_{yy} and ω

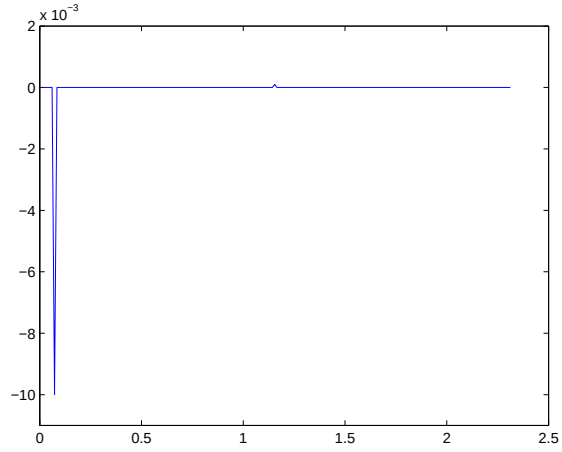

(b) The range of error

Figure 5.28: Comparison of ψ_{yy} and ω for the boundary conditions in chapter 4 and the ranges of error for ψ_{yy} and ω, where $R = 50000$, $\beta = 0.0997$ and grid sizes $N = 100$ and $m = 501$.

5.5 Case 3

In case 3, we focus on the study of the same problem discussed in chapter 4, namely a two-dimensional boundary layer flow in a channel with a suction, and we solve it, as in the earlier chapter, by using the steady Navier-Stokes equations, but in this case we work with changed boundary conditions, mostly on the upper wall.

All the numerical methods and techniques used in the solution of the problem here are exactly as the ones employed in chapter 4, where they are described in greater detail. The boundary conditions for the flow which we are using here (see figure (5.29)) are similar to those studied by Alam & Sandham (2000) and are given by

$$\begin{array}{llllll} \psi = \psi_b & \& & \omega = \omega_b & \text{for} & x = 0, & 0 \le y \le y_{max}, \\ \psi_{xx} = 0 & \& & \omega - \psi_{yy} = 0 & \text{for} & x = x_{max}\ , & 0 \le y \le y_{max}, \\ \psi = 0 & \& & \psi_y = 0 & \text{for} & y = 0, & 0 \le x \le x_{max}\ , \\ \psi_y = 1 & \& & \psi = y - S(x) & \text{for} & y = y_{max}, & 0 \le x \le x_{max}. \end{array}$$

Here $S(x) = S_0 + \int_{x_0}^{x} S_a e^{-S_b(q-S_c)^2} dq$

where three constants, S_a, S_b and S_c, control the size, shape and location of the suction profile, respectively.

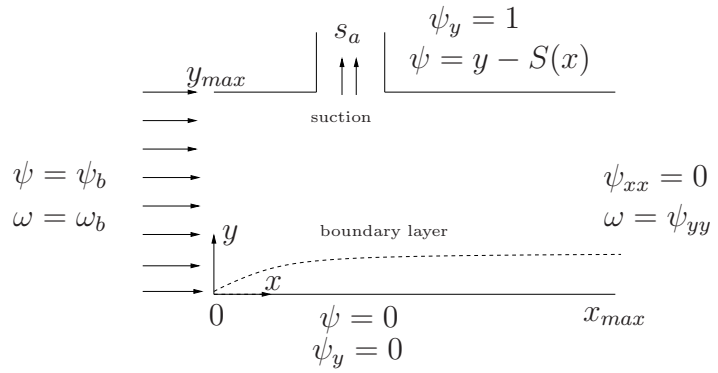

Figure 5.29: Sketch of channel with suction, with boundary conditions in case 3.

This case proved to be unsuitable for solving our particular problem because

we observed that the results are not convergent, meaning the solution is not grid independent as we will show in the following results.

5.5.1 Case 3: Results and Solutions

Here is a discussion of the results obtained in case 3.

We began by considering the flow through a channel without suction (see figure (5.30)) as shown below,

$$\begin{array}{llllll} \psi = \psi_b & \& & \omega = \omega_b & \text{for} & x = 0, & 0 \le y \le y_{max}, \\ \psi_{xx} = 0 & \& & \omega = \psi_{yy} & \text{for} & x = x_{max}\ , & 0 \le y \le y_{max}, \\ \psi = 0 & \& & \psi_y = 0 & \text{for} & y = 0, & 0 \le x \le x_{max}\ , \\ \psi_y = 1 & \& & \psi_{yy} = 0 & \text{for} & y = y_{max}, & 0 \le x \le x_{max}. \end{array}$$

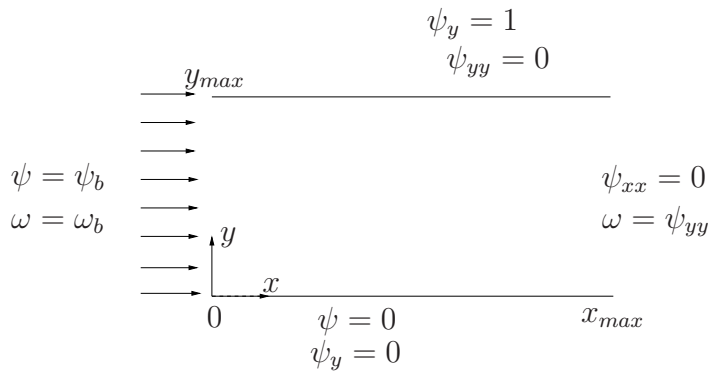

Figure 5.30: Sketch of channel without suction, with boundary conditions in case 3.

We observed a good convergence to the steady solution for values of $N = 101$ and $m = 501$ with $0 < Re < 100,000$.

After we observed a good convergence for the flow through a channel without suction, we investigated the two-dimensional boundary layer flow in a channel with a suction on the upper wall, similar to that studied by Alam & Sandham (2000) (see figure (5.29)).

Using a variety of Reynolds numbers Re, as well as different grid sizes and

suction ratios Sa to establish grid independence, we arrived at the following results:

In our computations with different values for Reynolds number we arrived at the suitable value for Reynolds number, $Re = 10000$, which is the value we will use throughout our calculations in this case. When we increased the values of the Reynolds numbers to $Re = 30000, 40000, 50000, 60000$ and fixed grid size $N = 100$ and $m = 501$, we obtained that our method was not convergent in basic flow.

We can see that the separation of a laminar boundary layer on the lower wall is the direct effect of an adverse pressure gradient produced by a suction port on the upper wall of a channel, see figure (5.31) for $y_{max} = 0.3$ where $Re = 20000$, $N = 100$ and $m = 501$.

Furthermore, we have investigated different values for y_{max}. We tested $y_{max} = 0.05$ and $y_{max} = 0.1$, but we found the results to be not grid independent, as shown below.

For $y_{max} = 0.05$ we show in figures (5.32) and (5.33) some streamline contour plots obtained from our computations for $Re = 10000$ and $Sa = 0.15$ by using fixed value for m with N being variable in figure (5.32) and vice versa in figure (5.33). Furthermore, figure(5.34) illustrates the velocity profile.

In contrast, for $y_{max} = 0.1$ figure (5.35) shows streamlines for different values of N and fixed values of m while figure (5.36) shows the opposite setup, meaning fixed value for N and various values for m where $Re = 10000$ and $Sa = 0.09$. Furthermore, the velocity profile is shown in figure (5.37)

These figures for the different values of y_{max} demonstrate clearly that, as the grid size changes, our results are not grid independent.

As we increase the adverse pressure gradient by increasing the size of the

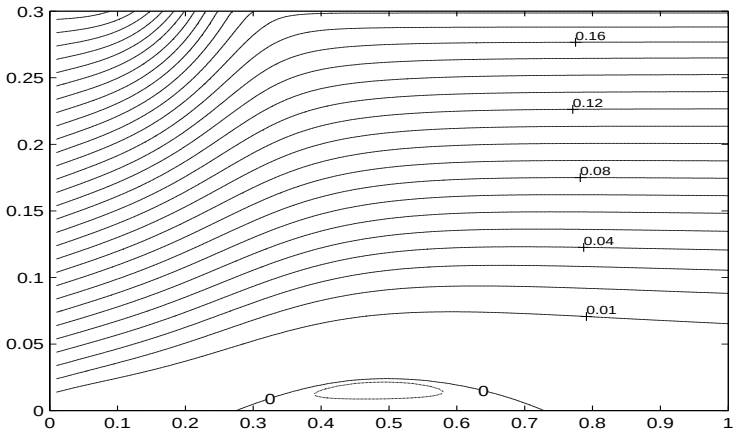

Figure 5.31: Streamline contour plots (case 3) where $R = 20000$, $Sa = 0.65$, $N = 100$ and $m = 501$. Solid line(-) for streamline level and dashed line(...) for separation bubble. Here contour levels are in intervals of (0.01).

suction port Sa in the upper wall, we observe that the steady separation bubble increases in size. This is illustrated in figures (5.38) and (5.39) for two values of y_{max} where we used different values for Sa. Figure (5.38) shows the result for $y_{max} = 0.05$ with fixed values for Reynolds number $Re = 10000$, $N = 101$ and $m = 501$, while figure (5.39) shows the result for $y_{max} = 0.1$ where Reynolds number is $Re = 10000$, $N = 140$ and $m = 501$.

5.6 Conclusions

We show in our work that a laminar boundary layer is forced to separate by the action of a suction profile applied at the upper wall of a channel, which leads to the development of a laminar separation bubble on the lower wall, whose size depends on the strength of the adverse pressure gradient.

In working with different test cases we introduced small changes in the boundary conditions, usually those located on the upper wall, which led us to observe

that the results change with the introduction of even slight changes in the boundary conditions, a fact which has also been mentioned by Hsiao & Pauley (1994)

Subsequently, we observed that the major differences between the results in case 1 and case 3 seem to be in relations to grid independence; this was the result of the different values of N and m for $Re = 10000$. In addition, through working with case 2 we observed that the boundary condition in the upper wall in case 1 is more relevant to our problem because the range of error between ψ_{yy} and ω for case 1 is less than that in case 2. On the other hand, the major difference between the results of the boundary conditions discussed in chapter 4 and the results in case 1 was that we observed only one solution in case 1, whereas we obtained two solutions and the turning point bifurcation in chapter 4.

Using a numerical technique to calculate a two dimensional boundary layer flow in a channel with a suction port on the upper wall, based on Chebychev collocation in one direction and combined with finite differences in the other direction we obtained good results and found the technique to be adequate for case 1.

From our calculations we arrived at the conclusion that the boundary conditions which are used in case 1 are the most suitable ones for solving our problem, as opposed to the boundary conditions employed in the other cases.

Our computations carried out in case 1 obtained good results and showed these results to be grid independent for different values of Reynolds numbers Re, as well as exhibiting good convergence throughout the domain.

We observe that the length of the separation bubble depends on the suction ratio β which in turn depends on the value of the Reynolds numbers meaning that the separation bubble becomes larger as the suction ratio increases and the increase in the value of the suction ratio is in direct relations to the decrease in the value of the Reynolds number Re.

In conclusion, the computations carried out for the basic flow in case 1 work well and we will use them in the next chapter to investigate the stability of separated flow, as well as to investigate bifurcation occurring in separated flow at large Reynolds numbers, using global stability analysis and linear temporal simulation.

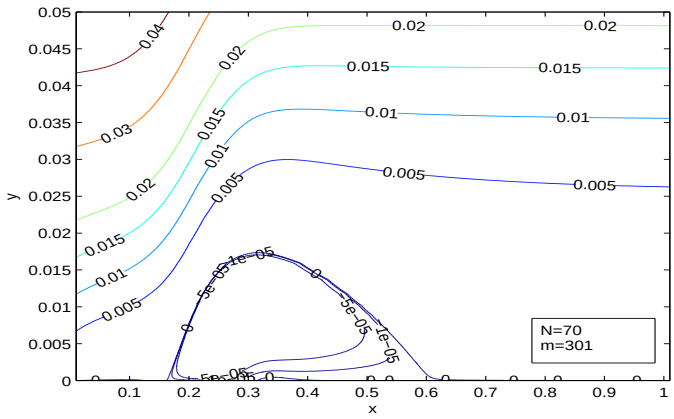

(a) N=70, m=301

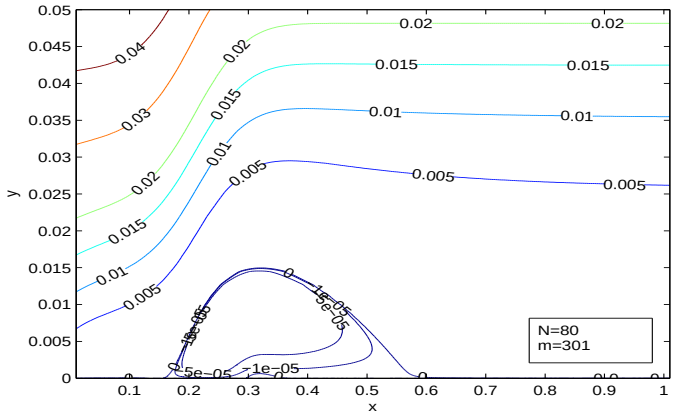

(b) N=80, m=301

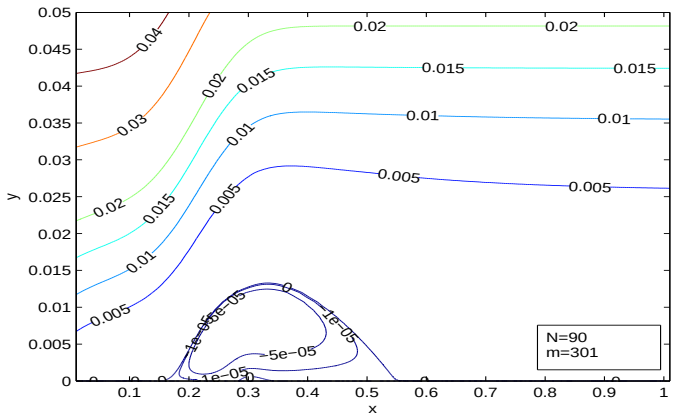

(c) N=90, m=301

Figure 5.32: Streamline contour plots (case 3) for $y_{max} = 0.05$, $R = 10000$, $Sa = 0.15$, and different grid sizes for $N = 70, 80, 90$ and $m = 301$.

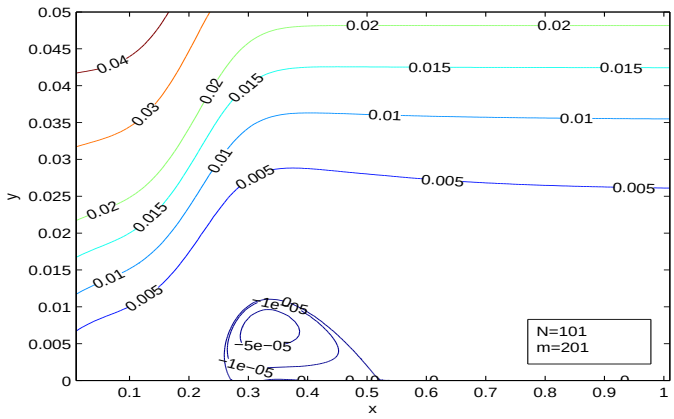

(a) N=101, m=201

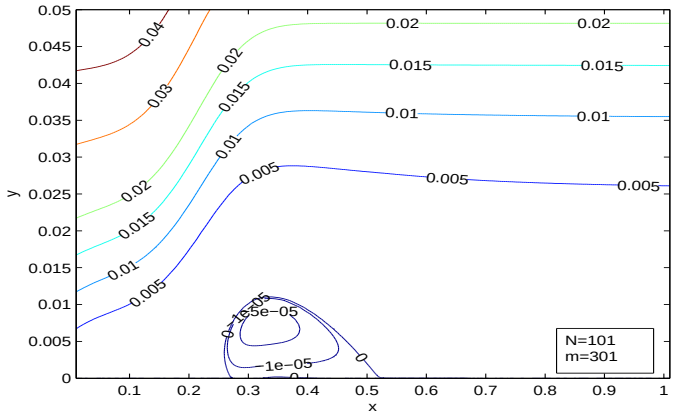

(b) N=101, m=301

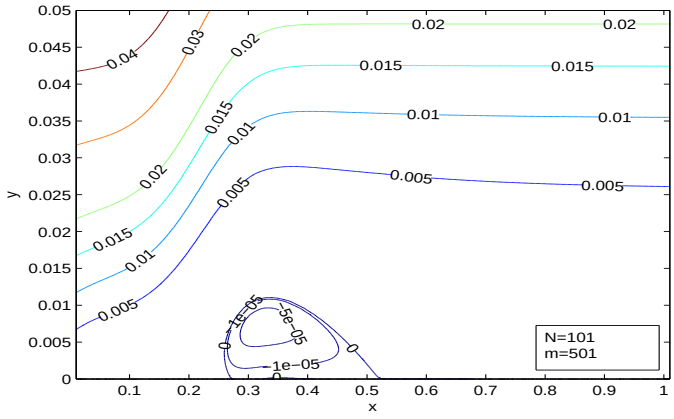

(c) N=101, m=501

Figure 5.33: Streamline contour plots (case 3) for $y_{max} = 0.05$, $R = 10000$, $Sa = 0.15$, and different grid sizes for $m = 201, 301, 501$ and $N = 101$.

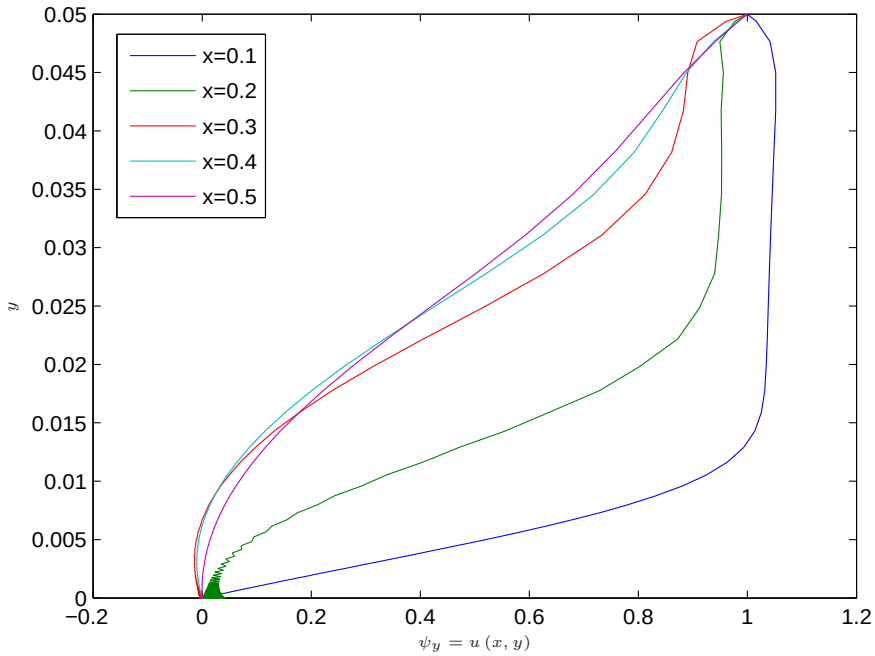

(a) m=301

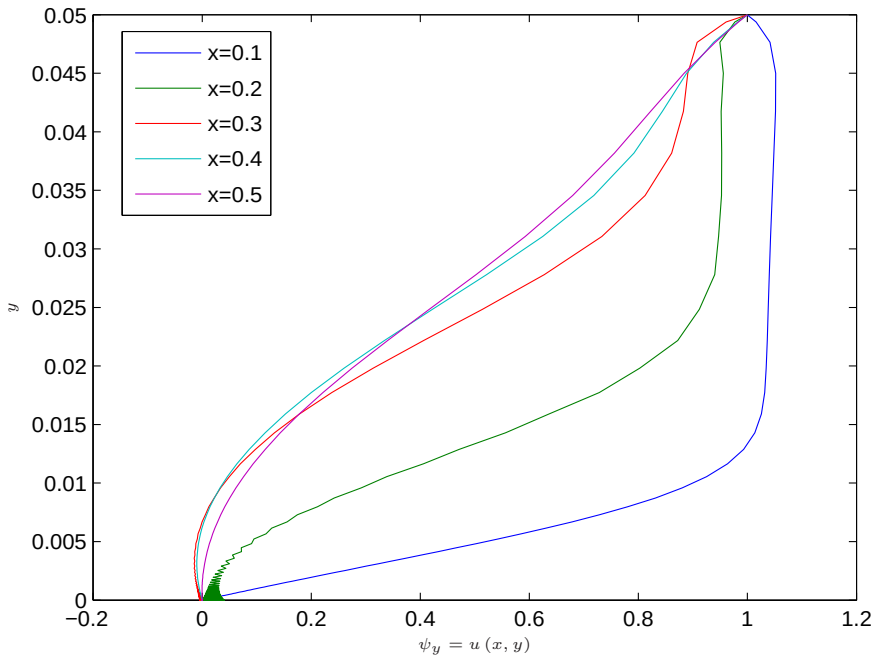

(b) m=501

Figure 5.34: Plot showing velocity profile (case 3) for different m at $y_{max} = 0.05$, $R = 10000$, $\beta = 0.15$, and $N = 101$.

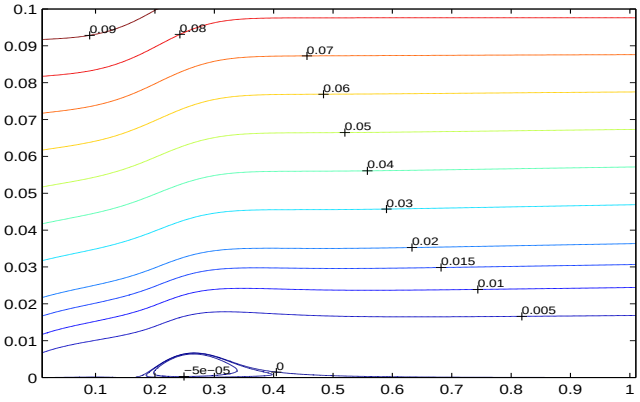

(a) N=120, m=501

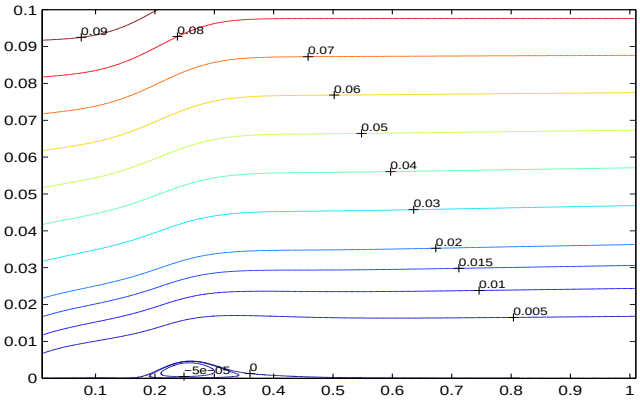

(b) N=130, m=501

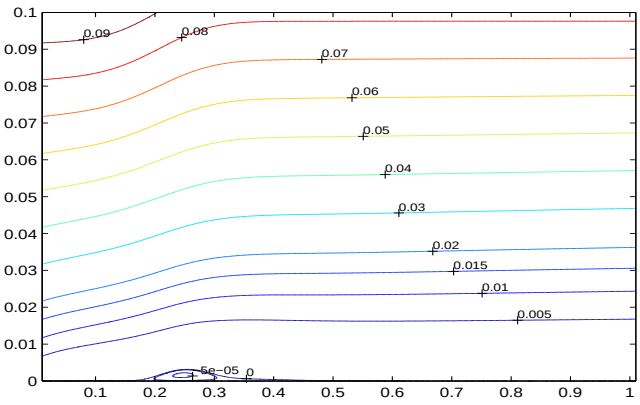

(c) N=140, m=501

Figure 5.35: Streamline contour plots (case 3) for $y_{max} = 0.1$, $R = 10000$, $Sa = 0.09$, and different grid sizes for $N = 120, 130, 140$ and $m = 501$.

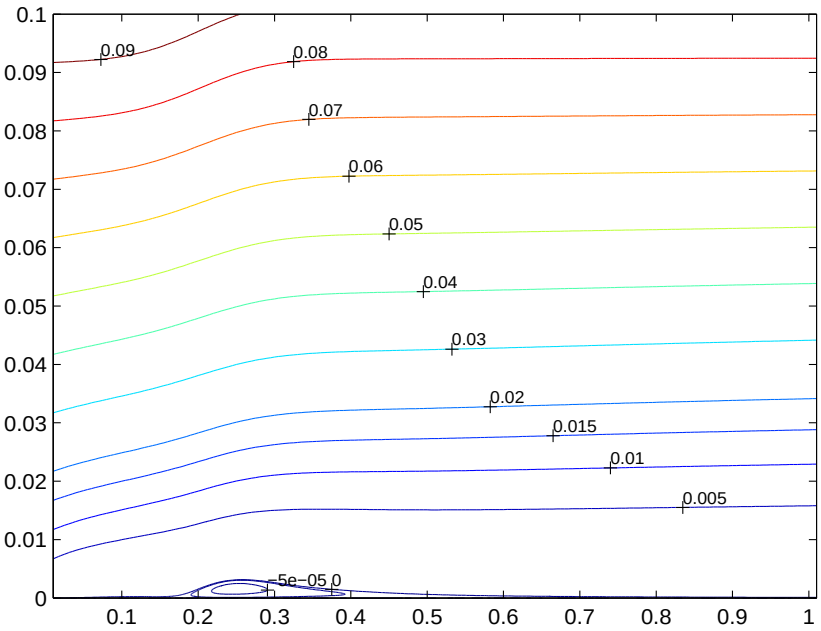

(a) N=100, m=201

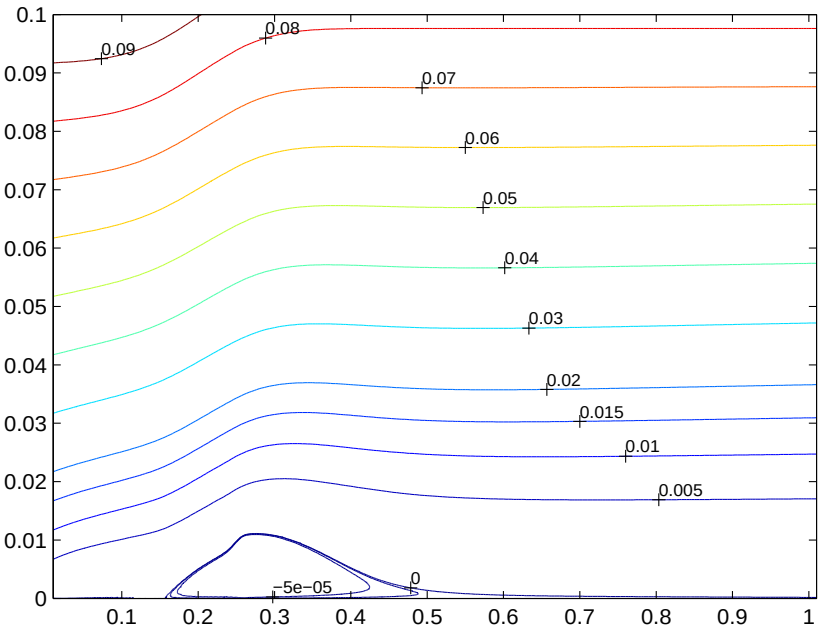

(b) N=100, m=301

Figure 5.36: Streamline contour plots (case 3) for $y_{max} = 0.1$, $R = 10000$, $Sa = 0.09$, and different grid sizes for $m = 201, 301$ and $N = 100$.

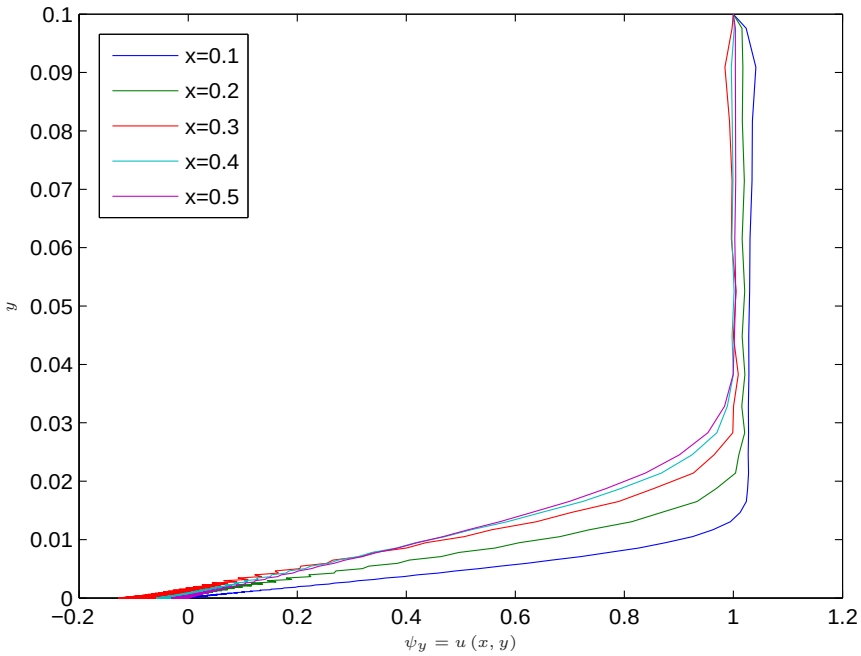

(a) m=201

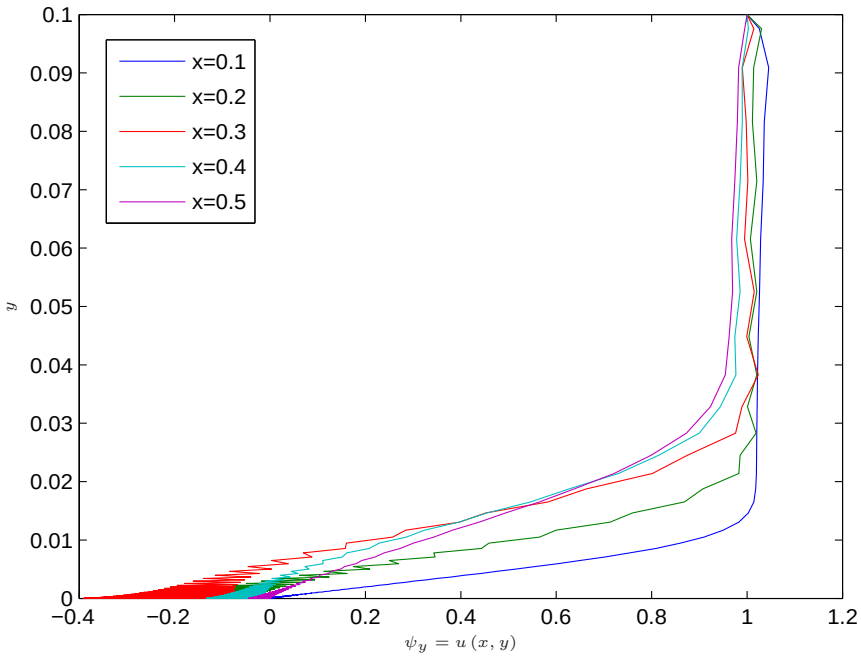

(b) m=301

Figure 5.37: Plot showing velocity profile (case 3) for different m at $y_{max} = 0.1$, $R = 10000$, $\beta = 0.09$, and $N = 100$.

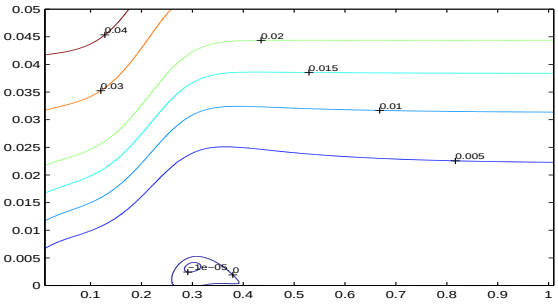

(a) $Sa = 0.13$

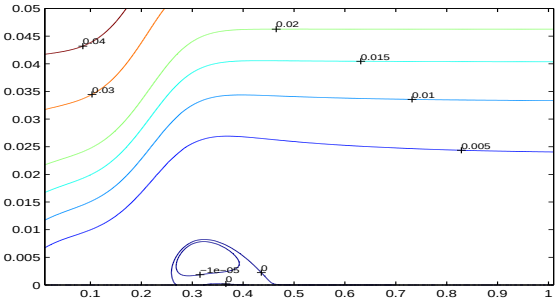

(b) $Sa = 0.14$,

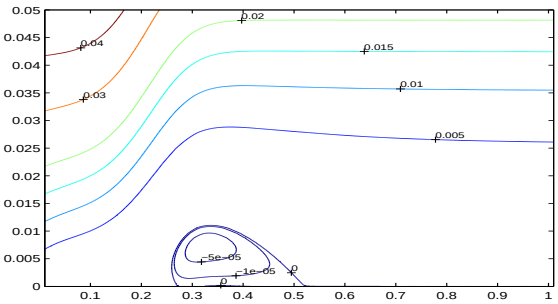

(c) $Sa = 0.15$

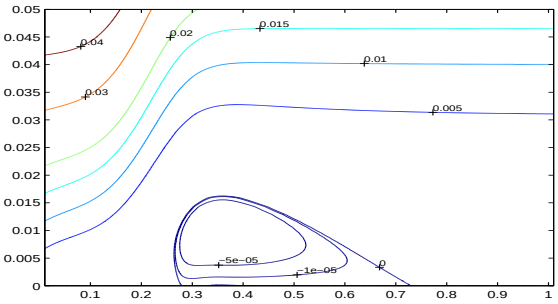

(d) $Sa = 0.17$

Figure 5.38: Streamline contour plots (case 3) for $y_{max} = 0.05$, $R = 10000$, $N = 101$ and $m = 501$ and different values of Sa.

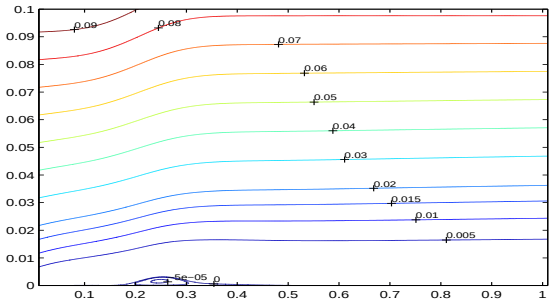

(a) $Sa = 0.09$

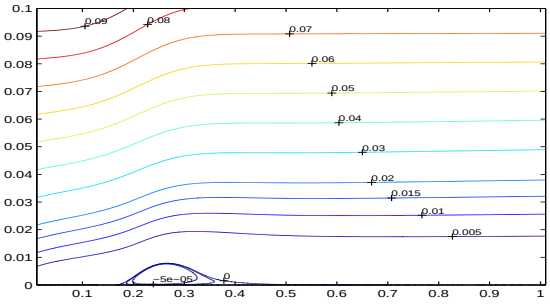

(b) $Sa = 0.11$,

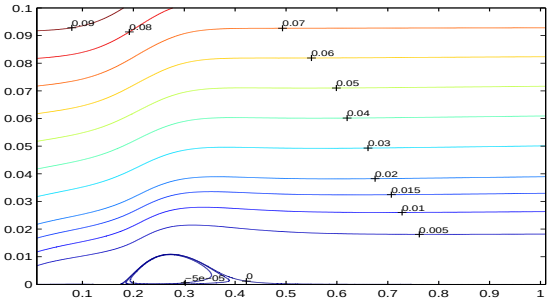

(c) $Sa = 0.12$

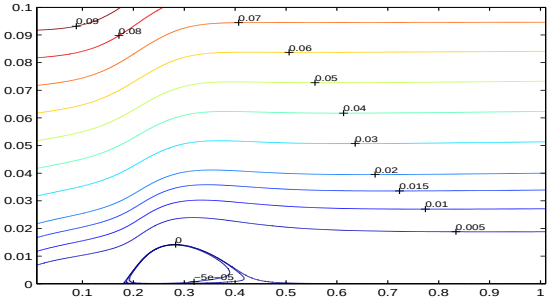

(d) $Sa = 0.13$

Figure 5.39: Streamline contour plots (case 3) for $y_{max} = 0.1$, $R = 10000$, $N = 140$ and $m = 501$ and different values of Sa.

Chapter 6

Case 1: Flow Stability

6.1 Introduction

In the previous chapter we obtained accurately calculated basic flow results for case 1 and here we will use these results to further investigate flow stability and bifurcations occurring in separated flow at large Reynolds number. The same global stability analysis and linear temporal simulation as in chapter 4 are used to analyze the stability of the flow. The computational details for these analyses have been presented comprehensively in chapter 4 and here we will focus on a complete presntation of the results for these calculations.

6.2 Global Stability Analysis

In the system we have formulated the eigenvalue can be real or complex and an unstable mode is indicated by a negative real part of the eigenvalue. Therefore, to determine the stability of the flow we have to know if the smallest magnitude of the real part of eigenvalue is positive or negative. Having first obtained eigenvalues λ and eigenvectors $\bar{\mathbf{T}}$ we then solved the generalized eigenvalue problem using

ARPACK to solve for the smallest magnitude eigenvalue and the eigenvector of our system.

In the beginning, in order to check convergence, we used various domain checks. Figure (6.1) demonstrates that the result is grid independent for different values of N, where $m = 501$ is fixed. On the other hand, as shown in Figure (6.2), when we used different values for m while the value for $N = 80$ remained fixed, we observed that for values of $m = 751$, $m = 901$ and $m = 1001$ the results remained grid independent, except for the value $m = 501$.

In chapter 4 we have expressed the general linear system (4.66) in the form of the generalized eigenvalue problem,

$$\bar{\mathbf{J}}\bar{\mathbf{T}} = \lambda\bar{\mathbf{R}}\bar{\mathbf{T}} \tag{6.1}$$

In this system, to ensure that ARPACK would not miss any unstable modes with a large imaginary part, we have generated many more eigenvalues than needed because ARPACK cannot specify that the smallest real part be calculated, but only the smallest magnitude complex number.

Figure (6.3) shows that we generated 200 eigenvalues, which is double the number of eigenvalues (nev) for determining the smallest eigenvalue throughout our calculations in the global stability analysis. The resulting graph in figure (6.3) shows that all the (nev) give the same smallest real part of eigenvalue and are in agreement with half of the 200 eigenvalues we generated in order to cross check our results. All these computations have been made using the same Re, β and grid size, which typically took the values, 10000, 0.219 and $N = 80$, $m = 501$, respectively.

Figure (6.4) shows the results of our computations for the eigenvalues with different values of σ to be convergent. σ is defined as a shift used in spectral

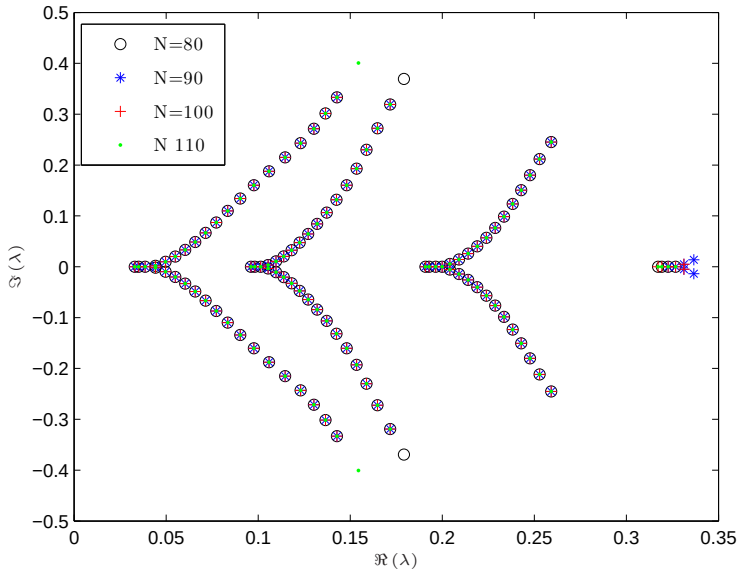

Figure 6.1: Plot showing eigenvalues at $R = 10000$, $\beta = 0.219$ and different grid sizes for $N = 80, 90, 100, 110$ and $m = 501$.

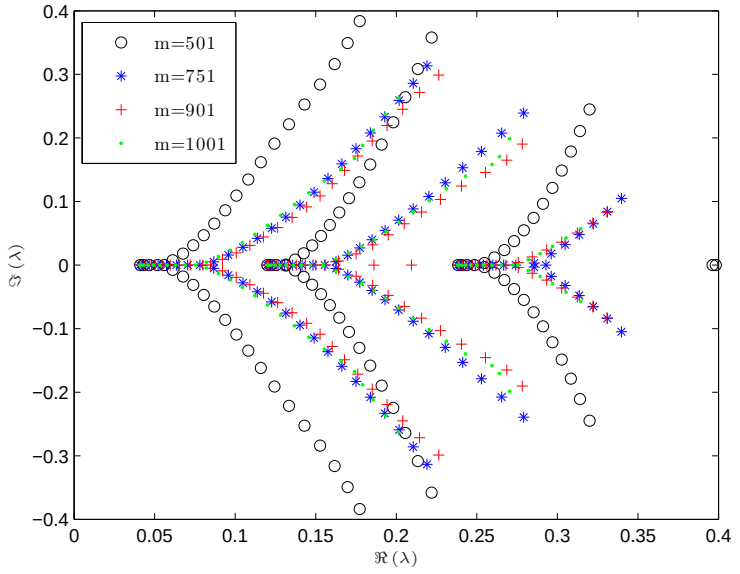

Figure 6.2: Plot showing eigenvalues at $R = 8000$, $\beta = 0.219$ and different grid sizes for $N = 80$ and $m = 501, 751, 901, 1001$.

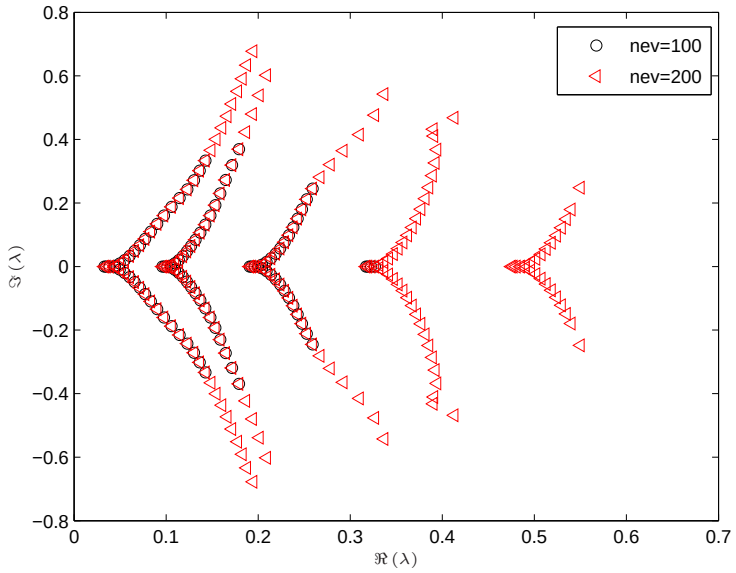

Figure 6.3: Plot showing that the number of eigenvalues are true at $R = 10000$, $\beta = 0.219$, $N = 80$ and $m = 501$.

transformation (ARPACK). Here, all the results for different σ have been calculated using the same grid size, 501 finite difference points, and 80 Chebychev points, as well as $Re = 10000$ and $\beta = 0.219$.

Figure (6.5) shows the comparison between increasing values of Re and the smallest real part of the eigenvalue $\Re(\lambda_s)$, with varying values for β. From this figure (6.5) and table (6.1) we conclude that when we increase the value of the Re the smallest real part of eigenvalue $\Re(\lambda_s)$ decreases very close to zero. Thus, we can see that the smallest real part of eigenvalue is independent of β for any given value of Re. The grid size we use here in this computation is $N = 80$, $m = 501$.

As explained previously, in the formulation of our system a stable mode is indicated by a positive real part of the eigenvalue, while a negative real part of the eigenvalue shows an unstable mode. For these computations we used ARPACK, to calculate eigenvalues as well as the corresponding eigenvectors.

The channel flow is linearly stable within the range of computed Re. These

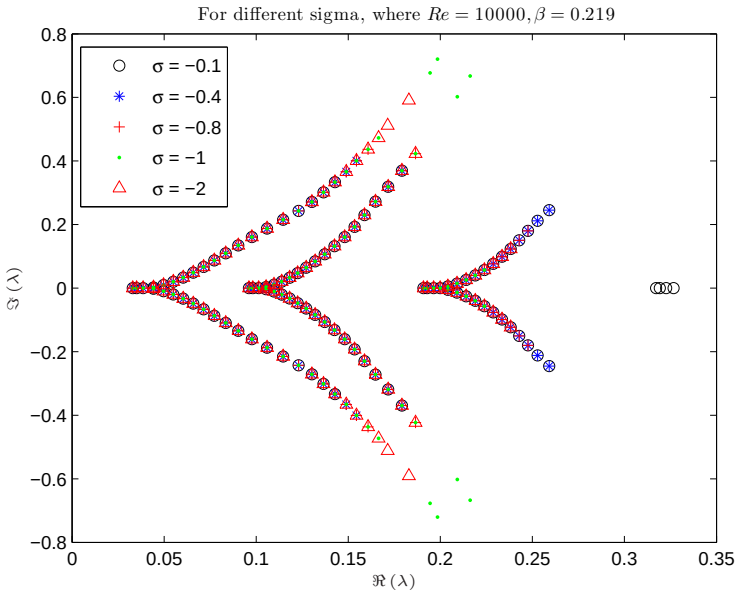

Figure 6.4: Plot showing the eigenvalues with varying shift-σ at $R = 10000$, $\beta = 0.219$, $N = 80$ and $m = 501$.

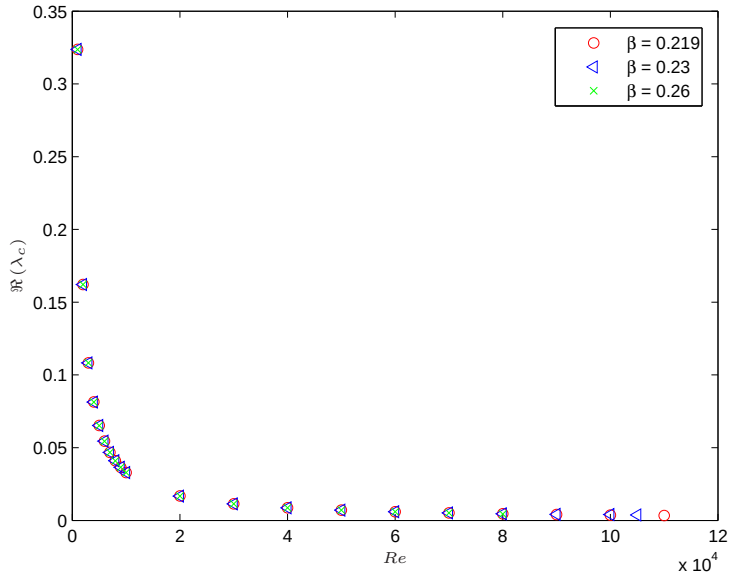

Figure 6.5: Comparison between increasing values of Re and the smallest real part of the eigenvalue $\Re(\lambda_s)$, with varying values for β at $N = 80$ and $m = 501$.

	$\beta = 0.219$	$\beta = 0.23$	$\beta = 0.26$
Re	$\Re(\lambda_s)$	$\Re(\lambda_s)$	$\Re(\lambda_s)$
1000	0.32369E+00	0.32368E+00	0.32365E+00
5000	0.65247E-01	0.65238E-01	0.65213E-01
10000	0.32941E-01	0.32932E-01	0.32908E-01
20000	0.16787E-01	0.16778E-01	0.16755E-01
30000	0.11398E-01	0.11390E-01	0.11368E-01
40000	0.86983E-02	0.86895E-02	0.86704E-02
50000	0.70690E-02	0.70599E-02	0.70444E-02
60000	0.59720E-02	0.59636E-02	0.59485E-02
70000	0.51784E-02	0.51743E-02	0.51338E-02
80000	0.45741E-02	0.45854E-02	0.43291E-02

Table 6.1: Comparison of Re and the smallest real part of the eigenvalue $\Re(\lambda_s)$ with different values for β at $N = 80$ and $m = 501$.

results are shown in figures (6.6) to (6.9) and we see the smallest eigenvalue is positive and close to zero, which shows that there is no unstable linear mechanism in this form.

In the next section we will use linear temporal simulation to affirm the results we obtained using global stability analysis, as well as attempt to find out any differences between the results obtained by using linear temporal simulation or global stability analysis.

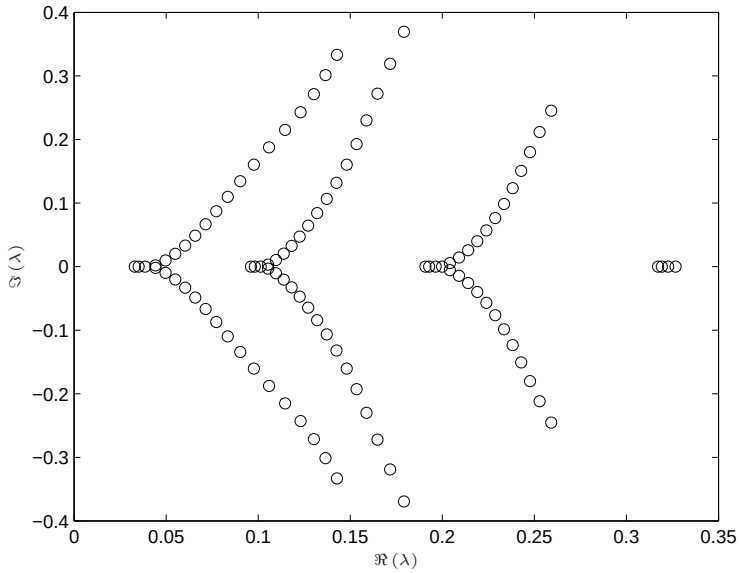

Figure 6.6: Plot showing the eigenvalues at $R = 10000$, $\beta = 0.219$, $N = 80$ and $m = 501$.

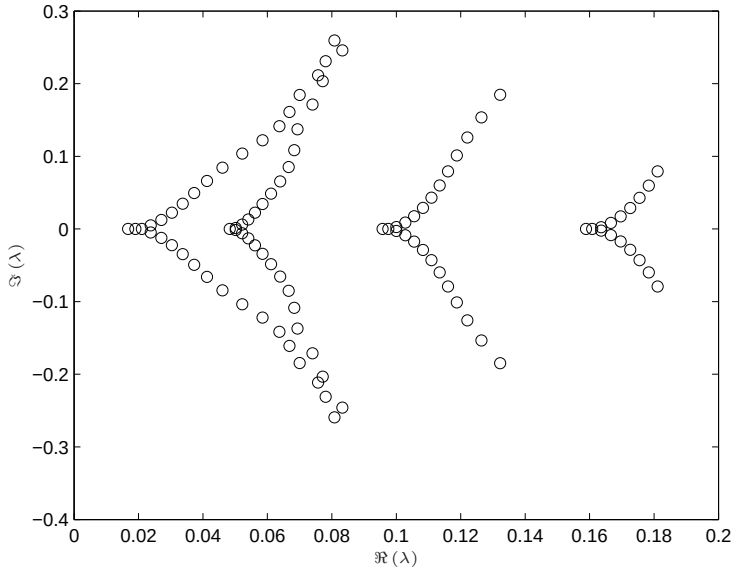

Figure 6.7: Plot showing the eigenvalues at $R = 20000$, $\beta = 0.219$, $N = 80$ and $m = 501$.

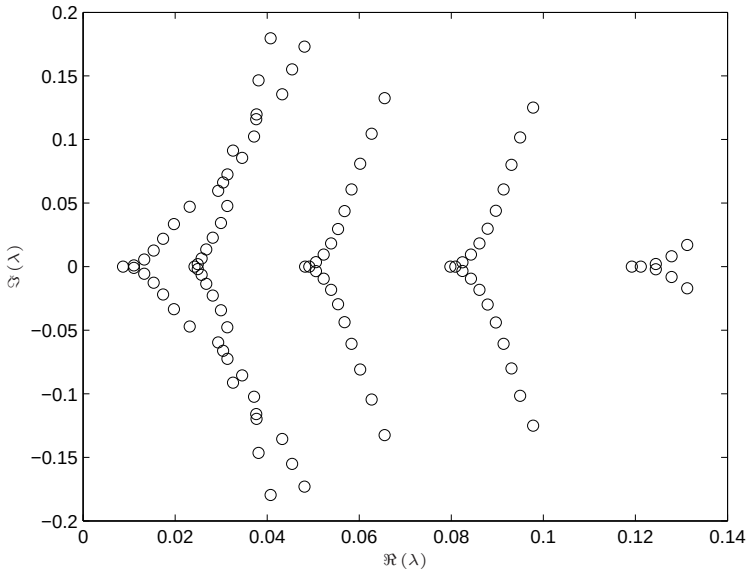

Figure 6.8: Plot showing the eigenvalues at $R = 40000$, $\beta = 0.219$, $N = 80$ and $m = 501$.

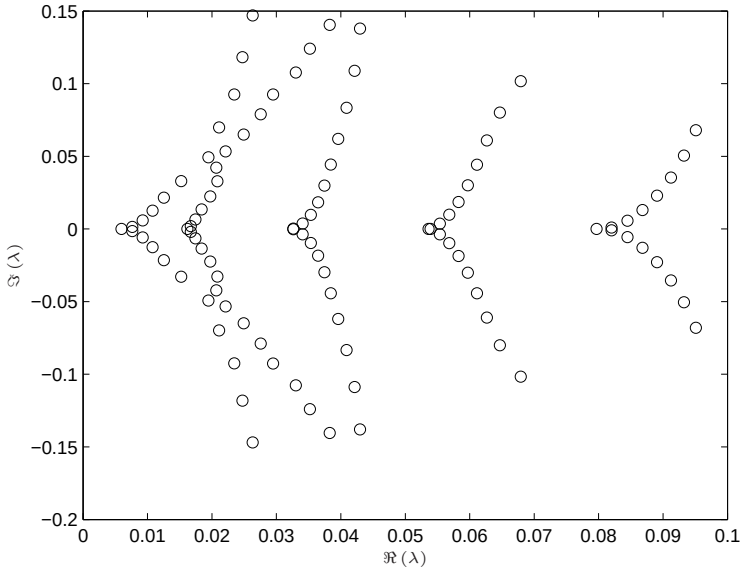

Figure 6.9: Plot showing the eigenvalues at $R = 60000$, $\beta = 0.219$, $N = 80$ and $m = 501$.

6.3 Linear Temporal Simulation

In this section we discuss the results obtained using linear temporal simulation in our investigation of flow stability. We proceeded in the same way as in section 4.9, using those same techniques, but with the boundary conditions of case 1.

We computed the simulation results using various grid sizes, time steps $\Delta(t)$, Reynolds numbers Re, and suction ratios β. Typically, we used 80 Chebychev and 501 finite difference points, as well as $Re = 40000$ and $\beta = 0.219$ up to time $(t = 300)$. In the beginning we test four different time steps $\Delta(t) = 0.1$, 0.05, 0.025 and 0.0125, to choose the one most suited to obtain an accurate convergent solution of our calculations. Figure (6.10) demonstrates that when we compute the value of velocity $u(x, y, t)$, at each time interval, where $(x, y) = (0.13, 1.5)$ a randomly chosen node, for each different time step, the first and second values for time step $\Delta(t) = 0.1$ and 0.05 do not give us convergence, while from $\Delta(t) = 0.025$ and 0.0125, $\Delta(t) = 0.025$ emerges as the most suitable and least time consuming one, which therefore will be used in our further calculations. Figure (6.10.a) shows the full time range $(t = 300)$, while in figure (6.10.b) we see a snapshot.

Figure (6.11), shows the evolution of $u(0.13, 1.5, t)$ with time t for increasing values of Re. From these figures it is evident that when we increase the value of Re above 40000, our solutions change from stable to unstable. We further confirmed this result when we computed the velocity $u(0.13, 1.5, t)$ up to $t = 1000$ for decreasing Re, see figure(6.12) .

After performing various grid size checks with increasing values for finite difference points (m) in x-direction, we observe that the solutions remain stable,but not grid independent, see figure (6.13).

Investigating the results for various values of β, we see in figure (6.14) that the results are stable and $\beta = 0.219$ is the most useful one for our calculations.

Figures (6.15) and (6.16) show the stream function perturbations ($\vec{\psi}$) and vorticity perturbations ($\vec{\omega}$) respectively, as they develop in time. It is evident that the disturbances take the form of growing wave packets moving downstream. The maximum amplitude of the initial wave packet is very large, but decreases dramatically with time until it reaches a finite value, then it oscillates about this value until it begins to increase again, moving downstream as time develops.

6.4 Conclusions

Having investigated flow stability, using global stability analysis and linear temporal simulation, we have arrived at the conclusion, after performing various grid checks, that the result in the global stability analysis computations is grid independent for different values of N and m, as well as for different (nev) and σ. We also have demonstrated that the smallest real parts of the eigenvalues are positive and close to zero and none of them cross the imaginary axis, which suggests that there is no unstable linear mechanism in this result. The numerical simulations on the other hand show that the results are stable until $Re = 40000$ but become unstable if this value increases. The disturbances take the form of growing wave packets moving downstream.

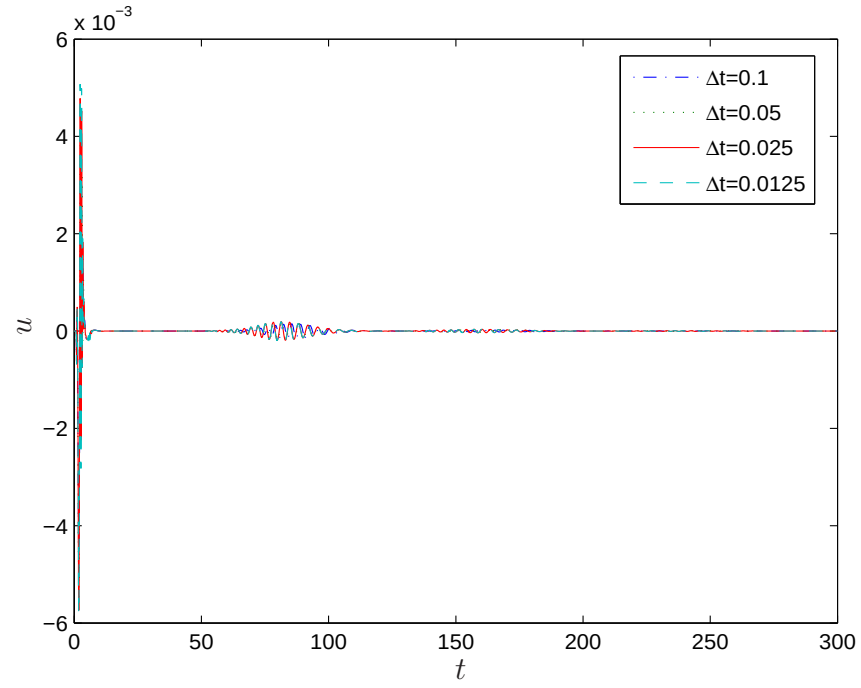

(a) Different time steps $\Delta(t)$

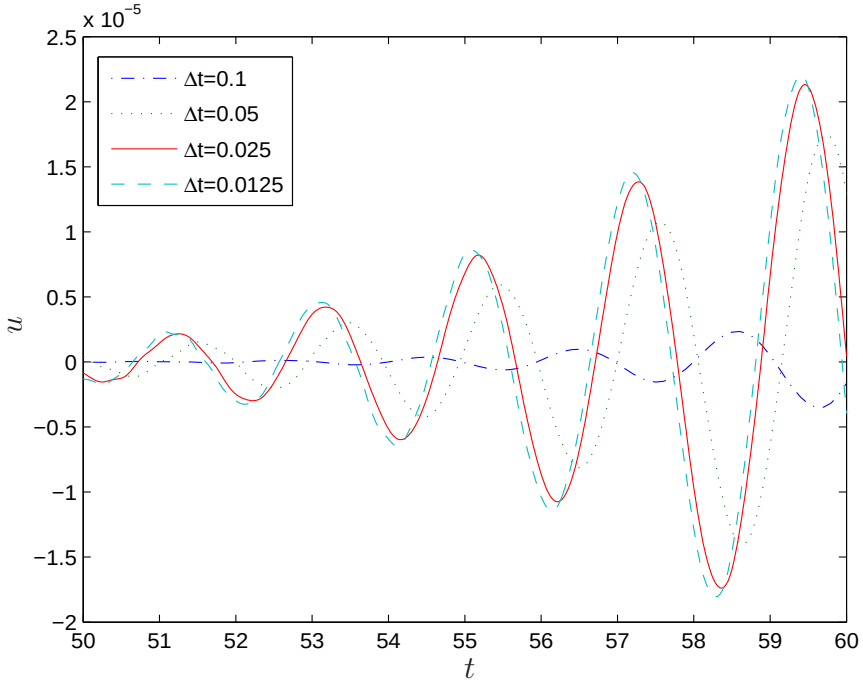

(b) Detailed view of the same signal

Figure 6.10: Plot showing $(u(0.13, 1.5, t))$ evolving with time t at different time steps $\Delta(t)$, where $R = 40000$, $\beta = 0.219$, $m = 501$ and $N = 80$.

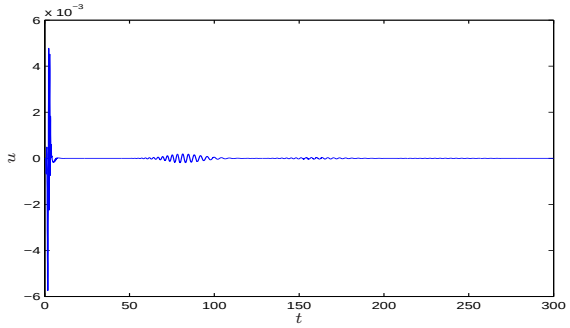

(a) $Re = 40000$

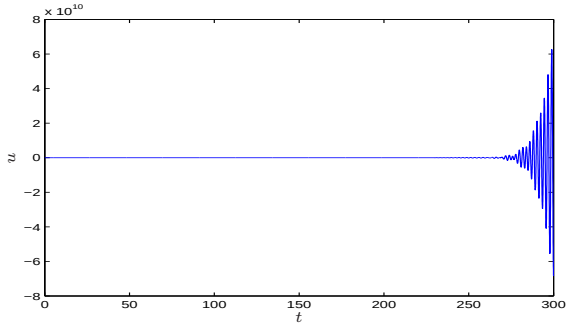

(b) $Re = 60000$

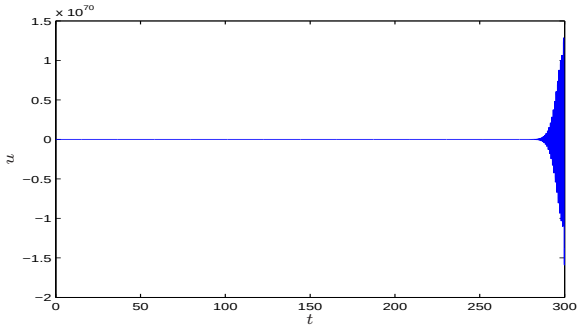

(c) $Re = 80000$

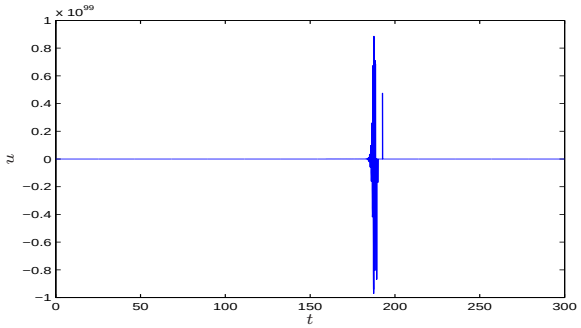

(d) $Re = 100000$

Figure 6.11: Plot showing $(u(0.13, 1.5, t))$ evolving with time t at different value of Re where $N = 80$, $m = 501$, and $\beta = 0.219$.

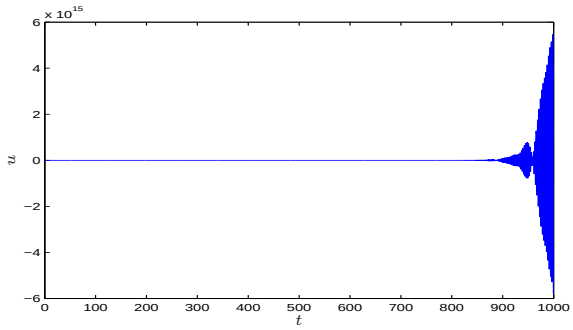

(a) $Re = 50000$

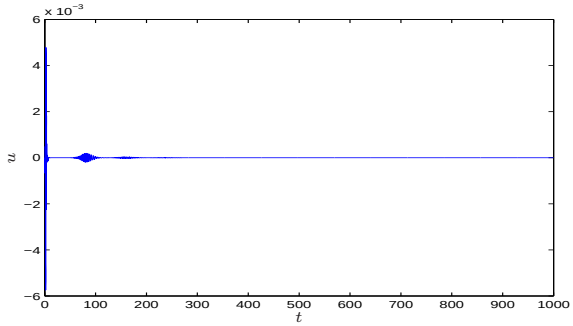

(b) $Re = 40000$

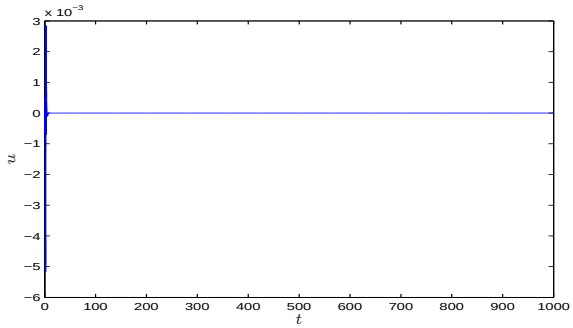

(c) $Re = 30000$

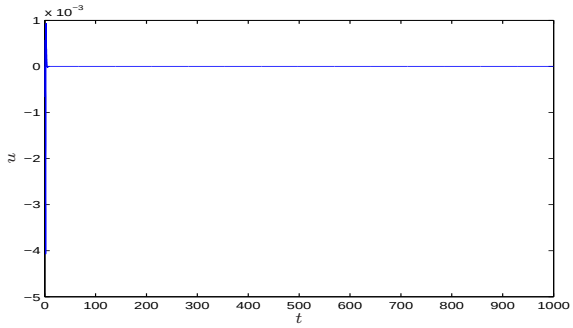

(d) $Re = 20000$

Figure 6.12: Plot showing $(u(0.13, 1.5, t))$ evolving with time $t = 1000$ at different value of Re where $N = 80$, $m = 501$, and $\beta = 0.219$.

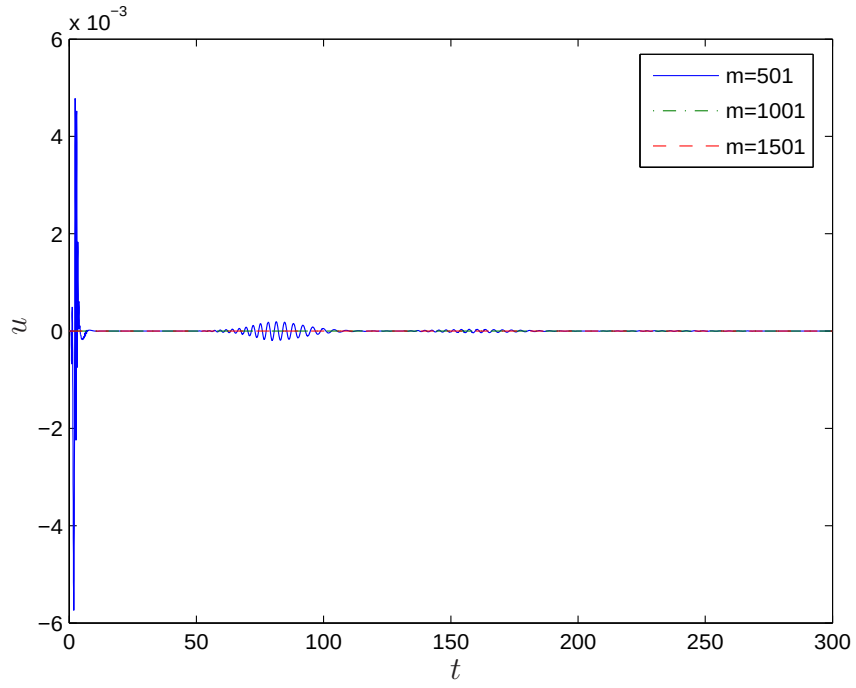

(a) Different m

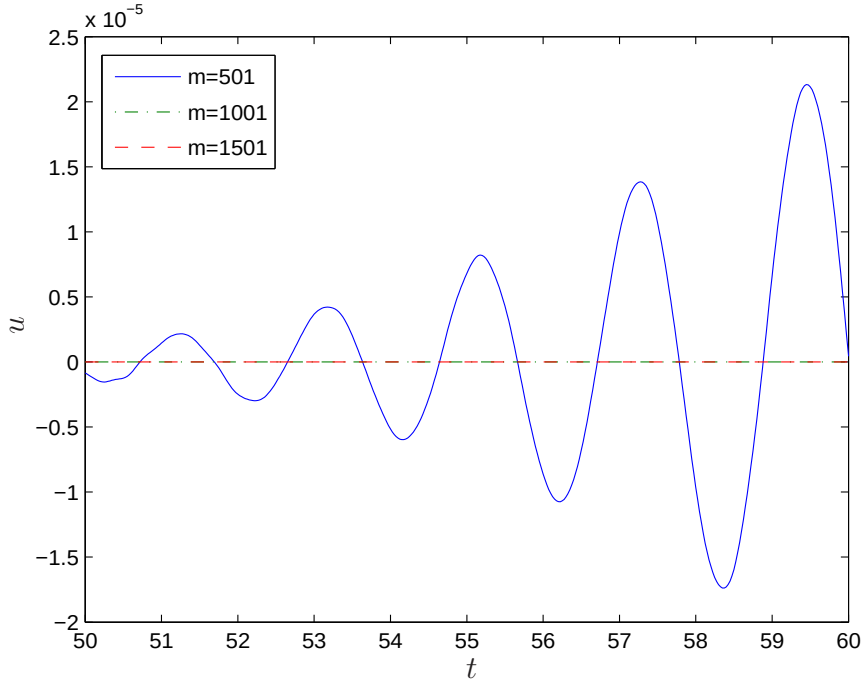

(b) Detailed view of the same signal

Figure 6.13: Plot showing $(u(0.13, 1.5, t))$ evolving with time t at different grid sizes for $m = 501, 1001, 1501$ and $N = 80$ where $R = 40000$, $\beta = 0.219$.

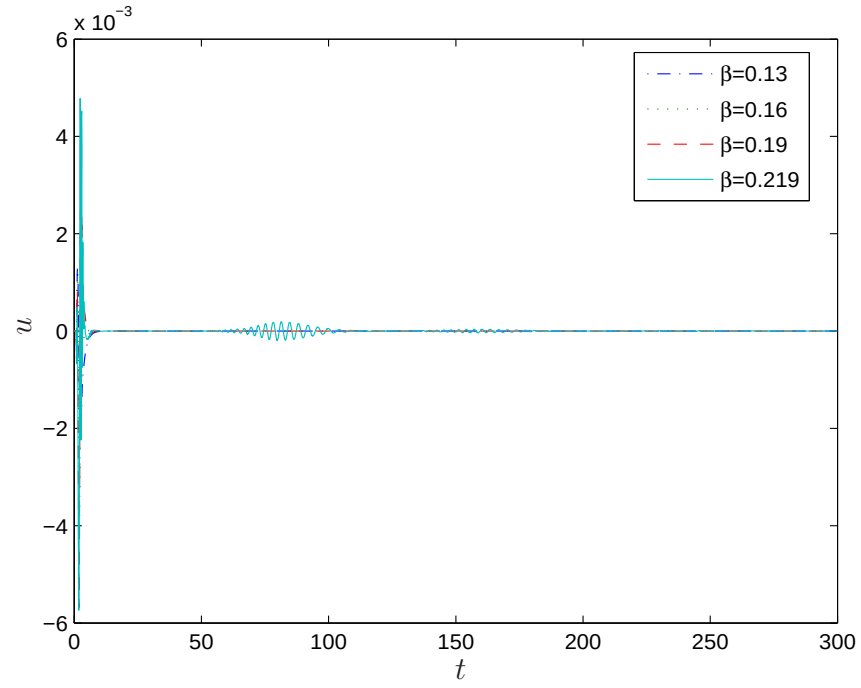

(a) Different values of β

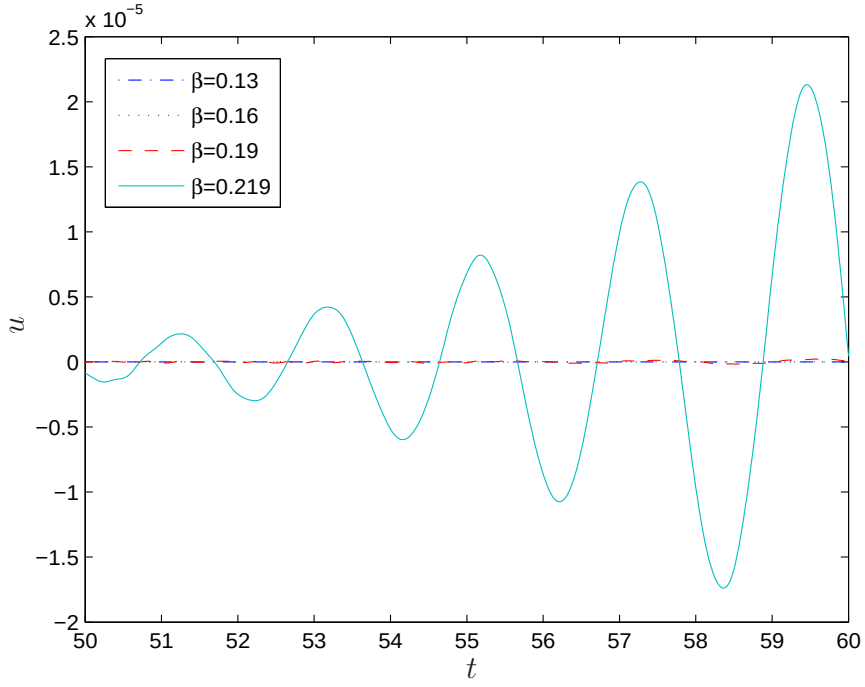

(b) Detailed view of the same signal

Figure 6.14: Plot showing $(u(0.13, 1.5, t))$ evolving with time t for different values of β, where $m = 501$, $N = 80$ and $R = 40000$.

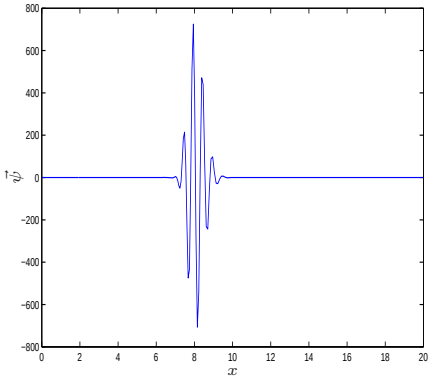

(a) $T = 20$

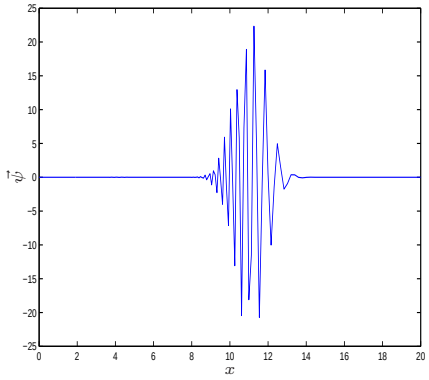

(b) $T = 40$

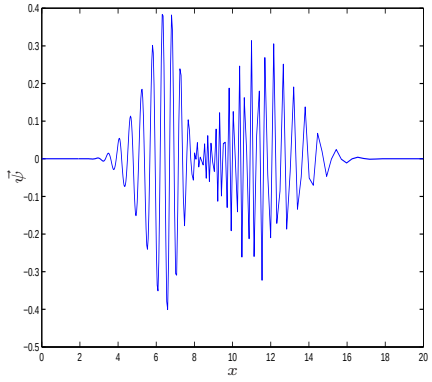

(c) $T = 60$

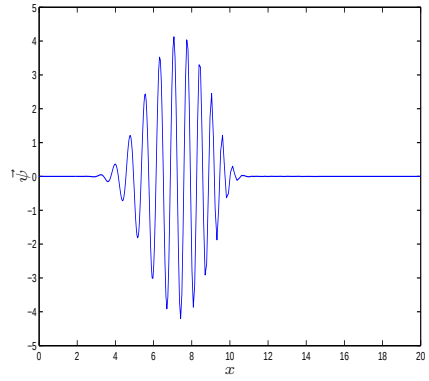

(d) $T = 80$

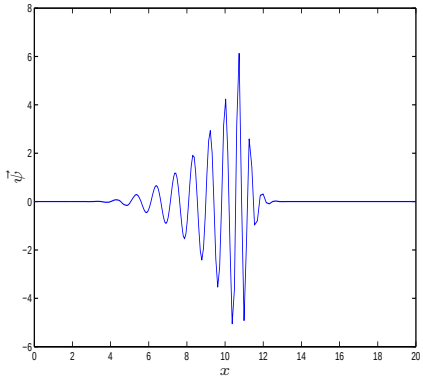

(e) $T = 100$

Figure 6.15: Plot showing evolving stream function perturbations $\vec{\psi}(x, 0.125)$ at different points in time where $N = 80$, $m = 501$, $Re = 40000$ and $\beta = 0.219$.

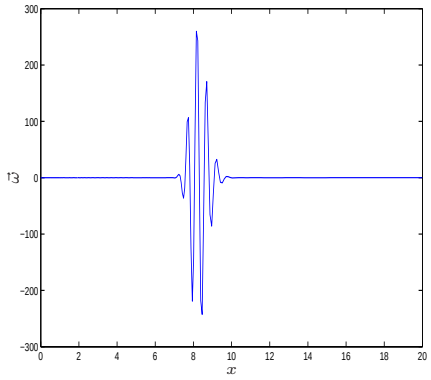

(a) $T = 20$

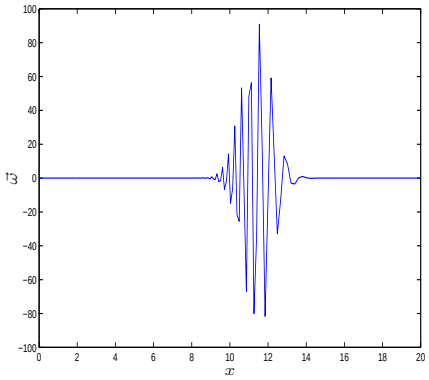

(b) $T = 40$

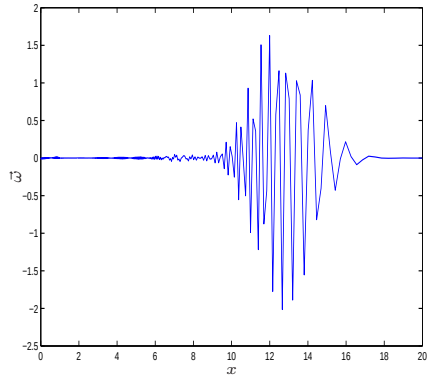

(c) $T = 60$

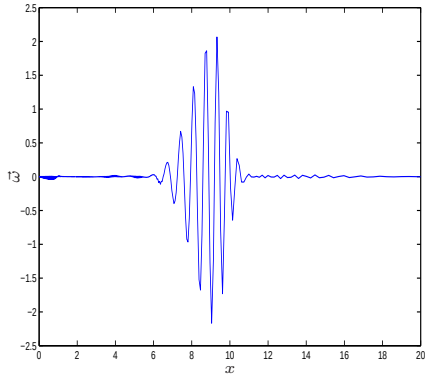

(d) $T = 80$

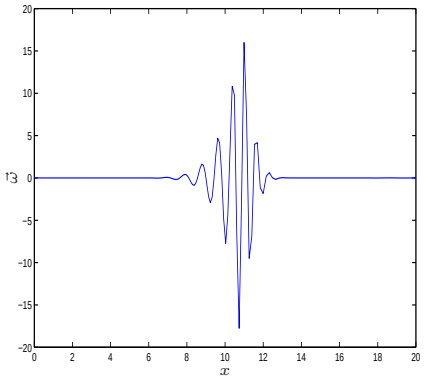

(e) $T = 100$

Figure 6.16: Plot showing evolving vorticity perturbations $\vec{\omega}(x, 0.125)$ at different points in time where $N = 80$, $m = 501$, $Re = 40000$ and $\beta = 0.219$.

Chapter 7

Conclusions

In our investigation into the stability and structure of a two dimensional boundary layer flow in a channel with a suction on the upper wall, we used several different techniques. The main goal of the thesis we have presented here is to develop the mathematical tools for computing the basic flow at large Reynolds numbers Re, identify the parameters which lead to a loss of flow stability and track bifurcations in separated flows. We solved the Navier-Stokes equations using global stability analysis combined with linear temporal simulation and the continuation algorithm to compute the steady state solutions and investigate the stability of a separated flow, as well as bifurcations. In the beginning, we employed Chebychev collocation in y-direction combined with finite difference method in x-direction to discretize the steady equations describing the flow. Newton linearization with correction terms were used to linearize the non linear equations which have resulted from this discretization, and finally we solved the emerging linear system of equations with a direct solver. This numerical technique had shown itself to be suitable for implementation in our main problem after having been tested in the work with the two test problems. The unique result of our study of this particular problem is the discovery and computation of two solutions and the turning

point as the solutions move from the lower to the upper branch. On the lower, first solution branch we found that a short separation bubble is the characteristic feature of the flow, whereas, on the second solution upper branch we had a large separation bubble. When we decreased the value of the Reynolds number Re the suction ratio β increased proportionately and caused the bubble on the lower branch to become larger, whereas, on the second solution upper branch, the result of an increase in the value of the Reynolds number Re was a decreasing suction ratio β and the subsequent enlargement of the separation bubble. This means that the length of the separation bubble depends on the size of the suction ratio β which, in turn, depends on the value of the Reynolds number.

Working with global stability analysis, we arrived at a generalized eigenvalue problem after having substituted the solutions from the basic flow into stability equations and discretized them. Then, we solved the emerging system using ARPACK, in order to obtain further eigenvalues and eigenvectors. The results of our computations using global stability analysis show that the flow became linearly stable with the first solution on the lower branch, but linearly unstable with the second solution on the upper branch. The smallest real part of the eigenvalue confirms the presence of the turning point as it changes signs while moving from the lower, stable solution branch to the upper, unstable solution branch. Flow stability results of the global stability analysis were further confirmed when we double-checked them using linear temporal simulation. When we compared the value of the smallest real part of the eigenvalue in the unstable solution on the upper branch with the results of the linear temporal simulation for various finite difference points m, we observed that the agreement is good. In addition, grid checks for convergence were performed for the stable solutions on the lower branch as well as the unstable solutions on the upper branch.

In our work with the two dimensional boundary layer flow in a channel with

a suction on the upper wall, we solved the steady Navier-Stokes equations with three different boundary conditions which we named case 1, 2, and 3, to determine their usefulness for our problem. The boundary conditions used in case 1 proved to be better than the ones we used in case 2 and 3 for solving our particular problem. Computations in the basic flow with the boundary conditions obtained in case 1 gave good results and these results were grid independent for different values of Reynolds number Re. In this instance, we observed only one solution where the length of the separation bubble depends on the suction ratio which depends on the value of the Reynolds number. This means that the separation bubble becomes larger with the increasing suction ratio, which itself is proportionate to the decrease in the value of the Reynolds number Re. Investigation of flow stability with global stability analysis and linear temporal simulation yielded that there is no linearly unstable mechanism in this result and the smallest real part of the eigenvalue never crosses the imaginary axis, meaning that the flow is linearly stable. Our numerical simulations showed us that the flow remained stable until $Re = 40000$, but became unstable when we increased this value.

Briefly, the general conclusions we arrived at in the current work are that the effect of an adverse pressure gradient produced by a suction port on the upper wall of a channel, leads to the separation of a laminar boundary layer with consequent formation of a separation bubble on the lower wall. The size of the separation bubble on the lower wall depends on the strength of the suction ratio which itself is dependent on the value of the Reynolds number Re. We observed as well that the solutions are subject to change in response to even the slightest modifications introduced in the boundary conditions. This is illustrated by the difference between the results obtained in chapter 4 and case 1, where we obtained two solutions and a turning point bifurcation in chapter 4, whereas case 1 yielded only one solution.

Comparisons between the results of our study and the available literature have been discussed in chapter 4. In all the cases studied here with their different boundary conditions we are in agreement with Alam & Sandham (2000) as to the separation bubble being located in the region of the strongest adverse pressure gradient, where the stronger suction results in producing a longer bubble. Some of our results, like, for example, our results in case 3, were not as suitable as the results obtained in chapter 4 and case 1 and therefore did not lend themselves to comparison with Alam & Sandham (2000), although the boundary conditions are similar. We also found our results to be in agreement with Cassel *et al.* (2007) in as far as an increase in the value of the Reynolds number Re produces a decrease in the critical suction ratio, as well as their description of the effect of a suction slot on the upper wall on the formation of a recirculation region in the lower wall.

7.1 Further Work

In this study we have presented new results in the computational tracking of bifurcations in a separated flow. Based on these results, and our general approach to the problem of flow stability, like the first time use of global stability analysis to calculate eigenvectors and eigenvalues for this particular problem, we feel that there is further work needed in the areas of globally unstable Tollmien-Schlichting modes. To pick up this kind of global instability modes, computations with much higher Reynolds numbers Re and more points of finite difference m, which means very fine grids, are needed. For the many possible applications in the real world, a three dimensional investigation would also be a valuable and challenging subject of further study, as might be solving the incompressible unsteady Navier-Stokes equations. and further investigating the stability of the unsteady, nonlinear flow.

Appendix A

Computational Details for the Second Test Problem

A.1 Discretization in x-Direction and y-Direction

Using discretization in x and y direction for the equations (3.70) and (3.71) to give the following discrete equation:

$$(D_y\psi)_{kj}\frac{\omega_{k+1j}-\omega_{k-1j}}{2\Delta x}-(D_y\omega)_{kj}\frac{\psi_{k+1j}-\psi_{k-1j}}{2\Delta x}=\frac{1}{Re}\frac{\omega_{k+1j}-2\omega_{kj}+\omega_{k-1j}}{(\Delta x)^2}$$
$$+\frac{1}{Re}\left(D_y^2\omega\right)_{kj}+F_1\left(x_k,y_j\right),$$

$$\omega_{kj}=\frac{\psi_{k+1j}-2\psi_{kj}+\psi_{k-1j}}{(\Delta x)^2}+\left(D_y^2\psi\right)_{kj},$$
$$1\le k\le m \qquad and \qquad 0\le j\le N. \tag{A.1}$$

The corresponding boundary conditions are given by

$$\begin{array}{llllll}
\psi_{1j}=0 & \& & \omega_{1j}=0 & \text{for} & x=0, & 0\leq j\leq N,\\
\psi_{mj}=0 & \& & \omega_{mj}=0 & \text{for} & x=\pi\ , & 0\leq j\leq N,\\
\psi_{k0}=0 & \& & \omega_{k0}=Re\sin x & \text{for} & y=0, & 1\leq k\leq m,\\
\psi_{kN}=e^{-Re^{\frac{1}{2}}}\sin(x) & \& & \omega_{kN}=(Re-1)\,e^{-Re^{\frac{1}{2}}}\sin(x) & \text{for} & y=1, & 1\leq k\leq m.
\end{array}$$

A.2 Linearizing the Equations

We have nonlinear equations (A.1) with their boundary conditions, so we need to use a Newton linearization and work with correction terms G_{kj} and H_{kj} where

$$\left\{\begin{array}{lcl}\psi_{kj} &=& \bar{\psi}_{kj}+G_{kj},\\ \omega_{kj} &=& \Omega_{kj}+H_{kj}\ ,\end{array}\right. \tag{A.2}$$

such that $|G_{kj}|\,,|H_{kj}\,|<<1$

By substituting (A.2) into (A.1) and their boundary conditions we obtain

$$\begin{aligned}&\left(D_y\,\bar{\psi}\right)_{kj}\frac{H_{k+1j}-H_{k-1j}}{2\Delta x}+\left(D_yG\right)_{kj}\frac{\Omega_{k+1j}-\Omega_{k-1j}}{2\Delta x}-\left(D_yH\right)_{kj}\frac{\bar{\psi}_{k+1j}-\bar{\psi}_{k-1j}}{2\Delta x}-\\ &\left(D_y\Omega\right)_{kj}\frac{G_{k+1j}-G_{k-1j}}{2\Delta x}-\frac{1}{Re}\frac{H_{k+1j}-2H_{kj}+H_{k-1j}}{(\Delta x)^2}-\frac{1}{Re}\left(D_y^2H\right)_{kj}=RB_{kj},\end{aligned} \tag{A.3}$$

where

$$\begin{aligned}RB_{kj} &= F_1\left(x_k,y_j\right)-\left(D_y\,\bar{\psi}\right)_{kj}\frac{\Omega_{k+1j}-\Omega_{k-1j}}{2\Delta x}+\left(D_y\Omega\right)_{kj}\frac{\bar{\psi}_{k+1j}-\bar{\psi}_{k-1j}}{2\Delta x}+\\ &\frac{1}{Re}\frac{\Omega_{k+1j}-2\Omega_{kj}+\Omega_{k-1j}}{(\Delta x)^2}+\frac{1}{Re}\left(D_y^2\Omega\right)_{kj},\end{aligned} \tag{A.4}$$

also we have

$$\frac{G_{k+1j}-2G_{kj}+G_{k-1j}}{(\Delta x)^2}+\left(D_y^2G\right)_{kj}-H_{kj}=(RA)_{kj}\,, \tag{A.5}$$

where

$$(RA)_{kj}=-\frac{\bar{\psi}_{k+1j}-2\,\bar{\psi}_{kj}+\bar{\psi}_{k-1j}}{(\Delta x)^2}-\left(D_y^2\,\bar{\psi}\right)_{kj}+\Omega_{kj}. \tag{A.6}$$

A.3 Solution of Discrete Equation

Let

$$T_k = \begin{pmatrix} G_k \\ H_k \end{pmatrix} \qquad \& \qquad G_k = \begin{pmatrix} G_{k0} \\ G_{k1} \\ \vdots \\ G_{kN} \end{pmatrix} \qquad \& \qquad H_k = \begin{pmatrix} H_{k0} \\ H_{k1} \\ \vdots \\ H_{kN} \end{pmatrix}. \quad \text{(A.7)}$$

Below is the form of the linear system which we obtain after Newton linearization

$$\mathbf{A}_k\mathbf{T}_{k-1} + \mathbf{B}_k\mathbf{T}_k + \mathbf{C}_k\mathbf{T}_{k+1} = \mathbf{R}_k \qquad 1 \le k \le m, \qquad \text{(A.8)}$$

where

$$\mathbf{A}_k = \begin{pmatrix} A_1 & A_2 \\ A_3 & A_4 \end{pmatrix},$$

$$\mathbf{B}_k = \begin{pmatrix} B_1 & B_2 \\ B_3 & B_4 \end{pmatrix},$$

$$\mathbf{C}_k = \begin{pmatrix} C_1 & C_2 \\ C_3 & C_4 \end{pmatrix},$$

$$\mathbf{R}_k = \begin{pmatrix} R_1 \\ R_2 \end{pmatrix}, \qquad \text{(A.9)}$$

where $\mathbf{T}_k$ in (A.8) is the vector of unknown streamfunction and vorticity.

The result of the linear system (A.8) when written in matrix form is:

$$\mathbf{JT} = \mathbf{R}, \qquad \text{(A.10)}$$

where

$$\mathbf{J} = \begin{bmatrix} \mathbf{B}_1 & \mathbf{C}_1 & & & & & & \\ \mathbf{A}_2 & \mathbf{B}_2 & \mathbf{C}_2 & & & & & \\ & \mathbf{A}_3 & \mathbf{B}_3 & \mathbf{C}_3 & & & & \\ & & \mathbf{A}_4 & \mathbf{B}_4 & \mathbf{C}_4 & & & \\ & & & \ddots & \ddots & \ddots & & \\ & & & & & \mathbf{A}_{m-1} & \mathbf{B}_{m-1} & \mathbf{C}_{m-1} \\ & & & & & & \mathbf{A}_m & \mathbf{B}_m \end{bmatrix}, \tag{A.11}$$

and

$\underline{\mathbf{T}}$ is a vector of correction terms to be found,

$\underline{\mathbf{R}}$ is a vector.

A.4 The Boundary Conditions

The boundary condition with Newton linearization becomes

$$\begin{array}{llll} G_{1j} = -\bar{\psi}_{1j} & H_{1j} = -\Omega_{1j} & \text{for} & x = 0, \\ G_{mj} = -\bar{\psi}_{mj} & H_{mj} = -\Omega_{mj} & \text{for} & x = \pi, \\ G_{k0} = -\bar{\psi}_{k0} & H_{k0} = Re \sin x_k - \Omega_{k0} & \text{for} & y = 0, \\ G_{kN} = e^{-Re^{\frac{1}{2}}} \sin(x_k) - \bar{\psi}_{kN} & H_{kN} = (Re-1)\, e^{-Re^{\frac{1}{2}}} \sin(x_k) - \Omega_{kN} & \text{for} & y = 1. \end{array}$$

As mentioned earlier the x boundary condition is implemented through the establishment of the matrix equations of the form (A.8) for the cases $k = 1$ and $k = m$. First though, the y boundary conditions are included in the problem and the final form of the matrices in (A.8) are given for $2 \leq k \leq m-1$.

Thus, the matrices for $2 \leq k \leq m-1$ are given by compare with (A.5) and the boundary condition

$$(\mathbf{A1})_k = \frac{1}{\Delta x^2}\mathbf{I}, \tag{A.12}$$

and

$$\begin{aligned} \mathbf{A1}_k(0,:) &= \mathbf{0}, \\ \mathbf{A1}_k(N,:) &= \mathbf{0}. \end{aligned} \tag{A.13}$$

$$(\mathbf{A2})_k = \mathbf{0}. \tag{A.14}$$

$$(\mathbf{B1})_k = \left(D_y^2\right) - \frac{2}{\Delta x^2}\mathbf{I}, \tag{A.15}$$

and

$$\begin{aligned} \mathbf{B1}_k(0,:) &= (1,0,\ldots,0), \\ \mathbf{B1}_k(N,:) &= (0,\ldots,0,1). \end{aligned} \tag{A.16}$$

$$(\mathbf{B2})_k = -\mathbf{I}, \tag{A.17}$$

and

$$\begin{aligned} \mathbf{B2}_k(0,:) &= \mathbf{0}, \\ \mathbf{B2}_k(N,:) &= \mathbf{0}. \end{aligned} \tag{A.18}$$

$$(\mathbf{C1})_k = \frac{1}{\Delta x^2}\mathbf{I}, \tag{A.19}$$

and

$$\begin{aligned} \mathbf{C1}_k(0,:) &= \mathbf{0}, \\ \mathbf{C1}_k(N,:) &= \mathbf{0}. \end{aligned} \tag{A.20}$$

$$(\mathbf{C2})_k = \mathbf{0}. \tag{A.21}$$

$$(\mathbf{R1})_k = \begin{pmatrix} -\bar{\psi}_{k0} \\ -\frac{\bar{\psi}_{k+1j}-2\bar{\psi}_{kj}+\bar{\psi}_{k-1j}}{(\Delta x)^2} - \left(D_y^2\,\bar{\psi}\right)_{kj} + \Omega_{kj} \\ e^{-Re^{\frac{1}{2}}}\sin(x_k) - \bar{\psi}_{kN} \end{pmatrix}.$$

Now, the matrices for $2 \leq k \leq m-1$ are given by comparison with (A.3) and the boundary condition

$$(\mathbf{A3})_k = \frac{1}{2\Delta x}\mathrm{diag}\left((\mathbf{D_y}\Omega)_{k,0}, (\mathbf{D_y}\Omega)_{k,1}, \ldots, (\mathbf{D_y}\Omega)_{k,j}, \ldots\right), \tag{A.22}$$

and

$$\begin{aligned} \mathbf{A3}_k(0,:) &= \mathbf{0}, \\ \mathbf{A3}_k(N,:) &= \mathbf{0}. \end{aligned} \tag{A.23}$$

$$(\mathbf{A4})_k = -\frac{1}{2\Delta x}\mathrm{diag}\left(\left(\mathbf{D_y}\,\bar{\psi}\right)_{k,0}, \left(\mathbf{D_y}\,\bar{\psi}\right)_{k,1}, \ldots, \left(\mathbf{D_y}\,\bar{\psi}\right)_{k,j}, \ldots\right) - \frac{1}{Re\Delta x^2}\mathbf{I}, \tag{A.24}$$

and

$$\begin{aligned} \mathbf{A4}_k(0,:) &= \mathbf{0}, \\ \mathbf{A4}_k(N,:) &= \mathbf{0}. \end{aligned} \tag{A.25}$$

$$\begin{aligned} (\mathbf{B3})_k = \frac{1}{2\Delta x}\mathrm{diag}\Big[&(\Omega_{k+1,0}-\Omega_{k-1,0}), (\Omega_{k+1,1}-\Omega_{k-1,1}), \ldots, \\ &(\Omega_{k+1,j}-\Omega_{k-1,j}), \ldots\Big]\mathbf{D_y}, \end{aligned} \tag{A.26}$$

and

$$\mathbf{B3}_k\left(0,:\right)=\mathbf{0},$$
$$\mathbf{B3}_k\left(N,:\right)=\mathbf{0}. \tag{A.27}$$

$$\left(\mathbf{B4}\right)_k=-\frac{1}{2\Delta x}\mathrm{diag}\Big[\left(\bar{\psi}_{k+1,0}-\bar{\psi}_{k-1,0}\right),\left(\bar{\psi}_{k+1,1}-\bar{\psi}_{k-1,1}\right),\ldots,$$
$$\left(\bar{\psi}_{k+1,j}-\bar{\psi}_{k-1,j}\right),\ldots\Big]\mathbf{D_y}+\frac{2}{Re\Delta x^2}\mathbf{I}-\frac{1}{Re}\left(\mathbf{D_y}^2\right), \tag{A.28}$$

and

$$\mathbf{B4}_k\left(0,:\right)=\left(1,0,\ldots,0\right),$$
$$\mathbf{B4}_k\left(N,:\right)=\left(0,\ldots,0,1\right). \tag{A.29}$$

$$\left(\mathbf{C3}\right)_k \;=\; -\frac{1}{2\Delta x}\mathrm{diag}\left(\left(\mathbf{D_y}\Omega\right)_{k,0},\left(\mathbf{D_y}\Omega\right)_{k,1},\ldots,\left(\mathbf{D_y}\Omega\right)_{k,j},\ldots\right), \tag{A.30}$$

and

$$\mathbf{C3}_k\left(0,:\right)=\mathbf{0},$$
$$\mathbf{C3}_k\left(N,:\right)=\mathbf{0}. \tag{A.31}$$

$$\left(\mathbf{C4}\right)_k=\frac{1}{2\Delta x}\mathrm{diag}\left(\left(\mathbf{D_y}\,\bar{\psi}\right)_{k,0},\left(\mathbf{D_y}\,\bar{\psi}\right)_{k,1},\ldots,\left(\mathbf{D_y}\,\bar{\psi}\right)_{k,j},\ldots\right)-\frac{1}{Re\Delta x^2}\mathbf{I}, \tag{A.32}$$

and

$$\mathbf{C4}_k\left(0,:\right)=\mathbf{0},$$
$$\mathbf{C4}_k\left(N,:\right)=\mathbf{0}. \tag{A.33}$$

$$(\mathbf{R2})_k = \begin{pmatrix} Re \sin x_k - \Omega_{k0} \\ RB_{kj} \\ (Re-1)\, e^{-Re^{\frac{1}{2}}} \sin(x_k) - \Omega_{kN} \end{pmatrix}.$$

Now, the matrices for $K = 1$ are given by

$$\mathbf{A}_1\mathbf{T}_0 + \mathbf{B}_1\mathbf{T}_1 + \mathbf{C}_1\mathbf{T}_2 = \mathbf{R}_1, \tag{A.34}$$

where

$$\begin{aligned} \mathbf{A}_1 &= \mathbf{0}, \\ \mathbf{B}_1 &= \mathbf{I}, \\ \mathbf{C}_1 &= \mathbf{0}, \end{aligned} \tag{A.35}$$

and

$$\mathbf{R}_1 = \begin{pmatrix} -\bar{\psi}_1 \\ -\Omega_1 \end{pmatrix}.$$

Now, the matrices for $k = m$ are given by

$$\mathbf{A}_m\mathbf{T}_{m-1} + \mathbf{B}_m\mathbf{T}_m + \mathbf{C}_m\mathbf{T}_{m+1} = \mathbf{R}_m, \tag{A.36}$$

$$\begin{aligned} \mathbf{A}_m &= \mathbf{0}, \\ \mathbf{B}_m &= \mathbf{I}, \\ \mathbf{C}_m &= \mathbf{0}, \end{aligned} \tag{A.37}$$

and

$$\mathbf{R}_m = \begin{pmatrix} -\bar{\psi}_m \\ -\Omega_m \end{pmatrix}.$$

A.5 Continuation

Here we use the continuation method which has been discussed in chapter one, to calculate the bifurcation diagram to follow the turning point. In section A.1 to A.4 we have obtained the solution for the test problem of Navier-Stokes equations.

Suppose we have a solution $\psi = \bar{\psi}$, $\omega = \Omega$ and $Re = \bar{Re}$, which is a solution to (A.1), for a given Re, by following the same method which has been used in chapter one we can find the unique solution $\mathbf{z}$ in the following equation

$$\mathbf{Jz} = -\frac{\partial \mathbf{f}}{\partial Re}. \tag{A.38}$$

Let us linearize with a perturbation (G_{kj}, H_{kj} and ΔRe) of the solution ($\bar{\psi}$, Ω and $\bar{Re}$) as

$$\begin{aligned} \psi_{kj} &= \bar{\psi}_{kj} + G_{kj} \qquad \text{where} \qquad |G_{kj}| \ll 1, \\ \omega_{kj} &= \Omega_{kj} + H_{kj} \qquad \text{where} \qquad |H_{kj}| \ll 1, \\ Re &= \bar{Re} + \Delta Re \qquad \text{where} \qquad |\Delta Re| \ll 1. \end{aligned} \tag{A.39}$$

Then, after linearizing for small $|G_{kj}|$, $|H_{kj}|$ and $|\Delta Re|$, substituting into (A.1) and neglecting the second-order terms we obtain

$$\begin{aligned} &\frac{H_{k+1j} - H_{k-1j}}{2\Delta x} \left(D_y \bar{\psi} \right)_{kj} + \left(D_y G \right)_{kj} \frac{\Omega_{k+1j} - \Omega_{k-1j}}{2\Delta x} - \left(D_y H \right)_{kj} \frac{\bar{\psi}_{k+1j} - \bar{\psi}_{k-1j}}{2\Delta x} \\ &- \frac{G_{k+1j} - G_{k-1j}}{2\Delta x} \left(D_y \Omega \right)_{kj} - \frac{1}{\bar{Re}} \frac{H_{k+1j} - 2H_{kj} + H_{k-1j}}{(\Delta x)^2} - \frac{1}{\bar{Re}} \left(D_y^2 H \right)_{kj} \\ &+ \left(\frac{\Delta Re}{\bar{Re}^2} \right) \left(D_y^2 \Omega \right)_{kj} + \left(\frac{\Delta Re}{\bar{Re}^2} \right) \frac{\Omega_{k+1j} - 2\Omega_{kj} + \Omega_{k-1j}}{(\Delta x)^2} = RB_{kj}, \end{aligned} \tag{A.40}$$

where

$$RB_{kj} = F_1(x_k, y_j) - \frac{\Omega_{k+1j} - \Omega_{k-1j}}{2\Delta x}\left(D_y\,\bar{\psi}\right)_{kj} + \left(D_y\Omega\right)_{kj}\frac{\bar{\psi}_{k+1j} - \bar{\psi}_{k-1j}}{2\Delta x} + \frac{1}{\bar{Re}}\frac{\Omega_{k+1j} - 2\Omega_{kj} + \Omega_{k-1j}}{(\Delta x)^2} + \frac{1}{\bar{Re}}\left(D_y^2\Omega\right)_{kj}, \tag{A.41}$$

and

$$\frac{G_{k+1j} - 2G_{kj} + G_{k-1j}}{(\Delta x)^2} + \left(D_y^2 G\right)_{kj} - H_{kj} = (RA)_{kj}, \tag{A.42}$$

where

$$(RA)_{kj} = -\frac{\bar{\psi}_{k+1j} - 2\,\bar{\psi}_{kj} + \bar{\psi}_{k-1j}}{(\Delta x)^2} - \left(D_y^2\,\bar{\psi}\right)_{kj} + \Omega_{kj}, \tag{A.43}$$

with the boundary condition

$$\begin{array}{llll}
\text{for} & x = 0, & G_{1j} = -\,\bar{\psi}_{1j} \quad H_{1j} = -\Omega_{1j} & 0 \le j \le N, \\
\text{for} & x = \pi, & G_{mj} = -\,\bar{\psi}_{mj} \quad H_{mj} = -\Omega_{mj} & 0 \le j \le N, \\
\text{for} & y = 0, & G_{k0} = -\,\bar{\psi}_{k0} \quad H_{k0} - (\Delta Re)\sin(x_k) = \bar{Re}\sin x_k - \Omega_{k0} & 1 \le k \le\ m,
\end{array}$$

$$\begin{array}{ll}
\text{for } y = 1, & G_{kN} + (\Delta Re)\left(\frac{\bar{Re}^{\frac{-1}{2}}}{2}\right)e^{-\bar{Re}^{\frac{1}{2}}}\sin(x_k) = e^{-\bar{Re}^{\frac{1}{2}}}\sin(x_k) - \bar{\psi}_{kN}, \\
\text{for } y = 1, & H_{kN} - (\Delta Re)\,e^{-\bar{Re}^{\frac{1}{2}}}\sin(x_k) + (\Delta Re)\left(\bar{Re} - 1\right)\left(\frac{\bar{Re}^{\frac{-1}{2}}}{2}\right)e^{-\bar{Re}^{\frac{1}{2}}}\sin(x_k) \\
= \left(\bar{Re} - 1\right)e^{-\bar{Re}^{\frac{1}{2}}}\sin(x_k) - \Omega_{kN} & 1 \le k \le\ m.
\end{array}$$

Let

$$T_k = \begin{pmatrix} G_k \\ H_k \end{pmatrix} \quad \& \quad G_k = \begin{pmatrix} G_{k0} \\ G_{k1} \\ \vdots \\ G_{kN} \end{pmatrix} \quad \& \quad H_k = \begin{pmatrix} H_{k0} \\ H_{k1} \\ \vdots \\ H_{kN} \end{pmatrix}.$$

Thus, we obtain a linear system of the form

$$\mathbf{A}_k\mathbf{T}_{k-1} + \mathbf{B}_k\mathbf{T}_k + \mathbf{C}_k\mathbf{T}_{k+1} + \mathbf{D}_k\Delta Re_k = \mathbf{R}_k \qquad 1 \le k \le m. \tag{A.44}$$

Then we rewrite this equation as

$$\left(\mathbf{J} \qquad \frac{\partial \mathbf{f}}{\partial Re}\right)(\mathbf{T} \qquad \Delta Re)^T = \mathbf{R}, \tag{A.45}$$

where

$$\mathbf{J} = \begin{bmatrix} \mathbf{B}_1 & \mathbf{C}_1 & & & & & \\ \mathbf{A}_2 & \mathbf{B}_2 & \mathbf{C}_2 & & & & \\ & \mathbf{A}_3 & \mathbf{B}_3 & \mathbf{C}_3 & & & \\ & & \mathbf{A}_4 & \mathbf{B}_4 & \mathbf{C}_4 & & \\ & & & \ddots & \ddots & \ddots & \\ & & & & \mathbf{A}_{m-1} & \mathbf{B}_{m-1} & \mathbf{C}_{m-1} \\ & & & & & \mathbf{A}_m & \mathbf{B}_m \end{bmatrix}, \tag{A.46}$$

$$\left(\frac{\partial \mathbf{f}}{\partial Re}\right) = (\mathbf{D}_1, \mathbf{D}_2, \ldots, \mathbf{D}_m)^T, \tag{A.47}$$

$$\mathbf{D}_k = \begin{pmatrix} \mathbf{L1}_k \\ \mathbf{L2}_k \end{pmatrix}, \tag{A.48}$$

$$\mathbf{L1}_k = (L1_{k0}, L1_{k1}, \ldots, L1_{kN})^T,$$

$$\mathbf{L2}_k = (L2_{k0}, L2_{k1}, \ldots, L2_{kN})^T,$$

and

$\mathbf{L1}_1 = \mathbf{L1}_m = \mathbf{L2}_1 = \mathbf{L2}_m = 0,$

$$\begin{aligned} L1_{kj} &= 0, \\ L1_{k0} &= 0, \\ L1_{kN} &= \left(\frac{\bar{Re}^{\frac{-1}{2}}}{2}\right) e^{-\bar{Re}^{\frac{1}{2}}} \sin(x_k), \end{aligned} \tag{A.49}$$

$$(L2)_{kj} = \left(\frac{1}{\bar{Re}^{\,2}}\right)\left(D_y^2\Omega\right)_{kj} + \left(\frac{1}{\bar{Re}^{\,2}}\right)\frac{\Omega_{k+1j} - 2\Omega_{kj} + \Omega_{k-1j}}{(\Delta x)^2}, \tag{A.50}$$

$$\begin{aligned} L2_{k0} &= -\sin(x_k), \\ L2_{kN} &= -e^{-\bar{Re}^{\frac{1}{2}}}\sin(x_k) + \left(\bar{Re} - 1\right)\left(\frac{\bar{Re}^{\frac{-1}{2}}}{2}\right)e^{-\bar{Re}^{\frac{1}{2}}}\sin(x_k). \end{aligned} \tag{A.51}$$

Having found $\left(\frac{\partial \mathbf{f}}{\partial Re}\right)$ from (A.47) we solve equation (A.38) to find the unique solution $\mathbf{z}$, and obtain $\frac{d\mathbf{T}}{ds}$ and $\frac{dRe}{ds}$ where

$$\frac{dRe}{ds} = \pm\frac{1}{\sqrt{\mathbf{z}^T\mathbf{z} + 1}}, \tag{A.52}$$

$$\frac{d\mathbf{T}}{ds} = \pm\frac{\mathbf{z}}{\sqrt{\mathbf{z}^T\mathbf{z} + 1}}. \tag{A.53}$$

After we obtain $\frac{d\mathbf{T}}{ds}$ and $\frac{dRe}{ds}$ the branch is continued by determining the appropriate choice of sign and we can update the initial iterate for Newton's method as

$$\mathbf{T}^{(0)} = \bar{\mathbf{T}} + \left(\frac{d\mathbf{T}}{ds}\right)\Delta s, \tag{A.54}$$

$$Re^{(0)} = \bar{Re} + \left(\frac{dRe}{ds}\right)\Delta s, \tag{A.55}$$

where is Δs is chosen.

As in the previous work in chapter 1, from the predictor step and the corrector we have obtained the solution for $\mathbf{a}$ and $\mathbf{b}$, being temporary vectors and we use them to obtain the new updates for ΔRe and $\Delta\mathbf{T}$.

A.6 The Turning Point Tracking Algorithm

Now, to track a turning point as a function of Re, we follow the bordering algorithm which has been disccussed in section (3.2.5). Therefore, the four linear

equations that are to be solved are equation (3.53) to equation (3.56), except that the parameter is Re instead of λ and $\mathbf{x}$ instead of $\boldsymbol{\theta}$. Equations (3.53) to (3.56) thus become

$$\mathbf{Ja} = -\mathbf{f}, \tag{A.56}$$

$$\mathbf{Jb} = -\frac{\partial \mathbf{f}}{\partial Re}, \tag{A.57}$$

$$\mathbf{Jc} = -\frac{\partial \mathbf{Jy}}{\partial \mathbf{x}}\mathbf{a}, \tag{A.58}$$

$$\mathbf{Jd} = -\frac{\partial \mathbf{Jy}}{\partial \mathbf{x}}\mathbf{b} - \frac{\partial \mathbf{Jy}}{\partial Re}, \tag{A.59}$$

where $\mathbf{a}, \mathbf{b}, \mathbf{c}$ and $\mathbf{d}$ are temporary vectors.

From the previous work in this section we obtain $\mathbf{a}$ and $\mathbf{b}$, when we use continuation method, we now want to obtain $\frac{\partial \mathbf{Jy}}{\partial \mathbf{x}}\mathbf{a}$.

First note that $\mathbf{J}(\boldsymbol{\psi}, Re)\,\mathbf{y}$ is given by

$$\mathbf{J}(\boldsymbol{\psi}, Re)\,\mathbf{y} = (\mathbf{J}_1, \ldots, \mathbf{J}_m)^T, \tag{A.60}$$

where

$$\mathbf{J}_k = \mathbf{A}_k(\boldsymbol{\psi})\,\mathbf{y}_{k-1} + \mathbf{B}_k(\boldsymbol{\psi})\,\mathbf{y}_k + \mathbf{C}_k(\boldsymbol{\psi})\,\mathbf{y}_{k+1}, \tag{A.61}$$

and coefficient matrices $\mathbf{A}_k$, $\mathbf{B}_k$, $\mathbf{C}_k$, have been defined earlier in section (A.4).

Now, the vector $\frac{\partial \mathbf{J}(\boldsymbol{\psi}, Re)}{\partial \boldsymbol{\psi}}\mathbf{ya}$ is defined by

$$\frac{\partial \mathbf{J}(\boldsymbol{\psi}, Re)}{\partial \boldsymbol{\psi}}\mathbf{ya} = \lim_{\sigma \to 0} \frac{\mathbf{J}(\boldsymbol{\psi} + \sigma\mathbf{a}, Re)\,\mathbf{y} - \mathbf{J}(\boldsymbol{\psi}, Re)\,\mathbf{y}}{\sigma}. \tag{A.62}$$

Let us write

$$\mathbf{y} = (\mathbf{y}_1, \ldots, \mathbf{y}_m)^T, \tag{A.63}$$

with

$$\mathbf{y}_k = (\mathbf{G}_k, \mathbf{H}_k)^T, \tag{A.64}$$

and

$$\mathbf{G}_k = \left(\mathbf{G}_{k0}, \ldots, \mathbf{G}_{kN}\right)^T, \tag{A.65}$$

$$\mathbf{H}_k = \left(\mathbf{H}_{k0}, \ldots, \mathbf{H}_{kN}\right)^T, \tag{A.66}$$

$$\tag{A.67}$$

and also

$$\mathbf{a} = \left(\boldsymbol{\alpha}_1, \boldsymbol{\beta}_1, \ldots, \boldsymbol{\alpha}_k, \boldsymbol{\beta}_k, \ldots, \boldsymbol{\alpha}_m, \boldsymbol{\beta}_m\right)^T, \tag{A.68}$$

$$\boldsymbol{\alpha}_k = \left(\boldsymbol{\alpha}_{k0}, \ldots, \boldsymbol{\alpha}_{kN}\right)^T, \tag{A.69}$$

$$\boldsymbol{\beta}_k = \left(\boldsymbol{\beta}_{k0}, \ldots, \boldsymbol{\beta}_{kN}\right)^T. \tag{A.70}$$

Then

$$\mathbf{J}\left(\boldsymbol{\psi}, Re\right)\mathbf{y} = \left(\mathbf{J}_1, \ldots, \mathbf{J}_k, \ldots, \mathbf{J}_m\right)^T, \tag{A.71}$$

with

$$\mathbf{J}_k = \left(\mathbf{J1}_k, \mathbf{J2}_k\right)^T, \tag{A.72}$$

and

$$\mathbf{J1}_k = \left(\mathbf{J1}_{k0}, \ldots, \mathbf{J1}_{kN}\right)^T, \tag{A.73}$$

$$\mathbf{J2}_k = \left(\mathbf{J2}_{k0}, \ldots, \mathbf{J2}_{kN}\right)^T, \tag{A.74}$$

$$\tag{A.75}$$

From earlier we note that,

$$\mathbf{J1}_{kj} = \frac{G_{k+1j} - 2G_{kj} + G_{k-1j}}{\left(\Delta x\right)^2} + \left(D_y^2 G_k\right)_{kj} - H_{kj}, \tag{A.76}$$

and

$$\mathbf{J2}_{kj} = \frac{H_{k+1j} - H_{k-1j}}{2\Delta x}\left(D_y\,\bar{\psi}_k\right)_{kj} + \left(D_y G_k\right)_{kj}\frac{\Omega_{k+1j} - \Omega_{k-1j}}{2\Delta x} - \left(D_y H_k\right)_{kj}$$
$$\frac{\bar{\psi}_{k+1j} - \bar{\psi}_{k-1j}}{2\Delta x} - \frac{G_{k+1j} - G_{k-1j}}{2\Delta x}\left(D_y\Omega_k\right)_{kj} - \frac{1}{\bar{Re}}\frac{H_{k+1j} - 2H_{kj} + H_{k-1j}}{\left(\Delta x\right)^2} - \frac{1}{\bar{Re}}\left(D_y^2 H_k\right)_{kj} \tag{A.77}$$

Since the dependence of $\mathbf{J}(\boldsymbol{\psi})$ on $\boldsymbol{\psi}$ is linear we see that

$$\frac{\partial \mathbf{J}(\boldsymbol{\psi}, Re)}{\partial \boldsymbol{\psi}}\mathbf{ya} = (\mathbf{P}_1, \ldots, \mathbf{P}_k, \ldots, \mathbf{P}_m)^T, \tag{A.78}$$

where

$$\mathbf{P}_k = (\mathbf{P1}_k, \mathbf{P2}_k)^T, \tag{A.79}$$

and

$$\mathbf{P1}_k = (\mathbf{P1}_{k0}, \ldots, \mathbf{P1}_{kN})^T, \tag{A.80}$$

$$\mathbf{P2}_k = (\mathbf{P2}_{k0}, \ldots, \mathbf{P2}_{kN})^T. \tag{A.81}$$

The calculation of the limit shows that

$$\mathbf{P1}_{kj} = \mathbf{0}. \tag{A.82}$$

$$\mathbf{P2}_{kj} = \frac{H_{k+1j} - H_{k-1j}}{2\Delta x}(D_y\boldsymbol{\alpha}_k)_{kj} + (D_yG)_{kj}\frac{\boldsymbol{\beta}_{k+1j} - \boldsymbol{\beta}_{k-1j}}{2\Delta x} - (D_yH)_{kj}$$
$$\frac{\boldsymbol{\alpha}_{k+1j} - \boldsymbol{\alpha}_{k-1j}}{2\Delta x} - \frac{G_{k+1j} - G_{k-1j}}{2\Delta x}(D_y\boldsymbol{\beta}_k)_{kj}, \tag{A.83}$$

$$2 \le k \le m-1,$$

$$1 \le j \le N-1, \tag{A.84}$$

and

$$\mathbf{P2}_{kj} = \mathbf{0} \qquad \text{otherwise.} \tag{A.85}$$

In the same way, but using $\mathbf{b}$ instead of $\mathbf{a}$ we obtain $\left[\frac{\partial \mathbf{Jy}}{\partial \mathbf{x}}\mathbf{b}\right]_{kj}$.

Also, by following the same way for $\mathbf{J}$ and since the dependence of $\mathbf{J}(Re)$ on Re is linear we have calculated $\left[\frac{\partial \mathbf{Jy}}{\partial Re}\right]_{kj}$ as

$$\left[\frac{\partial \mathbf{Jy}}{\partial Re}\right] = (\mathbf{E}_1, \ldots, \mathbf{E}_k, ..., \mathbf{E}_m)^T, \tag{A.86}$$

where

$$\mathbf{E}_k = (\mathbf{E1}_k, \mathbf{E2}_k)^T, \tag{A.87}$$

and

$$\mathbf{E1}_k = (\mathbf{E1}_{k0}, \ldots, \mathbf{E1}_{kN})^T, \tag{A.88}$$

$$\mathbf{E2}_k = (\mathbf{E2}_{k0}, \ldots, \mathbf{E2}_{kN})^T. \tag{A.89}$$

The calculation of the limit shows that

$$\mathbf{E1}_{kj} = \mathbf{0}. \tag{A.90}$$

$$\mathbf{E2}_{kj} = \frac{1}{\bar{R}\, e^2} \frac{H_{k+1j} - 2H_{kj} + H_{k-1j}}{(\Delta x)^2} + \frac{1}{\bar{R}\, e^2} \left(D_y^2 H\right)_{kj}, \tag{A.91}$$

$$2 \le k \le m-1$$

$$1 \le j \le N-1, \tag{A.92}$$

and

$$\mathbf{E2}_{kj} = \mathbf{0} \qquad \text{otherwise.} \tag{A.93}$$

Thus, by substituting the values into equations (A.58) and (A.59) we can obtain $\mathbf{c}$ and $\mathbf{d}$.

We can calculate the correction terms from all values for the variables $\mathbf{a}$, $\mathbf{b}$, $\mathbf{c}$ and $\mathbf{d}$, which we have obtained already, such that

$$\Delta Re = \frac{1 - \phi \cdot \mathbf{c}}{\phi \cdot \mathbf{d}}, \tag{A.94}$$

$$\Delta \mathbf{T} = \mathbf{a} + \Delta Re \mathbf{b}, \tag{A.95}$$

$$\Delta \mathbf{y} = \mathbf{c} + \Delta Re \mathbf{d} - \mathbf{y}. \tag{A.96}$$

At last, by these results we can obtain the values of $\mathbf{T}$, $\mathbf{y}$, and Re such that

$$\begin{aligned} \mathbf{T} &= \bar{\mathbf{T}} + \Delta\mathbf{T}, \\ Re &= \bar{Re} + \Delta Re, \\ \mathbf{y} &= \bar{\mathbf{y}} + \Delta\mathbf{y}. \end{aligned}$$

As demonstrated earlier in section (3.2.5), we can converge to the next turning point at the next value of a second parameter.

Appendix B

Computational Details for the BC's (Case 1)

The boundary conditions with Newton linearization for case 1 become

$$\begin{aligned}
&\text{for} \quad y = 0, \qquad G_{k0} = -\bar{\psi}_{k0}, \qquad \left(\tfrac{dz}{dy}\right)(\mathbf{D_z}G)_{k0} = -\tfrac{dz}{dy}\mathbf{D_z}\,\bar{\psi}_{k0},\\
&\text{for} \quad y = y_{max}, \qquad G_{kN} = -\bar{\psi}_{kN} + \beta\hat{\psi}_s + y_{max}, \qquad H_{kN} = -\Omega_{kN} + \beta\hat{\omega}_s,\\
&\text{for} \quad x = 0, \qquad G_{1j} = -\bar{\psi}_{1j} + y_j, \qquad H_{1j} = -\Omega_{1j},\\
&\text{for} \quad x = \infty, \qquad G_{mj} = -\bar{\psi}_{mj} + \tfrac{y_{max}}{2}(1-\beta)\left(\tfrac{y_j}{y_{max}}\right)^2\left(3 - \tfrac{y_j}{y_{max}}\right),\\
&\text{for} \quad x = \infty, \qquad H_{mj} = -\Omega_{mj} + \tfrac{3}{y_{max}}(1-\beta)\left(1 - \tfrac{y_j}{y_{max}}\right).
\end{aligned}$$

Thus, the matrices for $2 \le k \le m-1$ are given by comparison with (4.19) and the boundary conditions

$$(\mathbf{A1})_k = -\left(\frac{d^2\xi}{dx^2}\right)\frac{1}{2\Delta\xi}\mathbf{I} + \left(\frac{d\xi}{dx}\right)^2\frac{1}{\Delta\xi^2}\mathbf{I}, \tag{B.1}$$

and

$$\begin{aligned}
\mathbf{A1}_k\,(0,:) &= \mathbf{0},\\
\mathbf{A1}_k\,(N,:) &= \mathbf{0}.
\end{aligned} \tag{B.2}$$

$$(\mathbf{A2})_k = \mathbf{0}. \tag{B.3}$$

$$(\mathbf{B1})_k = \left(\frac{d^2z}{dy^2}\right)(\mathbf{D_z}) + \left(\frac{dz}{dy}\right)^2 (\mathbf{D_z}^2) - \left(\frac{d\xi}{dx}\right)^2 \frac{2}{\Delta\xi^2}\mathbf{I}, \tag{B.4}$$

and

$$\begin{aligned} \mathbf{B1}_k(0,:) &= (1,0,\ldots,0), \\ \mathbf{B1}_k(N,:) &= (0,\ldots,0,1). \end{aligned} \tag{B.5}$$

$$(\mathbf{B2})_k = -\mathbf{I}, \tag{B.6}$$

and

$$\begin{aligned} \mathbf{B2}_k(0,:) &= \mathbf{0}, \\ \mathbf{B2}_k(N,:) &= \mathbf{0}. \end{aligned} \tag{B.7}$$

$$(\mathbf{C1})_k = \left(\frac{d^2\xi}{dx^2}\right)\frac{1}{2\Delta\xi}\mathbf{I} + \left(\frac{d\xi}{dx}\right)^2 \frac{1}{\Delta\xi^2}\mathbf{I}, \tag{B.8}$$

and

$$\begin{aligned} \mathbf{C1}_k(0,:) &= \mathbf{0}, \\ \mathbf{C1}_k(N,:) &= \mathbf{0}. \end{aligned} \tag{B.9}$$

$$(\mathbf{C2})_k = \mathbf{0}. \tag{B.10}$$

$$(\mathbf{R1})_k = \begin{pmatrix} -\bar{\psi}_{k0} \\ (RA)_{kj} \\ -\bar{\psi}_{kN} + \beta\hat{\psi}_s + y_{max} \end{pmatrix}.$$

Now, the matrices for $2 \leq k \leq m-1$ are given by comparison with (4.17) and the boundary conditions

$$(\mathbf{A3})_k = \left(\frac{dz}{dy}\right) \mathrm{diag}\left((\mathbf{D_z}\Omega)_{k,0}, (\mathbf{D_z}\Omega)_{k,1}, \ldots, (\mathbf{D_z}\Omega)_{k,j}, \ldots\right) \left(\frac{d\xi}{dx}\right) \frac{1}{2\Delta\xi}\mathbf{I}, \tag{B.11}$$

and

$$\begin{aligned} \mathbf{A3}_k(0,:) &= \mathbf{0}, \\ \mathbf{A3}_k(N,:) &= \mathbf{0}. \end{aligned} \tag{B.12}$$

$$\begin{aligned} (\mathbf{A4})_k = & -\left(\frac{dz}{dy}\right) \mathrm{diag}\left(\left(\mathbf{D_z}\,\bar{\psi}\right)_{k,0}, \left(\mathbf{D_z}\,\bar{\psi}\right)_{k,1}, \ldots, \left(\mathbf{D_z}\,\bar{\psi}\right)_{k,j}, \ldots\right) \\ & \left(\frac{d\xi}{dx}\right) \frac{1}{2\Delta\xi}\mathbf{I} - \frac{1}{Re\Delta\xi^2}\left(\frac{d\xi}{dx}\right)^2 \mathbf{I} + \frac{1}{2Re\Delta\xi}\left(\frac{d^2\xi}{dx^2}\right)\mathbf{I}, \end{aligned} \tag{B.13}$$

and

$$\begin{aligned} \mathbf{A4}_k(0,:) &= \mathbf{0}, \\ \mathbf{A4}_k(N,:) &= \mathbf{0}. \end{aligned} \tag{B.14}$$

$$\begin{aligned} (\mathbf{B3})_k = & \left(\frac{d\xi}{dx}\right) \frac{1}{2\Delta\xi}\mathrm{diag}\Big[\left(\Omega_{k+1,0} - \Omega_{k-1,0}\right), \left(\Omega_{k+1,1} - \Omega_{k-1,1}\right), \ldots, \\ & \left(\Omega_{k+1,j} - \Omega_{k-1,j}\right), \ldots\Big] \left(\frac{dz}{dy}\right) \mathbf{D_z}, \end{aligned} \tag{B.15}$$

and

$$\begin{aligned} \mathbf{B3}_k(0,:) &= \left(\frac{dz}{dy}\right)\mathbf{D_z}, \\ \mathbf{B3}_k(N,:) &= (0,\ldots,0,1). \end{aligned} \tag{B.16}$$

$$
\begin{aligned}
(\mathbf{B4})_k &= -\left(\frac{d\xi}{dx}\right)\frac{1}{2\Delta\xi}\mathrm{diag}\Big[\left(\bar{\psi}_{k+1,0}-\bar{\psi}_{k-1,0}\right),\left(\bar{\psi}_{k+1,1}-\bar{\psi}_{k-1,1}\right),\ldots,\\
&\quad \left(\bar{\psi}_{k+1,j}-\bar{\psi}_{k-1,j}\right),\ldots\Big]\left(\frac{dz}{dy}\right)(\mathbf{D_z})+\frac{2}{Re\Delta\xi^2}\left(\frac{d\xi}{dx}\right)^2\mathbf{I}\\
&\quad -\frac{1}{Re}\left(\frac{dz}{dy}\right)^2(\mathbf{D_z}^2)-\frac{1}{Re}\left(\frac{d^2z}{dy^2}\right)\mathbf{D_z},
\end{aligned}
\tag{B.17}
$$

and

$$
\begin{aligned}
\mathbf{B4}_k(0,:)&=\mathbf{0},\\
\mathbf{B4}_k(N,:)&=\mathbf{0}.
\end{aligned}
\tag{B.18}
$$

$$
(\mathbf{C3})_k = -\left(\frac{dz}{dy}\right)\mathrm{diag}\left((\mathbf{D_z}\Omega)_{k,0},(\mathbf{D_z}\Omega)_{k,1},\ldots,(\mathbf{D_z}\Omega)_{k,j},\ldots\right)\left(\frac{d\xi}{dx}\right)\frac{1}{2\Delta\xi}\mathbf{I},
\tag{B.19}
$$

and

$$
\begin{aligned}
\mathbf{C3}_k(0,:)&=\mathbf{0},\\
\mathbf{C3}_k(N,:)&=\mathbf{0}.
\end{aligned}
\tag{B.20}
$$

$$
\begin{aligned}
(\mathbf{C4})_k &= \left(\frac{dz}{dy}\right)\mathrm{diag}\left(\left(\mathbf{D_z}\,\bar{\psi}\right)_{k,0},\left(\mathbf{D_z}\,\bar{\psi}\right)_{k,1},\ldots,\left(\mathbf{D_z}\,\bar{\psi}\right)_{k,j},\ldots\right)\\
&\quad \left(\frac{d\xi}{dx}\right)\frac{1}{2\Delta\xi}\mathbf{I}-\frac{1}{Re\Delta\xi^2}\left(\frac{d\xi}{dx}\right)^2\mathbf{I}-\frac{1}{2Re\Delta\xi}\left(\frac{d^2\xi}{dx^2}\right)\mathbf{I},
\end{aligned}
\tag{B.21}
$$

and

$$
\begin{aligned}
\mathbf{C4}_k(0,:)&=\mathbf{0},\\
\mathbf{C4}_k(N,:)&=\mathbf{0}.
\end{aligned}
\tag{B.22}
$$

$$(\mathbf{R2})_k = \begin{pmatrix} -\left(\frac{dz}{dy}\right)\left(\mathbf{D_z}\ \bar{\psi}\right)_{k0} \\ RB_{kj} \\ -\Omega_{kN} + \beta\hat{\omega}_s \end{pmatrix}.$$

Now, the matrices for $K = 1$ are given by

$$\mathbf{A}_1\mathbf{T}_0 + \mathbf{B}_1\mathbf{T}_1 + \mathbf{C}_1\mathbf{T}_2 = \mathbf{R}_1, \tag{B.23}$$

where

$$\begin{aligned} \mathbf{A}_1 &= \mathbf{0}, \\ \mathbf{B1}_1 = \mathbf{B4}_1 &= \mathbf{I}, \\ \mathbf{C}_1 &= \mathbf{0}, \end{aligned} \tag{B.24}$$

and

$$\mathbf{R}_1 = \begin{pmatrix} -\bar{\psi}_{1j} + y_j \\ -\Omega_{1j} \end{pmatrix}.$$

Now, the matrices for $k = m$ are given by

$$\mathbf{A}_m\mathbf{T}_{m-1} + \mathbf{B}_m\mathbf{T}_m + \mathbf{C}_m\mathbf{T}_{m+1} = \mathbf{R}_m, \tag{B.25}$$

$$\begin{aligned} \mathbf{A}_m &= \mathbf{0}, \\ \mathbf{B1}_m = \mathbf{B4}_m &= \mathbf{I}, \\ \mathbf{C}_m &= \mathbf{0}, \end{aligned} \tag{B.26}$$

and

$$\mathbf{R}_m = \begin{pmatrix} -\bar{\psi}_{mj} + \frac{y_{max}}{2}(1-\beta)\left(\frac{y_j}{y_{max}}\right)^2\left(3 - \frac{y_j}{y_{max}}\right) \\ -\Omega_{mj} + \frac{3}{y_{max}}(1-\beta)\left(1 - \frac{y_j}{y_{max}}\right) \end{pmatrix}.$$

Bibliography

Alam, M. & Sandham, N. D. 2000 Direct numerical simulation of 'short' laminar separation bubbles with turbulent reattachment. *J. Fluid Mech* **403**, 223–250.

Allgower, E. L. & Georg, K. 1990 *Numerical Continuation Methods*. Springer-Verlag.

Anderson, J. D. 2005 Ludwig prandtl's boundary layer. *J. American Institute of Physics* pp. 42–48.

Bazley, N. W. & Wake, G. C. 1978 The disappearance of criticality in the theory of thermal ignition. *ZAMP.* **29**, 971–976.

Boppana, V. B. L. 2007 *Flow Instability in a Lid-Driven Cavity and Circular Cylinder Cascade*. Ph.D. Thesis, University of Manchester.

Braun, S. 2006 *Recent Developments in the Asymptotic Theory of Separated Flows*. The Leverholme Trust and Manchester Institute of Mathematical Sciences.

Briley, W. R. 1971 A numerical study of laminar separation bubbles using the navier-stokes equations. *J. Fluid Mech* **47**, 713–736.

Burden, R. L. & Faires, J. D. 2001 *Numerical Analysis*. Brooks/Cole.

Canuto, C., Hussaini, M. Y., Quarteroni, A. & Zang, T. A. 1987 *Spectral Methods in Fluid Dynamics*. Springer.

Cassel, K. W., Sardesai, C., Braun, S. & Ruban, A. I. 2007 Sub-optimal control of unsteady separation in a channel. *American Physics Society, 60th Annual Meeting of the Divison of Fluid Dynamics* pp. 1–10.

Cliffe, K. A., Spence, A. & Tavener, S. J. 2000 The numerical analysis of bifurcation problems with application to fluid mechanics. *J. Acta Numerica.* pp. 39–132.

Conte, S. D. & de Boor, C. 1981 *Elementary Numerical Analysis , An Algorithmic Approach*. McGraw-Hill International Editions.

Degani, A. T., Li, Q. & Walker, J. D. A. 1996 Unsteady separation from the leading edge of a thin airfoil. *J. Phys. Fluid* **8**, 704–714.

Doedel, E. J. & Kernevez, J. P. 1986 *AUTO: Software for Continuation and Bifurcation Problems in Ordinary Differential Equations*. Caltech, Pasadena.

Fornberg, B. 1996 *A Practical Guide to Pseudospectral Methods*. Cambridge University Press.

Gajjar, J. S. B. & Azzam, N. A. 2004 Numerical solution of the navier-stokes equations for the flow in a cylinder cascade. *J. Fluid Mech.* **520**, 51–82.

Gaster, M. 1966 The structure and behavior of laminar separation bubbles. *AGARD CP* **4**, 830–854.

Govaerts, W. J. F. 2000 *Numerical Methods for Bifurcations of Dynamical Equilibria*. SIAM.

Haselgrove, C. B. 1961 The solution of nonlinear equations and of differential equations with two-point boundary conditions. *J. Comput.* **4**, 255–259.

Horton, H. P. 1968 *Laminar Separation in Two and Three-Dimensional Incompressible Flow*. Ph.D. Thesis, University of London.

Hsiao, C. T. & Pauley, L. L. 1994 Comparison of the triple-deck theory, interactive boundary layer method, and navier-stokes computation for marginal separation. *J. Fluid Engineering* **116**, 22–28.

Jones, B. M. 1938 Stalling. *J. R. Aero. Soc* **38**, 747–770.

Keller, H. B. 1977 *Numerical solution of bifurcation and nonlinear eigenvalue problems, in Application of Bifurcation Theory (P. Rabinowitz, ed.)*. Academic Press, New York, pp. 359-384.

Klopfenstein, R. W. 1961 Zeros of nonlinear functions. *J. Assoc. Comput.* **8**, 366–1961.

Lehoucq, R. B., Sorensen, D. C. & Yang, C. 1997 *ARPACK User's Guide: Solution of Large Scale Eigenvalue Problems with Implicitly Restarted Arnoldi Methods*. SIAM.

Lemke, C. E. & Howson, J. T. 1964 Equilibrium points of bimatrix games. *J. Appl. Math.* **12**, 413–423.

Logue, R. P. 2008 *Stability and Bifurcations Governed by the Triple Deck and Related Equations*. Ph.D. Thesis, University of Manchester.

Marquillie, M. & Ehrenstein, U. 2002 Numerical simulation of separating boundary layer flow. *J. Computers and Fluids* **31**, 683–693.

Marquillie, M. & Ehrenstein, U. 2003 On the onset of nonlinear oscillations in a separating boundary layer flow. *J. Fluid Mech* **490**, 169–188.

Marxen, O. & Henningson, D. 2007 Direct numerical simulation of a short laminar separation bubble and early stages of the bursting process. *J. Fluid Mech.* **96**, 235–243.

Nakamura, I. & Watanabe, T. 1985 Laminar boundary layer on a rotating circular cylinder in an axial flow. *J. Bulletin of JSME* **28 No. 243**, 1893–1898.

Owen, P. R. & Klanfer, L. 1955 On the laminar boundary layer separation from the leading edge of a thin aerofoil. *ARC Conf.Proc.220* **Proc.220**, 1–14.

Pauley, L. L., Moin, P. & Reynolds, W. C. 1990 The structure of two-dimensional separation. *J. Fluid Mech* **220**, 397–411.

Prandtl, L. 1905 Ueber fluessigkeitsbewegung bei sehr kleiner reibung. *III. Inter. Math. Kongr.* pp. 484–491.

Rheinboldt, W. C. 1986 *Numerical Analysis of Parameterized Nonlinear Equations*. Wiley-Interscience, New York.

Ruban, A. I. 1981 Asymptotic theory of short separation regions on the leading edge of a slender airfoil. *Izvestya Academii Nauk SSSR, Mekhanika Zhidkosti i Gaza 1,*

42-51 (Fluid Dynamics, Engl. Trans.) **17**, 33–41.

Salinger, A. G., Bou-Rabee, N. M., Pawlowski, R. P., Wilkes, E. D., Burroughs, E., Lehoucq, R. B. & Romero, L. A. 2002 *LOCA1.1 Library of Continuation Algorithms: Theory and Implementation Manual*. SAND.

Seydel, R. 1994 *Practical Bifurcation and Stability Analysis*. Springer Verlag.

Stewartson, K., Smith, F. T. & Kaups, K. 1982 Marginal separation. *Studies in Applied Mathematics* **67**, 45–61.

Sychev, V. V., Sychev, V. V., Ruban, A. I. & Korolev, G. L. 1998 *Asymptotic Theory of Separated Flows*. Cambridge University.

Trefethen, L. N. 2000 *Spectral Methods in Matlab*. SIAM.